

Medische Bibliotheek  
2006 E.U.R. 125

# Cardiac regeneration by cell therapy

Several chapters of this thesis are based on published papers, which are reproduced with permission of the co-authors and the publishers. Copyright of these papers remains with the publishers.

ISBN 10: 90-9020919-0  
ISBN 13: 978-9020919-7

Cover design: Rieteke Peteroff, adapted from “Het joodse bruidje” by Rembrandt Harmensz. van Rijn (ca. 1665), with permission of the Rijksmuseum Amsterdam.

Lay-out: E.J. van den Bos

Printed by PrintPartners Ipskamp, Deventer  
© 2006, E.J. van den Bos

# Cardiac regeneration by cell therapy

## Cardiale regeneratie door cel therapie

Proefschrift

ter verkrijging van de graad van doctor aan de Erasmus Universiteit  
Rotterdam op gezag van de rector magnificus

Prof. dr. S.W.J. Lamberts

en volgens besluit van het College voor Promoties.

De openbare verdediging zal plaatsvinden op 25 oktober  
2006 om 13:45

door

**Ewout-Jan van den Bos**  
geboren te Rotterdam

## Promotiecommissie

Promotores	:	Prof. dr. D.J. Duncker
	:	Prof. dr. M.L. Simoons
Overige leden	:	Prof. dr. W.J. van der Giessen
	:	Prof. dr. P.A. Doevendans
	:	Prof. dr. S. Janssens

Financial support by the Netherlands Heart Foundation for the publication of this thesis is gratefully acknowledged.





# Contents

## Part 1: Introduction

- Chapter 1. General introduction and outline of the thesis. 11  
van den Bos EJ, Davis BH, Taylor DA. *J Heart Lung Transplant* 2004;23:1217-27 and van den Bos EJ, Taylor DA. *Minerva Cardioangiol* 2003;51:227-43.

## Part 2: Animal models for cell transplantation studies

- Chapter 2. A novel model of cryoinjury-induced myocardial infarction 57  
in the mouse: a comparison with coronary artery ligation.  
van den Bos EJ, Mees BME, de Waard MC, de Crom R, Duncker DJ.  
*Am J Physiol Heart Circ Physiol* 2005;289:H1291-1300.

## Part 3: Injection techniques

- Chapter 3. Video-assisted thoracoscopic transplantation of myoblasts 83  
into the heart.  
Thompson RB, Parsa CJ, van den Bos EJ, Davis BH, Toloza EM, Klem I, Glower DD, Taylor DA. *Ann Thorac Surg* 2004;78:303-7.

## Part 4: Survival of cells after intracardiac transplantation

- Chapter 4. Dynamics of myoblast necrosis and apoptosis after 97  
transplantation into a myocardial infarction.  
van den Bos EJ, de Waard MC, Davis BH, Bergen JM, Taylor DA, Duncker DJ. Submitted.

## Part 5: Functional assessment of cell transplantation

- Chapter 5. Functional assessment of myoblast transplantation for 117  
cardiac repair with magnetic resonance imaging.  
van den Bos EJ, Thompson RB, Wagner A, Mahrholdt H, Morimoto Y, Thomson LE, Wang LH, Duncker DJ, Judd RM, Taylor DA. *Eur J Heart Fail* 2005;7:435-43.
- Chapter 6. A comparison of intracardiac cell transplantation: 137  
autologous skeletal myoblasts versus bone marrow cells.  
Thompson RB, Emani SM, Davis BH, van den Bos EJ, Morimoto Y, Craig D, Glower D, Taylor DA. *Circulation* 2003;108:II264-71.

<b>Part 6: Tracking cells after intramyocardial transplantation using magnetic resonance imaging</b>	
Chapter 7. Improved efficacy of stem cell labeling for magnetic resonance imaging studies by the use of cationic liposomes. van den Bos EJ, Wagner A, Mahrholdt H, Thompson RB, Morimoto Y, Sutton BS, Judd RM, Taylor DA. <i>Cell Transplant</i> 2003;12:743-56.	157
Chapter 8. High-resolution magnetic resonance imaging of iron-labeled myoblasts using a standard 1.5-T clinical scanner. Zhang Z, van den Bos EJ, Wielopolski PA, de Jong-Popijus M, Duncker DJ, Krestin GP. <i>MAGMA</i> 2004;17:201-9.	179
Chapter 9. <i>In vitro</i> imaging of single living human umbilical vein endothelial cells with a clinical 3.0-T MRI scanner. Zhang Z, van den Bos EJ, Wielopolski PA, de Jong-Popijus M, Bernsen MR, Duncker DJ, Krestin GP. <i>MAGMA</i> 2005;18:175-85.	197
Chapter 10. Magnetic resonance imaging of hemorrhage within reperfused myocardial infarcts. van den Bos EJ, Baks T, Moelker AD, Kerver W, van Geuns RJ, van der Giessen WJ, Duncker DJ, Wielopolski PA. <i>Eur Heart Journal</i> 2006;27:1620-6..	221
Chapter 11. General discussion, conclusions and future directions	241
Chapter 12. Summary - Samenvatting	263
Chapter 13. Colour section	271
Acknowledgments	291
List of publications	295
Curriculum Vitae	299

# Part 1

## Introduction



# Chapter 1

## General introduction and outline of the thesis

Adapted from:

van den Bos EJ, Davis BH, Taylor DA. *J Heart Lung Transplant* 2004;23:1217-27 and

van den Bos EJ, Taylor DA. *Minerva Cardioangiol* 2003;51:227-43.



During the last fifty years, we have seen enormous progress in the prevention and treatment of acute myocardial infarction (MI), one of the most prominent diseases in the Western world.<sup>1,2</sup> As a result, the incidence and prevalence of acute MI has gradually declined, and mortality and morbidity have been reduced. However, due to the increased lifespan post MI, the incidence of congestive heart failure (CHF) is rapidly increasing.<sup>2-4</sup>

Heart failure directly results from the death or dysfunction of cardiomyocytes and an inability of the heart to effectively regenerate this damaged region. These pathophysiological events lead to a process of cardiac remodeling that involves fibrosis, changes in wall stress, scar expansion and - if the injury is large enough - heart failure. Although pharmacological treatment has significantly improved survival, with further progression of heart failure, heart transplantation is the only current definitive treatment option.

At present, no approved clinical therapy treats the underlying defect in ischemic injury: the death of cardiomyocytes. As a result, heart failure has become the most prevalent cardiovascular disease in this century<sup>2-5</sup> and will likely strain health care costs as patients live longer.

In the last few years, cell therapy has emerged as a possible treatment for many types of disease.<sup>6</sup> Transplanting cells that are able to differentiate and replace dead or dysfunctional cardiomyocytes and vasculature, that may prevent transition to adverse remodeling or can induce cardiac regeneration via paracrine mechanisms could be a definitive therapy for cardiac ischemic injury.

The first study, describing the feasibility of transplanting myoblasts, the precursor cells of skeletal muscle, after MI was published in 1992.<sup>7</sup> In 1998, the first pre-clinical therapeutic benefit of transplanted myoblasts was demonstrated.<sup>8</sup> Since then, a number of cell types have been transplanted into injured myocardium with promising results.

## Endogenous cells for cardiac repair

Although the primary focus of most researchers to date has been on transplanting exogenous cells to repair injured myocardium, some very recent studies suggest that the myocardium may be capable of endogenous repair. Three main cell types have been suggested to take part in this process: adult cardiomyocytes,<sup>9-11</sup> bone marrow-derived progenitor cells<sup>12-17</sup> and putative cardiac stem cells.<sup>18-27</sup>

Several studies have reported the presence of cycling cardiomyocytes after MI, contrasting the traditional paradigm that the heart is a post-mitotic organ.<sup>9-11</sup> Multiple groups have delivered growth factors such as Granulocyte Colony Stimulating Factor (G-CSF)<sup>12</sup> or cytokines, such as High-Mobility Group Box 1 (HMGB1)<sup>13</sup> to mice prior to infarction and demonstrated significant cardiac repair secondary to mobilization of endogenous progenitor cells. Furthermore, studies in transplanted human hearts showed that, on histology, Y chromosome-positive cardiomyocytes could be found in male recipients of female donor hearts.<sup>14-16</sup> This suggests that cells from the recipient were able to migrate to the heart, engraft and differentiate into cardiomyocytes: A process referred to as cardiac chimerism.

However, in most studies a very low level, 0.2% to 1%, of cardiomyocytes was estimated to be of recipient origin.<sup>14,16</sup> Yet, in one study it was estimated to be as high as 30%,<sup>15</sup> but in this study several technical issues could have lead to a falsely high result.<sup>28,29</sup> This low level of cardiomyocyte formation contrasts with the repopulation of other cell types by endogenous cells in transplanted hearts: ~24% of endothelial cells and ~12% of Schwann cells were estimated to be derived from endogenous sources.<sup>17</sup>

Cardiac stem cells (CSCs) can be isolated from the myocardium and resemble the side population cells that can also be found in many other types of tissue, such as skeletal muscle or bone marrow.<sup>18</sup> These cardiac stem cells share in different proportions the stem cell-related antigens c-kit, MDR1, and Sca-1.<sup>19-22</sup> These cells, further, do not express markers of other cell lineages such as BMCs or myoblasts and are therefore lineage-negative. The number of CSCs per heart has been difficult to assess. It is estimated that this number is very limited: about 1 CSC per ~8.000 to ~40.000 myocardial cells.<sup>23,24</sup> The regenerative potential has been described in mouse and rat studies: When putative CSCs were injected into hearts directly or via intracoronary administration after MI, cells were reported to transdifferentiate in multiple cardiac lineages, thereby regenerating myocardium, preventing remodeling and ameliorating heart function.<sup>18,25,26</sup>

More recently, a cardiac progenitor cell was described, which could be identified by the presence of the Isl1 transcription factor, so called cardioblasts.<sup>27</sup> Although the presence of Isl1+ cells within the postnatal heart is very limited, about 40% of myocytes seem to be originally derived from these cardioblasts. These cells can be isolated, purified, cultured and cloned, and adopt a fully mature cardiomyocyte phenotype *in vitro*.<sup>27</sup> However, thus far the regenerative capacity of these cells *in vivo* still needs to be determined.

Taken together, these data suggest that the injured myocardium may be capable of repair. However, given the high number of patients that progress to heart failure after suffering a MI, this endogenous repair is incapable of meeting the physiological demand and of adequately repairing the damaged heart.

## Exogenous cells for cardiac repair

### Transplantation of cardiomyocytes

The most logical answer to the shortage of cardiomyocytes after MI might seem to be transplantation of cardiomyocytes into the scarred heart to regenerate part of the infarct region. Autologous, adult cardiomyocytes are preferred over embryonic,<sup>30</sup> neonatal<sup>31</sup> or fetal cardiomyocytes,<sup>32,33</sup> since the latter require immunosuppression. There have been several reports describing the beneficial effects of adult appendage or left ventricular (LV) septum-derived cardiomyocyte transplantation in rats<sup>34</sup> and pigs.<sup>35</sup> The transplanted cells engraft and form junctions with other grafted cells and with the host myocardium and are electrophysiologically integrated as evidenced by synchrony of calcium transients between donor and host cells.<sup>36</sup> However, the survival and engraftment of these adult cardiomyocytes, as quantified by the replacement of scar volume, is extremely small, presumably because a

large part of the adult cells are unable to survive within the hypoxic scar.<sup>37</sup> An alternative to this problem could be transplantation of embryonic, fetal or neonatal cardiomyocytes, which are more resistant to ischemia. This type of transplantation can yield stable, but small, grafts in rats with a corresponding increase in function.<sup>30-33</sup> However, this improvement in function is not consistent and was not observed in more chronic infarctions.<sup>38</sup>

These data suggest that, for effective repair, survival of the transplanted cardiomyocytes has to be significantly improved. Yet, this is difficult given the inability to replicate cardiomyocytes *in vitro* and their extreme sensitivity to ischemia *in vitro* and *in vivo*.

### Other cell types for cardiac repair

The original idea behind cell-based cardiac repair is that cells, when transplanted into the infarcted heart, can survive and receive sufficient cues to mature into appropriate cell types to regenerate myocardium, or increase contractility. Theoretically, a range of cell types could mediate repair including a host of stem and progenitor cells, but also undifferentiated or dedifferentiated tissue-derived cells. In addition to cardiomyocytes already discussed, they include embryonic stem cells (ESCs), umbilical cord blood cells,<sup>39</sup> tissue-derived fibroblasts,<sup>40</sup> smooth muscle cells,<sup>41</sup> circulating endothelial progenitor cells (EPCs),<sup>42</sup> adipose tissue-derived cells,<sup>43</sup> skeletal muscle progenitors or myoblasts and bone marrow-derived mesenchymal, endothelial and hematopoietic stem or progenitor cells. Myoblasts and bone marrow-derived cell types are discussed further down.

ESCs have several features that make them an excellent candidate for cellular cardiac therapy: (1) They have an unlimited proliferation potential<sup>44</sup> and (2) ESCs can form cardiomyocytes<sup>45,46</sup> with a distinct electrophysiologic<sup>47-49</sup> and contractile phenotype.<sup>50,51</sup> Several studies have demonstrated the feasibility of transplanting ESCs *in vivo*, using both mouse<sup>52-55</sup> as well as human<sup>56-58</sup> ESCs: The transplanted cells formed large proliferating grafts and integrated with host myocardial tissue. Although ESCs provide an exciting framework for cardiac repair, at present several issues limit their usefulness. The first is their very nature of being uncommitted to a given lineage. For example, although ESCs are capable of forming cardiomyocytes *in vitro*, they are not growth arrested *in vivo* and thus can potentially form teratomas after transplantation, especially if unpurified cells are used.<sup>59</sup> Therefore, purification methods should be developed that eliminate the risk of teratoma formation. A second disadvantage is the possible immune response against allogeneic cells. Finally, ethical issues still play a role in limiting the use of human embryonic cells for research.

Umbilical cord blood contains pluripotent cell populations. Recently, a human cell population was described with differentiation capacity into a variety of cell lines, including cardiomyocytes, the unrestricted somatic stem cells or USSCs.<sup>60</sup> Direct implantation of these cells after MI in a pig model improved regional perfusion and wall motion as well as global function.<sup>61</sup> Cells could be identified in the infarct region after 4 weeks. Although promising, these results could not be reproduced in our own laboratory in a pig model with intracoronary

injection of USSCs (data submitted for review). Restricted movement through the coronary vessel wall could be an explanation for this. More study is definitely needed to estimate the potential of these cells.

The use of EPCs for regenerative therapy were first described in hind-limb ischemia models.<sup>42</sup> These cells originate from bone-marrow, can be isolated from peripheral blood by CD34+ selection and grow well on fibronectin under conditions favoring endothelial cell differentiation. Early studies showed incorporation of these cells into newly formed vessels, thereby augmenting neovascularization of the infarct or ischemic area and improving global cardiac function.<sup>62,63</sup> These cells were also shown to be able to transdifferentiate into cardiomyocytes during coculture experiments with native cardiomyocytes,<sup>64</sup> although these experiments could not be reproduced by other laboratories.<sup>65</sup> Lately, several reports question the potential of these cells to contribute anatomically to neovascularization by incorporation into the vessel wall and suggest a paracrine pathway that induces new vessel growth by secretion of pro-arteriogenic growth factors. This will be discussed in the section on bone marrow-derived cells. Despite these controversies, the initial enthusiasm about EPCs was the trigger for the first large clinical trials using peripheral blood-derived EPCs in Germany.

## **Myoblasts for cardiac repair**

The first cell type that was used for cardiac repair in pre-clinical studies is the progenitor cell from adult skeletal muscle, the myoblast. Myoblasts were initially chosen to repair the damaged heart because they normally develop into striated muscle, can contract and can self-renew. Their normal function is, in fact, to regenerate skeletal muscle after injury or trauma. Applying this regenerative capacity to myocardium could result in new muscle grafts at the site of infarction. Since this thesis mainly focuses on cardiac regeneration using myoblasts several practical aspects of cell transplantation will be introduced using this cell type as a guideline.

### **Advantages and disadvantages of myoblasts for cardiac repair**

Using autologous skeletal myoblasts for transplantation overcomes many limitations associated with other cell-based treatments. First, using self-derived autologous cells generally removes the need for immunosuppression. Next, the large number of cells needed for functional cardiac improvement can be obtained from a relatively small muscle biopsy, so there is no shortage of donor tissue. Further, myoblasts are the only progenitor cells in the human body that normally develop a contractile apparatus, which makes them more likely to restore contractile function in the damaged fibrous region of the heart. Importantly, no ethical dilemma accompanies the use of myoblasts, as it does the use of allogeneic cells or ESCs. Since autologous myoblasts are primary cells, they do not possess significant risk of tumor formation associated with immortalized cell lines. Finally, myoblasts and muscle fibers are highly resistant to ischemia, which makes them better able to survive the hypoxic conditions within a MI.

Nonetheless, the use of myoblasts also has some theoretical disadvantages. For example, their very commitment to the myogenic lineage could preclude them from adapting to the cardiac workload or the cardiac electrical milieu. Similarly, their low level of connexin 43 expression<sup>66,67</sup> raises the question whether myoblasts are capable of electrical coupling with the surrounding myocardium<sup>68,69</sup> or whether arrhythmicity might be induced by their electrical properties.

### **Myoblast therapy in practice**

For myoblast therapy to succeed, several criteria must be met. The transplanted cells need to be (1) easily obtainable or expandable *in vitro*, (2) deliverable at the right location in the heart, (3) able to survive and engraft in sufficient numbers, (4) able to differentiate towards a phenotype that is adapted to cardiac work, (5) be electromechanically integrated without (6) significant side effects.

### ***Myoblasts culture***

Myoblasts are grown from biopsies of muscle with a high content of oxidative muscle fibers, to get cells better adapted to the cardiac workload.<sup>70-73</sup> The different muscles used are soleus muscle in rabbit,<sup>8</sup> semitendinosus or -membranosus in pigs<sup>74</sup> and tibialis anterior or extensor digitorum longus<sup>75,76</sup> in rats. Mouse myoblasts are usually isolated from all muscles from the hindleg or back.

A sufficient number of cells to repopulate an infarct scar comprising 20% of the left ventricular volume, can be grown from a biopsy of ~0.5 g in rabbits<sup>8</sup> or ~5 g in pigs. The usual biopsy size in humans is ~5 to 10 g. Most aponeurotic and fibrous tissue is removed from these biopsies. Most groups use enzymatic digestion in trypsin or collagenase to free the myoblasts from the basal lamina. The studies described in this thesis used mechanical mincing to 1 mm<sup>3</sup> pieces, which are plated down in DMEM and fetal bovine serum.<sup>8,77</sup> By triturating the muscle pieces at day 3, myoblasts are detached from the basal lamina and attach to the culture dish and start proliferating. This method results in a highly purified population of myoblasts, with desmin percentages above 90% after 3 weeks.<sup>77</sup> In addition to these two methods, myoblasts can also be obtained from single muscle fibers placed in a culture dish.<sup>78</sup> Myoblasts migrate from the fiber into the culture dish and can then be expanded *in vitro*, however, this method is no longer frequently used.

The muscle cells can then be expanded for 2 or 3 weeks to yield for example a total of 10<sup>8</sup> myoblasts from a 0.5 g rabbit biopsy. The cells are passaged when reaching 60-70% confluence, usually 3 or 4 times before injection. Passaging is kept to a minimum so the cells keep their proliferative capacity.

### ***Myoblast delivery***

There are several ways to inject myoblasts into the heart. These can be roughly divided into 5 techniques: Injection of cells via the epicardial surface; injection of cells via the endocardial

surface; injection of cells via the coronary sinus and through the venous wall; injection of cells into the coronary arterial circulation and injection of cells retrogradely into the venous system, where the last 4 methods are catheter-based techniques. Thus far the feasibility of the first 4 techniques have been demonstrated in both pre-clinical as well as clinical studies. Theoretically, cells can be delivered via injection into a peripheral vein, however, this technique has not been studied extensively and will not be discussed here.

The epicardial technique can be performed during open chest surgery<sup>79</sup> or via an endoscopic approach.<sup>80,81</sup> The epicardial approach offers several advantages over the endocardial technique. First, because the epicardium is under direct vision, the location of injected cells relative to the infarct area can be exactly determined. Secondly, delivery of cells can be performed parallel to the epicardial surface, which enables cell delivery in a large area of scar. Since a large number of cells can be delivered along the whole parallel needle tract, only a few injections are needed to cover a large part of the infarct area. Finally, confirmation of cell delivery is possible with the epicardial approach.

A less invasive endoscopic approach is described in this thesis, which retains the advantage of epicardial injection but does not require an open chest procedure.<sup>80,81</sup> Via this endoscopic video-assisted thoracoscopic (VATS) method, cells can be delivered in the anterior, lateral and posterior LV wall by several parallel injections. Further development of this minimally invasive technique could mean a breakthrough, with great benefit in clinical practice: Patients with comorbidity, not eligible for open heart surgery, could undergo this procedure with less peri-operative risk.

Endocardial delivery is performed using catheters with a retractable needle at the tip. Under fluoroscopy, by using electromechanical mapping systems<sup>74,82,83</sup> or combined fluoroscopy and magnetic resonance imaging (MRI) guidance,<sup>84,85</sup> the catheter tip can be maneuvered to the infarct area. This method has the advantage that it does not require general anesthesia and is minimally invasive, so it is suitable for very ill patients. However, the endoscopic approach limits cell delivery to multiple small needle tracts perpendicular to the surface of the heart and requires many injections to deliver a large dose of cells. Furthermore, since it is catheter-based, there is a substantial risk for cardiac perforation. Thus, cells are usually delivered in the peri-infarct zone, or only in infarct regions where the wall is thicker than 5 mm. Locating these infarct regions during the procedure can be difficult, even with electromechanical mapping systems. Nonetheless, endoventricular delivery of skeletal myoblasts makes this technique feasible in patients who are not candidates for surgery.

A further limitation of catheter-based cell delivery is the small dose of the perpendicular injections. A recently developed method that has overcome this limitation is the use of transvascular catheters, through which cells can be delivered via a catheter placed in the coronary sinus and moved through the coronary veins to the site of infarction.<sup>86,87</sup> This catheter can penetrate the wall of the coronary vein and inject cells in a more parallel geometry, similar to that obtained by epicardial delivery.

Technically the most sophisticated method for cell delivery is injection into the

coronary arteries. In a rabbit model, coronary delivery of myoblasts resulted in the presence of myoblasts in the perivascular area one week after injection, confirming the possibility that myoblasts can adhere to and cross the vascular endothelium.<sup>88</sup> This could be repeated in Langendorff perfused rat hearts.<sup>89</sup> The mechanisms that are responsible for the translocation of cells across the vessel wall are not clear, especially since myoblasts are thought not to migrate into the bloodstream under normal conditions.<sup>90</sup> One possible explanation might be that translocation is favoured by transient ischemia that results from capillary plugging.<sup>81</sup> Techniques to improve myoblast adhesion to the wall and migration into the scar area, could therefore be of further benefit. Despite these advantages, the number of intracoronary injected cells migrating through the vessel is small compared with direct injection techniques, furthermore a substantial risk for coronary embolism exists.<sup>89</sup>

A last method, without the risk for coronary embolism, is retrograde injection into the coronary venous system.<sup>92,93</sup> Furthermore, this technique has a large distribution area.

Each of the described methods has its advantages and disadvantages. A direct comparison is therefore needed to establish to best technique that yields a high number of grafted myoblasts at the right location with effective myocardial regeneration and functional benefit.

Aside from delivery technique, the best location of cell delivery also remains unclear. Thus far no study has directly assessed the relation between injection site and the efficiency of myoblast transplantation. Generally spoken, in animal studies, the center of the infarct has been chosen as the site of injection, whereas in clinical studies the peri-infarct zone is the location of choice. One study has suggested that reducing graft isolation from the surrounding normal myocardium may improve graft integration and electromechanical coupling,<sup>94</sup> whereas other investigators propose that injection into the center of the scar is less likely to allow development of re-entry circuits. Theoretically, cells injected into the periphery of the scar may experience improved vascular perfusion from the surrounding myocardium.

### ***Myoblast survival and engraftment***

It has been shown that the efficacy of myoblast transplantation depends on the number of transplanted myoblasts. Therefore, hypothetically, interventions aimed at improving myoblast survival and engraftment could improve the success of myoblast transplantation. Thus far, several quantitative studies have been performed on the number of surviving myoblasts in the heart and demonstrated various interventions to improve this survival<sup>95-97</sup> These include heat shock treatment of myoblasts<sup>95</sup> and pharmacological interventions aimed at attenuating oxidative stress<sup>96</sup> or inflammation.<sup>97</sup> These studies were performed in mouse models with healthy, non-infarcted hearts. In this thesis, a mouse infarct model was used for quantitative assessment of myoblast survival. All four studies showed a similar pattern of surviving myoblast numbers: The first minutes after injection a major part of myoblasts is lost, ranging from 60 to 82%, followed by a more gradual disappearance up to 24 hours

after injection. In previous studies<sup>95-97</sup> the immediate loss after injection was attributed to hyperacute cell death, however the study described in this thesis shows that limited cell retention plays an even more important role. These studies further showed that proliferation starts 12 to 24 hours after injection.

These data resemble studies performed in the field of Duchenne Muscular Dystrophy (DMD), where generally a large percentage of cell death is observed in the hours after injection.<sup>98-100</sup> In some studies, 90% cell death is reported during the first hour after injection.<sup>98</sup> Even though in DMD transfer therapy the injected cells are allogeneic, some comparisons with autologous intracardiac myoblast transplantation can be made. The cell death in DMD transplantation seems to be largely attributed to the inflammatory process in the muscle, since cells engineered to express anti-inflammatory markers can reduce cell death to a marked degree.<sup>100</sup> Multiple investigators have reported that delivery of cells in the first week after MI, when the inflammatory process is still markedly upregulated, decreases cell survival.<sup>101</sup> A second observation in DMD transfer therapy is that cell survival improves when a preplated fraction of cells with more undifferentiated myoblasts are used.<sup>102,103</sup> A similar technique has yet to be tested in intracardiac myoblast transplantation.

### *Differentiation of myoblasts in the heart*

After they are injected into the infarct area, myoblasts adhere to the surrounding collagen matrix and begin to proliferate or differentiate into myotubes.<sup>8,104</sup> Myotubes are generally observed after 3 days. A portion of the injected cells remain mononuclear. Likely, these cells are part of the proliferating population.<sup>105</sup> The proliferation capacity of myoblasts after injection is highly preserved in some areas, since they are able to replace up to ~75% of the transmural infarct with striated myotubes by 3 weeks after injection.<sup>8</sup> The area where they engraft does not always correspond with the needle tract along which they have been delivered. This suggests that they are able to migrate to a certain extent through the infarct tissue to a favourable engraftment site (unpublished data). The formed muscle cells are viable without any signs of apoptosis, even though apoptosis is visible in the fibrous region of the scar area, secondary to the ongoing remodeling process.<sup>8</sup>

All myotubes observed in the infarct area are positive for skeletal muscle markers, such as desmin or myogenin.<sup>8</sup> After 1 week, myotubes start expressing fast myosin heavy chain (MHC), and after 3 weeks, expression of slow MHC is observed.<sup>104</sup> A high percentage of the myotubes co-express both markers.<sup>105</sup> This expression pattern differs significantly from the skeletal muscle from which the biopsies were taken, suggesting that the cardiac environment or the cardiac workload alters the developmental program of the myoblasts to better comply with the continuous contraction of the heart. This expression pattern is also observed in human studies after autopsy.<sup>106</sup>

Myoblasts transplanted into cryoinjured myocardium appear to have multiple fates. In some cases cells appear to mature into multinucleated myotubes as would be expected in skeletal muscle. In other cases, they remain as more undifferentiated cells or

they undergo a phenotypical change to a more cardiac-like phenotype.<sup>107-110</sup> This phenotypic change or transdifferentiation of myoblasts into cardiomyocytes, is further suggested by the expression of phospholamban after 6 weeks *in vivo* – a protein normally only expressed in cardiac muscle.<sup>110</sup> Similarly, expression of the cardiac calcium ATPase SERCA-1 has been seen in intracardiac transplanted myoblasts.<sup>111</sup> Furthermore, limited expression of Troponin I, cardiac-MHC and connexin 43 has been reported.<sup>112</sup> Although these data suggest that myoblasts are indeed capable to transdifferentiate to a more cardiac phenotype, this conversion is strongly debated.<sup>113</sup> Strictly spoken, transdifferentiation describes the process of conversion of one committed cell into another with a distinct phenotype. For proof of myoblast transdifferentiation, several criteria should be met. The first criterion is that the transdifferentiated cells should be derived from the transplanted cells and not from host cells present in the scar area or from circulating cells. Secondly, it should be ruled out that non-myoblast progenitor cells, such as bone marrow-derived mesenchymal stem cells (MSCs), that contaminate the transplanted cells, are responsible for the differentiation to the cardiac phenotype. Thirdly, proof of transdifferentiation requires that the possibility of fusion between myoblasts and cardiomyocytes is ruled out. The first reports did not meet these criteria. More recently, cell fusion was demonstrated to occur at the graft host interface between myoblasts and cardiomyocytes.<sup>114</sup> Although a rare event, it probably accounts for the earlier reports of transdifferentiation.

### ***Electromechanical integration of transplanted myoblasts***

To be able to perform cardiac work, the transplanted cells should be able to electromechanically integrate with the surrounding host myocardium. However, there is a marked difference in the electromechanical innervation of skeletal and cardiac muscle. In skeletal muscle, each myotube is separately innervated by its own neuronal motor unit. The muscle action potential is generated at the motor end-plate and propagated via the cell membrane. In adult skeletal muscle, a very small number of gap junctions are formed. When myoblasts are isolated and expanded *in vitro*, the expression of gap junctions is markedly upregulated.<sup>67</sup> However, when they are switched to differentiation conditions to form myotubes, this expression disappears.<sup>115</sup> In cardiac muscle, the action potential is propagated via cell-cell contact through gap junctions. Therefore, proof of electromechanical integration of transplanted myoblasts would be expression of these gap junctions between host cardiomyocytes and transplanted cells. Normally though, the transplanted cells are surrounded by dense scar tissue. This scar tissue does not conduct electrical current, making action potential propagation into the grafted area unlikely.

The major gap junction protein in the myocardium is connexin 43. Expression of this protein in transplanted myoblasts has been observed in some studies at the site of donor and host cell contact by immunohistochemistry.<sup>112,116</sup> Furthermore, several investigators have reported the formation of junctions that resemble gap junctions on light or electron microscopy between the transplanted myoblasts and between cardiomyocytes

and myoblasts.<sup>107,108</sup> The cells expressing these junctions showed a distinct cardiomyocyte-like morphology as mentioned above. *In vitro*, myoblasts were shown to be able to form gap junctions with cardiomyocytes during coculture experiments. The same study showed that cocultures of myoblasts and cardiomyocytes can be electrically stimulated and contract synchronously.<sup>117</sup> Despite these observations, dye transfer experiments did not show electromechanical coupling in muscle explants.<sup>68</sup> In another study, a small population of transplanted myoblasts was observed that showed calcium transients in synchrony with host cardiomyocytes, implying electromechanical coupling.<sup>69</sup> However, at the same sites fused myoblasts and cardiomyocytes were observed, connexin 43+, that could have accounted for this observation. Furthermore, the calcium transients showed skeletal muscle-like characteristics. Although these results are convincing and argue against effective functional coupling between myoblasts and host myocardium, other “atypical” donor-derived junctions can play a role, such as heterotypic junctional complexes<sup>118</sup> or fibroblast-myocyte coupling.<sup>119</sup> Another explanation for the earlier observations of junctional complexes could be that these junctions are similar to the so called “low-resistance junctions” that are formed by myoblasts just prior to fusing to myotubes.<sup>120</sup>

In one study, myoblasts were genetically engineered to express high levels of connexin 43.<sup>115</sup> This study showed that it is possible to clone myoblasts that express high levels of connexin 43 after differentiation to myotubes. Furthermore, the transformed cells showed more rapid differentiation than controls, implying that there is an important role for connexin 43 during differentiation. Whether these cells show improved electromechanical coupling after injection into the heart remains to be investigated.

### ***Effects of myoblast transplantation on heart function and LV remodeling***

The efficacy of myoblast transplantation after MI has been shown in different animal models, including: mouse,<sup>89,121</sup> rat,<sup>87,122-134</sup> rabbit,<sup>8,77,135,136,137</sup> sheep<sup>105</sup> and dogs.<sup>138</sup> The functional improvement is seen both *in vivo* as well as *ex vivo* in the Langendorff model.<sup>125</sup> Myoblast transplantation improves global parameters of function such as ejection fraction, developing left ventricular pressure and dP/dt, and regional parameters such as stroke work at the infarct site,<sup>8,135,136,137</sup> wall thickening<sup>77</sup> and myocardial tissue velocities.<sup>105</sup> In a rat model, it was shown that the improvement in function is more pronounced in animals with a lower ejection fraction before myoblast transplantation.<sup>124</sup> Furthermore, the improvement in function is highly dependent on the number of injected cells.<sup>139</sup> Myoblast transplantation can also improve global heart function in models of doxorubicin-induced heart failure,<sup>140,141</sup> using both coronary and direct epicardial injections.

Myoblast grafting also improved diastolic properties of the infarct region, with improved compliance.<sup>8,136,137</sup> These data are further supported by the fact that transplanted fibroblasts that did not differentiate into a contractile phenotype, did not improve systolic function but had a beneficial effect on diastolic function similar to myoblasts, by increasing compliance of the scar.<sup>40</sup> The recognition that myoblast transplantation improves diastolic

function is especially important, since recently more attention is focused on the effects of diastolic dysfunction on the development of CHF.<sup>142</sup> However, it is not clear whether the diastolic improvement is caused by restoring active relaxation of the transplanted cells, or by a change in viscoelastic properties of the wall. Studies in larger animals using pressure/volume loops to study myocardial stiffness during diastole could be a valuable tool. Magnetic resonance imaging to characterize stress-strain relations or volume transients during diastolic ventricular filling is another option.

Myoblast transplantation also prevents deleterious morphological changes that are characteristic for left ventricular remodeling.<sup>8,92,125,132</sup> It prevents thinning of the left ventricular wall at the site of the infarct as well as the increase in end-diastolic and -systolic volumes. These effects are sustained even after 1 year in a sheep model.<sup>105</sup>

Although the mentioned studies show that myoblast transplantation has a beneficial regional and global effect on cardiac function, some comments should be made. It is possible that part of these effects can be attributed to a change in viscoelastic properties of the wall rather than to synchronous contraction of transplanted myoblasts with the myocardium. Further, it is possible that the decrease in wall thinning and end-diastolic volumes prevent a decrease in global pump function. It has also been suggested that secretion of cytokines and angiogenic factors can lead to an increase in global function of the heart by modulating remodeling of the remote myocardium.<sup>68,125</sup> Furthermore, there are some limitations to the use of color kinesis echocardiography and tissue Doppler imaging: These techniques measure regional movement and might therefore be influenced by cardiac motion or changes in cardiac load. Similarly, sonomicrometry only provides a measurement of change in scar length, but not of systolic thickening. Assessment of wall thickening by MRI needs high temporal resolution, especially with smaller animal models with high heart rates, to discern active thickening from passive post-systolic thickening. Newer echocardiography and MRI techniques such as strain and strain rate imaging, combined with dobutamine stress echocardiography or MRI might be useful in the future to more accurately assess the impact of the transplanted cells on regional function.<sup>143</sup> In conclusion, although several studies show an improvement in regional function and support the idea that the transplanted cells can contract synchronously with the surrounding myocardium, more data is needed to proof this hypothesis and other mechanisms should not be excluded.

### ***Safety of myoblast transplantation***

A possible deleterious effect of myoblast transplantation is the potential arrhythmogeneity of the cells caused by their differing electrical properties. As discussed above, electromechanical integration of myoblasts is limited in the first place due to their inability to form gap junctions and secondly due to their dihydropyridine phenotype, which is markedly different from cardiomyocytes.<sup>144,145</sup> Since myoblast transplantation results in isolated islands of skeletal muscle tissue, mostly surrounded by scar tissue, re-entry circuits can be formed. Furthermore, fusion events between cardiomyocytes and myoblasts can cause heterogeneous calcium

transients.<sup>69</sup> All these events can cause fatal arrhythmias. This can account for the modest rate in sudden death of treated animals.

However, so far only one animal study has been performed to adequately investigate this issue.<sup>146</sup> The concern about the safety of myoblast transplantation has risen since patients have shown sustained ventricular tachycardia (VT) shortly after myoblast transplantation.<sup>147</sup> The risk of VT seems to be elevated in the treated patient population. It must be remarked however, that these patients are merely suffering from end-stage heart disease, with a risk of arrhythmias that is already markedly increased. Furthermore, treatment with amiodarone seems to successfully lower the risk of ventricular arrhythmias.

## Bone marrow cells for cardiac repair

The first enthusiasm about the potential of bone marrow cells (BMCs) for cardiac repair arose in 1998 when it was reported that BMCs can contribute to skeletal muscle regeneration.<sup>148</sup> Since then several studies examined intracardiac transplantation of different types of bone marrow-derived cells. This enthusiasm was stimulated by several *in vitro* studies showing transdifferentiation of bone marrow-derived MSCs into cardiomyocytes, with the co-administration of 5-azacytidine,<sup>149,150</sup> that beat and express cardiomyocyte-specific markers. These cells also express functional adrenergic and muscarinic receptors<sup>150</sup> and have cardiac action potential characteristics.<sup>151</sup> This led to the hope that this process of transdifferentiation might occur *in vivo* to the same extent, thereby generating new heart muscle at the infarct site.

Most earlier studies of intracardiac BMC transplantation used the fraction enriched for hematopoietic stem cells (HSCs). In the first studies, few donor-derived cardiomyocytes were found although donor-derived endothelial cells were far more common (about ~1000 fold).<sup>152</sup> Larger-scale cardiac myocardial regeneration was reported in 2001:<sup>12,153</sup> Infarcted mouse hearts were injected with HSCs expressing the stem cell antigen c-kit. Up to ~68% of the infarct was regenerated by donor-derived cardiomyocytes and vascular structures. The new muscle restored contractility in the infarct scar, thereby improving global heart function. Although the regeneration of new myocardium with improvement in function by HSCs was repeatedly reported afterwards,<sup>154</sup> the ability of these cells to regenerate the heart is questioned more recently. Three important factors contribute to this: First, the discovery of fusion events between native cardiomyocytes and donor cells,<sup>155-158</sup> which can explain some of the earlier reports of transdifferentiation, second, the possibility of false-positive results when using only immunohistochemistry for detection of newly formed myocardium<sup>59</sup> and third, the recognition that the plasticity of HSCs is less than previously assumed.<sup>159-161</sup>

Other bone marrow-derived cells are less controversial such as the MSC fraction, bone marrow-derived EPCs or bone marrow-derived mononuclear cells (MNCs), whereas the last cell type has been used widely in clinical trials. MSCs reside in the stromal compartment of bone marrow and normally support hematopoiesis. Their multilineage potential was first described in 1999,<sup>162</sup> as well as their capacity to differentiate into cardiomyocytes *in vitro*<sup>149</sup>

and *in vivo*,<sup>150</sup> which was accompanied by an improvement in global heart function and induction of angiogenesis. Since then several small (mouse,<sup>163</sup> rats<sup>164-166</sup> and rabbits<sup>135,167</sup>) and large (dogs<sup>168</sup> and pig<sup>169,170</sup>) animal studies were performed. All these studies showed an improvement in global function and differentiation of donor cells into cardiomyocytes or vascular structures. A recently published randomised double-blind placebo-controlled study in pigs showed a significant improvement in both systolic as well as diastolic function together with an improvement in ejection fraction, which was accompanied by a reduction in infarct size and formation of new myocardium.<sup>170</sup> An advantage of this type of BMCs seems their immunomodulatory effect on their environment permitting them to survive allo-transplantation.<sup>170,171</sup> Furthermore, these cells seem to be suitable for gene-targeting therapy.<sup>172,173</sup> One important observation is that the intracoronary administration leads to microinfarctions possibly due to their bigger size as compared with HSCs.<sup>174</sup>

Bone marrow-derived EPCs, also called angioblasts, are less-well described in the literature and less characterized. Work on these cells was mainly done by one group resulting in two important reports. In the first paper, human angioblasts were isolated by CD34+ selection and injected into athymic, infarcted rat hearts.<sup>175</sup> Isolation was facilitated by G-CSF mobilization. These cells were shown to incorporate into the infarct vasculature in contrast with CD34- cells, thereby reducing cardiomyocyte apoptosis and improving cardiac function. In a second study, this effect was shown to be dose-dependent and furthermore, angioblast transplantation resulted in regeneration of myocardium by inducing cardiomyocyte cycling.<sup>176</sup> However, several authors have questioned the process of direct incorporation of bone marrow-derived cells into the vascular wall and instead propose a different mechanism: The development of neovasculature or collateral vessels could be induced by pro-arteriogenic factors secreted by the transplanted bone marrow-derived cells, possibly by the presence of large numbers of monocytes in these fractions.<sup>177,178</sup>

## Characterization of cell fate after transplantation

The ability to monitor cells after transplantation and determine cell fate is of critical importance. Especially since attention is focused more and more on cell types such as bone-marrow-derived cells with a variable capability of transdifferentiation, causing controversy about results. Several methods have thus far been employed to either determine cell fate with histology or non-invasively with newer imaging techniques in living animals or patients. These methods are used for cell tracking with the goal to determine: (1) cell location, (2) cell morphology, (3) cell survival, (4) cell proliferation, (5) cell differentiation and (6) cell fusion. First of all, to determine the location of cells between surrounding host cells, the transplanted cells need to have a unique identifier, such as a cell label or a unique intrinsic genetic difference with surrounding host cells.

Intrinsic genetic differences have, for example, been widely used in DMD studies,<sup>98</sup> where the transplanted cells can be identified by immunohistochemistry or *in situ* hybridization for the dystrophin gene, which is only expressed by the donor cells. In cardiac

cell therapy, the presence of myoblasts can be determined by immunohistochemistry using skeletal muscle markers that are only expressed by the myoblasts itself.<sup>8</sup> In other studies, *in situ* identification of Y-chromosome specific genes has been used after transplantation of male cells into female hosts.<sup>154</sup> The advantages of using intrinsic genetic differences, is that potentially adverse cell processing is not required to label cells before transplantation and immunohistochemistry is a relatively easy method, facilitated by a wide array of available antibodies. A disadvantage is that cells can transdifferentiate, thereby losing their unique genetic tag. Furthermore, since it is a “secondary” analysis, proper interpretation of staining requires suitable microscopic techniques that differentiate between background staining and cell staining and that can attribute staining to the right cells.<sup>28</sup>

To label cells pre-transplantation using non-genetic markers, several methods have been used thus far. The most important ones are: Fluorescent vital dyes that stain nuclei,<sup>77</sup> cytoplasm<sup>104</sup> or cell membranes<sup>134</sup> and metabolic labeling using modified nucleotides that incorporate into the donor cell DNA during culturing, such as tritiated thymidine<sup>104</sup> or bromodeoxyuridine.<sup>7</sup> A potential disadvantage of using vital dyes is that they can be released to surrounding cells after transplantation, either spontaneously or after cell necrosis. Another disadvantage that applies to both methods is that when cells proliferate, the marker is “diluted” thereby losing its detectability.

The use of genetic markers implies either transfecting cells with a reporter gene or using donor cells-derived from transgenic animals that carry lineage-restricted or ubiquitously expressed reporter genes.<sup>161</sup> Traditional gene transfer has its limitations in cell transplantation studies since transfection is mostly inefficient and cells lose their expression over time. Using viral vectors can improve efficiency, but reporter gene silencing is a well-known problem and virally encoded proteins can potentially induce an immune response. Cells isolated from transgenic animals do not have these disadvantages, however their use precludes autologous transplantation, thereby necessitating immunosuppression with unknown side-effects, furthermore making new transgenic animals for specific purposes requires years.

In order to monitor cells non-invasively after transplantation multiple imaging techniques have been explored. These newer modalities make it possible to determine cell fate during the course of the study, thereby identifying early determinators of the efficacy of cell transplantation. The two imaging modalities preferentially used these days are magnetic resonance imaging (MRI) and nuclear imaging. For non-invasive monitoring the success of the imaging technique depends on several characteristics, for example the minimum number of cells that can be detected, its temporal resolution and the availability of suitable non-toxic contrast agents for cell labeling.

MRI has several advantages over other imaging modalities: It offers high-resolution 3D imaging of the whole body and can detect cells up to single cell resolution.<sup>179-181</sup> Furthermore, interventional techniques have been developed to monitor real-time catheter-based cell injections.<sup>182</sup> Finally, MRI combines the possibility to image cell location and trafficking

with assessment of cardiac function and determination of location and extent of myocardial ischemia and infarction using delayed enhancement techniques. The most widely used MRI contrast agents for cellular labeling are iron oxide-based contrast agents, such as the dextran coated iron oxide particles. These include the (ultrasmall) superparamagnetic iron oxide particles, (U)SPIOs, as well as the monocrystalline iron oxide nanoparticles (MIONs).<sup>183,184</sup> These agents cause signal voids due to their magnetic susceptibility effect. They seem to be the preferred contrast agent currently. This is mainly due to their following properties: They induce the most change in signal per unit of metal and they are composed of biodegradable iron, which can thus be degraded and re-used by cells. In contrast, gadolinium-chelates, are less biocompatible, with potential toxicity following dechelation over time.<sup>184</sup>

To allow for successful cell detection *in vitro* and *in vivo*, non-toxic, high intracellular uptake of iron oxide is required. Several methods have been used in the past such as lectins<sup>185</sup> that increase uptake by cells, linking iron oxide to HIV tat peptide,<sup>186</sup> antibodies that bind to cell surface receptors<sup>187</sup> and are then internalized and iron oxide agents that are negatively charged thereby enhancing uptake.<sup>188</sup> However, one of the most successful methods developed, is the use of commercially available, transfection reagents, normally employed for genetic transfection of cells.<sup>189,190</sup> By combining transfection reagents with iron oxide preparations, endosomes are formed, which are easily taken up by a wide variety of cells. The amount and type of transfection reagent needs to be carefully titrated to prevent precipitation and the effect on cell behaviour needs to be carefully assessed for each cell type since some cell types seem to be inhibited in their normal differentiation by the labeling procedure<sup>191</sup> and toxic effects have been observed at high concentrations of transfection reagent or iron oxide.<sup>181</sup> The total amount of iron taken up by individual cells is in the range of 5 to 20 pg per cell, which primarily depends on the cell type.<sup>184</sup>

With the use of iron oxide contrast agents, detection up to single cell resolution is possible *in vitro* and detection of small clusters of cells is possible *in vivo*.<sup>192</sup> Several studies have investigated cell tracking after intracardiac injection within myocardial infarcts in mouse,<sup>193,194</sup> rabbit<sup>195</sup> and pig models.<sup>85,196-198</sup> It has been shown in several studies that transplanted cells can be followed for several weeks after transplantation into myocardial infarcts. Furthermore, MR-compatible injection catheters have been developed specifically for delivery of magnetically labeled therapeutics, such as cells.<sup>84</sup>

One disadvantage of using iron oxide agents for cell tracking within myocardial infarcts is that hemoglobin degradation products such as hemosiderin also have a strong magnetic susceptibility effect, thereby possibly hampering reliable detection of iron oxide-labeled cells.<sup>199</sup> Furthermore, the disadvantages of cell labeling methods mentioned above, such as label dilution and uptake of the label by surrounding cells after cell death also apply to iron oxide labeling. Another limitation of using iron oxide labeling is the difficulty discriminating between labeled cells, appearing as "black holes" and image artefacts. Furthermore, the signal loss induced by the presence of the labeled cells prevents MR evaluation of the tissue in question. Despite these disadvantages, the first "in human" studies

are being conducted, using iron oxide labeling for determining cell fate after transplantation for several clinical applications.<sup>200</sup>

Nuclear imaging techniques include single photon emission computed tomography (SPECT) and positron emission tomography (PET).<sup>201</sup> Cells are normally labeled by direct incubation with the radionuclide such as <sup>111</sup>In oxine<sup>202</sup> or <sup>18</sup>F-fluorodeoxyglucose.<sup>203</sup> Thus far successful cell tracking was demonstrated using these methods after intraventricular injection as well as intravenous injection in rats<sup>202,204,205</sup> and pigs.<sup>206</sup> Furthermore, in humans cells could be located in the infarct area after intracoronary injection.<sup>203</sup> Disadvantages of this technique include the lower spatial resolution in comparison to other modalities such as MRI. Furthermore, similar disadvantages as with iron oxide agents apply to radionuclides such as label dilution and uptake by surrounding cells. This is even more important in nuclear imaging because of the half-life of the radionuclide. Some of these disadvantages can be circumvented by the use of reporter gene nuclear imaging: A reporter gene of choice is transfected to the donor cells.<sup>207</sup> After transplantation a radionuclide that specifically binds to the reporter gene product is then injected, which causes accumulation of the radionuclide in the donor cells. Because this injection can be repeated, decay of the radionuclide is not a problem. Furthermore, because the reporter gene is only active when the donor cells are viable, the resulting signal can be attributed to the surviving cells.

Other non-invasive imaging techniques that can potentially become useful in cell transplantation studies include ultrasound imaging and optical bioluminescence imaging in small animals. Since these methods have not been studied thus far for cardiac cell transplantation studies, they will not be discussed here.

## Clinical studies on cell transplantation

### Myoblasts

Myoblast transplantation into the heart entered the clinical arena in early 2000, when a patient with severe CHF underwent this procedure during a coronary artery bypass grafting (CABG) operation by Philippe Ménasche in Paris.<sup>79</sup> Since then seven phase I safety and feasibility trials have been performed. Five of those were studies involving myoblast transplantation as an adjunct to CABG,<sup>147,208-211</sup> one involved endoventricular injections of myoblasts<sup>82</sup> and the last study used a coronary sinus approach.<sup>86</sup> Generally, patients are in heart failure class 2-3, with 2 to 3 vessel coronary disease and an ejection fraction ranging between 20 and 40%. Myoblasts are injected into akinetic scar regions. The number of cells injected ranges between 10 million to 1.2 billion. So far, some conclusions can be drawn: All studies involving CABG with adjunctive myoblast implantation documented increased EF and 3 studies showed increased regional function by echo in myoblast injected segments. However, since in those studies, myoblast-injected segments were also revascularized, this functional improvement cannot be exclusively attributed to the injected myoblasts. Secondly, the injection procedure itself appears to be safe. However, in 4 of 10 patients reported in the first study by Ménasche,<sup>147</sup> VTs developed in the first weeks after the procedure. It is unclear

whether they were procedure related. Yet, we cannot ignore the implication that electrical abnormalities are a real possibility. Antiarrhythmic drugs such as amiodarone seem to have been successfully used to prevent recurrent VTs in most of these patients. Furthermore, in most study protocols, implantable cardioverter defibrillators (ICDs) are now prophylactically implanted.

Thirdly, histological analysis of explanted human hearts after transplantation or at autopsy showed that the injected myoblasts differentiated to myotubes, even at 17.5 months after delivery.<sup>209,211,212</sup> These myotubes showed alignment parallel to the host tissue and were embedded in scar tissue.

Phase II trials on myoblast transplantation have started. One large multicenter double-blind placebo-controlled dose-ranging randomized study is implemented in France by the Ménasche group. This study will have contractility of the grafted regions as primary end-point. Furthermore, the incidence of arrhythmias will be closely monitored by implantable defibrillators in all patients. More patients are being included and follow-up data are pending.

### **Bone marrow-derived cells**

In contrast with myoblasts, BMCs moved much faster from pre-clinical studies to clinical trials, probably because extensive experience was already in place for bone marrow as a source for cell therapy. The first study of BMC transplantation was reported in 2002<sup>213</sup> and described intracoronary delivery of MNCs 7 days after acute MI. Since then, several clinical trials have been completed and are still under way, mainly focusing on cell therapy for acute MI, in contrast with myoblast studies that, thus far, mainly involved chronic ischemic heart disease. Most of the earlier acute MI clinical trials that have been completed were observational and used non-randomized control groups, all applying intracoronary injections.<sup>213-215</sup> These earlier studies showed the feasibility and safety of the procedure and suggested an improvement in global as well as regional function. Furthermore, these studies suggested an improvement in regional perfusion of the infarct area. Thus far, 3 randomized controlled studies were reported.<sup>216-218</sup> The first study was the BOOST trial, which included a total of 60 patients.<sup>216</sup> Bone marrow MNCs were injected into the infarct coronary artery 6 days after infarction in 30 patients and functional improvement at 6 months, as measured by MRI, was significantly more after cell transplantation (EF increased from 50.0 to 56.7% versus 51.3 to 52% in controls). However, the control group did not receive a bone marrow aspiration and sham injection: Therefore, a possible role of cytokine release during aspiration or a preconditioning effect of the repeated balloon inflation during injection of cells cannot be excluded. Recently, the 18-months outcomes of this study were reported: Rather disappointingly, no long-term benefits of BMC transplantation could be demonstrated in comparison with controls. This suggests that BMCs may accelerate recovery of function but do not provide a sustained, long term effect. In a second randomized controlled trial, the open-label control group did receive a bone marrow aspiration and sham injection.<sup>217</sup> This study reported an improvement in

regional as well as global function, a reduction in LV volumes and increased metabolism in the injected area as visualized by  $^{18}\text{F}$ -fluorodexoyglucose uptake. However in this study a different subset of BMCs was used: the MSC fraction. These cells have the ability to differentiate into multiple mesenchymal cell types such as fat, bone and cartilage as well as cardiomyocytes. Furthermore cells were injected much later after MI, with an average of 18 days, making a comparison with other studies more difficult. The first double-blind randomized placebo-controlled trial was reported in March 2006.<sup>218</sup> This trial included 33 patients with BMC transplantation and 34 patients with placebo injection 24 hours after acute MI. This trial showed no improvement in global LV function and no reduction in LV volumes or regional perfusion or metabolism. However, contrast enhanced MRI showed a significantly larger reduction in infarct volumes after BMC transplantation as compared with controls suggesting a beneficial effect on infarct remodeling. Furthermore, a trend was visible towards an enhanced recovery of regional function after BMC transplantation in patients with larger infarcts. However, in this trial cells were injected rather early, 24 hours, after infarction in contrast with other studies (3 days to 3 weeks after infarction), which might explain these differences.

Several trials investigated BMC transplantation for chronic MI. These trials were all small non-randomized open label studies. Cells were either injected via an endoventricular<sup>219</sup> or intracoronary route<sup>220</sup> or via a surgical route during CABG.<sup>221,222</sup> All studies reported beneficial effects of BMC transplantation on global function, reduction in LV volumes as well as an improvement in regional function, perfusion and metabolism. Furthermore, a marked reduction in infarct size was reported in one study suggesting new formation of heart muscle at the infarct site.<sup>220</sup>

Finally, the effect of BMC transplantation on refractory angina was investigated. In two phase I non-controlled trials, cells were injected via an endoventricular route with the help of an electromechanical mapping system (NOGA).<sup>223,224</sup> These trials mainly demonstrated an improvement in subjective symptoms, possibly as a result of the angiogenic potential of the injected cells.

In summary, the early BMC trials demonstrated the feasibility of the transplantation procedure, either via the intracoronary, endoventricular or surgical route. Thus far, one trial raised some concerns about safety, suggesting that injection of CD133+ progenitors is associated with increased incidence of coronary events.<sup>215</sup> No concerns about arrhythmogeneity, as with myoblast transplantation, have arisen so far.

## Aims and outline of the thesis

Although cell transplantation has already moved to clinical trials, still several more basic questions remain unanswered. Probably the main question is:

*What is the exact mechanism of functional improvement observed in pre-clinical as well as clinical studies?*

This is an important question, since the success of cell transplantation can only be improved when the cellular mechanisms of functional improvement are known. In order to be able to answer this question in the future, several aspects of cell transplantation, outlined below, still need evaluation in a pre-clinical setting.

Myoblasts have thus far been the most widely used cell type for intracardiac cell transplantation. Furthermore, myoblast populations are well-characterized, easy to grow and to transplant with high efficiency and thus form a suitable platform to elucidate several aspects of cell transplantation. Therefore the general aim of this thesis is:

*To evaluate several aspects of cell transplantation, such as animal models, injection techniques, cell survival, functional benefit and non-invasive imaging modalities thereby mainly focusing on myoblasts.*

## Animal models for cell transplantation studies

Various animal models are available for cell transplantation studies. Although larger animal models with a physiology similar to human physiology are necessary to evaluate the benefit of transplantation of a certain cell type before clinical trials can be initiated, mouse models do offer several advantages over larger animal models. These include practical aspects such as low cost and high-throughput as well as the possibility to use transgenic mice as donors and recipients. The most widely used mouse model of MI is LAD ligation. This model has several disadvantages: LAD ligation results in large, aneurysmatic infarcts of variable size with extensive infarct remodeling. This is not ideal for cell transplantation studies: Cell injection in a remodeled thin infarct is a difficult procedure, cells cannot be localized easily after extensive remodeling, infarcts of variable size hamper evaluation of anti-remodeling strategies since large numbers of animals are required. Therefore in **chapter 2** a novel mouse MI model is evaluated using cryoinjury. This method involves a liquid nitrogen-cooled cryoprobe that freezes part of the anterior wall. The effect of cryoinjury on global cardiac function is studied using echocardiography and left ventricular pressure measurements. Furthermore, remodeling of the infarct and remote myocardium is studied over time by histological and geometrical analysis, as well as reperfusion of the infarct area. Subsequently, the outcomes after cryoinjury are compared with LAD ligation.

### **Injection techniques**

Thus far, the most widely used cell injection method in clinical trials is via the coronary artery. Although this a well-established technique, it assumes that cells can cross the vessel barrier and home into the infarct area, an assumption that has not been extensively studied thus far. Direct injection during thoracotomy hypothetically offers many advantages over catheter-based methods such as direct visualization of the injection site and procedure. However, thoracotomy is an extensive operation with high comorbidity, thereby excluding very ill patients from this intervention. In order to combine the advantages of direct cell injection with an intervention with less morbidity we evaluated video-assisted thoracoscopic (VATS) myoblast implantation in a clinically-relevant pig model in **chapter 3**. For this purpose a prototype cell injection device was constructed in combination with standard VATS instruments. The efficacy of cell delivery was assessed by MRI.

### **Survival of cells after intracardiac transplantation**

Although improvement of the cell injection procedure will enhance cell delivery and cell retention, the resulting cell engraftment depends for a great deal on cell survival and proliferation. Several studies have indicated, regardless of cell type that survival is extremely limited the first days, in the order of 10 to 20%. However, thus far the exact dynamics of cell death during the first hours after transplantation, as well as the dominant mechanism, i.e. necrosis or apoptosis is not known. Therefore in **chapter 4** the dynamics of myoblast death after intracardiac transplantation are studied using the mouse cryoinfarction model that is evaluated in **chapter 2**. The mechanisms of myoblast death are investigated by using a novel histological method: Alizarin Red staining. This staining method has not been used thus far for determining cell necrosis after intracardiac transplantation. Apoptosis is studied using Tunel staining in combination with blocking studies using the broad-spectrum caspase inhibitor ZVAD-FMK. The role of oxidative stress in the acute cell death is evaluated using the anti-oxidant Tempol.

### **Functional assessment of cell transplantation**

Improvement of heart function after myoblast transplantation has been documented in multiple small and large animal models. Most studies used parameters of global function, few studies documented improved regional function using echocardiography or micromanometry. These studies suggested improvement in regional contractility as a result of synchronous contraction of transplanted myoblasts or rescue of ischemic myocardium within the infarct or border zones. The first phase I clinical studies also documented an improvement in regional function. Despite these results, there is still an ongoing debate whether myoblasts truly participate in an active contractile syncytium with the surrounding myocardium. Several more mechanistic studies documented hyperexcitability in transplanted myoblasts as well as contractile activity independent of the surrounding cardiomyocytes, arguing against a functional, electrically integrated syncytium.

An imaging method that is able to measure global and regional function as well as left ventricular geometry at the same time is MRI. Furthermore, MRI can identify the exact site of infarction by using contrast enhanced imaging. Therefore we postulated that MRI would be a suitable method to assess regional function by measurement of wall thickening at the infarct site after transplantation of myoblasts in a rabbit model of cryoinjury-induced MI. This study is described in **chapter 5**. Autologous myoblasts are cultured for 3 weeks and then injected into a 3-week old infarct. MRI is performed before injection as well as 4 weeks later. Wall thickening is measured at the infarct site as well as in the remote myocardium. Left ventricular wall volume and infarct volumes are calculated. Furthermore, immunohistochemistry is used to determine the fate of the transplanted myoblasts.

Bone marrow-derived cells are nowadays the cell types most widely used in clinical studies. A variety of cell types can be derived from bone marrow, each with its own distinct characteristics and differentiation capabilities. Several bone marrow-derived cell types have been reported to be able to transdifferentiate into myogenic cells such as cardiomyocytes, for example the MSCs. This would imply that bone marrow-derived cells are able to improve regional contractility to the same extent as myoblasts if the hypothesis is true that the transplanted cells are indeed electromechanically integrated with the surrounding myocardium. Therefore we used the same rabbit cryoinfarction model as described in **chapter 5** and transplanted myoblasts and MSCs into the infarct region 2 weeks after infarction. This study is described in **chapter 6**. Regional stroke work at the infarct site was assessed using micromanometry and sonomicrometry instead of MRI, since this method was evaluated extensively in previous studies. Histology of the infarct tissue was used to identify differentiation into contractile cells by immunohistochemistry for contractile proteins.

### **Tracking cells after intramyocardial transplantation using magnetic resonance imaging**

**Chapter 5 and 6** both used immunohistochemistry to determine cell fate after transplantation. The location of the transplanted cells was determined by fluorescent labeling with a nuclear marker. The disadvantage of this labeling method is that the transplanted cells cannot be tracked non-invasively at an earlier time point. Early non-invasive detection could potentially supply additional information on parameters that determine the success of cell transplantation. Several non-invasive imaging methods have been adapted for cell tracking, these include MRI and nuclear imaging. Therefore the experience gained in **chapter 5** with MRI of rabbit hearts was used to develop a non-invasive method for tracking autologous myoblasts after intracardiac transplantation. To be detectable with MRI, cells need to be labeled with contrast agents. Thus far the contrast agents that generate the highest contrast-to-noise ratios are iron oxide-based contrast agents, such as superparamagnetic iron oxide or SPIO. However, cellular uptake is limited when cells are directly incubated with these agents. Therefore in **chapter 7** we evaluate a novel method to label rabbit myoblasts with SPIO using cationic liposomes that are normally employed as transfection reagents. The uptake

of SPIO is compared with standard incubation of cells with SPIO without those liposomes. The uptake is quantified by a phenanthroline assay. Furthermore, the effect of the labeling method on proliferation, differentiation and viability of the cells is assessed. To demonstrate the feasibility of the labeling method for *in vivo* cell detection, labeled myoblasts are injected into cryoinjured rabbit hearts, the model described in **chapter 5 and 6**, which are then scanned with a standard clinical MRI scanner.

The detectability of injected cell groups by *in vivo* magnetic resonance imaging will probably be different from *in vitro* detectability of single cells. To determine the *in vitro* detectability of cells, in **chapter 8** the same labeling method is evaluated for labeling of pig myoblasts using similar parameters. Furthermore, in this study the possibility to image fixed, single myoblasts *in vitro* is assessed. In **chapter 9** the labeling and imaging of single, living, proliferating human umbilical vein endothelial cells (HUVECs) is studied over longer time periods.

SPIO labeling could be used in clinical studies to determine cell fate by MRI, since several FDA-approved SPIO contrast agents exist. However, in clinical practice, acute MI is treated by rapid reperfusion therapy. Reperfusion can cause reperfusion injury, microvascular obstruction and damage, resulting in hemorrhage. It is known that hemorrhage degradation products such as hemosiderin have a strong magnetic susceptibility effect, which could hamper detection of iron oxide-labeled cells. To investigate this potential confounding factor, a clinically relevant, MI model is set up in pigs in **chapter 10**. Infarcts are created by balloon occlusion followed by reperfusion after 2 hours, approximating the clinical setting closely. Infarcts are scanned *in vivo* and *ex vivo* after 1 week and 5 weeks. Injections of HUVECs, labeled according to the protocol described in **chapter 9**, are performed *ex vivo* to determine the detectability of these cells against a background of hemorrhage-induced signal voids.

Finally in the general discussion in **chapter 11**, the results of the studies in this thesis are evaluated and conclusions are drawn. Furthermore, an outline for future studies is proposed.

## References

1. Braunwald E. Evolution of the management of acute myocardial infarction: a 20th century saga. *Lancet* 1998;352:1771-4.
2. Heidenreich PA, McClellan M. Trends in treatment and outcomes for acute myocardial infarction: 1975-1995. *Am J Med* 2001;110:165-74.
3. Hellermann JP, Jacobsen SJ, Gersh BJ, Rodeheffer RJ, Reeder GS, Roger VL. Heart failure after myocardial infarction: a review. *Am J Med* 2002;113:324-30.
4. Braunwald E. The Denolin lecture. Congestive heart failure: a half century perspective. *Eur Heart J* 2001;22:825-36.
5. Zannad F, Briancon S, Juilliere Y, Mertes PM, Villemot JP, Alla F, Virion JM. Incidence, clinical and etiologic features, and outcomes of advanced chronic heart failure: The EPICAL study. *J Am Coll Cardiol* 1999;33:734-42.
6. Lovell-Badge R. The future for stem cell research. *Nature* 2001;414:88-91.
7. Marelli D, Desrosiers C, El-Alfy M, Kao RL, Chiu RCJ. Cell transplantation for myocardial repair: an experimental approach. *Cell Transplant* 1992;1:383-90.
8. Taylor DA, Atkins BZ, Hungspreugs P, Jones TR, Reedy MC, Hutcherson KA, Glower DD, Kraus WE. Regenerating functional myocardium: improved performance after skeletal muscle myoblast transplantation. *Nat Med* 1998;4:929-33.
9. Kajstura J, Leri A, Finato N, Di Loreto C, Beltrami CA, Anversa P. Myocyte proliferation in end-stage cardiac failure in humans. *Proc Natl Acad Sci USA* 1998;95:8801-5.
10. Anversa P, Kajstura J. Ventricular myocytes are not terminally differentiated in the adult mammalian heart. *Circ Res* 1998;83:1-14.
11. Beltrami AP, Urbanek K, Kajstura J, Yan SM, Finato N, Bussani R, Nadal-Ginard B, Silvestri F, Leri A, Beltrami CA, Anversa P. Evidence that human cardiac myocytes divide after MI. *N Engl J Med* 2001;344:1750-7.
12. Orlic D, Kajstura J, Chimenti S, Limana F, Jakoniuk I, Quaini F, Nadal-Ginard B, Bodine DM, Leri A, Anversa P. Mobilized bone marrow cells repair the infarcted heart, improving function and survival. *Proc Natl Acad Sci USA* 2001;98:10344-9.
13. Limana F, Germani A, Zacheo A, Kajstura J, Di Carlo A, Borsellino G, Leoni O, Palumbo R, Battistini L, Rastaldo R, Muller S, Pompilio G, Anversa P, Bianchi ME, Capogrossi MC. Exogenous high-mobility group box 1 protein induces myocardial regeneration after infarction via enhanced cardiac C-kit<sup>+</sup> cell proliferation and differentiation. *Circ Res* 2005;97:73-83.
14. Laflamme MA, Myerson D, Saffitz JE, Murry CE. Evidence for cardiomyocyte repopulation by extracardiac progenitors in transplanted human hearts. *Circ Res* 2002;90:634-40.
15. Quaini F, Urbanek K, Beltrami AP, Finato N, Beltrami CA, Nadal-Ginard B, Kajstura J, Leri A, Anversa P. Chimerism of the transplanted heart. *N Engl J Med* 2002;346:5-15.

16. Hruban RH, Long PP, Perlman EJ, Hutchins GM, Baumgartner WA, Baughman KL, Griffin CA. Fluorescence in situ hybridization for the Y-chromosome can be used to detect cells of recipient origin in allografted hearts following cardiac transplantation. *Am J Pathol* 1993;142:975-80.
17. Minami E, Laflamme MA, Saffitz JE, Murry CE. Extracardiac progenitor cells repopulate most major cell types in the transplanted human heart. *Circulation* 2005;112:2951-8.
18. Beltrami AP, Barlucchi L, Torella D, Baker M, Limana F, Chimenti S, Kasahara H, Rota M, Musso E, Urbanek K, Leri A, Kajstura J, Nadal-Ginard B, Anversa P. Adult cardiac stem cells are multipotent and support myocardial regeneration. *Cell* 2003;114:763-76.
19. Hierlihy AM, Seale P, Lobe CG, Rudnicki MA, Megeney LA. The post-natal heart contains a myocardial stem cell population. *FEBS Lett* 2002;530:239-43.
20. Urbanek K, Torella D, Sheikh F, De Angelis A, Nurzynska D, Silvestri F, Beltrami CA, Bussani R, Beltrami AP, Quaini F, Bolli R, Leri A, Kajstura J, Anversa P. Myocardial regeneration by activation of multipotent cardiac stem cells in ischemic heart failure. *Proc Natl Acad Sci USA* 2005;102:8692-7.
21. Linke A, Muller P, Nurzynska D, Casarsa C, Torella D, Nascimbene A, Castaldo C, Cascapera S, Bohm M, Quaini F, Urbanek K, Leri A, Hintze TH, Kajstura J, Anversa P. Stem cells in the dog heart are self-renewing, clonogenic, and multipotent and regenerate infarcted myocardium, improving cardiac function. *Proc Natl Acad Sci USA* 2005;102:8966-71.
22. Urbanek K, Rota M, Cascapera S, Bearzi C, Nascimbene A, De Angelis A, Hosoda T, Chimenti S, Baker M, Limana F, Nurzynska D, Torella D, Rotatori F, Rastaldo R, Musso E, Quaini F, Leri A, Kajstura J, Anversa P. Cardiac stem cells possess growth factor-receptor systems that following activation regenerate the infarcted myocardium improving ventricular function and long-term survival. *Circ Res* 2005;97:663-73.
23. Leri A, Kajstura J, Anversa P. Cardiac stem cells and mechanisms of myocardial regeneration. *Physiol Rev* 2005;85:1373-416.
24. Anversa P, Kajstura J, Leri A, Bolli R. Life and death of cardiac stem cells: a paradigm shift in cardiac biology. *Circulation* 2006;113:1451-63.
25. Messina E, De Angelis L, Frati G, Morrone S, Chimenti S, Fiordaliso F, Salio M, Battaglia M, Latronico MV, Coletta M, Vivarelli E, Frati L, Cossu G, Giacomello A. Isolation and expansion of adult cardiac stem cells from human and murine heart. *Circ Res* 2004;95:911-21.
26. Dawn B, Stein AB, Urbanek K, Rota M, Whang B, Rastaldo R, Torella D, Tang XL, Rezazadeh A, Kajstura J, Leri A, Hunt G, Varma J, Prabhu SD, Anversa P, Bolli R. Cardiac stem cells delivered intravascularly traverse the vessel barrier, regenerate infarcted myocardium, and improve cardiac function. *Proc Natl Acad Sci USA* 2005;102:3766-71.

27. Laugwitz KL, Moretti A, Lam J, Gruber P, Chen Y, Woodard S, Lin LZ, Cai CL, Lu MM, Reth M, Platoshyn O, Yuan JX, Evans S, Chien KR. Postnatal isl1+ cardioblasts enter fully differentiated cardiomyocyte lineages. *Nature* 2005;433:647-53.
28. Taylor DA, Hruban R, Rodriguez ER, Goldschmidt-Clermont PJ. Cardiac chimerism as a mechanism for self-repair: does it happen and if so to what degree? *Circulation* 2002;106:2-4.
29. Jackson KA, Snyder DS, Goodell MA. Skeletal muscle fiber-specific green autofluorescence: potential for stem cell engraftment artifacts. *Stem Cells* 2004;22:180-7.
30. Roell W, Lu ZJ, Bloch W, Siedner S, Tiemann K, Xia Y, Stoecker E, Fleischmann M, Bohlen H, Stehle R, Kolossov E, Brem G, Addicks K, Pfitzer G, Welz A, Hescheler J, Fleischmann BK. Cellular cardiomyoplasty improves survival after myocardial injury. *Circulation* 2002;105:2435-41.
31. Muller-Ehmsen J, Peterson KL, Kedes L, Whittaker P, Dow JS, Long TI, Laird PW, Kloner RA. Rebuilding a damaged heart: long-term survival of transplanted neonatal rat cardiomyocytes after myocardial infarction and effect on cardiac function. *Circulation* 2002;105:1720-6.
32. Li RK, Jia ZQ, Weisel RD, Mickle DA, Zhang J, Mohabeer MK, Rao V, Ivanov J. Cardiomyocyte transplantation improves heart function. *Ann Thorac Surg* 1996;62:654-60.
33. Scorsin M, Hagege AA, Marotte F, Mirochnik N, Copin H, Barnoux M, Sabri A, Samuel JL, Rappaport L, Menasche P. Does transplantation of cardiomyocytes improve function of infarcted myocardium? *Circulation* 1997;96:II188-93.
34. Sakai T, Li RK, Weisel RD, Mickle DA, Kim EJ, Tomita S, Jia ZQ, Yau TM. Autologous heart cell transplantation improves cardiac function after myocardial injury. *Ann Thorac Surg* 1999;68:2074-80.
35. Li RK, Weisel RD, Mickle DA, Jia ZQ, Kim EJ, Sakai T, Tomita S, Schwartz L, Iwanochko M, Husain M, Cusimano RJ, Burns RJ, Yau TM. Autologous porcine heart cell transplantation improved heart function after a myocardial infarction. *J Thorac Cardiovasc Surg* 2000;119:62-8.
36. Rubart M, Pasumarthi KB, Nakajima H, Soonpaa MH, Nakajima HO, Field LJ. Physiological coupling of donor and host cardiomyocytes after cellular transplantation. *Circ Res* 2003;92:1217-24.
37. Zhang M, Methot D, Poppa V, Fujio Y, Walsh K, Murry CE. Cardiomyocyte grafting for cardiac repair: graft cell death and anti-death strategies. *J Mol Cell Cardiol* 2001;33:907-21.
38. Sakakibara Y, Tambara K, Lu F, Nishina T, Nagaya N, Nishimura K, Komeda M. Cardiomyocyte transplantation does not reverse cardiac remodeling in rats with chronic myocardial infarction. *Ann Thorac Surg* 2002;74:25-30.
39. Kadner A, Hoerstrup SP, Tracy J, Breyman C, Maurus CF, Melnitchouk S, Kadner G,

- Zund G, Turina M. Human umbilical cord cells: a new cell source for cardiovascular tissue engineering. *Ann Thorac Surg* 2002;74:S1422-8.
40. Hutcheson KA, Atkins BZ, Hueman MT, Hopkins MB, Glower DD, Taylor DA. Comparison of benefits on myocardial performance of cellular cardiomyoplasty with skeletal myoblasts and fibroblasts. *Cell Transplant* 2000;9:359-68.
  41. Li RK, Jia ZQ, Weisel RD, Merante F, Mickle DA. Smooth muscle cell transplantation into myocardial scar tissue improves heart function. *J Mol Cell Cardiol* 1999;31:513-22.
  42. Asahara T, Murohara T, Sullivan A, Silver M, van der Zee R, Li T, Witzenbichler B, Schatteman G, Isner JM. Isolation of putative progenitor endothelial cells for angiogenesis. *Science* 1997;275:964-7.
  43. Planat-Benard V, Menard C, Andre M, Puceat M, Perez A, Garcia-Verdugo JM, Penicaud L, Casteilla L. Spontaneous cardiomyocyte differentiation from adipose tissue stroma cells. *Circ Res* 2004;94:223-9.
  44. Amit M, Carpenter MK, Inokuma MS, Chiu CP, Harris CP, Waknitz MA, Itskovitz-Eldor J, Thomson JA. Clonally derived human embryonic stem cell lines maintain pluripotency and proliferative potential for prolonged periods of culture. *Dev Biol* 2000;227:271-8.
  45. Xu C, Police S, Rao N, Carpenter MK. Characterization and enrichment of cardiomyocytes derived from human embryonic stem cells. *Circ Res* 2002;91:501-8.
  46. Mummery C, Ward-van Oostwaard D, Doevendans P, Spijker R, van den Brink S, Hassink R, van der Heyden M, Ophhof T, Pera M, de la Riviere AB, Passier R, Tertoolen L. Differentiation of human embryonic stem cells to cardiomyocytes: role of coculture with visceral endoderm-like cells. *Circulation* 2003;107:2733-40.
  47. Maltsev VA, Wobus AM, Rohwedel J, Bader M, Hescheler J. Cardiomyocytes differentiated in vitro from embryonic stem cells developmentally express cardiac-specific genes and ionic currents. *Circ Res* 1994;75:233-44.
  48. Maltsev VA, Rohwedel J, Hescheler J, Wobus AM. Embryonic stem cells differentiate in vitro into cardiomyocytes representing sinusnodal, atrial and ventricular cell types. *Mech Dev* 1993;44:41-50.
  49. He JQ, Ma Y, Lee Y, Thomson JA, Kamp TJ. Human embryonic stem cells develop into multiple types of cardiac myocytes: action potential characterization. *Circ Res* 2003;93:32-9.
  50. Kehat I, Kenyagin-Karsenti D, Snir M, Segev H, Amit M, Gepstein A, Livne E, Binah O, Itskovitz-Eldor J, Gepstein L. Human embryonic stem cells can differentiate into myocytes with structural and functional properties of cardiomyocytes. *J Clin Invest* 2001;108:407-14.
  51. Dolnikov K, Shilkrut M, Zeevi-Levin N, Danon A, Gerecht-Nir S, Itskovitz-Eldor J, Binah O. Functional properties of human embryonic stem cell-derived cardiomyocytes. *Ann*

N Y Acad Sci 2005;1047:66-75.

52. Klug MG, Soonpaa MH, Koh GY, Field LJ. Genetically selected cardiomyocytes from differentiating embryonic stem cells form stable intracardiac grafts. *J Clin Invest* 1996;98:216-24.
53. Etzion S, Battler A, Barbash IM, Cagnano E, Zarin P, Granot Y, Kedes LH, Kloner RA, Leor J. Influence of embryonic cardiomyocyte transplantation on the progression of heart failure in a rat model of extensive myocardial infarction. *J Mol Cell Cardiol* 2001;33:1321-30.
54. Min JY, Yang Y, Converso KL, Liu L, Huang Q, Morgan JP, Xiao YF. Transplantation of embryonic stem cells improves cardiac function in postinfarcted rats. *J Appl Physiol* 2002;92:288-96.
55. Min JY, Yang Y, Sullivan MF, Ke Q, Converso KL, Chen Y, Morgan JP, Xiao YF. Long-term improvement of cardiac function in rats after infarction by transplantation of embryonic stem cells. *J Thorac Cardiovasc Surg* 2003;125:361-9.
56. Laflamme MA, Gold J, Xu C, Hassanipour M, Rosler E, Police S, Muskheli V, Murry CE. Formation of human myocardium in the rat heart from human embryonic stem cells. *Am J Pathol* 2005;167:663-71.
57. Kehat I, Khimovich L, Caspi O, Gepstein A, Shofti R, Arbel G, Huber I, Satin J, Itskovitz-Eldor J, Gepstein L. Electromechanical integration of cardiomyocytes derived from human embryonic stem cells. *Nat Biotechnol* 2004;22:1282-9.
58. Xue T, Cho HC, Akar FG, Tsang SY, Jones SP, Marban E, Tomaselli GF, Li RA. Functional integration of electrically active cardiac derivatives from genetically engineered human embryonic stem cells with quiescent recipient ventricular cardiomyocytes: insights into the development of cell-based pacemakers. *Circulation* 2005;111:11-20.
59. Laflamme MA, Murry CE. Regenerating the heart. *Nat Biotechnol* 2005;23:845-56.
60. Kogler G, Sensken S, Airey JA, Trapp T, Muschen M, Feldhahn N, Liedtke S, Sorg RV, Fischer J, Rosenbaum C, Greschat S, Knipper A, Bender J, Degistirici O, Gao J, Caplan AI, Colletti EJ, Almeida-Porada G, Muller HW, Zanjani E, Wernet P. A new human somatic stem cell from placental cord blood with intrinsic pluripotent differentiation potential. *J Exp Med* 2004;200:123-35.
61. Kim BO, Tian H, Prasongsukarn K, Wu J, Angoulvant D, Wnendt S, Muhs A, Spitkovsky D, Li RK. Cell transplantation improves ventricular function after a myocardial infarction: a preclinical study of human unrestricted somatic stem cells in a porcine model. *Circulation* 2005;112:106-104.
62. Kawamoto A, Gwon HC, Iwaguro H, Yamaguchi JI, Uchida S, Masuda H, Silver M, Ma H, Kearney M, Isner JM, Asahara T. Therapeutic potential of ex vivo expanded endothelial progenitor cells for myocardial ischemia. *Circulation* 2001;103:634-7.
63. Kawamoto A, Tkebuchava T, Yamaguchi J-I, Nishimura H, Yoon YS, Milliken C, Uchida S, Masuo O, Iwaguro H, Ma H, Hanley A, Silver M, Kearney M, Losordo DW, Isner

- JM, Asahara T. Intramyocardial transplantation of autologous endothelial progenitor cells for therapeutic neovascularization. *Circulation* 2003;107:461-8.
64. Badorff C, Brandes RP, Popp R, Rupp S, Urbich C, Aicher A, Fleming I, Busse R, Zeiher AM, Dimmeler S. Transdifferentiation of blood-derived human adult endothelial progenitor cells into functionally active cardiomyocytes. *Circulation* 2003;107:1024-32.
65. Gruh I, Beilner J, Blomer U, Schmiedel A, Schmidt-Richter I, Kruse ML, Haverich A, Martin U. No evidence of transdifferentiation of human endothelial progenitor cells into cardiomyocytes after coculture with neonatal rat cardiomyocytes. *Circulation* 2006;113:1326-34.
66. Angst BD, Khan LU, Severs NJ, Whitely K, Rothery S, Thompson RP, Magee AI, Gourdie RG. Associated spatial patterning of gap junctions and cell adhesion junctions during postnatal differentiation of ventricular myocardium. *Circ Res* 1997;80:88-94.
67. Balogh S, Naus CCG, Merrifield PA. Expression of gap junctions in cultured rat L6 cells during myogenesis. *Dev Biol* 1993;155:351-60.
68. Leobon B, Garcin I, Menasche P, Vilquin JT, Audinat E, Charpak S. Myoblasts transplanted into rat infarcted myocardium are functionally isolated from their host. *Proc Natl Acad Sci USA* 2003;100:7808-11.
69. Rubart M, Soonpaa MH, Nakajima H, Field LJ. Spontaneous and evoked intracellular calcium transients in donor-derived myocytes following intracardiac myoblast transplantation. *J Clin Invest* 2004;114:775-83.
70. Gibbs CL, Barclay CJ. Cardiac efficiency. *Cardiovasc Res* 1995;30:627-34.
71. Pette D. Fiber transformation and fiber replacement in chronically stimulated muscle. *J Heart Lung Transplant* 1992;11:S299-305.
72. Pin C, Merrifield PA. Developmental potential of rat L6 myoblasts in vivo following injection into regenerating muscles. *Dev Biol* 1997;188:147-66.
73. Edom F, Mouly V, Barbet JP, Fiszman MY, Butler-Browne GS. Clones of human satellite cells can express in vitro both fast and slow myosin heavy chains. *Dev Biol* 1994;164:219-29.
74. Dib N, Diethrich EB, Campbell A, Goodwin N, Robinson B, Gilbert J, Hobohm DW, Taylor DA. Endoventricular transplantation of allogenic skeletal myoblasts in a porcine model of myocardial infarction. *J Endovasc Ther* 2002;9:313-9.
75. Kelly AM. Satellite cells and myofiber growth in the rat soleus and extensor digitorum longus muscles. *Dev Biol* 1978;65:1-10.
76. Gibson MC, Schultz E. The distribution of satellite cells and their relationship to specific fiber types in soleus and extensor digitorum longus muscles. *Anat Rec* 1982;202:329.
77. van den Bos EJ, Thompson RB, Wagner A, Mahrholdt H, Morimoto Y, Thomson LE, Wang LH, Duncker DJ, Judd RM, Taylor DA. Functional assessment of myoblast transplantation for cardiac repair with magnetic resonance imaging. *Eur J Heart Fail*

- 2005;7:435-43.
78. Suzuki K, Murtuza B, Heslop L, Morgan JE, Smolenski RT, Suzuki N, Partridge TA, Yacoub MH. Single fibers of skeletal muscle as a novel graft for cell transplantation to the heart. *J Thorac Cardiovasc Surg* 2002;123:984-92.
  79. Menasche P, Hagege AA, Scorsin M, Pouzet B, Desnos M, Duboc D, Schwartz K, Vilquin JT, Marolleau JP. Myoblast transplantation for heart failure. *Lancet* 2001;347:279.
  80. Thompson RB, Parsa CJ, van den Bos EJ, Davis BH, Toloza EM, Klem I, Glower DD, Taylor DA. Video-assisted thoracoscopic transplantation of myoblasts into the heart. *Ann Thorac Surg* 2004;78:303-7.
  81. Carraro U. Video-assisted thoracoscopic transplantation of myoblasts into the heart. *Ann Thorac Surg* 2004;78:14-6.
  82. Smits PC, van Geuns RJ, Poldermans D, Bountiukos M, Onderwater EE, Lee CH, Maat AP, Serruys PW. Catheter-based intramyocardial injection of autologous skeletal myoblasts as a primary treatment of ischemic heart failure: clinical experience with six-month follow-up. *J Am Coll Cardiol* 2003;42:2063-9.
  83. Chazaud B, Hittinger L, Sonnet C, Champagne S, Le Corvoisier P, Benhaïem-Sigaux N, Untersee T, Su J, Merlet P, Rahmouni A, Garot J, Gherardi R, Teiger E. Endoventricular porcine autologous myoblast transplantation can be successfully achieved with minor mechanical cell damage. *Cardiovasc Res* 2003;58:444-50.
  84. Karmarkar PV, Kraitchman DL, Izbudak I, Hofmann LV, Amado LC, Fritzges D, Young R, Pittenger M, Bulte JW, Atalar E. MR-trackable intramyocardial injection catheter. *Magn Reson Med* 2004;51:1163-72.
  85. Garot J, Untersee T, Teiger E, Champagne S, Chazaud B, Gherardi R, Hittinger L, Gueret P, Rahmouni A. Magnetic resonance imaging of targeted catheter-based implantation of myogenic precursor cells into infarcted left ventricular myocardium. *J Am Coll Cardiol* 2003;41:1841-6.
  86. Siminiak T, Fiszer D, Jerzykowska O, Grygielska B, Rozwadowska N, Kalmucki P, Kurpisz M. Percutaneous trans-coronary-venous transplantation of autologous skeletal myoblasts in the treatment of post-infarction myocardial contractility impairment: the POZNAN trial. *Eur Heart J* 2005;26:1188-95.
  87. Brasselet C, Morichetti MC, Messas E, Carrion C, Bissery A, Bruneval P, Vilquin JT, Lafont A, Hagege AA, Menasche P, Desnos M. Skeletal myoblast transplantation through a catheter-based coronary sinus approach: an effective means of improving function of infarcted myocardium. *Eur Heart J* 2005;26:1551-6.
  88. Taylor DA, Silvestry SC, Bishop SP, Annex BH, Lilly RE, Glower DD, Kraus WE. Delivery of primary autologous skeletal myoblasts into the rabbit heart by coronary infusion: A potential approach to myocardial repair. *Proc Ass Am Phys* 1997;109:245-53.
  89. Suzuki K, Brand NJ, Smolenski RT, Jayakumar J, Murtuza B, Yacoub MH. Development of a novel method for cell transplantation through the coronary artery. *Circulation* 2000;102:III359-64.

90. McGeachie JK, Grounds MD. Cell proliferation in denervated skeletal muscle: does it provide a pool of potential circulating myoblasts? *Bibl Anat* 1992;29:173-93.
91. Neumeyer AM, DiGregorio DM, Brown RH. Arterial delivery of myoblasts to skeletal muscle. *Neurology* 1992;42:2258-62.
92. Suzuki K, Murtuza B, Fukushima S, Smolenski RT, Varela-Carver A, Coppen SR, Yacoub MH. Targeted cell delivery into infarcted rat hearts by retrograde intracoronary infusion: distribution, dynamics, and influence on cardiac function. *Circulation* 2004;110:II225-30.
93. Suzuki K, Murtuza B, Smolenski RT, Yacoub MH. Selective cell dissemination into the heart by retrograde intracoronary infusion in the rat. *Transplantation* 2004;77:757-9.
94. Soonpaa MH, Koh GY, Klug MG, Field LG. Formation of nascent intercalated disks between grafted cardiomyocytes and host myocardium. *Science* 1994;264:98-101.
95. Suzuki K, Smolenski RT, Jayakumar J, Murtuza B, Brand NJ, Yacoub MH. Heat shock treatment enhances graft cell survival in skeletal myoblast transplantation to the heart. *Circulation* 2000;102:III216-221.
96. Suzuki K, Murtuza B, Beauchamp JR, Smolenski RT, Varela-Carver A, Fukushima S, Coppen SR, Partridge TA, Yacoub MH. Dynamics and mediators of acute graft attrition after myoblast transplantation to the heart. *FASEB J* 2004;18:1153-5.
97. Suzuki K, Murtuza B, Beauchamp JR, Brand NJ, Barton PJ, Varela-Carver A, Fukushima S, Coppen SR, Partridge TA, Yacoub MH. Role of interleukin-1beta in acute inflammation and graft death after cell transplantation to the heart. *Circulation* 2004;110:II219-24.
98. Gussoni E, Blau HM, Kunkel LM. The fate of individual myoblasts after transplantation into muscles of DMD patients. *Nat Med* 1997;3:970-7.
99. Huard J, Acsadi G, Jani A, Massie B, Karpati G. Gene transfer into skeletal muscles by isogenic myoblasts. *Hum Gene Ther* 1994;5:949-58.
100. Beauchamps JR, Morgan JE, Pagel CN, Partridge TA. Quantitative studies of efficacy of myoblast transplantation. *Muscle Nerve* 1994;18:261.
101. Guerette B, Asselin I, Skuk D, Entman M, Tremblay JP. Control of inflammatory damage by anti-LFA-1: Increase success of myoblast transplantation. *Cell Transplant* 1997;6:101-7.
102. Tremblay JP, Guerette B. Myoblast transplantation: a brief review of the problems and of some solutions. *Basic Appl Myol* 1997;7:221-30.
103. Qu Z, Balkir L, van Deutekom JCT, Robbins PD, Pruchnic R, Huard J. Development of approaches to improve myoblast transfer therapy. *J Cell Biol* 1998;142:1257-67.
104. Murry CE, Wiseman RW, Schwartz SM, Hauschka SD. Skeletal myoblast transplantation for repair of myocardial necrosis. *J Clin Invest* 1996;98:2512-23.
105. Ghostine S, Carrion C, Souza LC, Richard P, Bruneval P, Vilquin JT, Pouzet B, Schwartz K, Menasche P, Hagege AA. Long-term efficacy of myoblast transplantation on

- regional structure and function after myocardial infarction. *Circulation* 2002;106:1131-6.
106. Pagani FD, DerSimonian H, Zawadzka A, Wetzel K, Edge AS, Jacoby DB, Dinsmore JH, Wright S, Aretz TH, Eisen HJ, Aaronson KD. Autologous skeletal myoblasts transplanted to ischemia-damaged myocardium in humans. Histological analysis of cell survival and differentiation. *J Am Coll Cardiol* 2003;41:879-88.
  107. Atkins BZ, Lewis CW, Kraus WE, Hutcheson KA, Glower DD, Taylor DA. Intracardiac transplantation of skeletal myoblasts yields two populations of striated cells in situ. *Ann Thorac Surg* 1999;67:124-9.
  108. Chiu RC, Zibaitis A, Kao RL. Cellular cardiomyoplasty: myocardial regeneration with satellite cell implantation. *Ann Thorac Surg* 1995;60:12-8.
  109. Yoon PD, Kao RL, Magovern GJ. Myocardial regeneration. Transplanting satellite cells into damaged myocardium. *Tex Heart Inst J* 1995;22:119-25.
  110. Dorfman J, Duong M, Zibaitis A, Pelletier MP, Shum-Tim D, Li C, Chiu RC. Myocardial tissue engineering with autologous myoblast implantation. *J Thorac Cardiovasc Surg* 1998;116:744-51.
  111. Koh GY, Klug MG, Soonpaa MH, Field LJ. Differentiation and long-term survival of C2C12 myoblast grafts in heart. *J Clin Invest* 1993;92:1548-54.
  112. Horackova M, Arora R, Chen R, Armour JA, Cattini PA, Livingston R, Byczko Z. Cell transplantation for treatment of acute myocardial infarction: unique capacity for repair by skeletal muscle satellite cells. *Am J Physiol Heart Circ Physiol* 2004;287:H1599-608.
  113. Reinecke H, Poppa V, Murry CE. Skeletal muscle stem cells do not transdifferentiate into cardiomyocytes after cardiac grafting. *J Mol Cell Cardiol* 2002;34:241-9.
  114. Reinecke H, Minami E, Poppa V, Murry CE. Evidence for fusion between cardiac and skeletal muscle cells. *Circ Res* 2004;94:56-60.
  115. Suzuki K, Brand NJ, Allen S, Khan MA, Farrell AO, Murtuza B, Oakley RE, Yacoub MH. Overexpression of connexin 43 in skeletal myoblasts: Relevance to cell transplantation to the heart. *J Thorac Cardiovasc Surg* 2001;122:759-66.
  116. Robinson SW, Cho PW, Levitsky HI, Olson JL, Hruban RH, Acker MA, Kessler PD. Arterial delivery of genetically labeled skeletal myoblasts to the murine heart: long-term survival and phenotypic modification of implanted myoblasts. *Cell Transplant* 1996;5:77-91.
  117. Reinecke H, MacDonald GH, Hauschka SD, Murry CE. Electromechanical coupling between skeletal and cardiac muscle. Implications for infarct repair. *J Cell Biol* 2000;149:731-40.
  118. Martinez AD, Hayrapetyan V, Moreno AP, Beyer EC. Connexin43 and connexin45 form heteromeric gap junction channels in which individual components determine permeability and regulation. *Circ Res* 2002;90:1100-7.
  119. Gaudesius G, Miragoli M, Thomas SP, Rohr S. Coupling of cardiac electrical activity

- over extended distances by fibroblasts of cardiac origin. *Circ Res* 2003;93:421-8.
120. Rash JE, Fambrough DM. Ultrastructural and electrophysiologic correlates of cell coupling and cytoplasmic fusion during myogenesis in vitro. *Dev Biol* 1973;30:166-80.
  121. Murtuza B, Suzuki K, Bou-Gharios G, Beauchamp JR, Smolenski RT, Partridge TA, Yacoub MH. Transplantation of skeletal myoblasts secreting an IL-1 inhibitor modulates adverse remodeling in infarcted murine myocardium. *Proc Natl Acad Sci USA* 2004;101:4216-21.
  122. Pouzet B, Vilquin JT, Hagege AA, Scorsin M, Messas E, Fiszman M, Schwartz K, Menasche P. Intramyocardial transplantation of autologous myoblasts: can tissue processing be optimized? *Circulation* 2000;102:III210-5.
  123. Rajnoch C, Chachques JC, Berrebi A, Bruneval P, Benoit MO, Carpentier A. Cellular therapy reverses myocardial dysfunction. *J Thorac Cardiovasc Surg* 2001;121:871-8.
  124. Pouzet B, Vilquin JT, Hagege AA, Scorsin M, Messas E, Fiszman M, Schwartz K, Menasche P. Factors affecting functional outcome after autologous skeletal myoblast transplantation. *Ann Thorac Surg* 2001;71:844-50.
  125. Jain M, DerSimonian H, Brenner DA. Cell therapy attenuates deleterious ventricular remodeling and improves cardiac performance after myocardial infarction. *Circulation* 2001;103:1920-7.
  126. Suzuki K, Murtuza B, Smolenski RT, Sammut IA, Suzuki N, Kaneda Y, Yacoub MH. Cell transplantation for the treatment of acute myocardial infarction using vascular endothelial growth factor-expressing skeletal myoblasts. *Circulation* 2001;104: I207-12.
  127. Rajnoch C, Chachques JC, Berrebi A, Bruneval P, Benoit MO, Carpentier A. Cellular therapy reverses myocardial dysfunction. *J Thorac Cardiovasc Surg* 2001;121:871-8.
  128. Scorsin M, Hagege A, Vilquin JT, Fiszman M, Marotte F, Samuel JL, Rappaport L, Schwartz K, Menasche P. Comparison of the effects of fetal cardiomyocyte and skeletal myoblast transplantation on postinfarction left ventricular function. *J Thorac Cardiovasc Surg* 2000;119:1169-75.
  129. Pouzet B, Ghostine S, Vilquin JT, Garcin I, Scorsin M, Hagege AA, Duboc D, Schwartz K, Menasche P. Is skeletal myoblast transplantation clinically relevant in the era of angiotensin-converting enzyme inhibitors? *Circulation* 2001;104:I223-8.
  130. Huwer H, Winning J, Vollmar B, Welter C, Lohbach C, Menger MD, Schafers HJ. Long-term cell survival and hemodynamic improvements after neonatal cardiomyocyte and satellite cell transplantation into healed myocardial cryoinfarcted lesions in rats. *Cell Transplant* 2003;12:757-67.
  131. Tambara K, Sakakibara Y, Sakaguchi G, Lu F, Premaratne GU, Lin X, Nishimura K, Komeda M. Transplanted skeletal myoblasts can fully replace the infarcted

- myocardium when they survive in the host in large numbers. *Circulation* 2003;108:II259-63.
132. Agbulut O, Vandervelde S, Al Attar N, Larghero J, Ghostine S, Leobon B, Robidel E, Borsani P, Le Lorc'h M, Bissery A, Chomienne C, Bruneval P, Marolleau JP, Vilquin JT, Hagege A, Samuel JL, Menasche P. Comparison of human skeletal myoblasts and bone marrow-derived CD133+ progenitors for the repair of infarcted myocardium. *J Am Coll Cardiol* 2004;44:458-63.
  133. Ye L, Haider HKh, Jiang S, Ling LH, Ge R, Law PK, Sim EK. Reversal of myocardial injury using genetically modulated human skeletal myoblasts in a rodent cryoinjured heart model. *Eur J Heart Fail* 2005;7:945-52.
  134. Ott HC, Kroess R, Bonaros N, Marksteiner R, Margreiter E, Schachner T, Laufer G, Hering S. Intramyocardial microdepot injection increases the efficacy of skeletal myoblast transplantation. *Eur J Cardiothorac Surg* 2005;27:1017-21.
  135. Thompson RB, Emani SM, Davis BH, van den Bos EJ, Morimoto Y, Craig D, Glower D, Taylor DA. Comparison of intracardiac cell transplantation: autologous skeletal myoblasts versus BMCs. *Circulation* 2003;108:II264-71.
  136. Atkins BZ, Hueman MT, Meuchel JM, Cottman MJ, Hutcheson KA, Taylor DA. Myogenic cell transplantation improves in vivo regional performance in infarcted rabbit myocardium. *J Heart Lung Transplant* 1999;18:1173-80.
  137. Atkins BZ, Hueman MT, Meuchel J, Hutcheson KA, Glower DD, Taylor DA. Cellular cardiomyoplasty improves diastolic properties of injured heart. *J Surg Res* 1999;85:234-42.
  138. He KL, Yi GH, Sherman W, Zhou H, Zhang GP, Gu A, Kao R, Haimen HB, Harvey J, Roos E, White D, Taylor DA, Wang J, Burkhoff D. Autologous skeletal myoblast transplantation improved hemodynamics and left ventricular function in chronic heart failure dogs. *J Heart Lung Transplant* 2005;24:1940-9.
  139. Ellis MJ, Emani SM, Colgrove SL, Glower DD, Taylor DA. Cell dosage is critical for improved contractility following cellular cardiomyoplasty. *Circulation* 2001;104:II-336. (Abstract)
  140. Scorsin M, Hagege AA, Dolizy I, Marotte F, Mirochnik N, Copin H, Barnoux M, le Bert M, Samuel JL, Rappaport L, Menasche P et al. Can cellular transplantation improve function in doxorubicin-induced heart failure? *Circulation* 1998;98: II151-6.
  141. Suzuki K, Murtuza B, Suzuki N, Smolenski RT, Yacoub. Intracoronary infusion of skeletal myoblasts improved cardiac function in doxorubicin-induced heart failure. *Circulation* 2001;104:II213-217.
  142. Aurigemma GP, Gaasch WH. Clinical practice. Diastolic heart failure. *N Engl J Med* 2004;351:1097-105.
  143. Fuster V, Sanz J, Viles-Gonzalez JF, Rajagopalan S. The utility of magnetic resonance imaging in cardiac tissue regeneration trials. *Nat Clin Pract Cardiovasc Med* 2006;3: S2-7.

144. Mikami A, Imoto K, Tanabe T, Mikami A, Imoto K, Tanabe T, Niidome T, Mori Y, Takeshima H, Narumiya S, Numa S. Primary structure and functional expression of the cardiac dihydropyridine-sensitive calcium channel. *Nature* 1989;340:230-3.
145. Tanabe T, Takeshima H, Mikami A, Flockerzi V, Takahashi H, Kangawa K, Kojima M, Matsuo H, Hirose T, Numa S. Primary structure of the receptor for calcium channel blockers from skeletal muscle. *Nature* 1987;328:313-8.
146. Fernandes S, Amirault JC, Lande G, Nguyen JM, Forest V, Bignolais O, Lamirault G, Heudes D, Orsonneau JL, Heymann MF, Charpentier F, Lemarchand P. Autologous myoblast transplantation after myocardial infarction increases the inducibility of ventricular arrhythmias. *Cardiovasc Res* 2006;69:348-58.
147. Menasche P, Hagege AA, Vilquin JT, Desnos M, Abergel E, Pouzet B, Bel A, Sarateanu S, Scorsin M, Schwartz K, Bruneval P, Benbunan M, Marolleau JP, Duboc D. Autologous skeletal myoblast transplantation for severe postinfarction left ventricular dysfunction. *J Am Coll Cardiol* 2003;41:1078-83.
148. Ferrari G, Cusella-De Angelis G, Coletta M, Paolucci E, Stornaiuolo A, Cossu G, Mavilio F. Muscle regeneration by bone marrow-derived myogenic progenitors. *Science* 1998;279:1528-30.
149. Makino S, Fukuda K, Miyoshi S, Konishi F, Kodama H, Pan J, Sano M, Takahashi T, Hori S, Abe H, Hata J, Umezawa A, Ogawa S. Cardiomyocytes can be generated from marrow stromal cells in vitro. *J Clin Invest* 1999;103:697-705.
150. Hakuno D, Fukuda K, Makino S, Konishi F, Tomita Y, Manabe T, Suzuki Y, Umezawa A, Ogawa S et al. Bone marrow-derived regenerated cardiomyocytes (CMG Cells) express functional adrenergic and muscarinic receptors. *Circulation* 2002;105:380-6.
151. Tomita S, Li RK, Weisel RD, Mickle DA, Kim EJ, Sakai T, Jia ZQ. Autologous transplantation of bone marrow cells improves damaged heart function. *Circulation* 1999;100:II247-56.
152. Jackson KA, Majka SM, Wang H, Pocius J, Hartley CJ, Majesky MW, Entman ML, Michael LH, Hirschi KK, Goodell MA. Regeneration of ischemic cardiac muscle and vascular endothelium by adult stem cells. *J Clin Invest* 2001;107:1395-402.
153. Orlic D, Kajstura J, Chimenti S, Jakoniuk I, Anderson SM, Li B, Pickel J, McKay R, Nadal-Ginard B, Bodine DM, Leri A, Anversa P. Bone marrow cells regenerate infarcted myocardium. *Nature* 2001;410:701-5.
154. Kajstura J, Rota M, Whang B, Cascapera S, Hosoda T, Bearzi C, Nurzynska D, Kasahara H, Zias E, Bonafe M, Nadal-Ginard B, Torella D, Nascimbene A, Quaini F, Urbanek K, Leri A, Anversa P. Bone marrow cells differentiate in cardiac cell lineages after infarction independently of cell fusion. *Circ Res* 2005;96:127-37.
155. Terada N, Hamazaki T, Oka M, Hoki M, Mastalerz DM, Nakano Y, Meyer EM, Morel L, Petersen BE, Scott EW. Bone marrow cells adopt the phenotype of other cells by spontaneous cell fusion. *Nature* 2002;416:542-5.

156. Ying QL, Nichols J, Evans EP, Smith AG. Changing potency by spontaneous fusion. *Nature* 2002;416:545-8
157. Alvarez-Dolado M, Pardal R, Garcia-Verdugo JM, Fike JR, Lee HO, Pfeffer K, Lois C, Morrison SJ, Alvarez-Buylla A. Fusion of bone-marrow-derived cells with Purkinje neurons, cardiomyocytes and hepatocytes. *Nature* 2003;425:968-73.
158. Shi D, Reinecke H, Murry CE, Torok-Storb B. Myogenic fusion of human bone marrow stromal cells, but not hematopoietic cells. *Blood* 2004;104:290-4.
159. Wagers AJ, Sherwood RI, Christensen JL, Weissman IL. Little evidence for developmental plasticity of adult hematopoietic stem cells. *Science* 2002;297:2256-9.
160. Balsam LB, Wagers AJ, Christensen JL, Kofidis T, Weissman IL, Robbins RC. Haematopoietic stem cells adopt mature haematopoietic fates in ischaemic myocardium. *Nature* 2004;428:668-73.
161. Murry CE, Soonpaa MH, Reinecke H, Nakajima H, Nakajima HO, Rubart M, Pasumarthi KB, Virag JI, Bartelmez SH, Poppa V, Bradford G, Dowell JD, Williams DA, Field LJ. Haematopoietic stem cells do not transdifferentiate into cardiac myocytes in myocardial infarcts. *Nature* 2004;428:664-8.
162. Pittenger MF, Mackay AM, Beck SC, Jaiswal RK, Douglas R, Mosca JD, Moorman MA, Simonetti DW, Craig S, Marshak DR. Multilineage potential of adult human mesenchymal stem cells. *Science* 1999;284:143-7.
163. Toma C, Pittenger MF, Cahill KS, Byrne BJ, Kessler PD. Human mesenchymal stem cells differentiate to a cardiomyocyte phenotype in the adult murine heart. *Circulation* 2002;105:93-8.
164. Dai W, Hale SL, Martin BJ, Kuang JQ, Dow JS, Wold LE, Kloner RA. Allogeneic mesenchymal stem cell transplantation in postinfarcted rat myocardium: short- and long-term effects. *Circulation* 2005;112:214-23.
165. Berry MF, Engler AJ, Woo YJ, Pirolli TJ, Bish LT, Jayasankar V, Morine KJ, Gardner TJ, Discher DE, Sweeney HL. Mesenchymal stem cell injection after myocardial infarction improves myocardial compliance. *Am J Physiol Heart Circ Physiol* 2006;290:H2196-203.
166. Zhang S, Jia Z, Ge J, Gong L, Ma Y, Li T, Guo J, Chen P, Hu Q, Zhang P, Liu Y, Li Z, Ma K, Li L, Zhou C. Purified human bone marrow multipotent mesenchymal stem cells regenerate infarcted myocardium in experimental rats. *Cell Transplant* 2005;14:787-98.
167. Thompson RB, van den Bos EJ, Davis BH, Morimoto Y, Craig D, Sutton BS, Glower DD, Taylor DA. Intracardiac transplantation of a mixed population of bone marrow cells improves both regional systolic contractility and diastolic relaxation. *J Heart Lung Transplant* 2005;24:205-14.
168. Silva GV, Litovsky S, Assad JA, Sousa AL, Martin BJ, Vela D, Coulter SC, Lin J, Ober J, Vaughn WK, Branco RV, Oliveira EM, He R, Geng YJ, Willerson JT, Perin

- EC. Mesenchymal stem cells differentiate into an endothelial phenotype, enhance vascular density, and improve heart function in a canine chronic ischemia model. *Circulation* 2005;111:150-6.
169. Shake JG, Gruber PJ, Baumgartner WA, Senechal G, Meyers J, Redmond JM, Pittenger MF, Martin BJ. Mesenchymal stem cells implantation in a swine myocardial infarct model: engraftment and functional effects. *Ann Thorac Surg* 2002;73:1919-26.
170. Amado LC, Saliaris AP, Schuleri KH, St John M, Xie JS, Cattaneo S, Durand DJ, Fitton T, Kuang JQ, Stewart G, Lehrke S, Baumgartner WW, Martin BJ, Heldman AW, Hare JML. Cardiac repair with intramyocardial injection of allogeneic mesenchymal stem cells after myocardial infarction. *Proc Natl Acad Sci USA* 2005;102:11474-9.
171. Saito T, Kuang JQ, Bittira B, Al-Khalidi A, Chiu RC. Xenotransplant cardiac chimera: immune tolerance of adult stem cells. *Ann Thorac Surg* 2002;74:19-24.
172. Mangi AA, Noiseux N, Kong D, He H, Rezvani M, Ingwall JS, Dzau VJ. Mesenchymal stem cells modified with Akt prevent remodeling and restore performance of infarcted hearts. *Nat Med* 2003;9:1195-201.
173. Lim SY, Kim YS, Ahn Y, Jeong MH, Hong MH, Joo SY, Nam KI, Cho JG, Kang PM, Park JC. The effects of mesenchymal stem cells transduced with Akt in a porcine myocardial infarction model. *Cardiovasc Res* 2006;70:530-42.
174. Vulliet PR, Greeley M, Halloran SM, MacDonald KA, Kittleson MD. Intra-coronary arterial injection of mesenchymal stromal cells and microinfarction in dogs. *Lancet* 2004;363:783-4.
175. Kocher AA, Schuster MD, Szabolcs MJ, Takuma S, Burkhoff D, Wang J, Homma S, Edwards NM, Itescu S. Neovascularization of ischemic myocardium by human bone-marrow-derived angioblasts prevents cardiomyocyte apoptosis, reduces remodeling and improves cardiac function. *Nat Med* 2001;7:430-6.
176. Schuster MD, Kocher AA, Seki T, Martens TP, Xiang G, Homma S, Itescu S. Myocardial neovascularization by bone marrow angioblasts results in cardiomyocyte regeneration. *Am J Physiol Heart Circ Physiol* 2004;287:H525-32.
177. Kinnaird T, Stabile E, Burnett MS, Lee CW, Barr S, Fuchs S, Epstein SE. Marrow-derived stromal cells express genes encoding a broad spectrum of arteriogenic cytokines and promote in vitro and in vivo arteriogenesis through paracrine mechanisms. *Circ Res* 2004;94:678-85.
178. Ziegelhoeffer T, Fernandez B, Kostin S, Heil M, Voswinckel R, Helisch A, Schaper W. Bone marrow-derived cells do not incorporate into the adult growing vasculature. *Circ Res* 2004;94:230-8.
179. Foster-Gareau P, Heyn C, Alejski A, Rutt BK. Imaging single mammalian cells with a 1.5 T clinical MRI scanner. *Magn Reson Med* 2003;49:968-71.
180. Shapiro EM, Skrtic S, Sharer K, Hill JM, Dunbar CE, Koretsky AP. MRI detection of single particles for cellular imaging. *Proc Natl Acad Sci USA* 2004;101:10901-6.
181. Zhang Z, van den Bos EJ, Wielopolski PA, de Jong-Popijus M, M. Bernsen, Duncker

- DJ, Krestin GP. In vitro imaging of single living human umbilical vein endothelial cells with a clinical 3.0T MRI scanner. *MAGMA* 2005;18:175-85.
182. Dick AJ, Guttman MA, Raman VK, Peters DC, Pessanha BS, Hill JM, Smith S, Scott G, McVeigh ER, Lederman RJ. Magnetic resonance fluoroscopy allows targeted delivery of mesenchymal stem cells to infarct borders in Swine. *Circulation* 2003;108:2899-2904.
183. Yeh TC, Zhang W, Ildstad ST, Ho C. Intracellular labeling of T-cells with superparamagnetic contrast agents. *Magn Reson Med* 1993;30:617-25.
184. Bulte JW, Kraitchman DL. Iron oxide MR contrast agents for molecular and cellular imaging. *NMR Biomed* 2004;17:484-99.
185. Bulte JW, Laughlin PG, Jordan EK, Tran VA, Vymazal J, Frank JA. Tagging of T cells with superparamagnetic iron oxide: uptake kinetics and relaxometry. *Acad Radiol* 1996;3:S301-3.
186. Josephson L, Tung CH, Moore A, Weissleder R. High-efficiency intracellular magnetic labeling with novel superparamagnetic-Tat peptide conjugates. *Bioconjug Chem* 1999;10:186-91.
187. Daldrup-Link HE, Rudelius M, Oostendorp RA, Settles M, Piontek G, Metz S, Rosenbrock H, Keller U, Heinzmann U, Rummeny EJ, Schlegel J, Link TM. Targeting of hematopoietic progenitor cells with MR contrast agents. *Radiology* 2003;228:760-7.
188. Wilhelm C, Billotey C, Roger J, Pons JN, Bacri JC, Gazeau F. Intracellular uptake of anionic superparamagnetic nanoparticles as a function of their surface coating. *Biomaterials* 2003;24:1001-11.
189. Zhang Z, van den Bos EJ, Wielopolski PA, de Jong-Popijus M, Duncker DJ, Krestin GP. High-resolution magnetic resonance imaging of iron-labeled myoblasts using a standard 1.5-T clinical scanner. *MAGMA* 2004;17:201-9.
190. Frank JA, Miller BR, Arbab AS, Zywicke HA, Jordan EK, Lewis BK, Bryant LH Jr, Bulte JW. Clinically applicable labeling of mammalian and stem cells by combining superparamagnetic iron oxides and transfection agents. *Radiology* 2003;228:480-7.
191. Kostura L, Kraitchman DL, Mackay AM, Pittenger MF, Bulte JW. Feridex labeling of mesenchymal stem cells inhibits chondrogenesis but not adipogenesis or osteogenesis. *NMR Biomed* 2004;17:513-7.
192. Shapiro EM, Sharer K, Skrtic S, Koretsky AP. In vivo detection of single cells by MRI. *Magn Reson Med* 2006;55:242-9.
193. Himes N, Min JY, Lee R, Brown C, Shea J, Huang X, Xiao YF, Morgan JP, Burstein D, Oettgen P. In vivo MRI of embryonic stem cells in a mouse model of MI. *Magn Reson Med* 2004;52:1214-9.
194. Kustermann E, Roell W, Breitbach M, Wecker S, Wiedermann D, Buehrle C, Welz A, Hescheler J, Fleischmann BK, Hoehn M. Stem cell implantation in ischemic mouse

- heart: a high-resolution magnetic resonance imaging investigation. *NMR Biomed* 2005;18:362-70.
195. van den Bos EJ, Wagner A, Mahrholdt H, Thompson RB, Morimoto Y, Sutton BS, Judd RM, Taylor DA. Improved efficacy of stem cell labeling for magnetic resonance imaging studies by the use of cationic liposomes. *Cell Transplant* 2003;12:743-56.
  196. Kraitchman DL, Heldman AW, Atalar E, Amado LC, Martin BJ, Pittenger MF, Hare JM, Bulte JW. In vivo magnetic resonance imaging of mesenchymal stem cells in myocardial infarction. *Circulation* 2003;107:2290-3.
  197. Hill JM, Dick AJ, Raman VK, Thompson RB, Yu ZX, Hinds KA, Pessanha BS, Guttman MA, Varney TR, Martin BJ, Dunbar CE, McVeigh ER, Lederman RJ. Serial cardiac magnetic resonance imaging of injected mesenchymal stem cells. *Circulation* 2003;108:1009-14.
  198. Baklanov DV, Demuinck ED, Thompson CA, Pearlman JD. Novel double contrast MRI technique for intramyocardial detection of percutaneously transplanted autologous cells. *Magn Reson Med* 2004;52:1438-42.
  199. Lee IH, Bulte JW, Schweinhardt P, Douglas T, Trifunovski A, Hofstetter C, Olson L, Spenger C. In vivo magnetic resonance tracking of olfactory ensheathing glia grafted into the rat spinal cord. *Exp Neurol* 2004;187:509-16.
  200. de Vries IJ, Lesterhuis WJ, Barentsz JO, Verdijk P, van Krieken JH, Boerman OC, Oyen WJ, Bonenkamp JJ, Boezeman JB, Adema GJ, Bulte JW, Scheenen TW, Punt CJ, Heerschap A, Figdor CG. Magnetic resonance tracking of dendritic cells in melanoma patients for monitoring of cellular therapy. *Nat Biotechnol* 2005;23:1407-13.
  201. Chemaly ER, Yoneyama R, Frangioni JV, Hajjar RJ. Tracking stem cells in the cardiovascular system. *Trends Cardiovasc Med* 2005;15:297-302.
  202. Brenner W, Aicher A, Eckey T, Massoudi S, Zuhayra M, Koehl U, Heesch C, Kampen WU, Zeiher AM, Dimmeler S, Henze E. 111In-labeled CD34+ hematopoietic progenitor cells in a rat myocardial infarction model. *J Nucl Med* 2004;45:512-8.
  203. Hofmann M, Wollert KC, Meyer GP, Menke A, Arseniev L, Hertenstein B, Ganser A, Knapp WH, Drexler H. Monitoring of bone marrow cell homing into the infarcted human myocardium. *Circulation* 2005;111:2198-202.
  204. Aicher A, Brenner W, Zuhayra M, Badorff C, Massoudi S, Assmus B, Eckey T, Henze E, Zeiher AM, Dimmeler S. Assessment of the tissue distribution of transplanted human endothelial progenitor cells by radioactive labeling. *Circulation* 2003;107:2134-9.
  205. Chin BB, Nakamoto Y, Bulte JW, Pittenger MF, Wahl R, Kraitchman DL. 111In oxine labelled mesenchymal stem cells SPECT after intravenous administration in myocardial infarction. *Nucl Med Commun* 2003;24:1149-54.
  206. Barbash IM, Chouraqui P, Baron J, Feinberg MS, Etzion S, Tessone A, Miller L, Guetta E, Zipori D, Kedes LH, Kloner RA, Leor J. Systemic delivery of bone marrow-derived mesenchymal stem cells to the infarcted myocardium: feasibility, cell migration, and body distribution. *Circulation* 2003;108:863-8.

207. Serganova I, Blasberg R. Reporter gene imaging: potential impact on therapy. *Nucl Med Biol* 2005;32:763-80.
208. Herreros J, Prosper F, Perez A, Gavira JJ, Garcia-Velloso MJ, Barba J, Sanchez PL, Canizo C, Rabago G, Marti-Climent JM, Hernandez M, Lopez-Holgado N, Gonzalez-Santos JM, Martin-Luengo C, Alegria E. Autologous intramyocardial injection of cultured skeletal muscle-derived stem cells in patients with non-acute myocardial infarction. *Eur Heart J* 2003;24:2012-20.
209. Pagani FD, DerSimonian H, Zawadzka A, Wetzel K, Edge AS, Jacoby DB, Dinsmore JH, Wright S, Aretz TH, Eisen HJ, Aaronson KD. Autologous skeletal myoblasts transplanted to ischemia-damaged myocardium in humans. Histological analysis of cell survival and differentiation. *J Am Coll Cardiol* 2003;41:879-88.
210. Siminiak T, Kalawski R, Fiszler D, Jerzykowska O, Rzezniczak J, Rozwadowska N, Kurpisz M. Autologous skeletal myoblast transplantation for the treatment of postinfarction myocardial injury: phase I clinical study with 12 months of follow-up. *Am Heart J* 2004;148:531-7.
211. Dib N, Michler RE, Pagani FD, Wright S, Kereiakes DJ, Lengerich R, Binkley P, Buchele D, Anand I, Swingen C, Di Carli MF, Thomas JD, Jaber WA, Opie SR, Campbell A, McCarthy P, Yeager M, Dilsizian V, Griffith BP, Korn R, Kreuger SK, Ghazoul M, MacLellan WR, Fonarow G, Eisen HJ, Dinsmore J, Diethrich E. Safety and feasibility of autologous myoblast transplantation in patients with ischemic cardiomyopathy: four-year follow-up. *Circulation* 2005;112:1748-55.
212. Hagege AA, Carrion C, Menasche P, Vilquin JT, Duboc D, Marolleau JP, Desnos M, Bruneval Pet al. Viability and differentiation of autologous skeletal myoblast grafts in ischaemic cardiomyopathy. *Lancet* 2003;361:491-2.
213. Strauer BE, Brehm M, Zeus T, Kostering M, Hernandez A, Sorg RV, Kogler G, Wernet P. Repair of infarcted myocardium by autologous intracoronary mononuclear bone marrow cell transplantation in humans. *Circulation* 2002;106:1913-8.
214. Schachinger V, Assmus B, Britten MB, Honold J, Lehmann R, Teupe C, Abolmaali ND, Vogl TJ, Hofmann WK, Martin H, Dimmeler S, Zeiher AM. Transplantation of progenitor cells and regeneration enhancement in acute myocardial infarction: final one-year results of the TOPCARE-AMI Trial. *J Am Coll Cardiol* 2004;44:1690-9.
215. Bartunek J, Vanderheyden M, Vandekerckhove B, Mansour S, De Bruyne B, De Bondt P, Van Haute I, Lootens N, Heyndrickx G, Wijns W. Intracoronary injection of CD133-positive enriched bone marrow progenitor cells promotes cardiac recovery after recent myocardial infarction: feasibility and safety. *Circulation* 2005;112:1178-83.
216. Meyer GP, Wollert KC, Lotz J, Steffens J, Lippolt P, Fichtner S, Hecker H, Schaefer A, Arseniev L, Hertenstein B, Ganser A, Drexler H. Intracoronary bone marrow cell transfer after myocardial infarction: eighteen months' follow-up data from the randomized, controlled BOOST (BOne marrOw transfer to enhance ST-elevation infarct regeneration) trial. *Circulation* 2006;113:1287-94.

217. Chen SL, Fang WW, Ye F, Liu YH, Qian J, Shan SJ, Zhang JJ, Chunhua RZ, Liao LM, Lin S, Sun JP. Effect on left ventricular function of intracoronary transplantation of autologous bone marrow mesenchymal stem cells in patients with acute myocardial infarction. *Am J Cardiol* 2004;94:92-5.
218. Janssens S, Dubois C, Bogaert J, Theunissen K, Deroose C, Desmet W, Kalantzi M, Herbots L, Sinnaeve P, Dens J, Maertens J, Rademakers F, Dymarkowski S, Gheysens O, Van Cleemput J, Bormans G, Nuyts J, Belmans A, Mortelmans L, Boogaerts M, Van de Werf F. Autologous bone marrow-derived stem-cell transfer in patients with ST-segment elevation myocardial infarction: double-blind, randomised controlled trial. *Lancet* 2006;367:113-21.
219. Perin EC, Dohmann HF, Borojevic R, Silva SA, Sousa AL, Mesquita CT, Rossi MI, Carvalho AC, Dutra HS, Dohmann HJ, Silva GV, Belem L, Vivacqua R, Rangel FO, Esporcatte R, Geng YJ, Vaughn WK, Assad JA, Mesquita ET, Willerson JT. Transendocardial, autologous bone marrow cell transplantation for severe, chronic ischemic heart failure. *Circulation* 2003;107:2294-302.
220. Strauer BE, Brehm M, Zeus T, Bartsch T, Schannwell C, Antke C, Sorg RV, Kogler G, Wernet P, Muller HW, Kosterling M. Regeneration of human infarcted heart muscle by intracoronary autologous bone marrow cell transplantation in chronic coronary artery disease: the IACT Study. *J Am Coll Cardiol* 2005;46:1651-8.
221. Li TS, Hamano K, Hirata K, Kobayashi T, Nishida M. The safety and feasibility of the local implantation of autologous bone marrow cells for ischemic heart disease. *J Card Surg* 2003;18:S69-75.
222. Stamm C, Westphal B, Kleine HD, Petzsch M, Kittner C, Klinge H, Schumichen C, Nienaber CA, Freund M, Steinhoff G. Autologous bone-marrow stem-cell transplantation for myocardial regeneration. *Lancet* 2003;361:45-6.
223. Tse HF, Kwong YL, Chan JK, Lo G, Ho CL, Lau CP. Angiogenesis in ischaemic myocardium by intramyocardial autologous bone marrow mononuclear cell implantation. *Lancet* 2003;361:47-9.
224. Fuchs S, Satler LF, Kornowski R, Okubagzi P, Weisz G, Baffour R, Waksman R, Weissman NJ, Cerqueira M, Leon MB, Epstein SE. Catheter-based autologous bone marrow myocardial injection in no-option patients with advanced coronary artery disease: a feasibility study. *J Am Coll Cardiol* 2003;41:1721-4.





## Part 2

Animal models for cell transplantation studies



## Chapter 2

A novel model of cryoinjury-induced myocardial infarction in the mouse: a comparison with coronary artery ligation



## Abstract

Mouse myocardial infarction (MI) models are frequently used research tools. The most commonly applied model is coronary artery ligation. However, coronary ligation often gives rise to apical aneurysmatic infarcts of variable size. Other infarct models include cryoinfarction, which produces reproducible infarcts of the anterior wall. Thus far, this model has not been extensively described in mice. Therefore we developed a murine cryoinfarction model and compared it with coronary ligation. Studies were performed under isoflurane anesthesia with a follow-up of 4 and 8 weeks. Cryoinfarction was induced using a 2 or 3 mm cryoprobe. 2D guided M-mode echocardiography was used to assess fractional shortening and left ventricular (LV) dimensions at baseline and endpoint. At endpoint, hemodynamics were assessed using a 1.4F Millar catheter. Pressure-diameter relations were constructed by combining echocardiography and hemodynamic data. Histologic and morphometric analysis of infarct and remote areas was performed.

At 4 weeks, 3 mm cryoinfarction resulted in decreased LV fractional shortening, as well as decreased global LV contractility and relaxation, which was comparable with coronary ligation. No adverse remodeling was observed at this time point in contrast with the ligation model. However, progressive LV remodeling occurred between 4 and 8 weeks after cryoinfarction with further decline in hemodynamic parameters and LV pump function. Histologically, cryoinfarction resulted in highly reproducible, transmural, cone shaped infarcts with reperfusion at a macrovascular level. These results indicate that the cryoinfarction model represents the anterior myocardial infarct with modest adverse remodeling and may thus be representative for infarcts encountered in clinical practice.

## Introduction

With the accumulating availability of various models of genetically modified mice there is a growing interest in murine models of myocardial infarction for the study of cardiac remodeling.<sup>1</sup> The most widely studied model of murine myocardial infarction is permanent ligation of the left anterior descending coronary artery (LAD).<sup>2,3</sup> Although highly representative of the ischemic cell death as occurs in humans, the ligation model is inherently associated with infarcts of variable size, requiring large group numbers of mice in studies that evaluate anti-remodeling therapies. Even more importantly, LAD ligation in the mouse heart typically leads to apical infarcts with large aneurysm formation causing a particular ventricular geometry. Therefore ligation-induced infarcts in the mouse heart appear less representative for infarcts encountered in clinical practice, where acute LAD occlusion followed by aggressive reperfusion therapy often leads to moderately sized infarcts of the anterior free wall.

Several alternative models of myocardial infarction have been proposed and studied over the years in various animal models, including infarction by freeze-thaw injury, or cryoinjury.<sup>4,5</sup> In the last years, cryoinjury has been mainly applied in studies on intra-cardiac cell transplantation.<sup>6-9</sup> However, to date, no study has been performed in order to elucidate the effects of cryoinjury on infarct size, heart function and left ventricular (LV) remodeling in the mouse. In this study we examined the effects of cryoinjury using echocardiography, hemodynamic measurements, pressure-diameter relations and histology and compared these with the results from coronary artery ligation.

## Methods

### Animals

All animal experiments were performed in accordance with the National Institutes of Health Guide for the Care and Use of Laboratory Animals (NIH Pub. No. 86-23, Revised 1996), and with the national and institutional regulations. Mice were ~10 weeks of age at the start of the experimental protocol. Experiments were performed using both males and females at random.

### Echocardiography

Mice were weighed, anesthetized with isoflurane and intubated using a 24G intravenous catheter with a blunt end. Mice were artificially ventilated with a mixture of O<sub>2</sub> and N<sub>2</sub>O (1/2, v/v) to which isoflurane (2.5-3.0%, v/v) was added at a rate of 80 strokes/minute using a rodent ventilator (SAR-830/P; CWE, Ardmore, PA) at 18 cm H<sub>2</sub>O inspiratory pressure. The mouse was placed on a heating pad to maintain body temperature at 37°C. The chest was dehaired using Veet hair removal (Reckitt Benckiser Inc, Parsippany, NJ). Echocardiograms were obtained with the Aloka SSD 4000 echo device (Aloka Company, Tokyo, Japan) using a 12-MHz probe. Images of the short and long axis were obtained in 2D- and M-mode settings

with simultaneous ECG gating as described before.<sup>10,11</sup>

## Cryoinfarction

A thoracotomy was performed through the 4<sup>th</sup> left intercostal space, the pericardium was opened and the heart was exposed. Cryoinfarction was produced by applying a cryoprobe of 2 or 3 mm in diameter (Cry-AC-3 B-800; Brymill Cryogenic Systems, Basingstoke, United Kingdom; Figure 1) to the anterior LV free wall followed by freezing for 10 seconds. The exact position of the probe was carefully set using the left atrium and pulmonary artery as anatomical landmarks. Rinsing with saline at room temperature was performed to allow non-traumatic detachment of the probe from the LV wall after freezing.

## Left anterior descending coronary artery ligation

Ligation of the LAD was performed as described before.<sup>2,3,12</sup> Briefly, a thoracotomy was performed through the 4<sup>th</sup> left intercostal space and the proximal LAD<sup>2,3</sup> was permanently ligated, by passing a 7-0 silk suture mounted on a tapered needle (BV-1; Ethicon, Somerville, NJ) around the artery. Sham animals underwent a thoracotomy without infarct induction. Control animals did not undergo any surgery.

## Hemodynamic measurements

Either 4 weeks or 8 weeks after infarction, echocardiography was repeated under anesthesia as described above. Following echocardiography, mice were instrumented for hemodynamic measurements. For this purpose, a polyethylene catheter (PE-10) was inserted into the left carotid artery and advanced into the aortic arch to measure aortic blood pressure. A 1.4F microtipped manometer (Millar Instruments, Houston, TX; calibrated prior to each experiment with a mercury manometer) was inserted via the right carotid artery and advanced into the LV lumen to measure LV pressure and its first derivative, LV dP/dt. Subsequently, baseline recordings

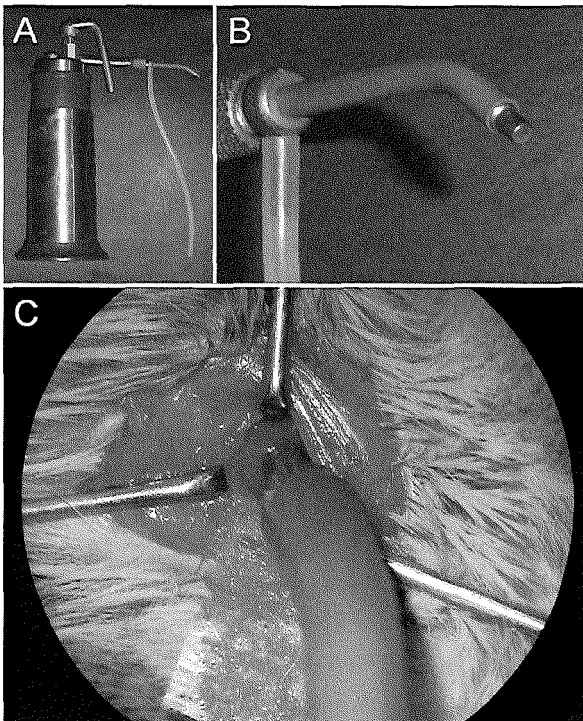


Figure 1. The cryoprobe used in this study (Panel A). Panel B shows an enlargement of the probe end of the 3 mm model. In Panel C the thoracotomy is shown, as seen through the stereomicroscope; the probe can be seen in contact with the anterior wall moments before freezing.

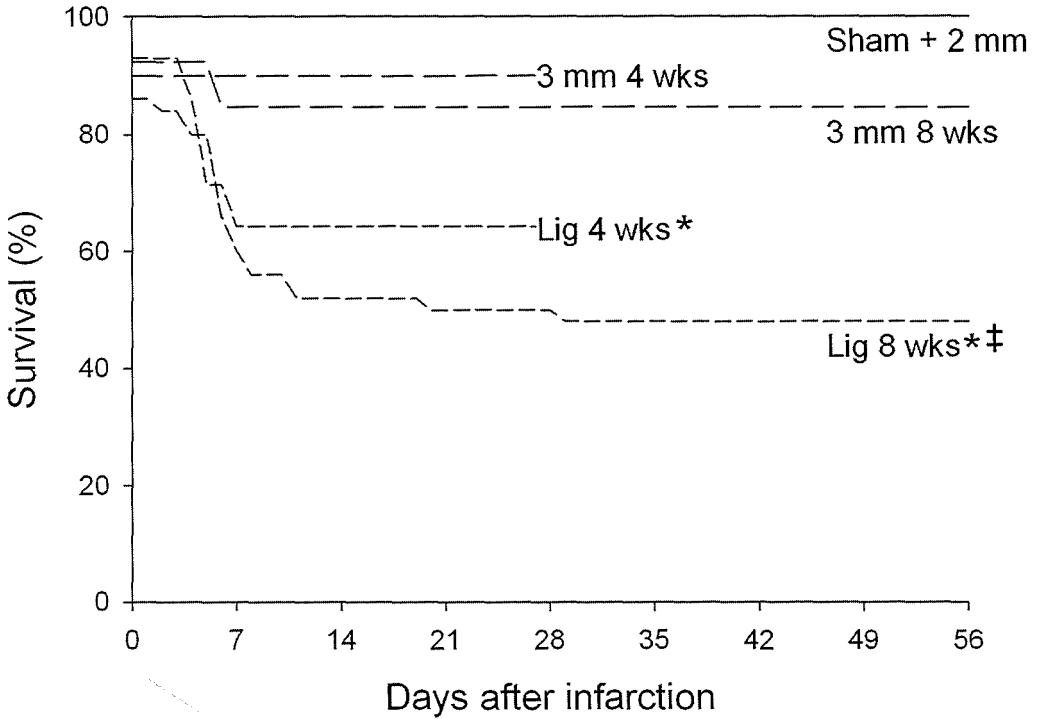


Figure 2. Survival curves in the sham, 2 mm cryoinfarction (2 mm), 3 mm cryoinfarction (3 mm) and coronary ligation (Lig) groups after 4 (4 wks) and 8 weeks (8 wks). Kaplan-Meier analysis showed a significant decrease in survival after coronary ligation compared with cryoinfarction after 8 weeks. \*P<0.05 vs. corresponding sham; ‡P<0.05 vs. corresponding 3 mm.

were obtained of aortic blood pressure, heart rate and LV pressure.

### Data analysis

Echocardiography data were stored for offline analysis. LV diameters at end-diastole (EDD) and end-systole (ESD) were measured from the M-mode images using Sigmascan Pro 5.0 Image Analysis software (SPSS Inc, Chigago, IL). Three consecutive beats were analyzed by a blinded observer. Twenty-one animals were randomly selected for analysis by a second blinded observer to calculate inter-observer variability. LV absolute shortening (EDD - ESD) and fractional shortening [(EDD - ESD)/EDD x 100%] were calculated. Hemodynamic data were recorded and digitized (sampling rate 5000 sec<sup>-1</sup> per channel) using an online four-channel data acquisition program (ATCODAS; Dataq Instruments, Akron, OH) for post-acquisition offline analysis with a program written in MATLAB (Mathworks, Natick, MA). Ten consecutive beats were selected for determination of heart rate (HR), LV peak systolic (LVSP) and end-diastolic pressures (LVEDP), diastolic aortic pressure (DAP) and the maximum rates of rise (LVdP/dt<sub>max</sub>) and fall (LVdP/dt<sub>min</sub>) of LV pressure as well as the rate of rise of LV pressure at a pressure of 30 mmHg (LVdP/dt<sub>p30</sub>). In addition the time constant of LV pressure decay  $\tau$ ,

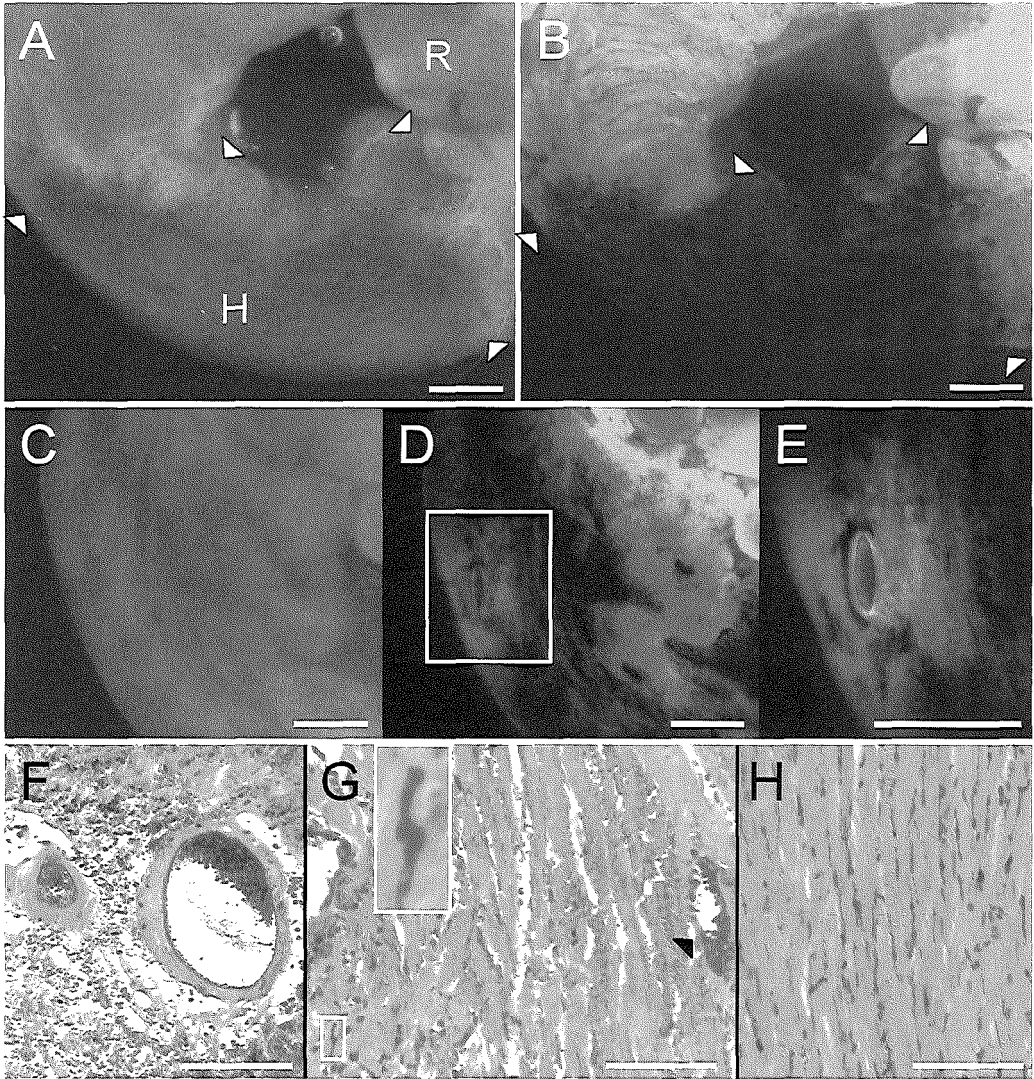


Figure 3. Panel A shows a 3 mm cryoinfarction after 2 days (delineated by white arrows). A large area of hemorrhage occupies the infarct center (indicated by H). R indicates remote healthy myocardium. The corresponding view under ultraviolet light is shown in Panel B: The infarct area is not stained indicating no-reflow caused by microvascular damage. Panel C shows a 3 mm cryoinfarction of a different heart. Less hemorrhage is visible. The corresponding view under ultraviolet light is shown in Panel D. The boxed region containing the LAD is shown at higher magnification in Panel E: Both the LAD and a small region around it are reperfused. Unisperse Blue was found in the LAD and larger vessels in all animals (arrow; Panel F and G, HE stain). Capillary reperfusion was selectively found along the endocardial borders (boxed region; Panel G, HE stain). Panel H shows reperfused capillaries in the remote non-infarcted myocardium. Bar represents 5 mm in Panels A to E and 100  $\mu$ m in Panels F to H.

an index of early LV relaxation, was computed as described earlier.<sup>10,13</sup>

Pressure-diameter relations were constructed with a program written in MATLAB, using the ECG signal for synchronization of the echocardiography M-mode dataset and the LV pressure signal. Data from four consecutive beats were averaged.

### **Infarct reperfusion, histology and morphometric measurements**

At the conclusion of each experiment, the heart and lungs were excised. The right ventricle and the atria were removed. Wet weights of left and right ventricle and lungs as well as tibia length were determined. The area of cryoinfarction could be easily identified macroscopically. The left ventricle was cut in two halves through the center of the infarct along the longitudinal axis. The half of the left ventricle comprising the interventricular septum was fixed overnight in freshly prepared paraformaldehyde (4%) in PBS. Paraffin sections from the infarct center were stained with hematoxylin-eosin (HE) and Masson's trichrome (MT). Sections were photographed using an Olympus BH 20 microscope (Olympus Corporation, Tokyo, Japan) and analyzed using Clemex Vision PE analysis software (Clemex Technologies, Longueuil, Canada). The infarct region was demarcated and the area was measured. Endocardial and epicardial infarct circumference were demarcated and the lengths measured. Infarct thickness was measured at the shortest distance between endocardium and epicardium. Cardiomyocyte size in the non-infarcted interventricular septum, i.e. remote myocardium, was determined by cross-sectional area measurements of cardiomyocytes in transverse orientation and at identical magnification.<sup>14</sup>

The other half of the left ventricle was embedded in optimal cutting temperature (OCT) compound (Tissue Tek; Sakura, Zoeterwoude, The Netherlands) and frozen in liquid nitrogen cooled-isopentane. Frozen sections were cut, air dried and fixed in acetone. Slides were then incubated with an anti-CD31 antibody (PharMingen, San Diego, CA) for one hour, followed by incubation with a goat anti-rat secondary antibody (Alex Fluor 568; Molecular Probes, Leiden, the Netherlands). Staining was analyzed using fluorescence microscopy (Axiovert S100; Zeiss, Oberkochen, Germany). Four to five images comprising the whole infarct area were taken at 200X. CD31-positive vessels were counted in each field and the vessel areas were measured using Clemex Vision PE analysis software, and both were expressed as measures per unit area as described before.<sup>15</sup>

To study reperfusion of the infarct territory in a more acute post-MI phase, additional mice were sacrificed 2 days after 3 mm cryoinfarction. Before sacrifice, either 50  $\mu$ l thioflavin S (4% solution in saline; Sigma, St. Louis, MO; n=3) or 50  $\mu$ l Unisperse Blue (50% suspension in saline; Ciba Specialty Chemicals, Maastricht, The Netherlands; n=3) was injected into the right ventricular lumen. Thioflavin S stained hearts were cut in 4 short-axis slices and photographed under ultraviolet light (365-nm wave length). Unisperse Blue stained hearts were processed for HE staining following the same protocol as described above.

Additional mice were sacrificed at 2 and 4 days for HE and MT staining only (n=3 at each time point).

## Statistics

Statistical analysis of all data was performed using one- or two-way ANOVA as appropriate, followed by Student-Newman-Keuls test or Tukey test. Analysis of echocardiography data was performed using two-way ANOVA for repeated measures followed by Tukey test. Data are reported as means  $\pm$  standard error of the mean (SEM). Statistical significance was accepted when  $P < 0.05$  (two-tailed). Statistical analysis was performed using SigmaStat software version 2.03 (SPSS Inc, Chigago, IL). Kaplan-Meier curves were constructed using StatView software version 5.0.1 (SAS Institute Inc, Cary, NC).

## Results

### Survival

A total of 147 mice were used for the study. In the control, sham and 2 mm cryoinfarction groups all animals survived. Total peri-procedural mortality (including the first 2 hours post-procedure) in the 3 mm cryoinfarction groups and ligation groups was 8.7% and 12.5%, respectively. Total mortality during the follow-up period was significantly lower after cryoinfarction compared with coronary ligation (Figure 2).

### Effect of surgery and gender

No significant differences between control ( $n=15$ ) and sham mice or between male and female mice were found in any of the hemodynamic or echocardiographic measurements.

### Infarct reperfusion, infarct histology and morphometry

Two days after cryoinfarction, large areas of no-reflow were observed macroscopically within the infarct center and epicardial borders after thioflavin S staining (Figure 3A and B). However, LAD and larger vessels were reperfused (Figure 3C, D and E). This was confirmed by Unisperse Blue staining: Only along the endocardial border reperfused capillaries were observed (Figure 3F, G and H).

Cryoinjury led to transmural MI in all animals (Figure 4A). Four days after infarction, an extensive area of coagulation necrosis with hemorrhage was observed in the center of the cryoinfarcts. Furthermore, a dense inflammatory infiltrate could be observed (Figure 4C). At higher magnification, vascular lacunae were visible with endothelial discontinuities (Figure 4D). Four weeks after infarction a transmural, paucicellular scar had formed, consisting of collagenous fibres with a short transition zone to healthy myocardium (Figure 4E and F). No surviving cardiomyocytes were observed within the infarct area or along the endocardial border. The LAD was patent in each cryoinfarcted animal at 4 and 8 weeks as observed by open vessels filled with erythrocytes (Figure 4G). In contrast, after coronary ligation, obliteration of the LAD and larger vessels was invariably observed (Figure 4H).

Coronary ligation also resulted in transmural MI in all animals (Figure 4B). However, along the endocardial wall and larger vessels small islands of surviving cardiomyocytes were

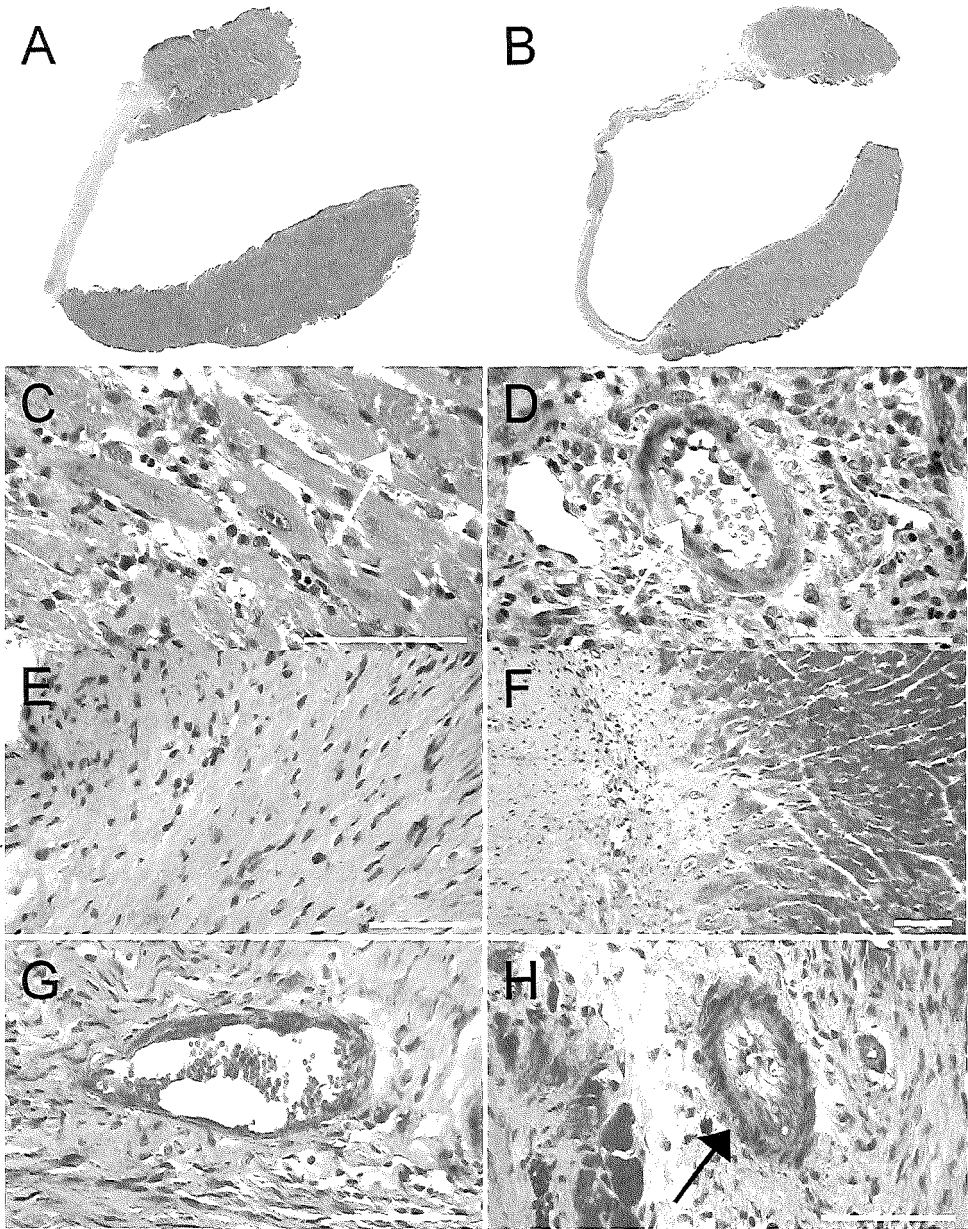


Figure 4. Panel A shows a 3 mm cryoinfarction at 8 weeks (MT stain). The infarct is smaller and thicker when compared with the 8-week old ligation infarction in Panel B. Panel C and D show a HE stain of a 4-day old cryoinfarction. Areas of hemorrhage (arrow) and a dense inflammatory infiltrate were observed (Panel C). Further, vascular lacunae were visible with endothelial discontinuities (arrow; Panel D). Four weeks after cryoinfarction a transmurular, paucicellular scar had formed, with short transition zones to healthy myocardium (Panel E and F, MT stain). At 8 weeks, the LAD was patent in all cryoinfarctioned animals (Panel G, MT stain); in contrast, obliteration of the LAD and larger vessels was invariably observed in the ligation infarctions (arrow; Panel H, MT stain). Bar represents 100  $\mu$ m.

**Table 1. Morphometric measurements**

		Cryo <sub>2mm</sub>	Cryo <sub>3mm</sub>	Ligation
n	4 weeks	6	9	10
	8 weeks		10	11
<b>Epicardial infarct length</b>				
4 weeks		2.3±0.1	3.4±0.2†	4.5±0.4†‡
8 weeks			3.4±0.2	4.6±0.3‡
<b>Endocardial infarct length</b>				
4 weeks		1.1±0.1	1.7±0.2	3.6±0.3†‡
8 weeks			1.8±0.2	3.8±0.3‡
<b>Infarct thickness</b>				
4 weeks		0.36±0.03	0.35±0.03	0.20±0.03†‡
8 weeks			0.26±0.04§§	0.11±0.01‡§
<b>Infarct area (mm<sup>2</sup>)</b>				
4 weeks		0.80±0.08	1.31±0.17	1.76±0.20†
8 weeks			1.16±0.11	1.54±0.14

†P<0.05 vs. corresponding Cryo<sub>2mm</sub>‡P<0.05 vs. corresponding Cryo<sub>3mm</sub>

§P&lt;0.05 vs. corresponding 4 weeks

§§P=0.05 vs. corresponding 4 weeks

Values are means ± SEM

present. Epicardial and endocardial infarct border lengths were significantly larger in the ligation groups compared with the 2 and 3 mm cryoinfarction groups (Table 1). Furthermore, the ligation infarcts were significantly thinner at 4 weeks compared with the cryoinfarction groups and significant infarct thinning occurred between 4 and 8 weeks in the ligation group. As a result, the ligation infarct areas were larger than the 3 mm cryoinfarcts at 4 and 8 weeks, although these differences were not significant (Table 1).

Vessel density and area per vessel as assessed by CD31 immunohistochemistry were not significantly different between cryoinfarction and ligation groups. However, vessel area as a percentage of total tissue area was significantly lower in the ligation group compared with the cryoinfarction and sham groups (Figure 5).

### Systemic hemodynamics and LV pressure derived indices of LV performance

Hemodynamic parameters are shown in Table 2. No significant differences between the

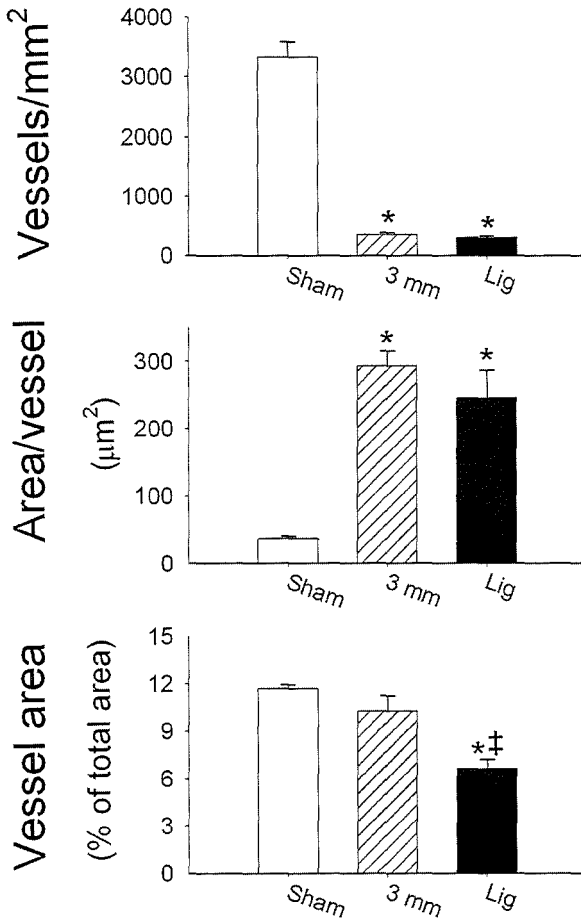


Figure 5. Vessel density and vessel area at 8 weeks. Number of vessels per mm<sup>2</sup> declined significantly in both infarction groups compared with the sham group. Average area per vessel increased significantly in both infarct groups. This resulted in a significant smaller total vessel area per total tissue area in the ligation group compared with the sham and 3 mm cryoinfarction groups. The tick label 3 mm indicates the 3 mm cryoinfarction group. Lig indicates the coronary ligation group. \*P<0.05 vs. corresponding sham; ‡P<0.05 vs. corresponding 3 mm.

of LVdP/dt<sub>min</sub> and  $\tau$  was observed in the 3 mm cryoinfarction group between 4 and 8 weeks, so that at 8 weeks LVdP/dt<sub>min</sub> and  $\tau$  were identical in the 3 mm cryoinfarction and ligation groups.

groups were observed in HR or DAP. Four weeks after coronary ligation a significant increase in LVEDP was observed compared with sham and the cryoinfarction groups. A small but significant difference in LVEDP between ligation and 3 mm cryoinfarction was still observed after 8 weeks. In both cryoinfarction groups and the coronary ligation groups a significant decrease in LVSP was observed after 4 weeks compared with sham.

Four weeks after infarction LVdP/dt<sub>max</sub> was significantly reduced in the 3 mm cryoinfarction and ligation groups compared with sham animals, which corresponded with the changes in the afterload-independent parameter LVdP/dt<sub>p30</sub>. At 8 weeks LVdP/dt<sub>max</sub> and LVdP/dt<sub>p30</sub> were identical in the 3 mm cryoinfarction and ligation groups (Figure 6).

LVdP/dt<sub>min</sub> was significantly reduced after 4 weeks in the 2 and 3 mm and ligation groups (Figure 6), which was accompanied by an increase in the early relaxation parameter  $\tau$ . However, as mentioned above no significant increase was seen in LVEDP in the cryoinfarction groups in contrast with coronary ligation (Table 2). A trend towards further deterioration

Table 2. Hemodynamic measurements

		Sham	Cryo <sub>2mm</sub>	Cryo <sub>3mm</sub>	Ligation
n	4 weeks	12	12	8	10
	8 weeks	8		11	20
HR (beats/min)	4 weeks	531±18	522±6	502±12	555±9
	8 weeks	554±11		531±9	524±8
LVEDP (mmHg)	4 weeks	4±1	3±2	5±1	11±2*†‡
	8 weeks	5±1		5±1	8±1‡
LVSP (mmHg)	4 weeks	101±3	84±4*	85±5*	88±3*
	8 weeks	83±5§		85±2	84±2
DAP (mmHg)	4 weeks	71±3	62±4	66±5	68±3
	8 weeks	59±4§		67±3	58±2§

\*P<0.05 vs. corresponding sham

† P<0.05 vs. corresponding Cryo<sub>2mm</sub>

‡ P<0.05 vs. corresponding Cryo<sub>3mm</sub>

§ P<0.05 vs. corresponding 4 weeks

Values are means ± SEM

### Echocardiography

2D-guided M-mode images were obtained at baseline and 4 or 8 weeks after infarction (Figure 7). Inter-observer variability was  $-3.3 \pm 0.8\%$  and  $-3.2 \pm 2.6\%$  for ED LV lumen diameter and FS, respectively, indicating the high reproducibility of the echo analysis.

Baseline ED lumen diameter was  $3.7 \pm 0.04$  mm for all groups (data not shown in Table 3). Cryoinfarction did not result in LV dilation at 4 weeks (Table 3; Figure 8). However, in the period between 4 and 8 weeks ED LV lumen diameter increased significantly in the 3 mm group compared with the sham group. In contrast, coronary ligation caused marked LV dilation already at 4 weeks, with only modest further LV dilation occurring between 4 and 8 weeks (Figure 8).

Baseline FS was  $33.9 \pm 0.6\%$  for all groups (data not shown in Table 3). Global LV pump function as indicated by FS was significantly reduced compared to sham in both cryoinfarction groups as well as in the ligation group after 4 weeks. A further significant decline was observed after 8 weeks in the 3 mm cryoinfarction group (Table 3).

### Cardiomyocyte hypertrophy and relative LV mass

Cardiomyocyte transverse cross-sectional area was significantly increased in the 3 mm cryoinfarction group after 8 weeks. However, this modest hypertrophy was not reflected in

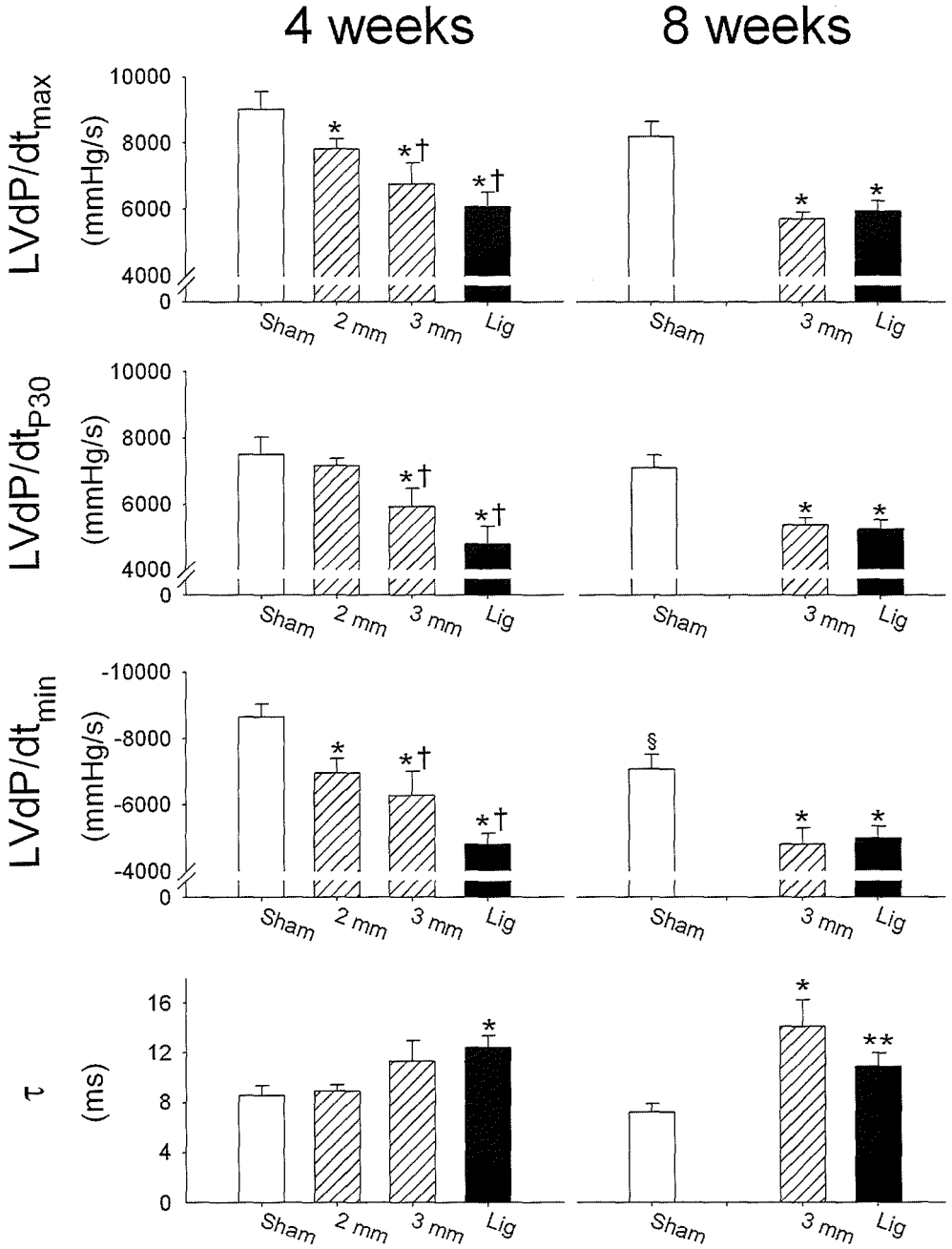


Figure 6. Systolic function parameters: LVdP/dt<sub>max</sub>, the afterload-independent parameter LVdP/dt<sub>p30</sub> and the diastolic function parameters: LVdP/dt<sub>min</sub> and τ. The tick labels 2 mm and 3 mm indicate the 2 mm and 3 mm cryoinfarction groups, respectively. Lig indicates the coronary ligation groups. \*P<0.05 vs. corresponding sham; †P<0.05 vs. corresponding 2 mm; ‡P<0.05 vs. corresponding 3 mm; §P<0.05 vs. corresponding 4 weeks; \*\*P=0.06 vs. corresponding sham.

Table 3. Echocardiography

		Sham	Cryo <sub>2 mm</sub>	Cryo <sub>3 mm</sub>	Ligation
n	4 weeks	12	12	9	9
	8 weeks	6		10	19
<b>End-diastolic lumen diameter (mm)</b>					
	4 weeks	3.9±0.1	4.0±0.1	4.0±0.1	5.4±0.3*†‡
	8 weeks	3.9±0.2		4.6±0.2*	5.7±0.2*‡
<b>Fractional shortening (%)</b>					
	4 weeks	34.0±0.8	22.3±1.4*	20.8±1.7*	10.3±1.6*†‡
	8 weeks	34.9±4.1		14.4±2.2*§	9.6±1.0*‡

\*P<0.05 vs. corresponding sham

†P<0.05 vs. corresponding Cryo<sub>2 mm</sub>

‡P<0.05 vs. corresponding Cryo<sub>3 mm</sub>

§P<0.05 vs. corresponding 4 weeks

Values are means ± SEM

increased LV weight/tibia length ratios likely due to the loss in viable tissue (Figure 9). In the ligation groups marked LV hypertrophy was observed already after 4 weeks, which was reflected by a marked increase in cardiomyocyte transverse cross-sectional area and LV weight/tibia length ratios (Figure 9).

### Pulmonary congestion and right ventricular hypertrophy

Signs of LV backward failure such as pulmonary congestion and RV hypertrophy were absent in the cryoinfarction groups after 4 or 8 weeks (Figure 9). In contrast, wet lung weight/tibia length ratios and RV weight/tibia length ratios were increased in the ligation groups at 4 and 8 weeks compared with sham and the 3 mm cryoinfarction groups.

## Discussion

In the present study we describe the functional and structural effects of cryoinjury-induced MI in the mouse and compare these with the effects of LAD ligation. Although cryoinjury has been previously described in mice,<sup>7,8,16</sup> this is the first study to directly compare both models using echocardiography and LV catheterization and to evaluate different sizes of cryoinjury. The principal findings of this study are: (a) Cryoinfarction in the mouse is a feasible and highly standardized method to create MI with low peri- and post-operative mortality; (b)

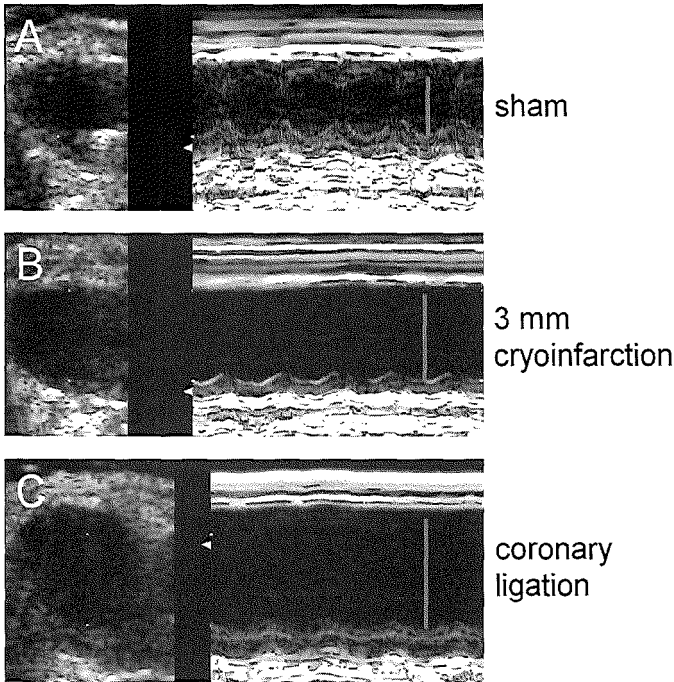


Figure 7. Representative 2D (left) and corresponding M-mode images (right) of a long axis view 8 weeks after sham operation (Panel A), 3 mm cryoinfarction (Panel B) or coronary ligation (Panel C). Cryoinfarction resulted in akinesis of the anterior wall and modest LV dilation. Coronary ligation resulted in anterior akinesis and marked LV dilation. The grey line indicates the end-diastolic lumen diameter.

cryoinfarction results in macrovascular reperfusion with microvascular reperfusion occurring selectively along the endocardial borders; (c) cryoinfarction results in loss of contractility and in diastolic dysfunction to a similar degree as LAD ligation after 8 weeks, however (d) with a more modest LV remodeling and no signs of overt backward LV failure.

### Previous studies

The induction of MI by coronary ligation in mice was initially described 20 years ago.<sup>17</sup> However, the chronic effects of LAD ligation on left ventricular function and remodeling have only more recently been documented in detail.<sup>2</sup> In this study ketamine/pentobarbital anesthesia was used, resulting in lower heart rates (230-270 beats/minute) than reported in the present study under isoflurane anesthesia (500-550 beats/minute), which is in the range of heart rates (450-650 beats/minute) that we<sup>18</sup> and others<sup>19,20</sup> observed in mice under awake conditions. Therefore the present study is, to our knowledge the first study that presents echocardiographic and hemodynamic data of a chronic MI mouse model under physiologic conditions obtained by the use of isoflurane anesthesia.

In recent years cryoinjury has been described in animals such as the rat<sup>4,6</sup> and rabbit.<sup>9</sup> Cryoinfarction in the mouse has only been described in three reports from the same research group.<sup>7,8,16</sup> In these studies a cryoprobe was used that was precooled in liquid nitrogen. The disadvantage of using a precooled probe is that several applications are necessary to obtain the desired effect because of rapid defrosting. The uniformity of the injury may therefore be less than when using the probe described in the present study. We used a commercially

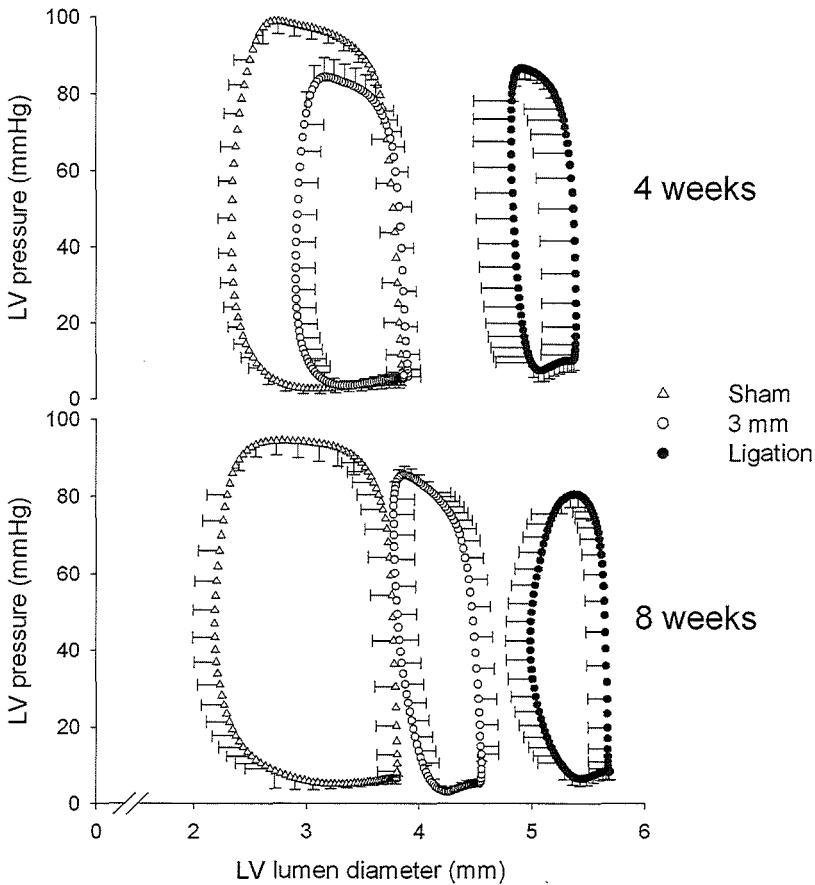


Figure 8. Pressure-diameter relations were constructed by combining echocardiography and LV pressure data. ECG gating was used to synchronize both signals. It can be appreciated that from 4 to 8 weeks a rightward shift occurred in the 3mm cryoinfarction group, indicating ongoing adverse remodeling. Legend: 3 mm indicates the 3 mm cryoinfarction group.

available probe with the capability of continuous freezing resulting in a well-defined area of necrosis.

In the 3 studies mentioned above<sup>7,8,16</sup> either echocardiography or LV catheterization was used as a functional endpoint, but both methods were never applied simultaneously. Our study is therefore the first to describe the effects of cryoinjury in a mouse model using both echocardiography and LV catheterization and to compare the outcomes directly with the more established model of LAD ligation.

### Pathophysiology of the cryoinfarction model

The pathophysiology of cryoinjury differs from LAD ligation because it results in acute cell death at the moment of freezing without concomitant ischemia. The injury caused by the

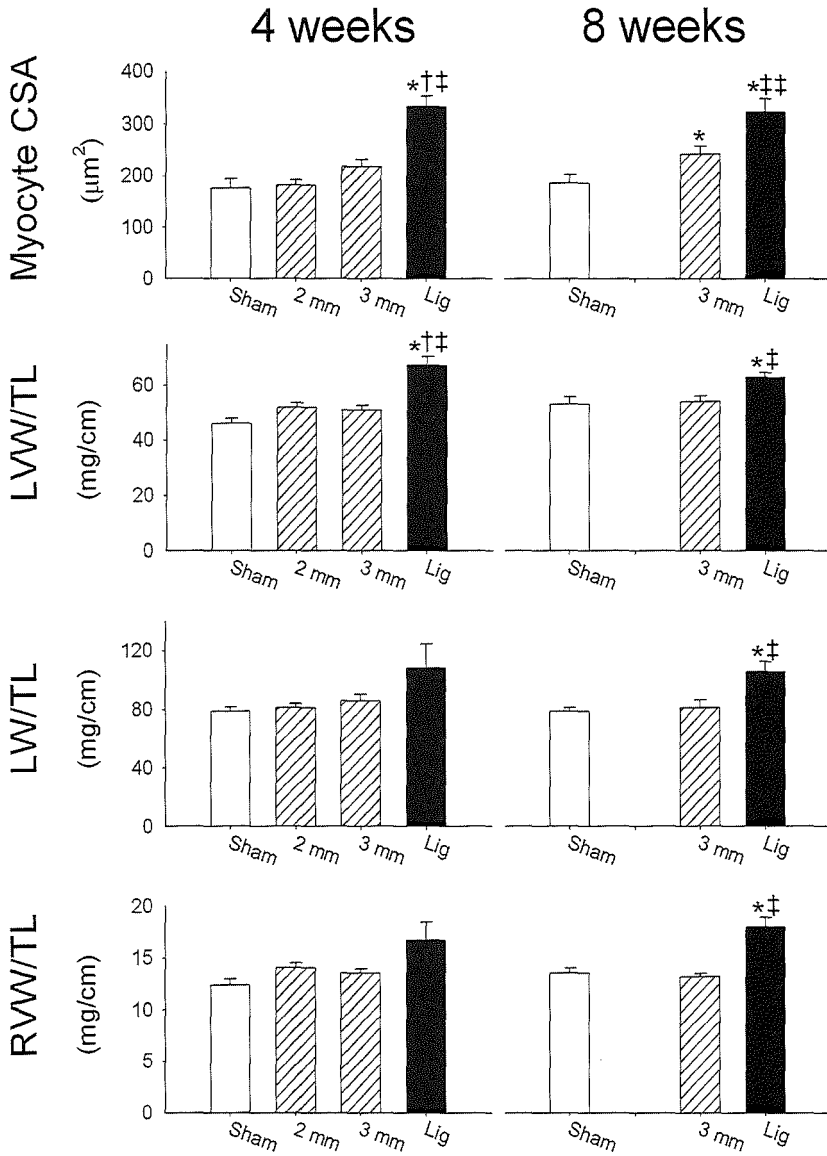


Figure 9. Parameters of global LV remodeling and LV backward failure. For the 3 mm cryoinfarction group a significant increase in myocyte transverse cross-sectional area (CSA) is observed at 8 weeks. However, LV weight/tibia length ratio (LVW/TL) is not increased in contrast with coronary ligation, where significant cardiomyocyte and LV hypertrophy is observed already at 4 weeks. No signs of LV backward failure were observed after cryoinfarction. In contrast: Significant increase in wet lung weight/tibia length ratio (LW/TL) and RV weight/tibia length (RVW/TL) was observed 4 and 8 weeks after coronary ligation, indicating pulmonary congestion and RV hypertrophy. The tick labels 2 mm and 3 mm indicate the 2 and 3 mm cryoinfarction groups, respectively. Lig indicates the coronary ligation groups. \* $P < 0.05$  vs. corresponding sham; † $P < 0.05$  vs. corresponding 2 mm; ‡ $P < 0.05$  vs. corresponding 3 mm; †‡ $P = 0.10$  vs. corresponding 3 mm. No significant differences were found between the 4- and 8-week time points.

freezing process probably results from the mechanical forces induced by formation of ice crystals both in the intracellular and extracellular space and inside the vasculature.<sup>21</sup>

The length of the epicardial cryoinfarct borders correlated closely with the size of the probe used, demonstrating the high predictability of the method (Table 1). Endocardial infarct length was about half of the epicardial length corresponding with the cone shaped lesion observed macroscopically.

Histology of the cryoinfarct area at 2 and 4 days post-infarction showed large areas of hemorrhage in the infarct center, consistent with findings by others.<sup>4,22</sup> Thioflavin S staining showed large no-reflow zones within the infarct center corresponding with microvascular damage. However, the macrovasculature was patent. This was confirmed by Unisperse Blue staining: Capillary reperfusion was selectively observed along endocardial borders. In contrast, the LAD and larger vessels were all reperfused. This likely led to the larger relative vessel area compared with ligation infarcts at 8 weeks (Figure 5). These findings might explain why infarct remodeling was less outspoken in the cryoinfarction model, since it has been proposed that the blood-filled vasculature can act as a “scaffolding” that supports surrounding necrotic myocardium.<sup>23</sup>

### LV function and remodeling after cryoinfarction

Four weeks after cryoinjury, FS was substantially reduced in the 2 mm and 3 mm cryoinfarction groups. This was accompanied by a significant effect on contractility as assessed by  $\text{LVdP}/\text{dt}_{\text{max}}$  and the afterload-independent variable  $\text{LVdP}/\text{dt}_{\text{p30}}$  in the 3 mm group, and by a significant effect on diastolic function as reflected by  $\text{LVdP}/\text{dt}_{\text{min}}$  and  $\tau$ . Since the decrease in  $\text{LVdP}/\text{dt}_{\text{p30}}$  was only modest in the 2 mm group, we chose to follow only the 3 mm group up to 8 weeks.

At 8 weeks, the effects on these parameters were similar in the 3 mm cryoinfarction group and ligation groups. It is therefore somewhat surprising that despite the extent of these changes, only modest LV remodeling and no signs of backward failure were observed after cryoinfarction contrasting with the marked alterations in the ligation model.

After 8 weeks a significant increase in cardiomyocyte cross-sectional area in the 3 mm cryoinfarction group was observed, although LV weight/tibia length ratios were not increased. However, it should be taken into account that because of tissue loss in the infarct area, initially a decrease in LV weights occurs, which likely explains this paradoxical observation.

In the sham group, a small but significant effect was seen on  $\text{LVdP}/\text{dt}_{\text{min}}$  at 8 weeks compared with 4 weeks suggesting slight diastolic dysfunction, although this may have been caused in part by the lower LVSP in the 8 weeks sham group as the less load-dependent parameter  $\tau$  was not significantly changed. To our knowledge, no studies have investigated the effect of thoracotomy in the mouse on hemodynamic function at 2 time points. An effect of relief of pericardial constraint after pericardectomy could play a role, as it has been described that LV dilation and hypertrophy occurs in humans after pericardectomy.<sup>24</sup>

However, in the present study no LV remodeling was observed in the sham group at 8 weeks and no significant differences were observed between sham and control animals at 8 weeks. Another possible explanation would be that adhesions in the area of surgery exerted a negative effect.

In a previous cryoinfarction study, using a 4 mm cryoprobe, more adverse remodeling was reported after 4 weeks compared with the 3 mm probe in our study.<sup>16</sup> This corresponded with larger infarct areas reported. However, in our study more systolic and diastolic LV dysfunction was observed after 4 weeks using the 3 mm probe. This apparent discrepancy could be due in part to differences in anesthesia. In the present study isoflurane was used, whereas the agent tribromoethanol was used in the other study.

In our model the largest probe used was 3 mm in diameter because larger probe sizes did not fit well with our thoracotomy, since the area of freezing extends far beyond the actual probe size. This effect is not seen when a pre-cooled probe is used as in the study mentioned above.<sup>16</sup> Since, in our study, a significant adverse effect on LV function was found using a 3 mm probe, already at 4 weeks, we did not explore the effects of larger freeze injuries.

### **Methodological considerations**

No overt heart failure was seen after cryoinjury, likely due to the smaller infarct size in comparison with coronary ligation. We therefore feel that the cryoinfarction model should not be used to replace existing heart failure models. Rather it could serve as a model for the assessment of therapeutic interventions aimed at reducing cardiac remodeling and improving cardiac function after infarction, such as therapies aimed at cardiac regeneration using progenitor cells or growth factors.

The follow-up period in this study was 8 weeks. Probably the 8-week period is adequate to assess the degree of left ventricular remodeling or the effect of therapeutic interventions after cryoinfarction. Earlier studies reported marked effects on LV remodeling after 4 weeks in a cryoinfarction model<sup>16</sup> or 6 weeks in a LAD ligation model.<sup>2</sup> Our coronary ligation model resulted in a significant degree of LV remodeling after 4 weeks. However, since adverse remodeling in the cryoinfarction group only became apparent in the period between 4 and 8 weeks, longer follow-up periods may be studied in the future to assess the long-term effects of cryoinfarction.

### **Future studies**

The cryoinfarction model described is potentially an ideal model to evaluate interventions aimed at restoration of cardiac function or cardiac regeneration after myocardial infarction without a setting of overt heart failure. Thus, this model would be useful in cell transplantation studies<sup>6,8,9,25</sup> as (a) cells could then be easily injected at well-defined locations; (b) macrovascular reperfusion could be beneficial for cellular repair; (c) the repair process could be studied in an organised and very reproducible way and (d) the mouse model would

offer the possibility to investigate multiple (transgenic) cell types.

## **Conclusions**

This study describes the functional and histologic characteristics of a chronic, murine model of cardiac cryoinfarction and compares these with the classical model of MI through permanent coronary ligation. The results show that cryoinfarction is a technique with high peri-procedural survival resulting in reproducible infarcts leading to significant LV dysfunction and a modest degree of ventricular remodeling over a period of 8 weeks. These features make our cryoinfarction model a useful tool for analysis of functional effects of various interventions for cardiac regeneration such as cell therapy.

## References

1. Svenson KL, Bogue MA, Peters LL. Invited review: Identifying new mouse models of cardiovascular disease: a review of high-throughput screens of mutagenized and inbred strains. *J Appl Physiol* 2003;94:1650-9.
2. Patten RD, Aronovitz MJ, Deras-Mejia L, Pandian NG, Hanak GG, Smith JJ, Mendelsohn ME, Konstam MA. Ventricular remodeling in a mouse model of myocardial infarction. *Am J Physiol* 1998;274:H1812-20.
3. Salto-Tellez M, Yung Lim S, El-Oakley RM, Tang TP, Almsharqi ZA, Lim SK. Myocardial infarction in the C57BL/6J mouse: a quantifiable and highly reproducible experimental model. *Cardiovasc Pathol* 2004;13:91-7.
4. Ciulla MM, Paliotti R, Ferrero S, Braidotti P, Esposito A, Gianelli U, Busca G, Cioffi U, Bulfamante G, Magrini F. Left ventricular remodeling after experimental myocardial cryoinjury in rats. *J Surg Res* 2004;116:91-7.
5. Taylor CB, Davis CB Jr, Vawter GF, Hass GM. Controlled myocardial injury produced by a hypothermal method. *Circulation* 1951;3:239-53.
6. Murry CE, Wiseman RW, Schwartz SM, Hauschka SD. Skeletal myoblast transplantation for repair of myocardial necrosis. *J Clin Invest* 1996;98:2512-23.
7. Roell W, Fan Y, Xia Y, Stoecker E, Sasse P, Kolossov E, Bloch W, Metzner H, Schmitz C, Addicks K, Hescheler J, Welz A, Fleischmann BK. Cellular cardiomyoplasty in a transgenic mouse model. *Transplantation* 2002;73:462-5.
8. Roell W, Lu ZJ, Bloch W, Siedner S, Tiemann K, Xia Y, Stoecker E, Fleischmann M, Bohlen H, Stehle R, Kolossov E, Brem G, Addicks K, Pfitzer G, Welz A, Hescheler J, Fleischmann BK. Cellular cardiomyoplasty improves survival after myocardial injury. *Circulation* 2002;105:2435-41.
9. Taylor DA, Atkins BZ, Hungspreugs P, Jones TR, Reedy MC, Hutcheson KA, Glower DD, Kraus WE. Regenerating functional myocardium: improved performance after skeletal myoblast transplantation. *Nat Med* 1998;4:929-33.
10. Kamphoven JH, Stubenitsky R, Reuser AJ, Van Der Ploeg AT, Verdouw PD, Duncker DJ. Cardiac remodeling and contractile function in acid alpha-glucosidase knockout mice. *Physiol Genomics* 2001;5:171-9.
11. Tanaka N, Dalton N, Mao L, Rockman HA, Peterson KL, Gottshall KR, Hunter JJ, Chien KR, Ross J Jr. Transthoracic echocardiography in models of cardiac disease in the mouse. *Circulation* 1996;94:1109-17.
12. de Waard MC, van Deel ED, Merkus D, van Haperen R, de Crom R, Duncker DJ. Beneficial effect of exercise training on cardiac function is lost in mice that overexpress endothelial NO synthase. *Circulation* 2004;110:III299. (Abstract)
13. van der Velden J, Merkus D, Klarenbeek BR, James AT, Boontje NM, Dekkers DH, Stienen GJ, Lamers JM, Duncker DJ. Alterations in myofilament function contribute to left ventricular dysfunction in pigs early after myocardial infarction. *Circ Res*

- 2004;95:e85-95.
14. Passier R, Zeng H, Frey N, Naya FJ, Nicol RL, McKinsey TA, Overbeek P, Richardson JA, Grant SR, Olson EN. CaM kinase signaling induces cardiac hypertrophy and activates the MEF2 transcription factor *in vivo*. *J Clin Invest* 2000;105:1395-1406.
  15. Virag JJ, Murry CE. Myofibroblast and endothelial cell proliferation during murine myocardial infarct repair. *Am J Pathol* 2003;163:2433-40.
  16. Brede M, Roell W, Ritter O, Wiesmann F, Jahns R, Haase A, Fleischmann BK, Hein L. Cardiac hypertrophy is associated with decreased eNOS expression in angiotensin AT2 receptor-deficient mice. *Hypertension* 2003;42:1177-82.
  17. Zolotareva AG, Kogan ME. Production of experimental occlusive myocardial infarction in mice. *Cor Vasa* 1978;20:308-14.
  18. Duncker DJ, van Haperen R, van Deel ED, de Waard MC, Mees B, de Crom R. Endothelial nitric oxide synthase in cardiovascular homeostasis and disease. In: *The Physiological Genomics of the Critically Ill Mouse*. Ed: Ince C, Kluwer Academic Publishers, Dordrecht, The Netherlands, 2004.
  19. Palakodeti V, Oh S, Oh BH, Mao L, Hongo M, Peterson KL, Ross J Jr. Force-frequency effect is a powerful determinant of myocardial contractility in the mouse. *Am J Physiol* 1997;273:H1283-90.
  20. Yang XP, Liu YH, Rhaleb NE, Kurihara N, Kim HE, Carretero OA. Echocardiographic assessment of cardiac function in conscious and anesthetized mice. *Am J Physiol* 1999;277:H1967-74.
  21. Mazur P. Cryobiology: the freezing of biological systems. *Science* 1970;168:939-49.
  22. Huwer H, Nikoloudakis N, Rissland J, Vollmar B, Menger MD, Schafers HJ. In vivo analysis of microvascular injury after myocardial cryothermia. *J Surg Res* 1998;79:1-7.
  23. Reffelmann T, Hale SL, Dow JS, Kloner RA. No-reflow phenomenon persists long-term after ischemia/reperfusion in the rat and predicts infarct expansion. *Circulation* 2003;108:2911-7.
  24. Tischler MD, Rowan M, LeWinter MM. Increased left ventricular mass after thoracotomy and pericardiotomy. A role for relief of pericardial constraint? *Circulation* 1993;87:1921-7.
  25. Suzuki K, Murtuza B, Beauchamp JR, Smolenski RT, Varela-Carver A, Fukushima S, Coppen SR, Partridge TA, Yacoub MH. Dynamics and mediators of acute graft attrition after myoblast transplantation to the heart. *FASEB J* 2004;18:1153-5.



# Part 3

## Injection techniques



## Chapter 3

### Video-assisted thoracoscopic (VATS) transplantation of myoblasts into the heart

Thompson RB, Parsa CJ, van den Bos EJ, Davis BH, Toloza EM, Klem I, Glower DD, Taylor DA.  
Ann Thorac Surg 2004;78:303-7.



## Abstract

**Purpose-** Currently, cells are transplanted into injured myocardium either via thoracotomy for open surgical delivery or via catheterization for endoventricular or intracoronary delivery; both methods have limitations. Open surgical delivery limits the potential patient population, whereas catheter-based delivery limits the ability to visualize the injection site and confirm delivery of the cells to the appropriate region. In this study, we examine the feasibility of cell transplantation into myocardium using a minimally invasive thoracoscopic approach.

**Description-** Seven swine underwent thoracoscopic cell transplantation. Utilizing a prototype injection device, ~10 million myoblasts were injected into the anterior, lateral, posterior, and apical regions of myocardium. Animals were recovered up to 7 days and, after euthanasia, hearts were explanted for histology.

**Evaluation-** All seven swine had successful delivery of myoblasts into the defined injection sites, as confirmed by analysis of an operative video, magnetic resonance imaging of iron oxide-labeled cells and histologic examination.

**Conclusions-** Thoracoscopic cellular cardiomyoplasty is feasible and allows the surgeon the benefits of direct visualization of the cell injection while minimizing morbidity associated with open cell delivery.

## Introduction

Cell transplantation to repopulate injured myocardium has shown to be an effective therapy for improving both systolic and diastolic ventricular function pre-clinically.<sup>1-3</sup> Consequently, both in the U.S. and Europe, safety and efficacy trials are underway to evaluate cell therapy as a new tool for cardiac repair.<sup>4,5</sup> Current delivery methods are either via an open surgical approach during coronary artery bypass grafting (CABG) or left ventricular assist device insertion, or via catheter-based delivery. Each of these methods has benefits and limitations. Percutaneous catheter delivery of cells has the benefit of being minimally invasive but lacks direct visualization of the injection region and precludes delivery to thin scarred regions. Open surgical delivery necessitates a sternotomy or thoracotomy but allows precise delivery of cells to the desired region.

By utilizing a video-assisted thoracoscopic (VATS) approach, we set forth to deliver cells to distinct areas of the heart with limited acute morbidity, while obtaining the benefits of precise delivery under direct visualization.

Several limitations to video-assisted cell transplantation have been theorized: primarily a limited access to some areas of the myocardium - especially the posterior wall - and a difficulty in delivering cells to the beating heart (even under direct visualization). We conducted this experimental study to investigate the technical feasibility of VATS-based cellular cardiomyoplasty and to address those potential concerns.

## Materials and methods

All animals used received humane care in compliance with Duke University Institutional Animal Care and Use Committee (IACUC) guidelines and in compliance with "Guide for the Care and Use of Laboratory Animals" published by the National Institutes of Health (NIH publication 85-23, revised 1985).

### Surgical technique

Seven swine (40-50 kg) were anesthetized with ketamine (10 mg/kg IM) and acepromazine (2 mg/kg IM) and intubated in the right main stem bronchus under fluoroscopic guidance. General anesthesia was maintained with isoflurane (2-5%). A 10 mm thoracoport (U.S. Surgical Corporation, Norwalk, CT) was inserted in the 7<sup>th</sup> intercostal space mid axillary line. A 30 degree thoracoscope (Stryker Corporation, Kalamazoo, MI) was introduced through this port into the chest. Under direct visualization, a 5 mm port was inserted in the 8<sup>th</sup> intercostal space anterior axillary line. After placing the port, the trochar was removed to allow the introduction of both endoscopic shears and grasper, as shown in Figure 1A.

A pericardial window was developed in a longitudinal fashion, exposing a large section of left ventricular myocardium. An injection port was placed directly superior to the apex of the heart, lateral to the sternum and left internal mammary artery. Utilizing a prototype cell injection device developed in our laboratory, equipped with an angled 25

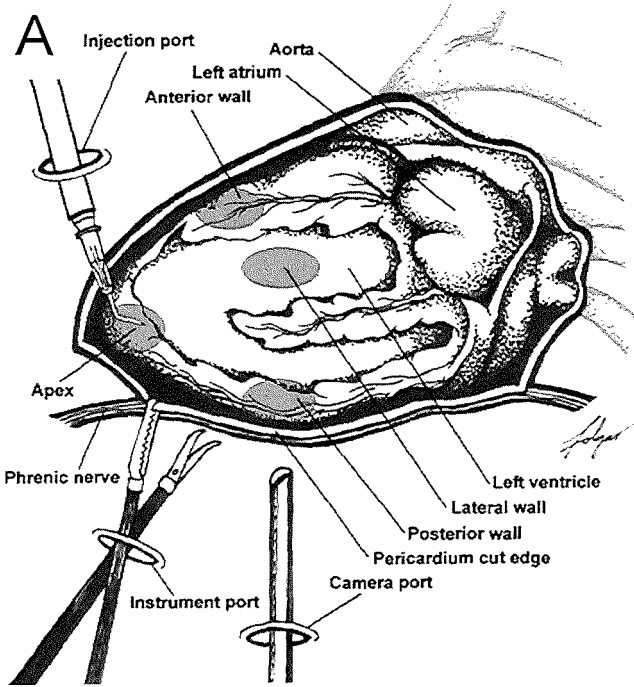
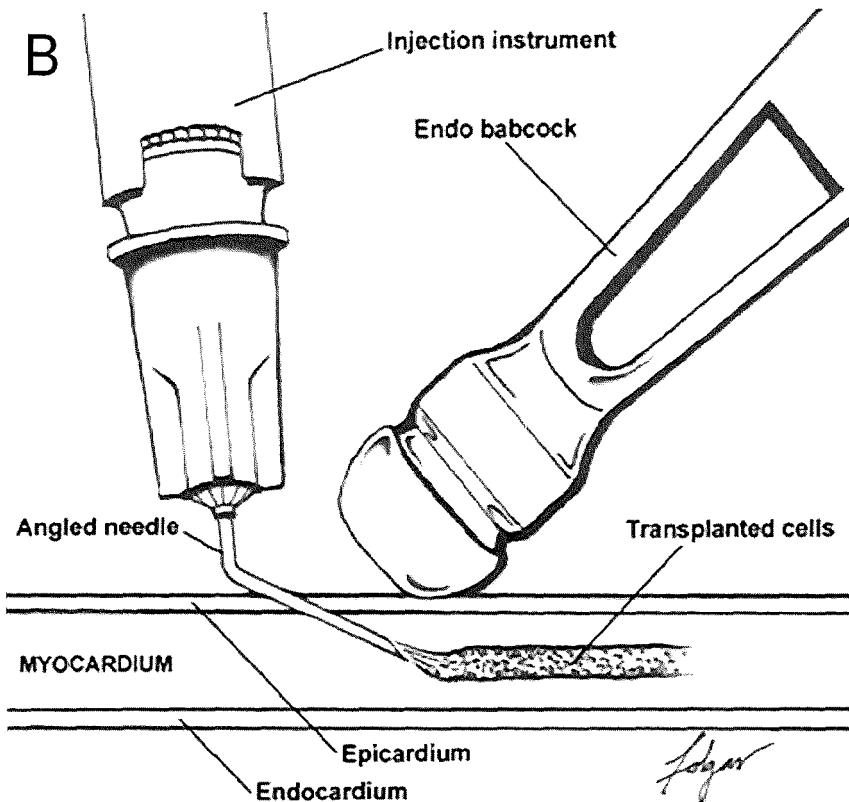


Figure 1. Panel A shows a schematic depiction of the components necessary for successful VATS cell transplantation, including instrument selection and defined cell delivery sites. The four areas of the heart highlighted in grey, represent major potential infarct zones that were targeted for cell delivery. Panel B shows that precise delivery of cells to the myocardium is accomplished via a combined use of an angled needle and stabilization of the heart with an endo-babcock. This allows layering of the cells in a site parallel to the epicardial surface.



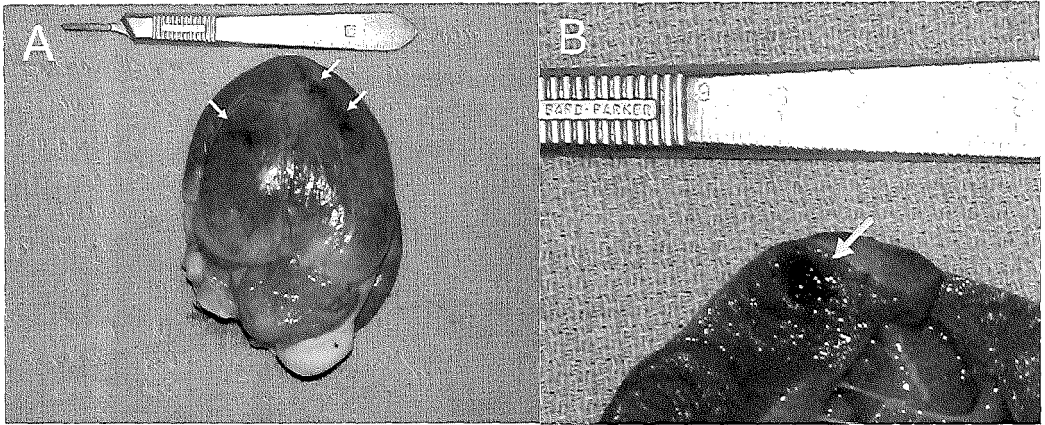


Figure 2. A representative explanted heart 4 hours post injection of  $2.5 \times 10^6$  myoblasts in each of four sites (posterior not visible) (Panel A), showing transmurial injection of pthalo blue dye (Panel B). Arrows indicate injected areas.

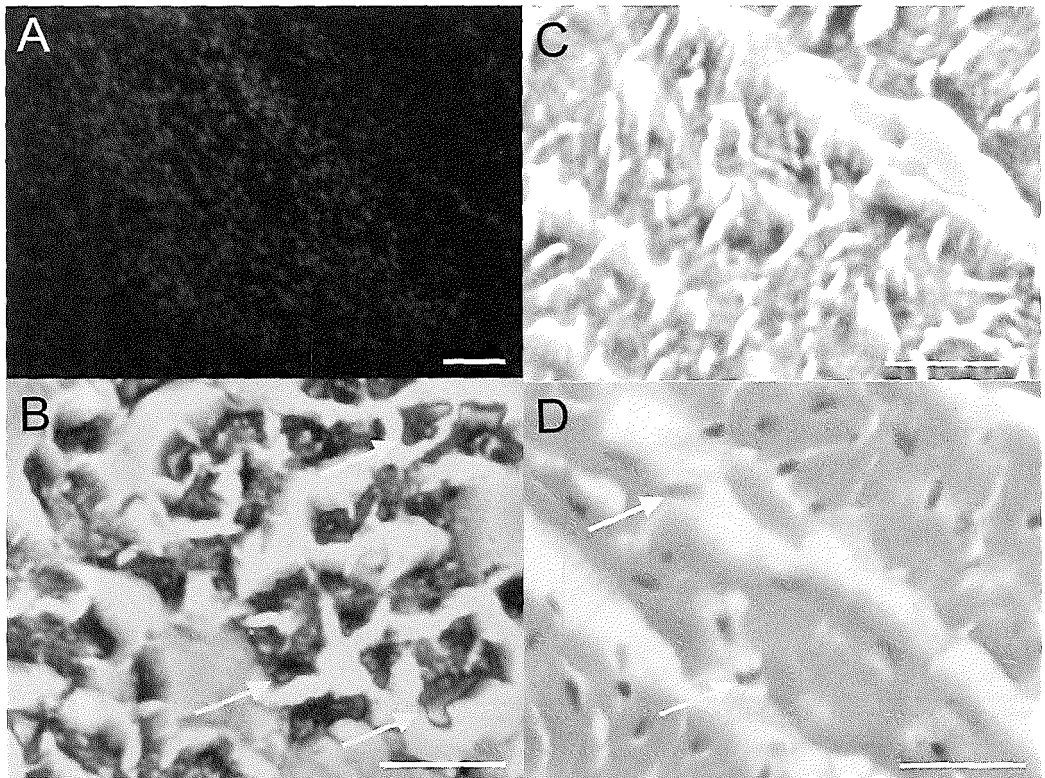


Figure 3. DAPI-labeled (Panel A) myoblasts directly injected into myocardium. Iron oxide-labeled (Panel B) skeletal myoblasts appear blue after Prussian Blue staining. Panel C is a negative control of a non-injected area. Panel D is an HE stain of the same area as in Panel B. Arrows indicate injected cells. Original magnification 200X. Bar indicates  $100 \mu\text{m}$ .

gauge needle,  $1 \times 10^7$  DAPI-labeled heterologous skeletal myoblasts were injected per animal in multiple areas of the left ventricular myocardium (Figure 1A), along with a pthalo blue marker dye. These areas included the anterior, lateral and posterior wall, and apex of the left ventricle. The use of an angled needle in the injection device allowed placement of the cells in a line parallel to the epicardial surface (Figure 1B). After successful injection of cells and dye, a single chest tube was placed under direct visualization through the 5 mm port site. The remaining port sites were closed in two layers, and the animals were allowed to recover and extubated. Chest tubes were removed after the animals were disconnected from positive pressure ventilation. Animals were monitored for 4 hours post-operatively, at which time they were euthanized and hearts were excised for histology.

Two animals were injected with myoblasts that were labeled additionally with Feridex superparamagnetic ironoxide particles (SPIO; Berlex Laboratories, NJ), which allows detection of iron-labeled cells *in vivo* by magnetic resonance imaging (MRI).<sup>6</sup> These animals survived for 7 days prior to MRI.

### Cell culture technique

Tissue from a 500-700 mg hindlimb biopsy of a heterologous swine was mechanically dissected into  $1 \text{ mm}^3$  pieces and washed once in sterile phosphate buffered saline (PBS), prior to resuspension and plating in myoblast growth medium, consisting of 10% fetal bovine serum and 0.5% gentamicin (10 mg/ml). The tissue fragments were triturated after 3 days, and the tissue was removed after 5 days. The myoblasts were expanded in myoblast growth medium at densities of less than 70% for 14 days (2-4 passages). Cells were incubated for 4 hours with  $10 \text{ }\mu\text{g/ml}$  of the fluorescent marker 4',6-diamidino-2-phenylindole (DAPI; Sigma, St. Louis, MO), prior to harvesting for injection. For injection,  $1 \times 10^7$  myoblasts per animal were trypsinized, washed twice in PBS, resuspended in 1.0 ml of saline for injection and loaded into the injection device.

For Feridex labeling cells were incubated with Feridex at  $10 \text{ }\mu\text{g/ml}$  and Lipofectamine 2000 (Gibco, Gaithersburg, MD) at  $3 \text{ }\mu\text{g/ml}$  in OptiMEM reduced serum medium (Gibco, Gaithersburg, MD) for 24 hours, followed by extensive washing in PBS.

### Cell viability

After passage through the injection device, cell viability was assessed by a standard Trypan Blue (TB) exclusion. The number of viable cells (exclusion of TB) was counted under a microscope using a hemacytometer and expressed as a percentage of the total number of cells (TB uptake).

### Magnetic resonance imaging

Two animals were studied with MRI 7 days after injection of SPIO-labeled myoblasts into the posterior wall. MRI was performed using a 1.5 Tesla clinical scanner (Sonata; Siemens

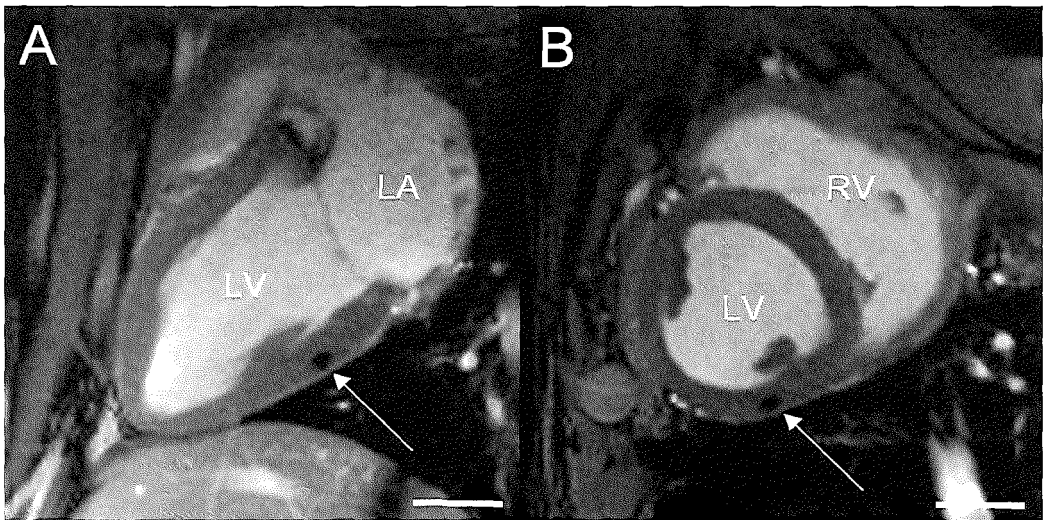


Figure 4. MRI cine images showing a long axis (Panel A) and short axis (Panel B) of the same animal. Injected myoblasts are visible as a black dot in the posterior wall (white arrow). LV indicates left ventricle; RV, right ventricle and LA, left atrium. Bar indicates 2 cm.

AG, Erlangen, Germany). ECG gated cine MR images were acquired of the whole left ventricle using a Steady State Free Precession (SSFP) pulse sequence, obtaining both long as well as short axis views. Imaging parameters were as follows: FOV=280x254 mm<sup>2</sup>, TE=1.86 ms, TR=33.39 ms, in plane resolution=1.09x1.09 mm<sup>2</sup>, slice thickness=5 mm.

### Histology

After explanting the hearts, the cell-injected areas of the myocardium were identified. These areas were embedded in OCT freezing medium, frozen in liquid nitrogen-cooled liquid nitrogen and cut on a cryostat in 5 micron thick serial sections. Sections were analyzed for the presence of DAPI and iron oxide-labeled cells. Iron was detected with a standard Prussian Blue iron stain (Sigma, St. Louis, MO) according to the manufacturer's instructions.

### Results

Passage of cells through the injection device did not influence viability, which was measured at >98% for 3 different cell populations. Marker dye was identified in the anterior, lateral, posterior and apical left ventricular wall after explant (Figure 2). Successful delivery of cells to all 7 animals was confirmed by histological identification of fluorescently labeled non-native cells in the injection locations of each heart (Figure 3). Cine MRI analysis of 2 animals showed the presence of iron oxide-labeled myoblasts in the posterior LV wall 7 days after injection (Figure 4, arrows). In addition, all seven swine successfully tolerated the procedure and survived until the euthanasia point either 4 hours or 7 days post-operatively.

To successfully reach all described areas of the heart, some minor variation in port

placement was necessary. In addition, to reach the posterior wall, the heart was elevated using an endo-retractor. To achieve optimal cell delivery without leakage, we developed a technique that combines heart stabilization and injection at an acute angle. Without angling the injection needle significant leakage was noted. Thus a bent needle that mimics our long-standing surgical protocol was incorporated in the injection device. Additionally, when failing to stabilize the myocardium it became more difficult to precisely deliver the cells to the marked location.

No hemodynamically significant arrhythmias were seen when manipulating the heart; however, some PVCs could be documented, particularly after the heart stabilization procedure. Of note, when incising the pericardium, it was critical to create a sufficiently large window so as to not only be able to maneuver the myocardium and deliver cells to the appropriate areas, but also to prevent atrial herniation, which temporarily occurred in one animal until the window was enlarged.

## Discussion

As research in cell therapy has progressed, the actual injection process has come under more scrutiny due to the realization of the importance of precise delivery of cells and the difficulty in generating vigorous engraftment. Furthermore, it has become clear that the positive functional outcome is directly related to the number of cells delivered.<sup>7</sup> To provide a minimally invasive surgical technique that allows maximum cell delivery we developed a VATS approach. In this feasibility study we show that by utilizing a thoracoscopic approach, cells can be effectively transplanted into host myocardium at all major potential infarct zones of the left ventricle, including the posterior wall, while still maintaining a precise direct visual delivery.

Of the currently described available delivery modalities, open chest cell delivery, usually as an adjunct to CABG, has received the most study. This open technique has had early success in a patient population that receives concurrent revascularization.<sup>4</sup> However, this need for revascularization has also confounded interpretation of any functional improvement seen in these patients. Thoracoscopic approaches provide the ability to deliver cells to injured myocardium without the need for sternotomy. The ability to deliver cells as an independent procedure, without CABG, should allow investigators to pinpoint functional improvement in patients after only cell therapy.

The other major technique currently used for delivery of cells is a catheter-based approach, in which an injection catheter is introduced either into the left ventricle, or via the femoral vein into the coronary sinus and great cardiac vein for access to the left ventricle. These techniques require either fluoroscopic guidance or ventricular mapping technology to define infarct zones, but still are unable to provide any direct visualization.<sup>8</sup> Further, under fluoroscopic guidance, precise localization of infarct zones is difficult and engraftment potentially suffers, as opposed to direct surgical injection, which has the potential to yield vigorous deposits in precise areas. Similarly, ventricular electrophysiologic mapping requires

interrogation of dozens of locations on the endocardium and takes a significant amount of time. Finally, catheter-based delivery is limited to areas greater than 5 mm in thickness, due to possible perforation, which limits the patient population to those who have not undergone significant wall thinning.

Thoracoscopic cell transplantation could offer the cardiac surgeon an excellent opportunity to provide a select group of patients, in whom revascularization is not indicated, the option to receive the benefit of cell therapy. VATS cell delivery offers clear benefits over both open surgical and catheter-based delivery. Of note, our study clearly only examines feasibility, and lacks any controlled comparison with other injection techniques regarding cell engraftment or effect on functional parameters. Our intent was to investigate the ability to successfully deliver cells by this technique to all areas of the left ventricle at risk for infarction. Ongoing pre-clinical studies are aimed at comparing various delivery techniques (open, catheter-based and VATS) and their effect on cardiac physiology, cell engraftment, and morbidity.

## References

1. Taylor DA, Atkins BZ, Hungspreugs P, Jones TR, Reedy MC, Hutcheson KA, Glower DD, Kraus WE. Regenerating functional myocardium: improved performance after skeletal myoblast transplantation. *Nat Med* 1998;8:929-33.
2. Orlic D, Kajstura J, Chimenti S, Jakoniuk I, Anderson SM, Li B, Pickel J, McKay R, Nadal-Ginard B, Bodine DM, Leri A, Anversa P. Bone marrow cells regenerate infarcted myocardium. *Nature* 2001;410:701-5.
3. Tomita S, Mickle DA, Weisel RD, Jia ZQ, Tumiati LC, Allidina Y, Liu P, Li RK. Improved heart function with myogenesis and angiogenesis after autologous porcine bone marrow stromal cell transplantation. *J Thorac Cardiovasc Surg* 2002;123:1132-40.
4. Menasche P, Hagege AA, Scorsin M, Pouzet B, Desnos M, Duboc D, Schwartz K, Vilquin JT, Marolleau JP. Myoblast transplantation for heart failure. *Lancet* 2001;357:279-280.
5. Strauer BE, Brehm M, Zeus T, Kostering M, Hernandez A, Sorg RV, Kogler G, Wernet P. Repair of infarcted myocardium by autologous intracoronary mononuclear bone marrow cell transplantation in humans. *Circulation* 2002;106:1913-8.
6. Garot J J, Untersee T, Teiger E, Champagne S, Chazaud B, Gherardi R, Hittinger L, Gueret P, Rahmouni A. Magnetic resonance imaging of targeted catheter-based implantation of myogenic precursor cells into infarcted left ventricular myocardium. *J Am Coll Cardiol* 2003;41:1841-6
7. Ellis MJ, Emani SM, Colgrove SL, Glower DG, Taylor DA. Cell dosage is critical for improved contractility following cellular cardiomyoplasty. *Circulation* 2001;104:II-336.
8. Dib N, Dietrich EB, Campbell A, Goodwin N, Robinson B, Gilbert J, Hobohm DW, Taylor DA. Endoventricular transplantation of allogeneic skeletal myoblasts in a porcine model of myocardial infarction. *J Endovasc Ther* 2002;9:313-9.



## Part 4

Survival of cells after intracardiac transplantation



# Chapter 4

## Mechanisms and dynamics of myoblast death after transplantation into a myocardial infarction



## Abstract

The relative contribution of necrosis versus apoptosis to myoblast death after intracardiac transplantation has not been assessed in a model of myocardial infarction (MI). In the present study we quantified myoblast necrosis and apoptosis *in vivo* in a mouse model of MI. Furthermore, the effect of caspase inhibition and attenuation of oxidative stress was assessed.

C3H mice were anesthetized using isoflurane and mechanically ventilated. They received an intracardiac injection of  $300 \times 10^3$  syngeneic, 4',6-diamidino-2-phenylindole (DAPI) labeled,  $C_2C_{12}$  myoblasts immediately after cryoinfarction. Mice were euthanized 0, 3, 6, 12, 24, 36 and 72 hours after injection and Alizarin Red and TUNEL staining were performed to quantify necrosis and apoptosis, respectively. Total grafted myoblast numbers were determined by counting DAPI-labeled myoblasts. A subset of experiments was performed under broad-spectrum caspase inhibition by ZVAD-FMK or with co-administration of the anti-oxidant 4-hydroxyl-2,2,6,6-tetramethylpiperidine-1-oxyl (Tempol) to study the role of oxidative stress.

Myoblast death occurred principally via necrosis during the first hours after injection ( $38 \pm 3\%$  at 3 hours), whereas apoptosis only played a limited role ( $11 \pm 4\%$  at 3 hours;  $P < 0.05$  versus necrosis). The rate of necrosis was blunted by Tempol at 6 hours (from  $32 \pm 4\%$  to  $17 \pm 4\%$ ), but not by ZVAD-FMK, thereby significantly increasing total grafted myoblast numbers at 36 hours as compared with the control group ( $111 \pm 23 \times 10^3$  versus  $38 \pm 11 \times 10^3$ , respectively).

These results indicate that myoblast death after injection into an acute myocardial infarction occurs principally via acute necrosis, likely as a result of oxidative stress.

## Introduction

Intracardiac myoblast transplantation prevents cardiac adverse remodeling after myocardial infarction (MI) and restores heart function.<sup>1-4</sup> The beneficial effect of myoblast transplantation increases with larger numbers of transplanted myoblasts.<sup>5</sup> Previous studies of myoblast death after intracardiac transplantation have shown several interventions that attenuate acute myoblast death and thereby increase the number of engrafting myoblasts.<sup>6-9</sup> These include heat-shock treatment of transplanted myoblasts<sup>6,7</sup> and pharmacological interventions aimed at reducing oxidative stress<sup>8</sup> or inflammation.<sup>9</sup> However, the exact mechanism underlying myoblast death after transplantation, i.e. necrosis or apoptosis, has not been studied to date.

Previous studies pertaining to cell survival following intracardiac injection were based on the detection of  $\beta$ -galactosidase<sup>6</sup> or [<sup>14</sup>C]-thymidine<sup>8,9</sup> in combination with donor-derived, Y chromosome gene markers.<sup>6,8,9</sup> The last two presumably require DNA degradation followed by phagocytosis before becoming undetectable, such that they may not represent the actual number of viable myoblasts.<sup>10-12</sup> A purported disadvantage of  $\beta$ -galactosidase is the potential immune response against the transgene<sup>13</sup> or down-regulation of its expression after transplantation.<sup>10</sup> A histologic method without these disadvantages, Alizarin Red (AR) staining, has been used to detect skeletal muscle<sup>14,15</sup> and myoblast necrosis<sup>16</sup> and to study the dynamics of myoblast death in Duchenne Muscular Dystrophy (DMD) studies.<sup>10</sup> However, the use of this stain to detect necrosis of intracardiac transplanted myoblasts has not been reported.

Therefore, in the present study we assessed myoblast necrosis and apoptosis *in vivo* after intracardiac injection in a murine cryoinfarction model using AR and terminal deoxynucleotidyl transferase-mediated dUTP nick end-labeling or TUNEL staining. Secondly, the effect of pharmacological reduction of oxidative stress on myoblast necrosis and apoptosis *in vivo* was studied, as this was previously shown to be very effective in reducing myoblast death.<sup>8</sup>

## Methods

The study complied with the regulations of the Animal Care Committee of the Erasmus MC and the Guide for the Care and Use of Laboratory Animals published by the US National Institutes of Health (NIH Publication No. 85-23, revised 1996).

### Cell culture

C<sub>2</sub>C<sub>12</sub> cells were purchased from the American Type Tissue Culture Collection (LGC Promochem, Teddington, UK) and grown in Dulbecco's Modified Eagle Medium (DMEM) with 10% horse serum (HS) and 0.5% gentamicin (all from Gibco, Gaithersburg, MD).

Twenty-four hours before injection, cells were replated at a concentration of  $2.5 \times 10^3$  cells per cm<sup>2</sup> dish surface. Cells were labeled overnight with the fluorescent dye 4',6-diamidino-

2-phenylindole (DAPI; 10 µg/ml; Sigma, St. Louis, MI) to allow identification of the cells after transplantation (Figure 1A and B).<sup>4</sup> Cells were harvested just before transplantation. The maximal time between harvest and injection was kept at 2 hours. A Trypan blue exclusion assay was performed of each cell sample before injection.

### Cryoinfarction and cell injection

Cryoinfarction was induced in C3H mice (~10 weeks of age), as described.<sup>17</sup> In brief: Mice were anesthetized and artificially ventilated with a mixture of O<sub>2</sub> and N<sub>2</sub>O (1/2, v/v) to which isoflurane (2.5-3.0%, v/v) was added. A thoracotomy was performed through the 4<sup>th</sup> left intercostal space, the pericardium was opened and the heart was exposed. Cryoinfarction was induced by applying a cryoprobe of 2 mm diameter (Brymill Cryogenic Systems, Basingstoke, United Kingdom) to the anterior wall during 10 seconds. Five minutes after induction of cryoinfarction, 3x10<sup>5</sup> cells in 5 µl PBS were injected from the infarct center to the infarct border in a transverse plane using a Hamilton syringe (Model 802 RN; Hamilton Bonaduz AG, Bonaduz, Switzerland) and 30G needle (Figure 1C). The thoracotomy was closed in layers.

In a subset of experiments, cells were injected in a solution of the broad-spectrum caspase inhibitor ZVAD-FMK at a final concentration of 100 µM (ZVAD<sub>low dose</sub>) or 400 µM (ZVAD<sub>high dose</sub>). The last group also received an injection of ZVAD-FMK (3 mg/kg, IP) 1 hour before cryoinfarction. The final concentration of the dimethyl sulfoxide vehicle was identical in both ZVAD-FMK groups. In a last subset of experiments, cells were injected in a solution of 4-hydroxyl-2,2,6,6-tetramethylpiperidine-1-oxyl (Tempol; 10 µg/5 µl PBS).

### Histology

At different time points (0, 3, 6, 12, 24, 36 and 72 hours) after infarction mice were euthanized by cervical dislocation. Hearts were excised, rinsed in saline and immediately frozen in OCT compound (TissueTek, Sakura, Japan) in liquid nitrogen-cooled isopentane. Hearts were cut at a cryomicrotome in 6 µm sections with 30 µm intervals, resulting in ~80 sections per heart covering the whole infarct area and kept frozen at -60°C. On the day of AR or TUNEL staining, sections were inspected by fluorescence microscopy using an inverted microscope (Axiovert S100; Zeiss, Oberkochen, Germany). DAPI-labeled cells could be identified and photographed using both fluorescence and light microscopy at 200X magnification.

### Alizarin Red stain

AR staining to detect necrotic cells was performed using a modification of a previously described protocol.<sup>10</sup> In brief: Sections were immersed for 20 seconds in 2% Alizarin Red (Sigma, St. Louis, MO) in distilled water at pH 5.4 followed by dehydration through PBS (pH 5.4), acetone, acetone/xylene (1:1) and xylene. Sections were then coverslipped and photographed using normal light microscopy. Myoblast necrosis was determined by marking all DAPI positive cells using SigmaScan image analysis software (Version 5.0.0; SPSS Inc, Chigago, IL) and copying the overlay to the AR images. Myoblast necrosis was then

calculated by dividing the total number of red, calcium loaded myoblasts, which were DAPI positive by the total number of DAPI positive myoblasts, multiplied by 100.

### **TUNEL stain**

TUNEL staining to detect apoptosis was performed using the In Situ Cell Death Detection Kit (TMR Red; Roche Diagnostics, France) according to the manufacturer's instructions. Fluorescence images were acquired and analyzed as described above for the AR stain.

### **Total grafted myoblast number**

DAPI positive myoblasts were counted in each section using Clemex Vision PE analysis software (Clemex Technologies, Longueuil, Quebec, Canada), using a pre-defined conversion factor from DAPI fluorescent area to number of cells. This conversion factor was determined by manually counting the total number of cells in 3 random hearts. This method was then validated for 3 more random hearts. For the 30  $\mu\text{m}$  intervals the mean cell number of the 2 bordering sections was assumed.

### **CD45 immunohistochemistry**

Sections were fixed in acetone, dried and blocked in blocking buffer (0.1% bovine serum albumine in PBS; Gibco, Gaithersburg, MD). Sections were then incubated in an anti-CD45 antibody (Sigma, St. Louis, MI) at 1:200 dilution followed by secondary staining using an Alexa fluor 568 conjugated antibody (Molecular Probes, Leiden, The Netherlands). Staining was analyzed by fluorescence microscopy. The grafts were photographed at 200X. The number of CD45 positive cells within each myoblast graft was counted and expressed as units per grafted area.

### **Statistical analysis**

Statistical analysis of all data was performed using one- or two-way ANOVA as appropriate followed by Student-Newman-Keuls test. Data are reported as means  $\pm$  standard error of the mean (SEM). Statistical significance was accepted when  $P < 0.05$  (two-tailed). Statistical analysis was performed using SigmaStat software (Version 2.03; SPSS Inc, Chigago, IL).

## **Results**

### **Cell injection**

Before injection 100% DAPI labeling was observed. Viability as assessed by Trypan blue staining before injection was  $95.4 \pm 1.7\%$ , and not below 92.6%. Backflow of the injectate was observed in one animal, which was therefore excluded. One animal was excluded because no transmural infarction was observed. The 58 remaining animals all survived the experimental protocol and all received successful cell injections as judged by the presence of DAPI-labeled cells within the cryoinfarcted area (Figure 1D, E and F).

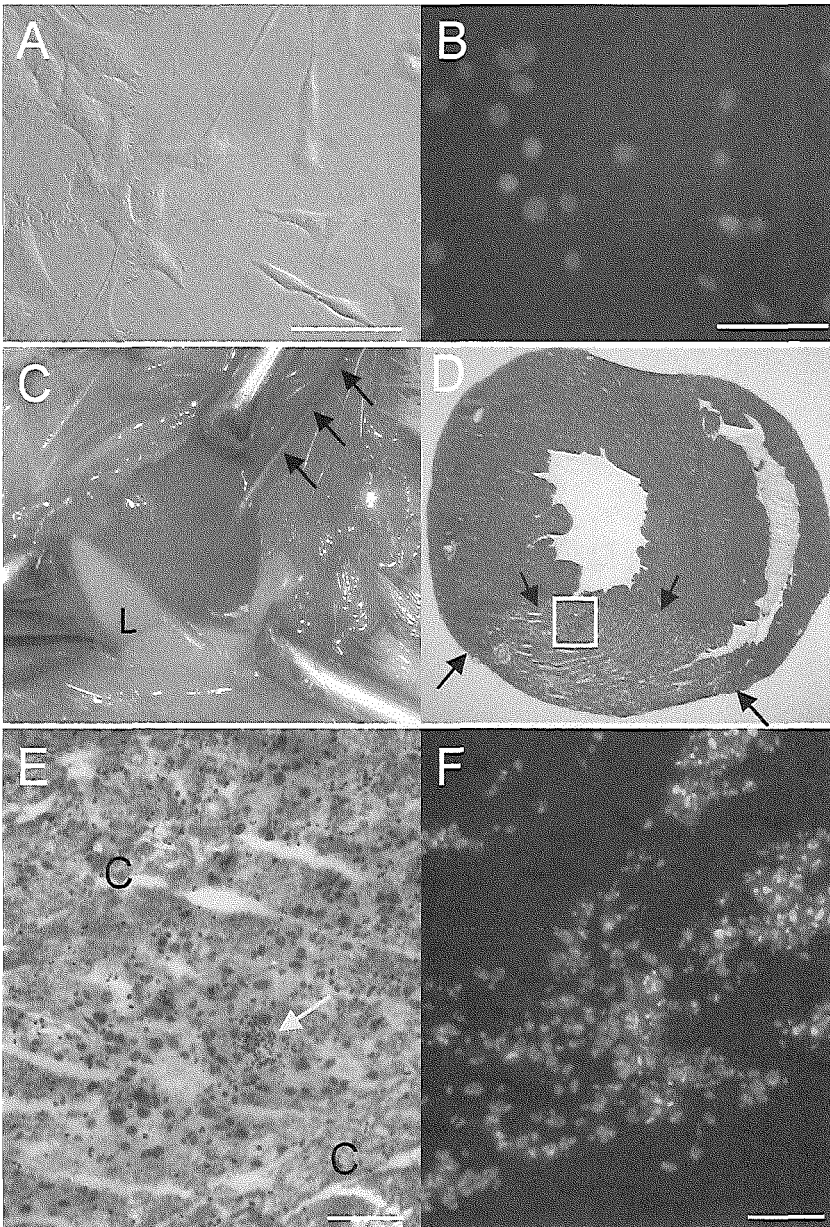


Figure 1.  $C_2C_{12}$  myoblasts (Panel A) were labeled overnight with DAPI (Panel B, same field) before injection. Cells were injected with a 30G needle (black arrows) into the centre and border of a cryoinfarction 5 minutes after injury (Panel C). The infarct area is visible as a dark circle. L indicates the left lung. Panel D shows a hematoxylin-eosin stain of a transverse section through the cryoinfarction 6 hours after myoblast injection. The infarct area is indicated by black arrows. The boxed region contains the grafted area and is shown at higher magnification in Panel E. Grafted cells have larger nuclei than the surrounding necrotic cardiomyocytes (indicated by C). A small group of inflammatory cells is indicated by the yellow arrow. Panel F shows the fluorescence image of the same field: Grafted cells are identified by the nuclear DAPI stain. Bar indicates 100  $\mu$ m.

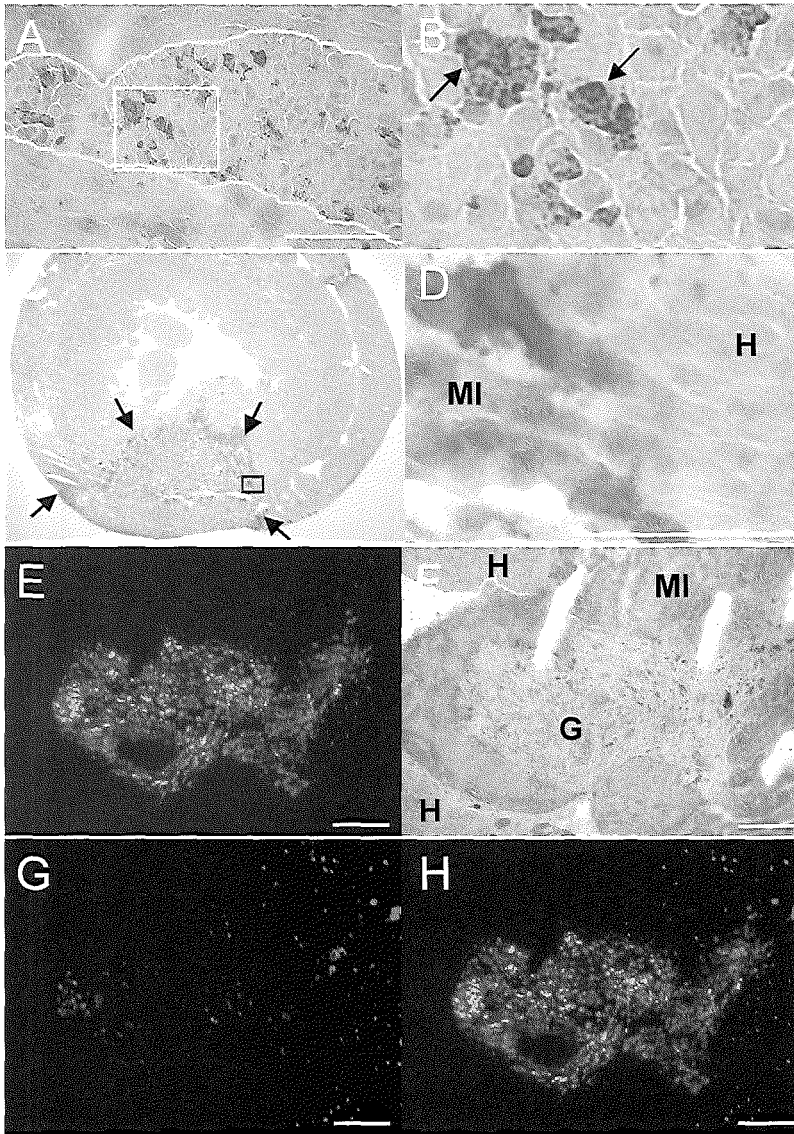


Figure 2. Panel A shows an Alizarin Red (AR) staining of an area with grafted myoblasts 3 hours after injection. The graft is delineated by the white line. The boxed region is shown in Panel B at higher magnification. Necrotic myoblasts are stained as a result of intracellular calcium uptake (black arrows). Necrotic myoblasts are surrounded by healthy, unstained myoblasts. Nuclei stain faintly grey (white arrow). Panel C shows an AR stain of a transverse section through a cryoinfarction, 3 hours after injection: The cone-shaped infarct area takes up the stain and can therefore be discerned from the healthy remote myocardium. The boxed region is shown in Panel D at higher magnification. Necrotic cardiomyocytes in the infarct border (indicated by MI) are also stained, contrasting with the healthy surrounding myocardium (indicated by H). Panel E shows a myoblast graft, 6 hours after injection. The corresponding region after AR staining is shown in Panel F. The graft is indicated by G, the cryoinfarcted area by MI and the healthy, surrounding myocardium by H. Panel G shows the same section as in Panel E after TUNEL staining. Apoptotic nuclei are easily identified. An overlay of Panels E and G is shown in Panel H. Bar indicates 100  $\mu$ m.

## Alizarin Red and TUNEL staining

AR stained necrotic transplanted myoblasts (Figure 2A and B), which could be distinguished from cryoinjured cardiomyocytes as shown in Figure 2C and D. Representative images of AR and TUNEL staining are shown in Figure 2E to H. As indicated in Figure 3A, necrosis was the predominant form of myoblast death up to 72 hours and was maximal the first 3 hours after injection ( $38 \pm 3\%$ ), followed by a gradual decline. Apoptosis played a more limited role ( $11 \pm 4\%$  at 3 hours). At 0 hours, AR did not stain any of the cryoinjured cardiomyocytes or grafted cells, possibly due to insufficient calcium uptake at this time point, as previously described<sup>10</sup> (data not shown). Therefore, instead, results of the Trypan blue exclusion assay are depicted at 0 hours.

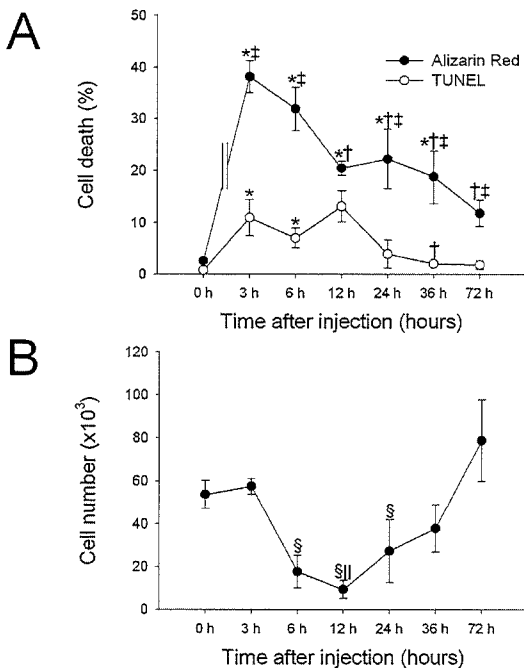


Figure 3. Panel A shows the percentage necrosis and apoptosis over time as determined by AR and TUNEL staining, respectively. For the AR 0 hours time point, the results of the Trypan blue exclusion assay are shown. Panel B shows the total number of grafted myoblasts, viable and non-viable, as quantified by counting total DAPI positive nuclei within each heart.

n=4 to 6 animals for each datapoint

\* $P < 0.05$  vs. corresponding 0 hours

† $P < 0.05$  vs. corresponding 3 hours

‡ $P < 0.05$  vs. corresponding TUNEL

§ $P < 0.05$  vs. corresponding 72 hours

|| $P = 0.06$  vs. corresponding 3 hours

## Total grafted myoblast number

It was assured that DAPI labeling identified all grafted and proliferating myoblasts: No leakage of the dye was observed to CD45 positive cells or neighbouring cardiomyocytes. Furthermore, no grafted areas were identified with myoblasts that had lost their DAPI labeling at 72 hours.

Total grafted and total viable myoblast numbers are shown in Figure 3B. Cell retention at 0 hours was  $18 \pm 2\%$  of the injected cell population. A significant decline in cell numbers was observed from 3 to 12 hours. From 12 hours up to 72 hours a significant increase in cell numbers occurred.

## Inflammatory response

Inflammatory cell infiltration of the grafted cell pockets is shown in Figure 4. Inflammatory cell infiltration was first observed at 6 hours after injection and was maximal at 12 hours after injection, followed by a gradual decline over 72 hours.

## Effects of ZVAD-FMK and Tempol

Co-administration of a low dose ZVAD-

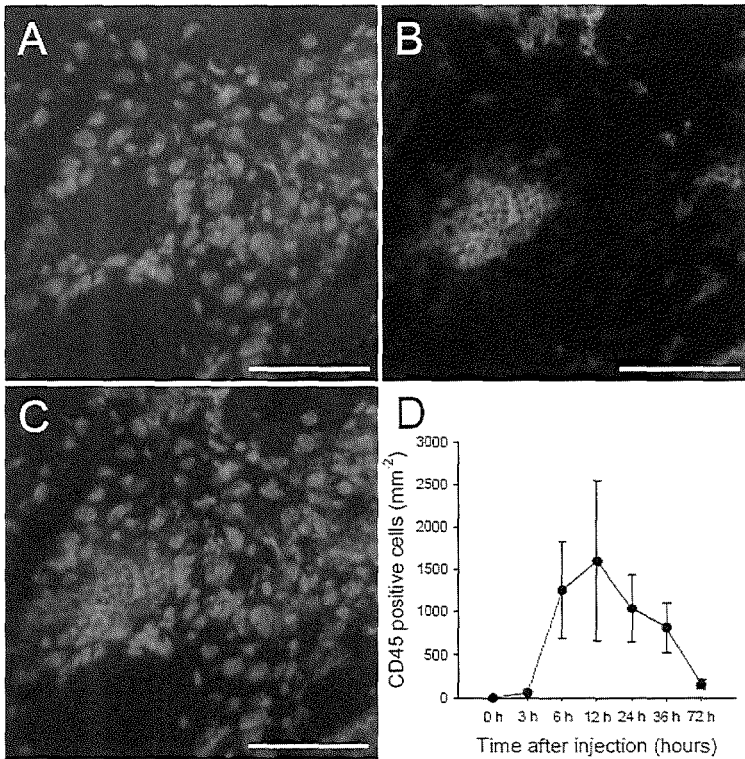


Figure 4. Panel A shows an area with grafted myoblasts 6 hours after injection. Panel B shows the corresponding region after CD45 staining. An overlay of Panel A and B is shown in Panel C. Panel D shows the number of infiltrating inflammatory (CD45 positive) cells within the grafts. Bar indicates 100  $\mu$ m.

FMK did not affect necrosis or apoptosis at 6 or 36 hours, however a high dose ZVAD-FMK significantly reduced apoptosis at 6 hours (from  $7 \pm 2\%$  to  $1 \pm 1\%$ ), without affecting necrosis (Figure 5). Inflammatory cell infiltration was significantly reduced at 6 hours in both ZVAD-FMK groups.

Co-administration of Tempol significantly reduced necrosis at 6 hours (from  $32 \pm 4\%$  to  $17 \pm 4\%$ ; Figure 5), without an effect on apoptosis. This caused a significant increase in total grafted myoblast number at 36 hours compared with the control group ( $111 \pm 23 \times 10^3$  versus  $38 \pm 11 \times 10^3$ ). Further, a significant decrease in inflammatory cell infiltration was seen at 6 hours compared with the control group.

## Discussion

### Methodological considerations

In the present study, a mouse cryoinfarction model was used that has been recently described.<sup>17</sup> Although the pathophysiology of this model is different from LAD ligation, it offers some advantages to study myoblast death mechanisms and dynamics. First, cryoinfarction creates a well-defined region of myocardial necrosis,<sup>17</sup> which facilitates injection of cells at a chosen location. This was confirmed by the present study: In all animals the injected cells were found within the infarct center or border, and only a limited number

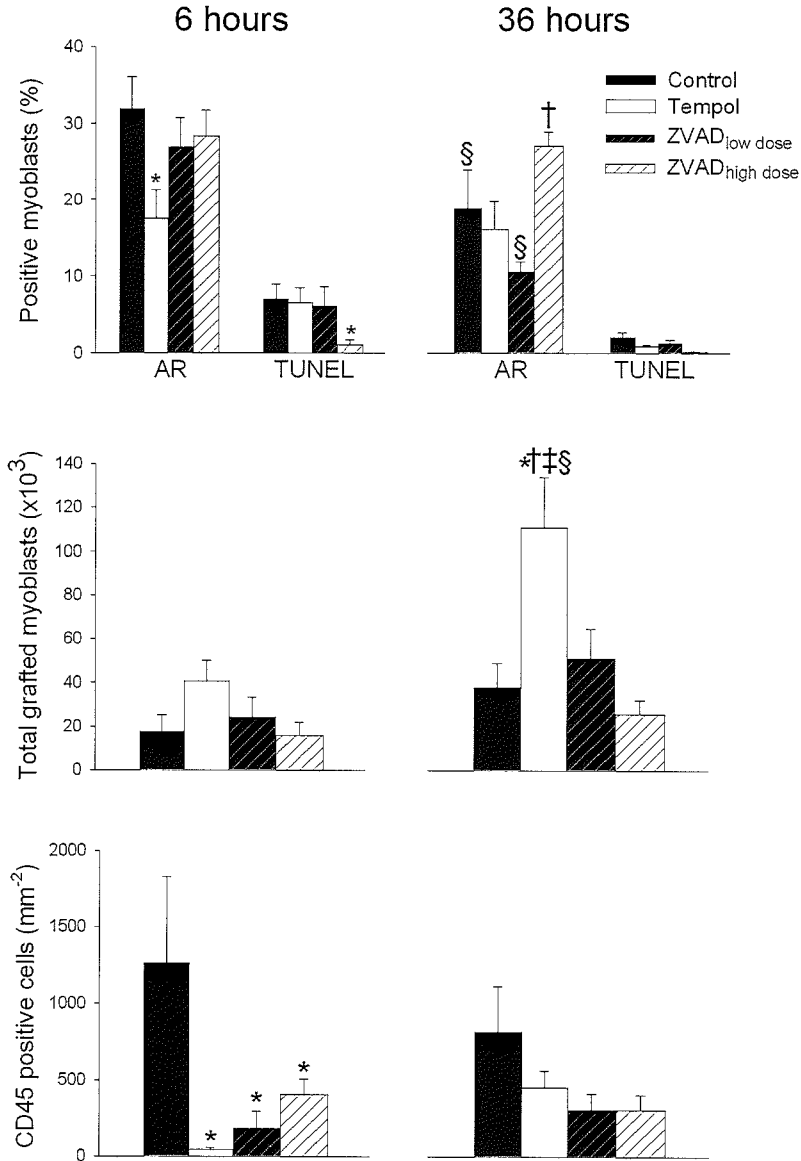


Figure 5. Necrosis and apoptosis (AR and TUNEL, respectively), total grafted myoblast number and CD45 positive cells per mm<sup>2</sup> of grafted area at 6 and 36 hours in control, Tempol, ZVAD<sub>low dose</sub> and ZVAD<sub>high dose</sub> groups.

\*P<0.05 vs. corresponding control

†P<0.05 vs. corresponding ZVAD<sub>low dose</sub>

‡P<0.05 vs. corresponding ZVAD<sub>high dose</sub>

§P<0.05 vs. corresponding 6 hours

of cells outside the infarct. Second, the infarct area is smaller and less infarct remodeling occurs,<sup>17</sup> therefore the whole infarct area can be sectioned and analyzed. Finally, since cryoinfarction results in no-reflow, leaving only a rim of endocardial microvessels intact,<sup>17</sup> it creates an environment that is deleterious to the injected cells, making it easy to detect the effect of various interventions.

The murine skeletal muscle cell line C<sub>2</sub>C<sub>12</sub> was used.<sup>18,19</sup> Use of this cell line for intracardiac transplantation studies has been previously described.<sup>20,21</sup> A cell line offers an advantage over primary cells: An identical and pure population of cells can be used for each experiment, reducing variance in study outcomes. Furthermore, since this cell line was originally isolated from the C3H strain no immune response is expected after *in vivo* injection. C<sub>2</sub>C<sub>12</sub> myoblasts have been used for differentiation studies<sup>22</sup> as well as studies of apoptosis<sup>23,24</sup> and share many characteristics with primary myoblasts. Despite these advantages of a cell line it must be taken into account that C<sub>2</sub>C<sub>12</sub> cells were previously shown to proliferate excessively and induce transmural replacement of myocardial infarctions.<sup>20</sup> Although this latter study was done in nude mice and although this effect was not seen in other studies,<sup>21</sup> care should be taken to use this cell type for more chronic studies since these cells might behave differently than primary mouse myoblasts.

AR staining has been used to determine necrosis of muscle fibers in skeletal muscle biopsies.<sup>15</sup> More recently the staining procedure was adapted and successfully used to determine necrosis of myoblasts after their transplantation into skeletal muscle.<sup>10</sup> The staining relies on the fact that a cell takes up calcium when the cell membrane is disrupted, as occurs early in necrosis.<sup>25</sup> This leads to the intracellular deposition of calcium, which is stained deep red by AR. Necrotic cardiomyocytes within the cryoinjured area also stained red with AR as depicted in Figure 2D. This observation has been reported before.<sup>26</sup> Because the staining relies on intracellular calcium uptake, which takes time after the cell membrane has been disrupted, no staining was observed at 0 hours. However, at 3 hours both the cryoinjured area as well as the donor cell pockets showed enough calcium uptake for reliable identification of necrotic cells. Since AR staining requires unstained sections, double-staining with TUNEL was not possible. It therefore remains unknown whether AR identifies any cells late in apoptosis when membrane integrity is lost. Using electron microscopy to identify specific changes associated with necrosis or apoptosis could possibly be used to evaluate this in more detail.

TUNEL staining has been extensively described in the literature for different cell types including C<sub>2</sub>C<sub>12</sub> myoblasts.<sup>27,28</sup> In one of those studies, TUNEL corresponded with activation of caspase 3 under hypoxic conditions.<sup>28</sup> Although caspase 3 activity could be quantified directly *in vivo* by immunohistochemistry,<sup>10</sup> this method is limited in the sense that it cannot discriminate between cells that actually undergo apoptosis and those with elevated levels of active caspase 3, but which have not progressed toward apoptosis.

A possible limitation of the present model is that myoblasts were transplanted in the acute setting of myocardial cryoinjury. In the acute phase, the environment is likely more

hostile and detrimental to the donor cells than when they are transplanted several days later or into a healing injury or infarction. Therefore, oxidative stress and acute necrosis could have been a more important causative factor of cell death in this phase than several days after infarction.

### Dynamics and mechanisms of myoblast death

Recent studies suggested that a biphasic pattern of myoblast death exists after injection into the heart<sup>8,9</sup> or into skeletal muscle for DMD:<sup>29-33</sup> Initially, during the first hours, ~60% of the cells are lost followed by a more gradual disappearance of cells up to 72 hours after transplantation.

In the present study, the majority of cells were lost during the injection procedure, likely due to limited retention of the injected cells as discussed below. Lowest number of grafted myoblasts was measured at 12 hours, which was  $2 \pm 1\%$  of the original cell population, containing  $7 \pm 3 \times 10^3$  viable cells. After 12 hours numbers increased to  $23 \pm 6\%$  of the original population at 72 hours, with  $70 \pm 19 \times 10^3$  viable cells, indicating that proliferation started 12 hours after injection. In previous studies, using a mouse model and a different myoblast cell line, proliferation caused an increase in cell numbers after 24 hours.<sup>8,9</sup> However, in these studies no data between 10 minutes and 24 hours were collected. In a rat model, proliferation only started after 3 days, however, in this study primary cells were used with a low percentage of myogenic cells and only two time points were assessed (3 days and 15 days).<sup>6</sup>

Necrosis was the predominant mechanism of cell death, peaking at 3 hours followed by a gradual decline up to 72 hours. The role of apoptosis appeared to be limited since (1) the maximal percentage of TUNEL positive cells was only  $13 \pm 3\%$  at 12 hours, followed by a rapid decline; (2) ZVAD<sub>high dose</sub> significantly reduced the percentage of TUNEL positive cells without affecting the total number of grafted myoblasts at 6 hours and finally (3) Tempol significantly increased cell numbers at 36 hours without affecting the percentage of TUNEL positive myoblasts.

### Causes of myoblast death

Both oxidative stress and inflammation have been shown to play an important role in the acute myoblast death after injection into healthy, non-infarcted myocardium: Reduction of oxidative stress by Cu/Zn-superoxide dismutase (Cu/Zn-SOD) co-administration<sup>8</sup> improved survival 10 min after injection and reduction of inflammation by an anti-IL-1 $\beta$  antibody significantly improved survival at 24 hours, without an effect on the acute myoblast death.<sup>9</sup> In the present study, it was found that the maximum rate of necrosis occurred after 3 hours, a time point at which little inflammatory cells were present in the grafted areas. We therefore hypothesized that oxidative stress would be a main determinant of the acute cell death in the present model.

To test our hypothesis, the radical scavenging, SOD-mimetic Tempol, was used

to decrease oxidative stress by *in vivo* co-administration. Tempol is a water-soluble and membrane-permeable radical scavenger.<sup>34</sup> Co-administration of Tempol significantly reduced myoblast necrosis at 6 hours, thereby increasing total myoblast numbers at 36 hours, suggesting that oxidative stress was a main determinant of the acute cell death.

It is difficult to predict how long this protective effect of Tempol will last, since little information on Tempol pharmacokinetics is available after local injection. A previous study using magnetic resonance spectroscopy, showed that the half-life after intravenous injection is in the range of 1 minute.<sup>35</sup> After subcutaneous injection, half-life is about 5 minutes. Half-life after injection into a cryoinfarcted area could be a little longer, since there is no-reflow after cryoinfarction,<sup>17</sup> limiting wash-out of the drug. However, based on our data, it can be assumed that the effect of Tempol is mediated within the first hours after injection. Therefore, it seems likely that a major source of free-radicals are the damaged cardiomyocytes or grafted necrotic myoblasts at the site of injection.

Furthermore, Tempol prevented inflammatory infiltration of the graft as assessed by CD45 staining. This could be due to the fact that less inflammatory cells are attracted due to the limited donor cell necrosis. To elucidate a possible mechanism, measurement of inflammatory cytokines could possibly be of help.<sup>9</sup> Surprisingly, ZVAD<sub>low dose</sub> or ZVAD<sub>high dose</sub> co-administration also significantly reduced inflammatory infiltration at 6 hours, despite the fact that ZVAD<sub>low dose</sub> did not have any effect on necrosis or apoptosis at this time point. This might explain the trend towards a reduction of myoblast necrosis at 36 hours in the ZVAD<sub>low dose</sub> group (P=0.33 vs. corresponding control). In the ZVAD<sub>high dose</sub> group, an unexpected trend towards an increase in necrosis was seen at 36 hours (P=0.16 vs. corresponding control) despite a significant reduction in apoptosis at 6 hours. The reason for this unspecific, adverse effect is unknown. A cytotoxic effect of ZVAD-FMK on cell survival has been described for other cell types such as neutrophils.<sup>36</sup>

## Cell retention

Limited retention of injected cells has been proposed as an important cause of limited myoblast engraftment.<sup>8,9</sup> However, thus far, few studies have directly addressed this factor. In the present study, hearts were taken out and frozen immediately after injection. Only  $18 \pm 2\%$  of injected cells were found at 0 hours, even though cell injection was carefully monitored through the stereomicroscope and macroscopic leakage was only observed in 1 out of 60 animals.

Because of this apparent large contribution of leakage during injection to graft size, interventions aimed at promoting cell retention could have an important impact on the success of myoblast transplantation. One could think of injecting cells within a scaffold of extracellular matrix, or the use of plugging devices or surgical techniques to close the needle tract at the moment of injection or withdrawal.

## References

1. Taylor DA, Atkins BZ, Hungspreugs P, Jones TR, Reedy MC, Hutcheson KA, Glower DD, Kraus WE. Regenerating functional myocardium: improved performance after skeletal muscle myoblast transplantation. *Nat Med* 1998;4:929-33.
2. Ghostine S, Carrion C, Souza LC, Richard P, Bruneval P, Vilquin JT, Pouzet B, Schwartz K, Menasche P, Hagege AA. Long-term efficacy of myoblast transplantation on regional structure and function after myocardial infarction. *Circulation* 2002;106:1131-6.
3. Menasche P, Hagege AA, Vilquin JT, Desnos M, Abergel E, Pouzet B, Bel A, Sarateanu S, Scorsin M, Schwartz K, Bruneval P, Benbunan M, Marolleau JP, Duboc D. Autologous skeletal myoblast transplantation for severe postinfarction left ventricular dysfunction. *J Am Coll Cardiol* 2003;41:1078-83.
4. van den Bos EJ, Thompson RB, Wagner A, Mahrholdt H, Morimoto Y, Thomson LE, Wang LH, Duncker DJ, Judd RM, Taylor DA. Functional assessment of myoblast transplantation for cardiac repair with magnetic resonance imaging. *Eur J Heart Fail* 2005;7:435-43.
5. Pouzet B, Vilquin JT, Hagege AA, Scorsin M, Messas E, Fiszman M, Schwartz K, Menasche P. Factors affecting functional outcome after autologous skeletal myoblast transplantation. *Ann Thorac Surg* 2001;71:844-50.
6. Maurel A, Azarnoush K, Sabbah L, Vignier N, Le Lorc'h M, Mandet C, Bissery A, Garcin I, Carrion C, Fiszman M, Bruneval P, Hagege A, Carpentier A, Vilquin JT, Menasche P. Can cold or heat shock improve skeletal myoblast engraftment in infarcted myocardium? *Transplantation* 2005;80:660-5.
7. Suzuki K, Smolenski RT, Jayakumar J, Murtuza B, Brand NJ, Yacoub MH. Heat shock treatment enhances graft cell survival in skeletal myoblast transplantation to the heart. *Circulation* 2000;102:III216-21.
8. Suzuki K, Murtuza B, Beauchamp JR, Smolenski RT, Varela-Carver A, Fukushima S, Coppen SR, Partridge TA, Yacoub MH. Dynamics and mediators of acute graft attrition after myoblast transplantation to the heart. *FASEB J* 2004;18:1153-5.
9. Suzuki K, Murtuza B, Beauchamp JR, Brand NJ, Barton PJ, Varela-Carver A, Fukushima S, Coppen SR, Partridge TA, Yacoub MH. Role of interleukin-1beta in acute inflammation and graft death after cell transplantation to the heart. *Circulation* 2004;110:II219-24.
10. Skuk D, Caron NJ, Goulet M, Roy B, Tremblay JP. Resetting the problem of cell death following muscle-derived cell transplantation: detection, dynamics and mechanisms. *J Neuropathol Exp Neurol* 2003;62:951-67.
11. Holmgren L, Szeles A, Rajnavolgyi E, Folkman J, Klein G, Ernberg I, Falk KI. Horizontal transfer of DNA by the uptake of apoptotic bodies. *Blood* 1999;93:3956-63.
12. Manfredi AA, Iannacone M, D'Auria F, Rovere-Querini P. The disposal of dying cells

- in living tissues. *Apoptosis* 2002;7:153-61.
13. Yuasa K, Sakamoto M, Miyagoe-Suzuki Y, Tanouchi A, Yamamoto H, Li J, Chamberlain JS, Xiao X, Takeda S. Adeno-associated virus vector-mediated gene transfer into dystrophin-deficient skeletal muscles evokes enhanced immune response against the transgene product. *Gene Ther* 2002;9:1576-88.
  14. Jennische E, Hansson HA. Postischemic skeletal muscle injury: patterns of injury in relation to adequacy of reperfusion. *Exp Mol Pathol* 1986;44:272-80.
  15. Dubowitz V. *Muscle biopsy a practical approach*. 2<sup>nd</sup> Edition. Bailliere Tindall, London, UK, 1985.
  16. Skuk D, Caron N, Goulet M, Roy B, Espinosa F, Tremblay JP. Dynamics of the early immune cellular reactions after myogenic cell transplantation. *Cell Transplant* 2002;11:671-81.
  17. van den Bos EJ, Mees BM, de Waard MC, de Crom R, Duncker DJ. A novel model of cryoinjury-induced myocardial infarction in the mouse: A comparison with coronary artery ligation. *Am J Physiol Heart Circ Physiol* 2005;289:H1291-00.
  18. Yaffe D, Saxel O. Serial passaging and differentiation of myogenic cells isolated from dystrophic mouse muscle. *Nature* 1977;270:725-7.
  19. Blau HM, Chiu CP, Webster C. Cytoplasmic activation of human nuclear genes in stable heterocaryons. *Cell* 1983;32:1171-80.
  20. Reinecke H, Murry CE. Transmural replacement of myocardium after skeletal myoblast grafting into the heart. Too much of a good thing? *Cardiovasc Pathol* 2000;9:337-44.
  21. Koh GY, Klug MG, Soonpaa MH, Field LJ. Differentiation and long-term survival of C2C12 myoblast grafts in heart. *J Clin Invest* 1993;92:1548-54.
  22. Deng X, Ewton DZ, Pawlikowski B, Maimone M, Friedman E. Mirk/dyrk1B is a Rho-induced kinase active in skeletal muscle differentiation. *J Biol Chem* 2003;278:41347-54.
  23. Dallabrida SM, Ismail N, Oberle JR, Himes BE, Rupnick MA. Angiopoietin-1 promotes cardiac and skeletal myocyte survival through integrins. *Circ Res* 2005;96:e8-e24.
  24. Dominov JA, Houlihan-Kawamoto CA, Swap CJ, Miller JB. Pro- and anti-apoptotic members of the Bcl-2 family in skeletal muscle: a distinct role for Bcl-2 in later stages of myogenesis. *Dev Dyn* 2001;220:18-26.
  25. Trump BF, Berezsky IK. The role of cytosolic Ca<sup>2+</sup> in cell injury, necrosis and apoptosis. *Curr Opin Cell Biol* 1992;4:227-32.
  26. Chatelain P, Kapanci Y. Histological diagnosis of myocardial infarction: the role of calcium. *Appl Pathol* 1984;2:233-9.
  27. da Costa KA, Badea M, Fischer LM, Zeisel SH. Elevated serum creatine phosphokinase in choline-deficient humans: mechanistic studies in C2C12 mouse myoblasts. *Am J Clin Nutr* 2004;80:163-70.
  28. Cho DH, Hong YM, Lee HJ, Woo HN, Pyo JO, Mak TW, Jung YK. Induced inhibition

- of ischemic/hypoxic injury by APIP, a novel Apaf-1-interacting protein. *J Biol Chem* 2004;279:39942-50.
29. Qu Z, Balkir L, van Deutekom JC, Robbins PD, Pruchnic R, Huard J. Development of approaches to improve cell survival in myoblast transfer therapy. *J Cell Biol* 1998;142:1257-67.
  30. Camirand G, Caron NJ, Turgeon NA, Rossini AA, Tremblay JP. Treatment with anti-CD154 antibody and donor-specific transfusion prevents acute rejection of myoblast transplantation. *Transplantation* 2002;73:453-61.
  31. Hodgetts SI, Spencer MJ, Grounds MD. A role for natural killer cells in the rapid death of cultured donor myoblasts after transplantation. *Transplantation* 2003;75:863-71.
  32. Lee-Pullen TF, Bennett AL, Beilharz MW, Grounds MD, Sammels LM. Superior survival and proliferation after transplantation of myoblasts obtained from adult mice compared with neonatal mice. *Transplantation* 2004;78:1172-6.
  33. Bouchentouf M, Benabdallah BF, Tremblay JP. Myoblast survival enhancement and transplantation success improvement by heat-shock treatment in mdx mice. *Transplantation* 2004;77:1349-56.
  34. Thiernemann C. Membrane-permeable radical scavengers (Tempol) for shock, ischemia-reperfusion injury, and inflammation. *Crit Care Med* 2003;31:S76-84.
  35. Kuppusamy P, Wang P, Shankar RA, Ma L, Trimble CE, Hsia CJ, Zweier JL. In vivo topical EPR spectroscopy and imaging of nitroxide free radicals and polynitroxyl-albumin. *Magn Reson Med* 1998;40:806-11.
  36. Cowburn AS, White JF, Deighton J, Walmsley SR, Chilvers ER. z-VAD-fmk augmentation of TNF alpha-stimulated neutrophil apoptosis is compound specific and does not involve the generation of reactive oxygen species. *Blood* 2005;105:2970-2.



## Part 5

### Functional assessment of cell transplantation



# Chapter 5

## Functional assessment of myoblast transplantation for cardiac repair with magnetic resonance imaging

van den Bos EJ, Thompson RB, Wagner A, Mahrholdt H, Morimoto Y, Thomson LE, Wang LH, Duncker DJ, Judd RM, Taylor DA. Eur J Heart Fail 2005;7:435-43.



## Abstract

**Background-** Contraction of transplanted myoblasts and the effect on function and remodeling after myocardial infarction remain controversial.

**Aim-** We used magnetic resonance imaging (MRI) to study wall thickening and left ventricular (LV) function and geometry after myoblast transplantation.

**Methods and results-** Three weeks after cryo-infarction rabbits were randomized to receive an injection with  $\sim 2 \times 10^8$  myoblasts (n=8) or medium (n=9) into the scar. Cine MRI and contrast enhanced MRI images were acquired before injection (baseline) and 4 weeks later (endpoint). Regional wall thickening was measured at the site of transmural hyperenhancement. In the control group regional wall thickening decreased to  $-15.3 \pm 8.6\%$  at baseline, which further decreased to  $-18.3 \pm 5.7\%$  at endpoint. Further, end-diastolic volume increased from  $3.96 \pm 0.27$  to  $5.00 \pm 0.46$  ml and end-systolic volume from  $2.23 \pm 0.19$  to  $2.96 \pm 0.30$  ml (both  $P < 0.05$  vs. baseline), which was accompanied by increased LV wall volumes ( $P < 0.05$  vs. baseline). In contrast, myoblast transplantation increased regional wall thickening from  $-11.9 \pm 15.9\%$  at baseline to  $26.9 \pm 17.0\%$  ( $P < 0.05$  vs. control), which resulted in significantly improved 2-D ejection fractions at the infarct level and attenuation of end-diastolic and end-systolic volumes and wall volume.

**Conclusion-** Intracardiac myoblast transplantation after myocardial infarction improves regional wall thickening and prevents progressive left ventricular remodeling.

## Introduction

Myocardial infarction results in loss of contractile tissue. Transplantation of contractile cells into the infarct scar represents a promising new therapy for restoring cardiac function. Intracardiac transplantation of skeletal myoblasts results in viable grafts and the formation of myotubes in the scar area.<sup>1-3</sup> Furthermore, myoblast transplantation has been shown to improve global and regional heart function and prevent left ventricular (LV) remodeling in various species including rats,<sup>2,4</sup> rabbits,<sup>3</sup> sheep<sup>5</sup> and recently humans.<sup>6</sup> However, active contraction of the transplanted cells in the infarct and its contribution to improved regional and global heart function remains controversial, partly because of limitations of the methods used for measuring regional function.

Studies in sheep and rats using color kinesis echocardiography,<sup>2,5,9</sup> showed increased myocardial velocity gradients at the site of the infarct after myoblast transplantation. However the limitation of this method is that the site of the infarct cannot be reproducibly localized during repeated measurements. Further, cardiac motion can influence the signal.

We previously used sonomicrometry and micromanometry to show improvement in regional function after myoblast transplantation.<sup>3</sup> However, this method only measures epicardial shortening between a single pair of crystals without measuring wall thickening at the infarct site. Further, the influence of regional improvement on global function and LV geometry in this model was not assessed.

Magnetic resonance imaging is a rapidly developing technique for assessment of heart function,<sup>10</sup> and LV geometry. MRI makes it possible to determine the exact location of the infarct by using contrast enhanced (ce) imaging<sup>11</sup> and it allows for repeated measurements of wall thickening at the infarct site. Further, by using MRI, changes in two dimensional ejection fraction at the infarct level and global ejection fraction can be accurately measured over time together with changes in LV volumes associated with ventricular remodeling.<sup>12</sup>

We used our model of cryoinjured rabbit hearts,<sup>3</sup> and implanted skeletal myoblasts 3 weeks after injury. All animals underwent cine and ce MRI before injection of cells (baseline) and 4 weeks later (endpoint).

## Materials and methods

### Cryoinfarction and muscle biopsy

The investigation conforms with the Guide for the Care and Use of Laboratory Animals published by the US National Institutes of Health (NIH Publication No. 85-23, revised 1985). Twenty-four New Zealand White rabbits, weighing 3.5 to 4.5 kg, underwent a left thoracotomy under isoflurane anesthesia and tracheal ventilation. A 1 cm cryoprobe (Brymill Cryogenic Systems, Basingstoke, United Kingdom) was placed on the antero-lateral wall of the ventricle for 35 seconds. During the same session a ~0.5 g soleus biopsy was taken from the hindlimb.

## Cell culture

After removal of aponeurotic tissue, the muscle biopsy was minced and grown in Dulbecco's Modified Eagle's Medium (DMEM), supplemented with 10% fetal bovine serum (FBS) and 0.5% gentamicin (10 mg/ml) (Gibco, Gaithersburg, MD). After 3 days the muscle biopsy was triturated, fed with growth medium and replated. Cells were passaged 1:4 when reaching approximately 70% confluency. After the first passage, growth medium was changed for DMEM with 20% horse serum. Before injection cells were labeled overnight with the nuclear fluorescent marker 4',6-diamidino-2-phenylindole (DAPI; Sigma, St. Louis, MO) at 10 µg/ml. Cultures were at passage 4 at the time of injection.

To confirm purity of the transplanted cells, a subset of cells were grown on glass coverslips, fixed with 5% paraformaldehyde, and blocked for 1 hour in phosphate buffered saline (PBS) with 5% HS and 5% FBS. Primary staining was carried out using a monoclonal anti-desmin antibody (Sigma, St. Louis, MO) at 1:200 dilution, followed by secondary staining. Staining was analyzed on a Nikon TE 200 Eclipse fluorescent inverted microscope. The number of desmin positive cells was counted in multiple fields and expressed as a percentage of the total cell number.

## Myoblast transplantation

Animals that survived 3 weeks after infarction were randomized to receive an injection of culture medium or myoblasts. For injection, cells were harvested by trypsinization, washed twice in DMEM and resuspended in DMEM. A left thoracotomy was performed and 3 injections of 330 µl were delivered in a transversal plane into the center of the infarct using a 25G needle.

## Magnetic resonance imaging

Animals were studied 20 days after infarction (baseline) and 4 weeks after cell transplantation (endpoint) by cine MRI and ce MRI. MRI was performed using a 1.5 Tesla clinical MRI scanner (Sonata; Siemens AG, Erlangen, Germany) with a flexible radiofrequency receiver coil. Animals were sedated with ketamine (50 mg/kg) and acepromazine (1 mg/kg). MRIs were ECG gated. Both cine and corresponding ce MRIs were prescribed every 4 mm from base to apex, starting at the level of the mitral valve, which resulted in 4 to 5 short axis slices. Scout transversal and sagittal views ensured correct determination of the short-axis planes. A long-axis cine was also prescribed.

Cine MRI images were acquired using a FLASH sequence. Typical imaging parameters were the following: repetition time=35 ms, echo time=4.8 ms, bandwidth=195 kHz, flip angle=30°, in plane resolution=0.3x0.3 mm<sup>2</sup> and slice thickness=2 mm. Ce-MRI was performed directly after administration of 0.3 mmol/kg Gd-DTPA. T1-weighting was achieved using a FLASH sequence. Inversion time (TI) was adjusted to obtain the highest contrast between healthy myocardium and infarct area. Typical image parameters were: repetition time=1350 ms, echo time=4.8 ms, bandwidth=130 kHz, in plane resolution=0.3x0.3

mm<sup>2</sup> and slice thickness=2 mm. Ce MR images were ECG gated to end-diastole. Four weeks after injection all cine and ce images were repeated (endpoint). Those short axis slices were imaged that corresponded to the slices at baseline based upon anatomical landmarks.

Additionally, to provide healthy controls, 5 non-infarcted animals were studied by cine MRI following the same MRI protocol.

### Data analysis

#### Image registration

For each pair of cine and ce images the centerpoint of the heart was defined, and the myocardium was divided into 12 circumferential segments. Those segments in which the infarct was totally transmural along the whole endocardial line, were used for calculation of regional wall thickening. All segments that did not contain any hyperenhancement were selected for calculation of wall thickening of remote non-infarcted myocardium. The short axis slices were defined as infarct slices ( $S_{\text{infarct}}$ ), when they contained a segment with transmural infarction on the corresponding contrast enhanced slice at baseline. All other slices were defined as non infarct slices ( $S_{\text{non infarct}}$ ) (Figure 1).

The views acquired at endpoint were rotated to exactly match the baseline views and the angle was recorded.

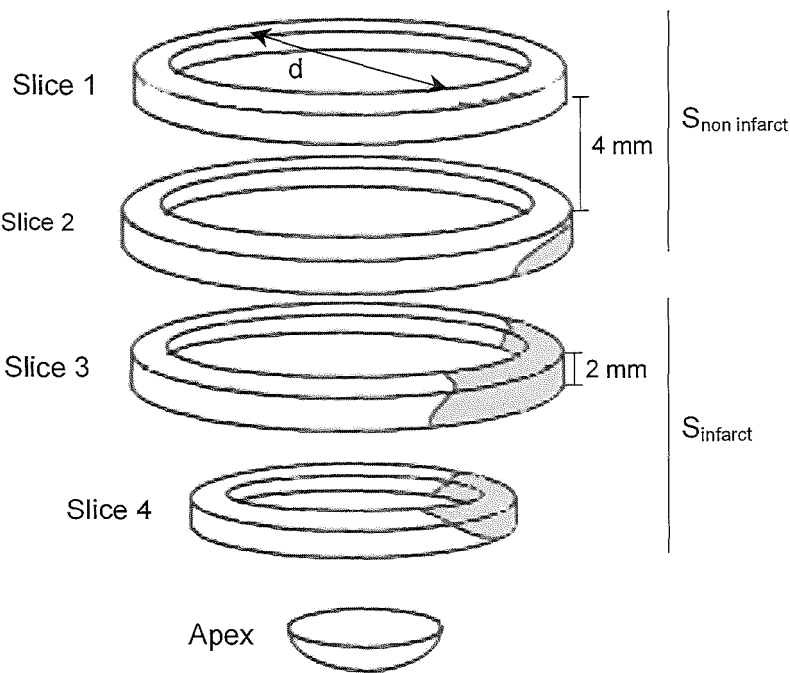


Figure 1. Schematic representation of MRI short axis views.

***Wall thickening***

End-diastolic and -systolic short axis slices were chosen by determining the image with the largest and smallest LV areas. Endocardial and epicardial borders were manually traced using NIH image 1.6. Image analysis was performed twice on separate occasions by 1 observer blinded to the treatment groups with a minimal time interval of 2 months and by a second blinded observer to calculate intra- and interobserver variability. A self written computer program was used to calculate end-diastolic and -systolic wall thickness in 12 segments using the modified centerline method.<sup>13</sup> Wall thickening was expressed as a percentage of end-diastolic thickness.

***Ejection fraction and ventricular geometry***

From the manual border tracings, end-diastolic and end-systolic areas, LV circumference and LV diameters were calculated. End-diastolic and -systolic volumes were determined by multiplying the left ventricular endocardial areas in diastole and systole times the slice thickness. For the view intervals, an average area was calculated by summing the areas in adjacent slices and dividing them by two. Thickness of the intervals equaled the distance between the two adjacent slices. For the most apical interval, a thickness was calculated by subtracting the thickness of the other views and intervals from the mean systolic long axis length. This resulted in total end-diastolic volume (EDV) and total end-systolic volume (ESV). Global EF ( $EF_{\text{global}}$ ) was expressed as:

$$EF_{\text{global}} = \frac{\text{EDV} - \text{ESV}}{\text{EDV}} \times 100\%$$

For calculation of 2-D ejection fractions (fractional LV lumen area reduction) at the level of each short-axis slice, end-diastolic (EDA) and -systolic (ESA) endocardial areas were used and 2-D EF was expressed as:

$$2\text{-D EF} = \frac{\text{EDA} - \text{ESA}}{\text{EDA}} \times 100\%$$

Mean end-diastolic infarct thickness was calculated from those segments that contained hyperenhanced area along the whole epicardial surface. Infarct circumference was measured along the hyperenhanced epicardial surface.

**Histological analysis**

After the last scan, animals were weighed, euthanized with pentobarbital and hearts were excised. LV wet weights were determined. Ventricles were kept in 30% sucrose overnight, frozen in OCT embedding medium in liquid nitrogen and sliced on a cryostat in series of 10 sections of 6 micron thickness through the whole infarct area. From every series the last 2 sections were stained with hematoxylin-eosin and Goldner's Trichrome. The other sections were fixed with 5% paraformaldehyde and permeabilized with 1% Tween. Sections were

blocked 1 hour. Primary antibody staining was carried out using the following rabbit-specific antibodies: anti-desmin, anti-fast myosin heavy chain (MHC), anti-slow MHC, anti-connexin 43 (all from Sigma, St. Louis, MO) and anti-troponin I (Chemicon, Temecula, CA) (all diluted 1:200). This was followed by secondary staining for 60 minutes.

### Statistical analysis

Continuous data are expressed as mean  $\pm$  SEM. Inter group comparisons were made using two-way ANOVA. Intra group comparisons were made using a two-tailed paired t-test.  $P < 0.05$  was considered statistically significant.

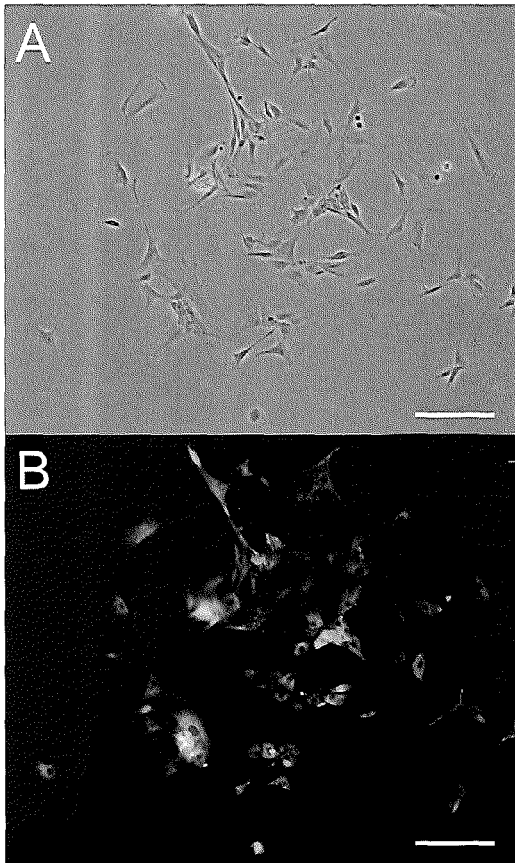


Figure 2. Normal light (left Panel) and corresponding fluorescent micrographs (right Panel) of desmin stained myoblasts after 3 weeks of culture. Original magnification is 200X. Bar indicates 100  $\mu$ m.

## Results

Three animals died in the first 24 hours after the first thoracotomy, 2 animals died during the second procedure and 1 animal died during the baseline scan. One animal was excluded after the baseline scan, because there was no transmural infarction. This left a total of 8 cell treated animals and 9 control animals to complete the study.

### Cell culture

Cultures yielded an average of  $189 \times 10^6$  cells (150 to  $240 \times 10^6$  cells), with more than 90% of desmin positive cells ( $92.3 \pm 4.2\%$ ) (Figure 2).

### Cryoinfarction and LV function

The effects of cryoinjury on LV function and geometry is shown in Table 1.

### Hyperenhancement and infarct size

A total of 72 and 68 short axis views were analyzed in the control and cell treated groups respectively, resulting in a mean number of matching short axis slices per animal of 4.0 and 4.3 respectively. Four short axis views in the control group and 3 in the cell treated group were excluded

**Table 1. Left ventricular function and geometry after cryoinjury**

	Non-infarcted, healthy (n=5)	Cryoinjury (n=17)
Ejection fraction, %	56.1±1.2	43.0±1.2*
LV end-diastolic volume, ml	3.06±0.22	4.02±0.18*
LV end-systolic volume, ml	1.35±0.12	2.29±0.13*
Stroke volume, ml	1.71±0.12	1.73±0.09
Heart rate, beats/min	225±4	221±3
Cardiac output, ml/min	384±25	380±18
Long-axis end-diastolic length, mm	24.4±0.22	25.0±0.04
Wall volume, including infarct, ml	4.04±0.22	4.48±0.17

\*P<0.05 vs. non-infarcted

from final analysis because image levels were too apical to allow for accurate wall thickness determination, thus yielding a total of 68 (x12 circumferential segments) and 65 (x12 circumferential segments) short axis views and 816 and 780 segments in the control and cell treated group respectively for analysis of wall thickening.

In the control group 150 of the 816 segments (18.4%) showed hyperenhancement and in 62 segments (7.6%) the infarct was transmural. In the cell treated group 136 of the 780 segments (17.4%) showed hyperenhancement and in 66 segments (8.5%) the infarct was transmural. All segments with transmural infarction were used for calculation of regional wall thickening.

Inter-observer variability was  $-4.2\pm 1.6\%$  and  $-1.3\pm 3.6\%$  for LV EDV and ESV

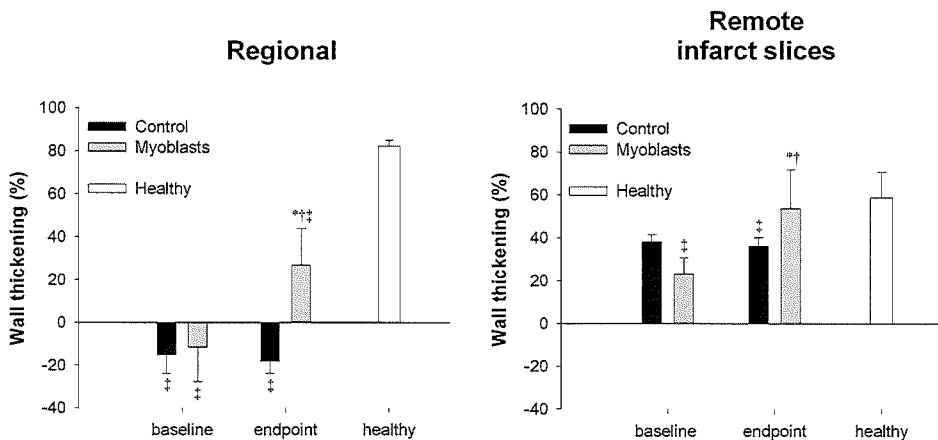


Figure 3A. Regional wall thickening at baseline and endpoint in the two groups (left panel) and wall thickening in the remote area of the slices defined as infarct (right panel). \*P<0.05 versus corresponding baseline; †P<0.05 change in myoblast versus control group; ‡P<0.05 versus healthy.

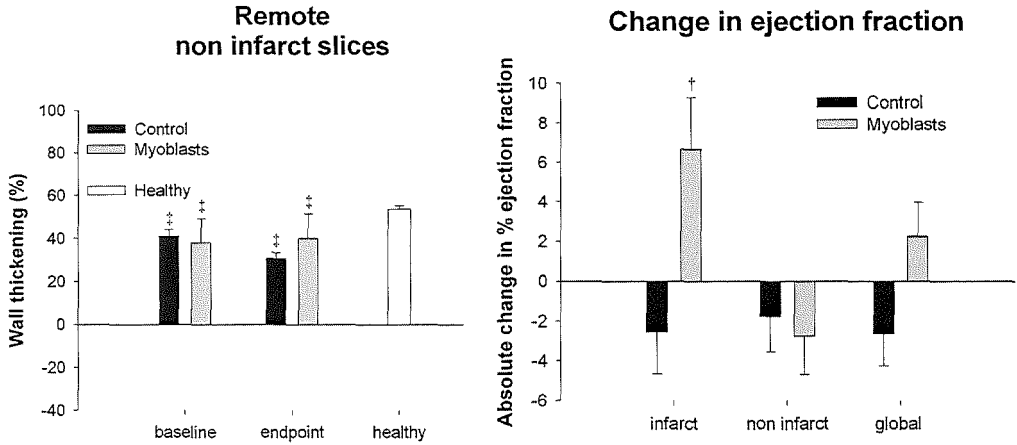


Figure 3B. Wall thickening at baseline and endpoint in the two groups in the remote area of the slices defined as infarct non infarct (left panel). Right panel shows two dimensional ejection fractions (fractional area reduction) at the infarct and non infarct level and global ejection fraction. †P<0.05 change in myoblast versus control group; ‡P<0.05 versus healthy.

respectively and intra-observer variability was  $-0.2 \pm 1.5\%$  and  $0.3 \pm 4.0\%$ , respectively, indicating the high reproducibility of the method.

### Regional wall thickening

Cryoinjury resulted in decreased regional wall thickening of  $-15.3 \pm 8.6\%$  in the control group and  $-11.9 \pm 15.9\%$  in the cell treated group indicating dyskinesia. Four weeks after injection (endpoint), regional wall thickening was further decreased in the control group ( $-18.3 \pm 5.7\%$ ), whereas in the cell treated group a significant increase was seen to  $26.9 \pm 17.0\%$  ( $P=0.029$ ; change in myoblast group vs control, Figure 3). For comparison, mean regional wall thickening in 4 anterolateral segments of slice 3 and 4 of healthy non-infarcted animals was  $82.0 \pm 2.8\%$  (Figure 3A). Further, in the myoblast group an increase was seen in wall thickening in the remote areas of the infarcted slices from  $23.3 \pm 5.6\%$  to  $55.5 \pm 15.6\%$  ( $P=0.002$ ; change in myoblast group vs control, Figure 3B). This increase was not seen in the non infarct levels of either group (Figure 3C).

Figure 4A shows representative long axis cine MRI images through the center of the infarct of 3 control and 3 cell treated rabbits at end-point. Figure 4B shows short axis views of 3 different animals of both groups. A severe impairment in wall thickening is visible in the control animals at the site of the infarct, whereas in the myoblast treated animals regional and remote wall thickening at the infarct level is improved. Figure 4C shows short axis views of a control and myoblast treated animal at baseline and endpoint and illustrates the improved regional wall thickening.

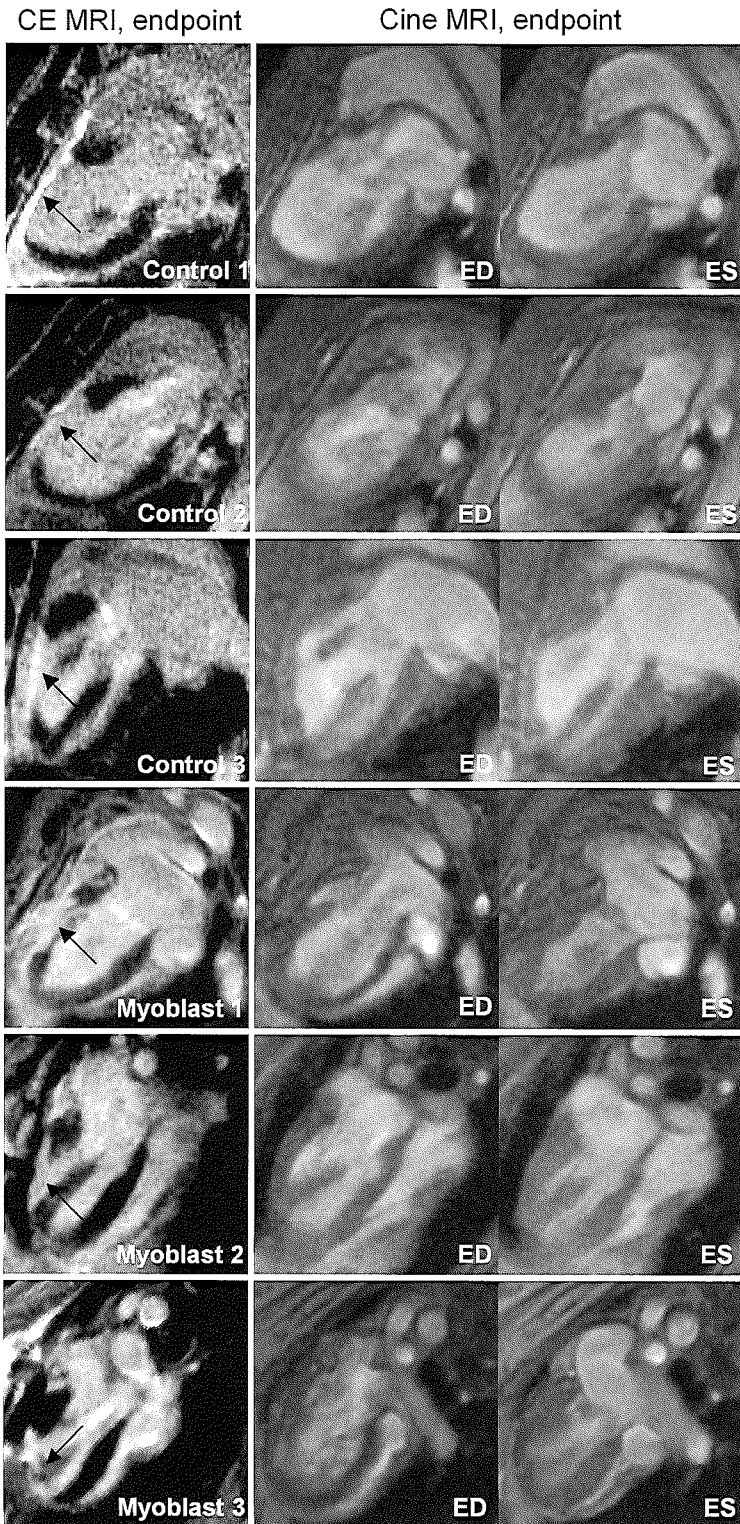


Figure 4A. Representative contrast enhanced and cine MRI long axis views of 3 control and 3 myoblast treated animals at endpoint. Wall thickening is impaired in the infarct regions of the control animals. This is accompanied by increased LV end-diastolic and -systolic volumes. ED indicates end-diastolic; ES, end-systolic. Arrows in first column indicate the hyperenhanced infarct region.

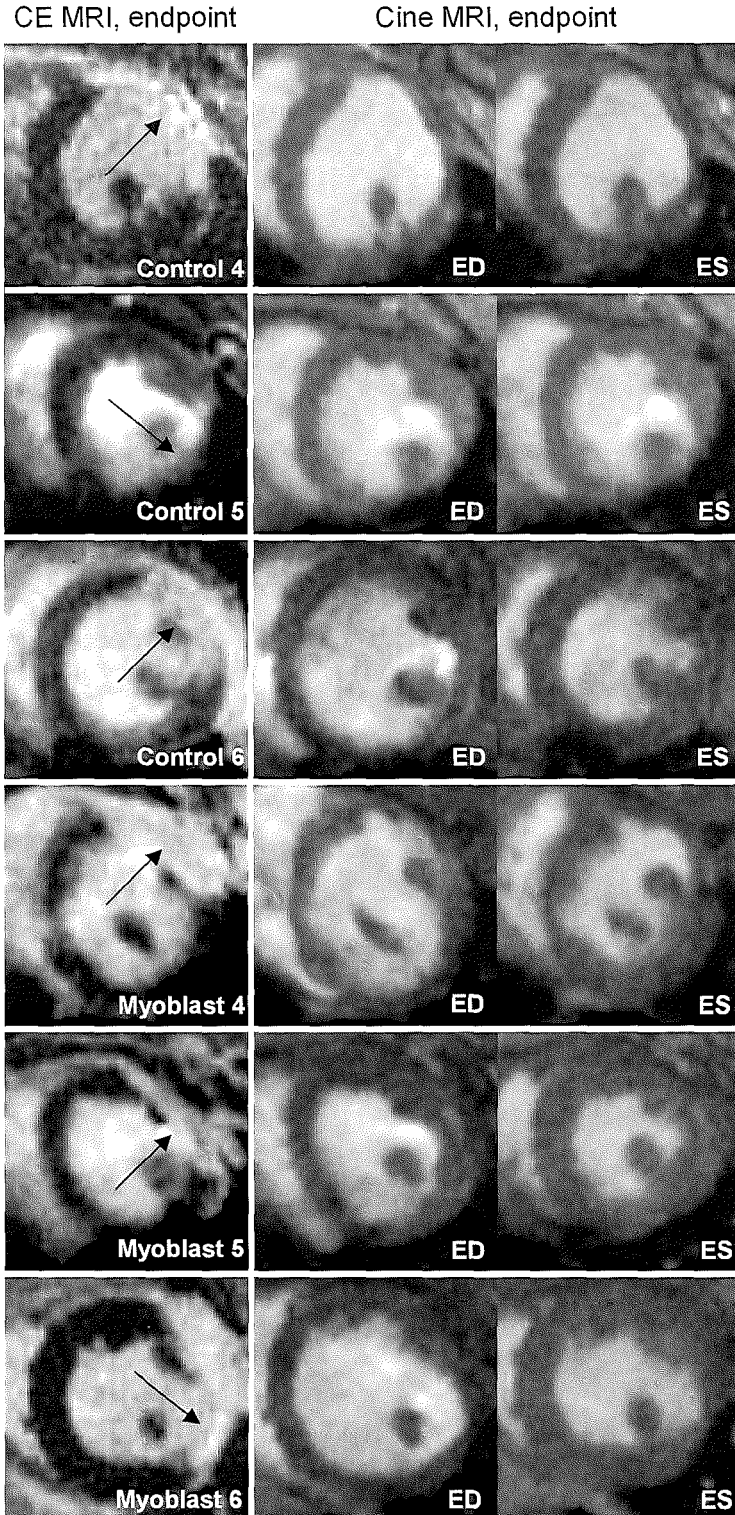


Figure 4B. Representative ce and cine MRI short axis views of 3 different control and 3 myoblast treated animals at endpoint. Wall thickening is impaired in the infarct regions of the control animals. Myoblast transplantation not only improves regional function, but also improves wall thickening in the remote myocardium. ED indicates end-diastolic; ES, end-systolic. Arrows in first column indicate the hyperenhanced infarct region.

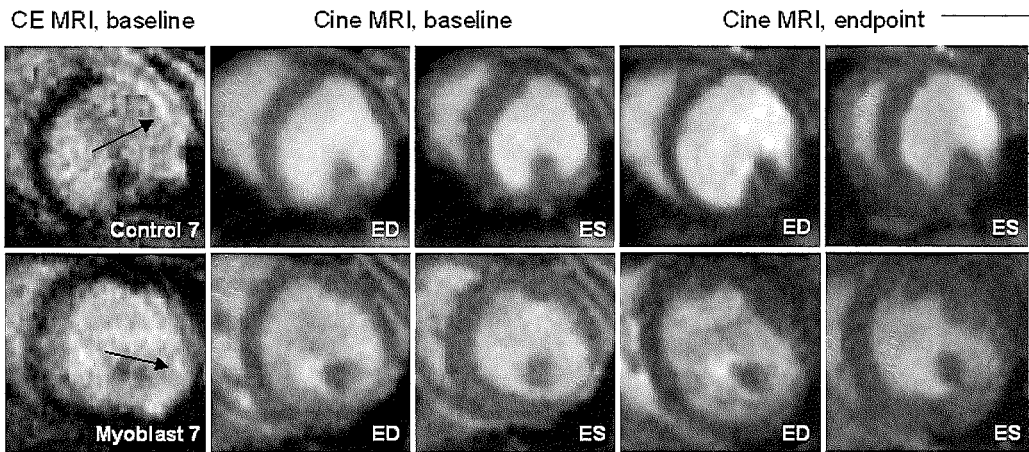


Figure 4C. Representative ce and cine MRI short axis view of a control and myoblast treated animals at baseline and at endpoint. Arrows indicate the hyperenhanced infarct.

### Ejection fraction and geometry

Two dimensional EF at infarct level improved significantly in the myoblast group, from  $34.7 \pm 3.0\%$  at baseline to  $41.3 \pm 2.2\%$  at end-point, whereas in the control group there was a decrease from  $38.8 \pm 2.1\%$  to  $36.2 \pm 1.3\%$  ( $P=0.049$ ; change myoblast group vs. control, Figure 3B). However, global ejection fraction did not change significantly in the control or myoblast treated group. Changes in LV function and geometry in the myoblast and control group are shown in Table 2.

The functional improvement in the myoblast group was further accompanied by prevention of LV remodeling as indicated by smaller LV cavity volumes and LV wall thicknesses and volumes (Table 2). This was also reflected by LV/body weight ratios ( $1.70 \pm 0.06$  in control vs.  $1.40 \pm 0.03$  in the myoblast group;  $P < 0.01$ ). The measured wall volumes correlated well with LV wet weights ( $P < 0.001$ ) indicating the good correlation between MRI and true values.

### Histology

Myoblast transplantation resulted in engraftment of cells in all cell treated animals as determined by fluorescence microscopy of the DAPI-labeled cells. The grafts covered approximately 60% of the scar area. In the grafted areas cells were found with the histological characteristics of skeletal muscle cells and skeletal myotubes, which aligned parallel to the collagen and elastin fibers of the scar. Most myotubes were surrounded by dense collagenous scar tissue (Figure 5A and B). Muscle cells stained positively for slow (Figure 5C and D) and fast (Figure 5E, F and G) MHC in the grafted areas. Staining for troponin I and connexin 43 was negative (data not shown).

**Table 2. Left ventricular geometry and function at baseline and at endpoint**

	Control (n=9)		Myoblasts (n=8)	
	Baseline	Endpoint	Baseline	Endpoint
<b>Infarct slices, end-diastolic values</b>				
Epicardial circumference, mm	65.2±1.3	70.7±1.7*	65.8±1.7	64.3±1.4†
Infarct circumference, mm	17.9±0.8	18.8±1.5	16.5±0.2	16.3±0.1
LV lumen diameter, mm	14.0±0.4	15.6±0.5‡	13.8±0.5	14.2±0.5
LV wall thickness, mm	2.78±0.09	3.09±0.09	3.01±0.63	2.83±0.54†
Infarct thickness, mm	2.3±0.1	2.4±0.2	2.5±0.2	2.5±0.1
2D Ejection fraction, %	38.8±2.1	36.2±1.3	34.7±3.0	41.3±2.2†
<b>Non infarct slices, end-diastolic values</b>				
Epicardial circumference, mm	68.7±1.2	73.1±1.8‡	71.7±0.5	71.7±0.4
Left ventricle diameter, mm	15.4±0.4	16.0±0.5	15.9±0.6	15.9±0.3
Wall thickness, mm	2.83±0.11	3.46±0.20*	3.11±0.69	2.97±0.54
2D Ejection fraction, %	47.6±1.9	45.8±2.1	47.8±1.4	45.0±2.6
<b>Total left ventricle</b>				
Long-axis length, end-diastolic, mm	24.9±0.8	27.3±0.8	25.1±0.4	25.5±0.6
Wall volume, end-diastolic, ml	4.3±0.2	5.4±0.4	4.4±0.2	4.4±0.3†
Left ventricular end-diastolic volume, ml	3.96±0.27	5.00±0.46*	4.10±0.24	4.37±0.27
Left ventricular end-systolic volume, ml	2.23±0.19	2.96±0.30*	2.37±0.16	2.43±0.17
Stroke volume, ml	1.72±0.14	2.05±0.19	1.68±0.13	1.94±0.14
Heart frequency, beats/min	227±4	243±3*	215±5	239±3*
Cardiac output, ml/min	386±28	501±48	357±26	462±29*
Ejection fraction global, %	43.7±1.8	41.1±1.6	42.3±1.7	44.5±1.2

\*P&lt;0.05 vs. corresponding baseline

†P&lt;0.05 change in myoblast group vs. control group

‡P&lt;0.10 vs. corresponding baseline

## Discussion

### Methodological considerations

The pathophysiology of the infarct can differ in a cryoinfarction model. However, the biologic variability associated with the size of the infarct induced by coronary artery occlusion, makes evaluation of therapeutic interventions difficult. Therefore we used cryoinfarction to create infarcts of equal size. The functional and geometrical data obtained at baseline show that the model causes compensated LV remodeling, without much change in stroke volumes or cardiac output (Table 1). Little variability was observed between animals at baseline indicating the high reproducibility of the method.

Further, MRI is potentially an important tool for following engraftment of cells in an infarct. When cells engraft throughout the scar and form islands of viable tissue,

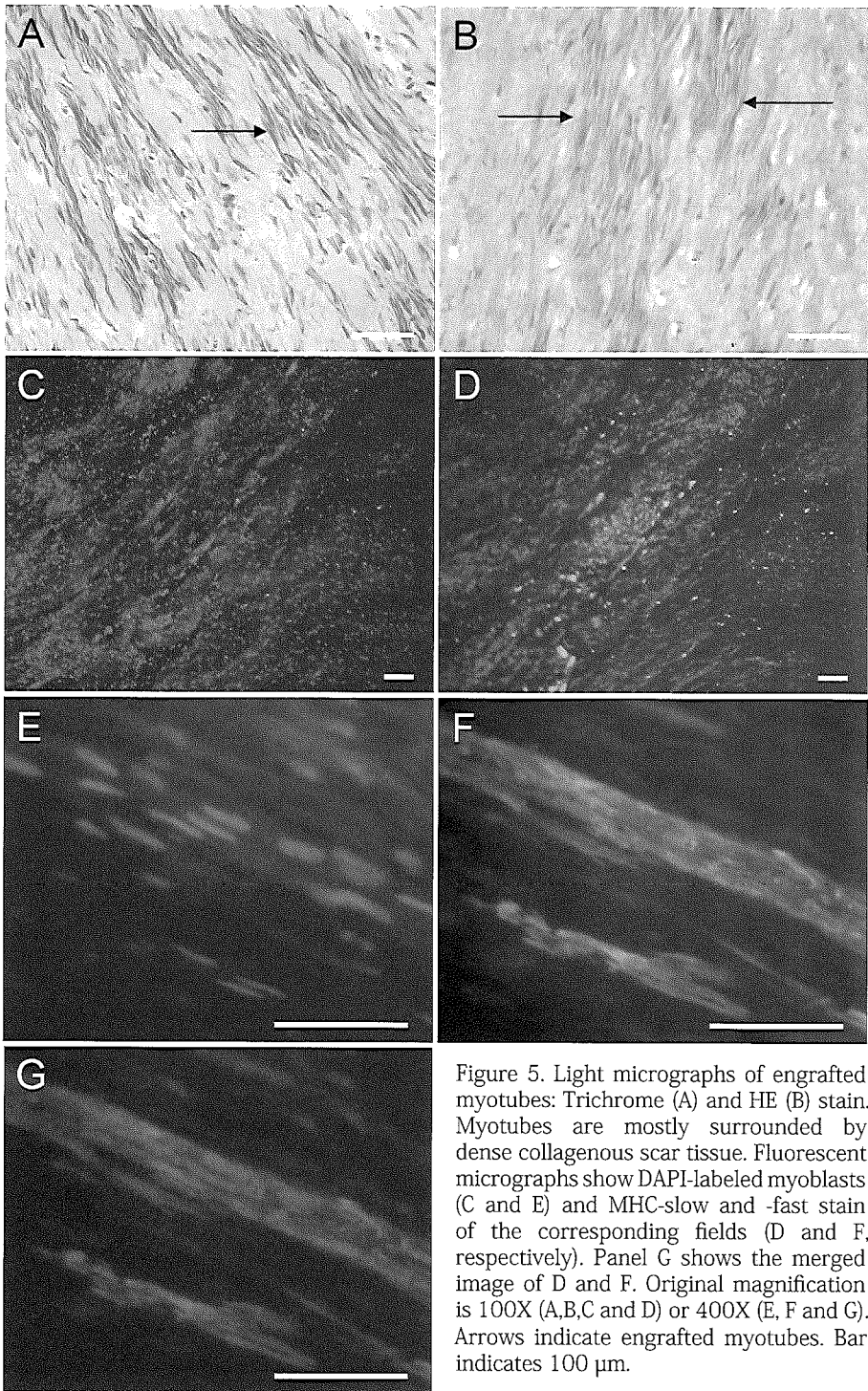


Figure 5. Light micrographs of engrafted myotubes: Trichrome (A) and HE (B) stain. Myotubes are mostly surrounded by dense collagenous scar tissue. Fluorescent micrographs show DAPI-labeled myoblasts (C and E) and MHC-slow and -fast stain of the corresponding fields (D and F, respectively). Panel G shows the merged image of D and F. Original magnification is 100X (A,B,C and D) or 400X (E, F and G). Arrows indicate engrafted myotubes. Bar indicates 100  $\mu$ m.

hyperenhancement could hypothetically become less. However, the in plane resolution in this study was 0.3x0.3 mm with 2 mm slice thickness. Further, the heart rate in this rabbit model was 250 beats/minute, limiting temporal resolution. Higher in plane resolutions and smaller slice thickness to limit spatial volume effects are necessary for adequately assessing this possibility in a follow-up study.

### **Regional and global LV function**

No expression of the gap junction marker connexin 43 was found in the grafted areas in this study, implying that there is no electrical integration of the myoblasts and myotubes with the surrounding myocardium. This is in concordance with previous studies.<sup>17</sup> A mechanism that is likely to be responsible for the activation of myotubes are stretch activated ion channels, that respond to the contraction of the healthy surrounding myocardium and cause excitation contraction coupling.<sup>14</sup>

One could argue that myoblasts improve the function of remaining cardiomyocytes that survive in the necrotic area. However, no viable troponin I expressing cells were found in the cryoinjured area of the control or cell treated rabbits. The possible influence of tethering<sup>15</sup> on regional wall thickening was limited by only looking at those segments with transmural infarction. Nonetheless, wall thickening in the segments with non-transmural infarcts showed a similar improvement (from  $19.1 \pm 15.3\%$  to  $46.3 \pm 17.0\%$  after cell treatment versus  $14.1 \pm 9.7\%$  to  $3.3 \pm 4.5\%$  in the controls;  $P=0.033$ ), suggesting a similar contractile effect of cell treatment in the border zones.

Although the regional functional improvement corresponded with increased 2-D ejection fractions at the infarct level, this caused only a small increase in global ejection fraction in the myoblast group ( $P=0.14$ ; change in myoblast group vs. control). However, baseline global ejection fraction in this cryoinjury model only decreased from  $56.1 \pm 1.2\%$  to  $43.0 \pm 1.2\%$  and stroke volume was maintained at baseline. It has been shown that the beneficial effect of myoblast transplantation is the largest in animals with the lowest initial ejection fractions.<sup>4</sup> Further, it could take longer than 4 weeks to see a significant improvement in global function. Finally, it is possible that the number of animals in this study is too small to detect a significant difference between groups.

### **LV geometry**

The cryoinfarction model resulted in compensated remodeling with marked LV dilation, but without manifest LV hypertrophy after 3 weeks. Stroke work and cardiac output could therefore be maintained. The improvement in regional function after myoblast transplantation prevented further cardiac remodeling, with smaller LV end-diastolic and end-systolic volumes, smaller LV diameters and less hypertrophy at endpoint compared to controls. This is important, since increase in LV volumes after myocardial infarction is one of the most powerful predictors of reduced survival.<sup>16</sup>

### **Arrhythmic events**

There have been recent reports of myoblast transplantation resulting in ventricular arrhythmias in patients,<sup>6</sup> which would limit its clinical usefulness. However, in this study, none of the deaths could be attributed to arrhythmic events. This is consistent with other pre-clinical studies. Further, Holter monitoring in 6 myoblast transplanted animals did not show any arrhythmias. The differences between clinic and pre-clinic could potentially be based upon the number of injections (fewer in pre-clinical studies), injection location (more in center in pre-clinical studies) or age of the infarcts (in pre-clinical studies more recent infarcts).

### **Conclusions**

Myoblast transplantation restores wall thickening and improves regional cardiac function, thereby preventing progression of cardiac remodeling. Magnetic resonance imaging is a valuable tool for assessing the effects of cell transplantation on cardiac function and LV geometry and could thus be a valuable tool to determine the long term outcomes in this model.

## References

1. Reinecke H, Poppa V, Murry CE. Skeletal muscle stem cells do not transdifferentiate into cardiomyocytes after cardiac grafting. *J Mol Cell Cardiol* 2002;34:241-9.
2. Pouzet B, Vilquin JT, Hagege AA, Scorsin M, Messas E, Fiszman M, Schwartz K, Menasche P. Intramyocardial transplantation of autologous myoblasts: can tissue processing be optimized? *Circulation* 2000;102:III210-5.
3. Taylor DA, Atkins BZ, Hungspreugs P, Jones TR, Reedy MC, Hutcheson KA, Glower DD, Kraus WE. Regenerating functional myocardium: improved performance after skeletal myoblast transplantation. *Nat Med* 1998;4:929-33.
4. Pouzet B, Vilquin JT, Hagege AA, Scorsin M, Messas E, Fiszman M, Schwartz K, Menasche P. Factors affecting functional outcome after autologous skeletal myoblast transplantation. *Ann Thorac Surg* 2001;71:844-50.
5. Ghostine S, Carrion C, Souza LC, Richard P, Bruneval P, Vilquin JT, Pouzet B, Schwartz K, Menasche P, Hagege AA. Long-term efficacy of myoblast transplantation on regional structure and function after myocardial infarction. *Circulation* 2002;106: I131-6.
6. Menasche P, Hagege AA, Vilquin JT, Desnos M, Abergel E, Pouzet B, Bel A, Sarateanu S, Scorsin M, Schwartz K, Bruneval P, Benbunan M, Marolleau JP, Duboc D. Autologous skeletal myoblast transplantation for severe postinfarction left ventricular dysfunction. *J Am Coll Cardiol* 2003;41:1078-83.
7. Reinecke H, MacDonald GH, Hauschka SD, Murry CE. Electromechanical coupling between skeletal and cardiac muscle. Implications for infarct repair. *J Cell Biol* 2000;149:731-40.
8. Reinecke H, Poppa V, Murry CE. Skeletal muscle stem cells do not transdifferentiate into cardiomyocytes after cardiac grafting. *J Mol Cell Cardiol* 2002;34:241-9.
9. Rajnoch C, Chachques JC, Berrebi A, Bruneval P, Benoit MO, Carpentier A. Cellular therapy reverses myocardial dysfunction. *J Thorac Cardiovasc Surg* 2001;121:871-8.
10. Choi KM, Kim RJ, Gubernikoff G, Vargas JD, Parker M, Judd RM. Transmural extent of acute myocardial infarction predicts long-term improvement in contractile function. *Circulation* 2001;104:1101-7.
11. Wagner A, Mahrholdt H, Holly T, Elliott MD, Regenfus M, Parker M, Klocke FJ, Bonow RO, Kim RJ, Judd RM. Contrast MRI detects subendocardial myocardial infarcts which are missed by routine nuclear imaging. *Lancet* 2003, 361:374-379.
12. Watzinger N, Lund GK, Higgins CB, Wendland MF, Weinmann HJ, Saeed M. The potential of contrast-enhanced magnetic resonance imaging for predicting left ventricular remodeling. *J Magn Reson Imaging* 2002;16:633-40.
13. van Ruge FP, van der Wall EE, Spanjersberg SJ, de Roos A, Matheijssen NA, Zwinderman AH, van Dijkman PR, Reiber JH, Brusckhe AV. Magnetic resonance

- imaging during dobutamine stress for detection and localization of coronary artery disease. Quantitative wall motion analysis using a modification of the centerline method. *Circulation* 1994;90:127-38.
14. Guharay F, Sachs F. Stretch-activated single ion channel currents in tissue-cultured embryonic chick skeletal muscle. *J Physiol* 1984;352:685-701.
  15. Kerber RE, Marcus ML, Ehrhardt J, Wilson R, Abboud FM. Correlation between echocardiographically demonstrated segmental dyskinesis and regional myocardial perfusion. *Circulation* 1975;52:1097-1104.
  16. Pfeffer MA, Pfeffer JM. Ventricular enlargement and reduced survival after myocardial infarction. *Circulation* 1987;75:IV93-7.



# Chapter 6

## A comparison of intracardiac cell transplantation: autologous skeletal myoblasts versus bone marrow cells



## Abstract

**Background-** Multiple cell types are being proposed for cardiac repair but side by side comparisons are lacking. We tested the hypothesis that intracardiac transplantation of autologous bone marrow or skeletal muscle-derived progenitor cells improve regional heart function to a similar degree.

**Methods and results-** Thirty-nine New Zealand White rabbits underwent cryoinjury of the left ventricle and simultaneous hindlimb bone marrow aspiration or soleus muscle biopsy. Both muscle and bone marrow cells were expanded *in vitro*. After two weeks,  $10^8$  skeletal muscle (SM group) or bone marrow-derived mesenchymal stem cells (BM group) were injected into the cryoinjured region (SM: n=12; BM: n=8). Media alone was injected into the remaining animals (Control: n=16). Regional systolic function was measured using micromanometry and sonomicrometry at baseline before and 4 weeks after cell injection. Cell treatment resulted in a similar degree of improvement in a derivative of stroke work in the SM and BM groups (P=0.0026 and P=0.0085 vs. Control, respectively). No significant difference was seen between BM and SM groups (P=0.94). On histology, engraftment of cells was found in all cell treated animals. Injected myoblasts formed myotubes throughout the scar that expressed slow and fast myosin heavy chain. Bone marrow cells differentiated towards a myogenic phenotype, as indicated by expression of desmin and  $\alpha$ -sarcomeric actin in the engrafted areas.

**Conclusion-** In conclusion, transplantation of bone marrow-derived mesenchymal stem cells increases regional systolic heart function after myocardial infarction to a similar degree as skeletal myoblasts.

## Introduction

Cellular therapy for heart failure has risen to the forefront of cardiac research. Several pre-clinical and clinical studies indicate that both skeletal muscle and bone marrow-derived progenitor cells can successfully repopulate injured myocardium and improve heart function.<sup>1-5</sup> Increasing clinical use has created interest in evaluating the particular capability of each cell type to repair the injured heart.

Two of the most widely used cell types for cardiac repair today are skeletal muscle-derived progenitors, or myoblasts, and bone marrow-derived progenitors. Both cell types share advantages over other cells proposed for cardiac repair in that they are readily available, autologous, and easily expanded *in vitro*.

Myoblasts engraft,<sup>6</sup> differentiate towards a phenotype adapted to cardiac workload<sup>7</sup> and improve heart function.<sup>1,8</sup> Bone marrow progenitor cells are reported to have the capacity to differentiate into cardiomyocytes both *in vitro*<sup>9</sup> and *in vivo*<sup>5</sup> and improve global heart function pre-clinically.<sup>4,10</sup> However, to date, no study has been performed to directly compare these two cell types with respect to their improvement of cardiac function.

In this study, we transplanted equal numbers of myoblasts or bone marrow-derived mesenchymal stem cells (MSCs) into the center of cryoinjured rabbit hearts in three parallel tracts and compared the improvement in regional systolic function using micromanometry and sonomicrometry.

## Materials and methods

All experiments were conducted in accordance with guidelines published in the Guide for the Care and Use of Laboratory Animals (NIH publication no. 86-23, revised 1985) and under the protocols approved by the Institutional Animal Care and Use Committee at Duke University.

### Surgical preparation

New Zealand White rabbits (n=39), weighing 3.5 to 4.5 kg, were premedicated with intramuscular ketamine (50 mg/kg) and xylazine (5 mg/kg). Endotracheal intubation was performed, and the animals were mechanically ventilated. Anesthesia was maintained with 2% isoflurane.

A soleus muscle biopsy or femoral bone marrow aspirate was then performed from the left hindlimb. A left thoracotomy through the fourth intercostal space was performed, as previously described<sup>11</sup> and the heart was exposed. A cryoprobe (diameter 1.4 cm) cooled to -70°C (Frigitronics-Cooper Surgical, Trumbull, CT) was applied to the epicardial surface of the anterolateral left ventricular (LV) wall for 3 minutes to create a transmural cryoinjury of approximately 1.5 cm in diameter. The chest was closed in layers. Fourteen days after cryoinjury, the animals underwent a second thoracotomy for initial data acquisition using sonomicrometry and micromanometry and injection of either skeletal myoblasts (SM; n=12),

bone marrow cells (BM; n=8) or media (Control; n=16) in the infarct area.

Four weeks after cell injection, a third thoracotomy was performed, and sonomicrometry and micromanometry measurements were repeated. After recording final data, animals were euthanized and hearts were excised for histologic analysis.

A separate subset of animals (n=3) had identical surgical procedures, but were transplanted with lysed DAPI-labeled myoblasts and bone marrow cells. These animals were sacrificed 7 days after cell injection.

### **Expansion of myoblasts**

Tissue from a 500-700 mg soleus biopsy was mechanically dissected and washed once in phosphate buffered saline (PBS). The tissue was then plated in myoblast growth medium, consisting of Dulbecco's Modified Eagle's Medium (DMEM) with 20% horse serum (HS) and 0.5% gentamicin (10 mg/ml). The tissue fragments were triturated after 3 days. After another 3 days, the tissue was removed, and the myoblasts were fed with myoblast growth medium. Cells were fed every other day and were passaged when reaching ~70% confluency, resulting in 2-3 passages before injection. The day before injection, cells were labeled overnight with the nuclear stain 4',6-diamidino-2-phenylindole (DAPI, 10 µg/ml; Sigma, St. Louis, MO). For injection, cells were washed with PBS to remove all DAPI, trypsinized, washed twice more, counted, and resuspended at  $10^8$  cells per ml of DMEM.

### **Expansion of bone marrow cells**

Bone marrow aspirates were plated in bone marrow growth medium, consisting of DMEM/F12 supplemented with 10% fetal bovine serum (FBS), and 0.5% gentamicin. After 3 days in culture, the flasks were washed twice with PBS to remove floating cells and adherent cells were fed every third day. Bone marrow cultures were maintained at less than 50% confluence and passaged 3 to 5 times before injection. The day before injection, cells were labeled with DAPI. For injection, bone marrow cells were washed with PBS to remove excess DAPI, trypsinized, washed twice more, counted and resuspended at  $10^8$  cells/ml in 1.0 ml of DMEM.

### **Characterization of the injected cell population**

For fluorescence activated cell sorting (FACS) analysis of bone marrow-derived progenitors, cells were trypsinized and blocked for 15 minutes with blocking buffer, consisting of Hank's Balanced Salt Solution supplemented with 3% FBS, 2mM EDTA, and 10mM HEPES buffer. Cells were stained with a rabbit specific polyclonal FITC-labeled CD45 antibody (Serotec, Raleigh, NC) for 30 minutes, washed twice, and resuspended in blocking buffer for analysis using a FACS Vantage SE flow cytometer (BD Biosciences, San Jose, CA).

A portion of the injected cell populations was plated on glass coverslips, grown overnight and fixed in 5% paraformaldehyde for 10 minutes. Cells were permeabilized in 0.2% NP-40 and 0.2% Tween in PBS for 10 minutes. Blocking was performed for 1 hour in

PBS with 5% HS and 5% FBS. Cells were then incubated in primary monoclonal anti-desmin antibody (1:200) for 90 minutes followed by a Phycoerythrin (PE) conjugated anti-mouse secondary antibody (1:200) in blocking buffer. Staining was analyzed on a Nikon TE 200 Eclipse inverted microscope and the number of desmin positive cells was counted and expressed as a percentage of the total cell number.

### Physiologic data acquisition

Micromanometry and sonomicrometry were performed 14 days after cryoinfarction (baseline) and 4 weeks after cell injection as follows. A pair of ultrasonic dimension transducers (Sonometrics Corp, London, Ontario, Canada) were sutured to the epicardial surface, within 2 mm of the border of the cryoinjured region in the plane of the LV minor axis. A 3.0F micromanometer (Millar Instruments, Houston, TX) was inserted into the LV cavity via the left atrium. Data were then collected using a sonomicrometry acquisition system (Sonometrics Corp, London, Ontario, Canada). Hemodynamical data that were collected, both at baseline and after 4 weeks, included heart rate, LV end-diastolic pressures and  $dP/dt_{max}$ .

### Data analysis

Physiologic data were analyzed using Cardiosoft software (Sonometrics Corp, London, Ontario, Canada). The cardiac cycle was defined using the first derivative of LV pressure ( $dP/dt$ ) as detailed previously.<sup>12</sup>

A regional systolic performance index ( $SW_A$ ) analogous to Stroke Work was defined as the area within a plot of pressure versus dimension and calculated as the integral of ventricular pressure ( $P$ ) with respect to the epicardial segment length ( $L$ ):

$$SW_A = \int PdL$$

LV end-diastolic and peak pressure were obtained from the LV pressure waveform. Maximal  $dP/dt$  was obtained from the first derivative of the LV pressure waveform. Systolic shortening (SS) was defined as the difference in epicardial segment length between end-diastole ( $L_{ED}$ ) and end-systole ( $L_{ES}$ ) and was expressed as a percentage of the end-diastolic segment length:

$$SS = (L_{ED} - L_{ES}) \times 100 / L_{ED}$$

All cardiac cycles in a 10 second data acquisition period were analyzed and the beat-to-beat indices were averaged over that period.

### Histologic analysis

Hearts were cut into 5 transverse slices, embedded in OCT freezing medium and frozen in liquid nitrogen-cooled isopentane. Twelve serial 6  $\mu$ m thick sections were cut from each

slice on a cryostat. Sections were air dried overnight, fixed in 5% paraformaldehyde and permeabilized in 1% Tween. Sections were stained with primary rabbit specific monoclonal antibodies to desmin, slow and fast myosin heavy chain (MHC), connexin-43 and  $\alpha$ -sarcomeric actin (all from Sigma, St. Louis, MO) and a monoclonal antibody against troponin I (Chemicon, Temecula, CA), all diluted 1:200 in blocking buffer, for 90 minutes. Secondary antibody staining was performed with a PE conjugated anti-mouse antibody (Molecular Probes, Leiden, the Netherlands) for 1 hour. Section 11 and 12 from series were stained with hematoxylin-eosin (H&E) and Goldner's Trichrome respectively. Sections were examined under standard light and fluorescence microscopy after background subtraction. Engraftment of DAPI-labeled cells was quantified by drawing the engrafted areas and calculating the areas as a percentage of total infarct area, using Image Pro analysis software.

### Statistical analysis

All data are reported as mean  $\pm$  SEM. A difference in response over time was tested using two-way ANOVA with repeated measures. If the overall F test for a group by time interaction was statistically significant, pair-wise Student's t tests were used to determine statistical significance of pair-wise differences. Differences in proportions were tested for statistical significance using Fischer's Exact Test. Results were considered statistically significant at  $P < 0.05$ .

## Results

### Cell culture

Cultures yielded greater than  $10^8$  myoblasts or bone marrow cells for each animal after 2 weeks. All myoblast cultures were greater than 90% desmin positive ( $92.3 \pm 3.2\%$ ), indicating the high purity of the injected population (Figure 1A and B). All myoblast cultures formed myotubes *in vitro*. Bone marrow progenitor cells showed greater than 80% CD45 negative cells as analyzed by FACS. Bone marrow cultures showed desmin positivity of 1.1% ( $\pm 0.4\%$ ; Figure 1C and D).

### Regional systolic performance

A stroke work analog, using pressure/segment length measurements, was obtained for each animal at baseline (before injection) and 4 weeks after injection (Table 1). Regional stroke work increased after treatment in 8 of 8 (100%) bone marrow cell treated animals. Myoblast treated animals showed improvement in 9 of 12 animals (75%), whereas control animals showed improvement in 4 of 16 animals (25%) ( $P < 0.01$  vs. control for SM and BM).

Quantitative analysis of the mean change in stroke work over time showed a significant improvement in the cell treated groups compared to baseline (Figure 2A). Change in SW was  $9.3 \pm 3.3$  mm\*mmHg in the Myoblast group,  $7.4 \pm 1.6$  mm\*mmHg in the Bone Marrow group, and  $-0.9 \pm 1.3$  mm\*mmHg in the Control group ( $P = 0.0026$  and  $P = 0.0085$ , SM and BM).

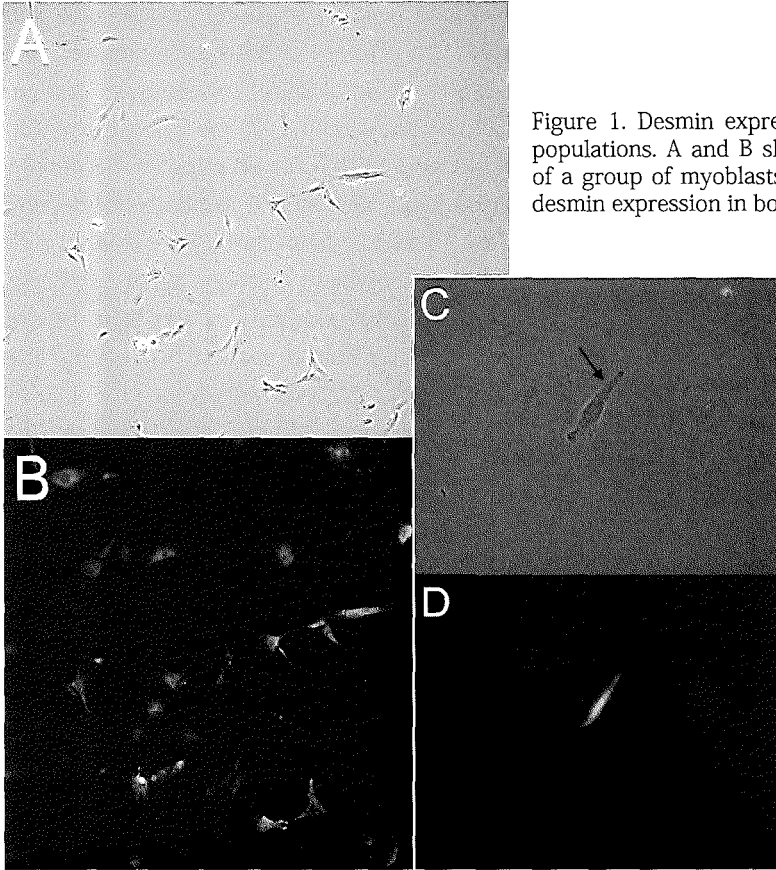


Figure 1. Desmin expression in the injected cell populations. A and B show corresponding fields of a group of myoblasts, whereas C and D show desmin expression in bone marrow-derived cells.

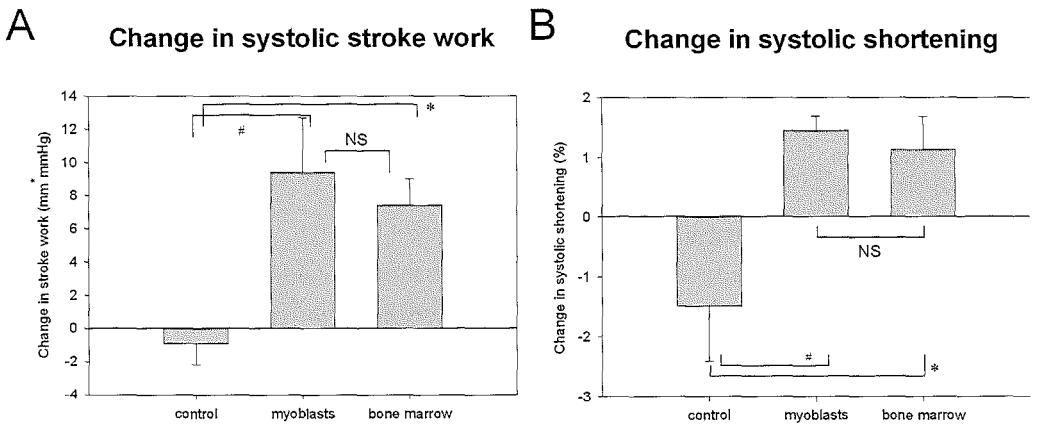


Figure 2. Changes in systolic stroke work from baseline to 4 weeks after cell transplantation (A) and change in percentage systolic shortening (B) for control (n=16), myoblasts (n=12) and bone marrow (n=8) groups (#P=0.0026 and \*P=0.0085 vs. Control in A; #P=0.006 and \*P=0.01 vs. Control in B).

vs. Control, respectively). Change in systolic shortening showed a similar treatment effect of both cell types (SM  $1.44 \pm 0.34\%$ , BM  $1.13 \pm 1.14\%$ , Control  $-1.48 \pm 0.63\%$ ;  $P=0.006$  and  $P=0.01$  for SM and BM group vs. Control respectively; Figure 2B). There were no significant differences between the SM and BM group ( $P=0.9$  and  $0.4$  for change in stroke work and systolic shortening, respectively). After accounting for heart rate variability, by reanalyzing the data using heart rate as an independent covariate, the statistical outcomes were not affected.

## Hemodynamics

There were no differences in LV end-diastolic pressure or  $dP/dt_{\max}$  between groups at baseline or 4 weeks after injection, nor was there a statistical difference in the change of those measures between groups over time (Table 1). The findings were not affected when reexamined with heart rate as an independent covariate.

**Table 1. Left ventricular function pre- and post-injection**

	Pre-injection			Post-injection		
	Control (n=16)	Bone marrow (n=8)	Myoblasts (n=12)	Control (n=16)	Bone marrow (n=8)	Myoblasts (n=12)
LV end-diastolic pressure (mmHg)	$8.06 \pm 1.39$	$8.79 \pm 2.33$	$6.43 \pm 0.73$	$6.69 \pm 0.66$	$3.54 \pm 1.30$	$6.45 \pm 1.55$
Stroke work	$-1.3 \pm 1.3$	$-2.3 \pm 1.4$	$-4.0 \pm 1.2$	$-2.1 \pm 1.1$	$5.1 \pm 2.7^*$	$5.3 \pm 2.3^*$
Systolic shortening (%)	$-0.43 \pm 0.41$	$-1.27 \pm 0.71$	$-0.86 \pm 0.20$	$-1.92 \pm 0.70$	$-0.15 \pm 1.14^*$	$0.59 \pm 0.35^*$
$dP/dt_{\max}$ (mmHg/s)	$1997 \pm 135$	$2144 \pm 277$	$1873 \pm 131$	$1641 \pm 213$	$1943 \pm 260$	$1482 \pm 121$

\* $P < 0.05$ , change between pre- and post- vs. control.

## Histology

Sections from the left ventricle of each study animal were examined to ensure that a transmural cryoinjury had occurred. Sections through the center of the scar from each cell treated animal were examined using standard light microscopy and fluorescent microscopy to identify engrafted DAPI-labeled cells. No DAPI positive cells were found in the animals injected with lysed cells. Transplanted cells from both treatment groups engrafted in all portions of the scar, typically covering approximately ~70% of the infarct area (Figure 3). Injected myoblasts remained relatively close to the initial injection sites, and were typically surrounded by dense collagen rich scar tissue. A portion of these areas showed areas of

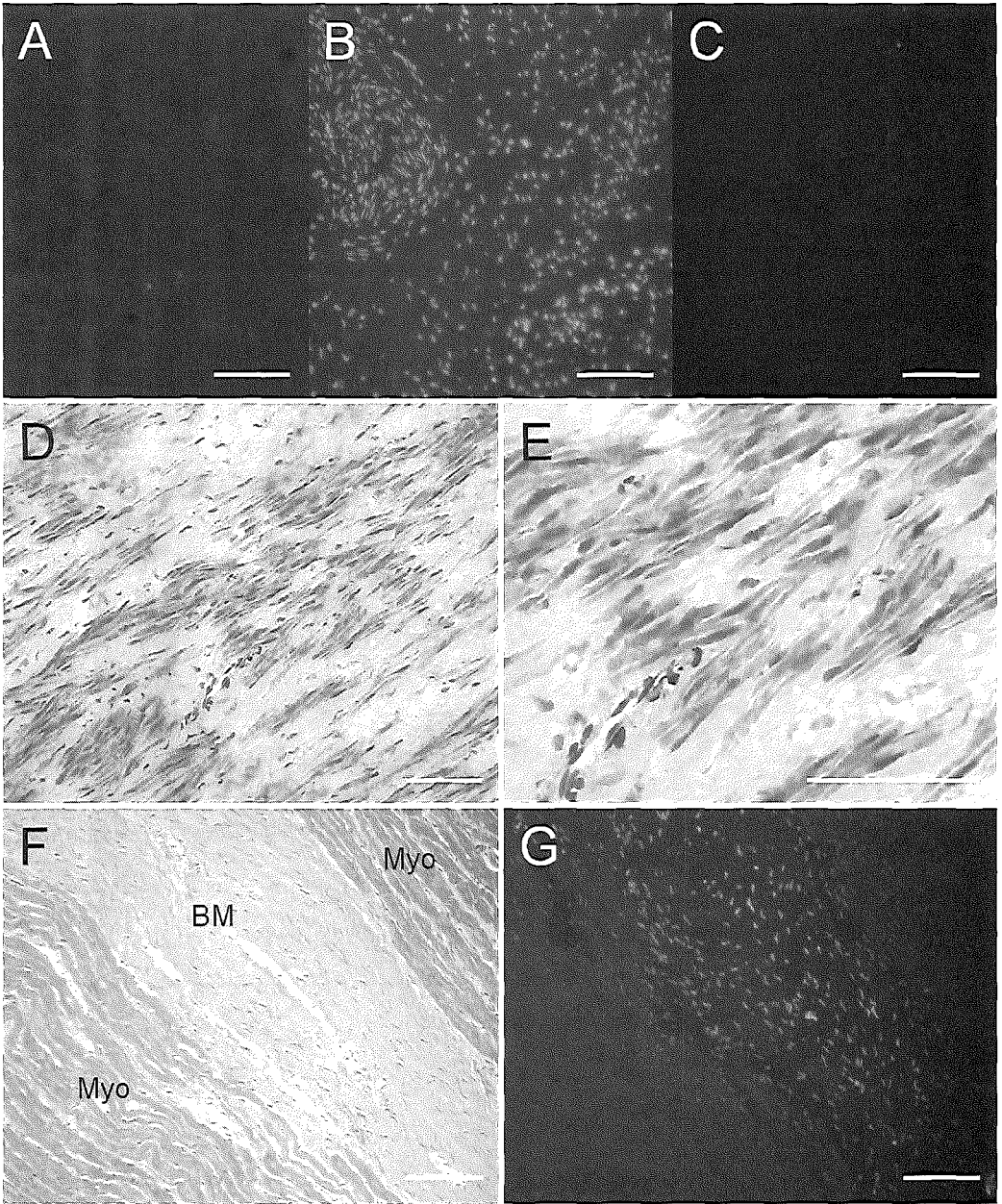


Figure 3. Fluorescence micrograph of a control heart (Panel A), a bone marrow engrafted heart (Panel B) and a heart injected with lysed, labeled cells (Panel C; 200X, original magnification). The DAPI nuclear stain is easily identified in Panel B. Panel D (200X) and E (400X) show a Trichrome stain of myoblast engrafted hearts. There is myotube formation with peripheral nuclei surrounded by dense collagen rich fibrous tissue in the center of the scar. Normal light and corresponding fluorescence micrographs (F and G) of engrafted bone marrow cells (BM) show close contact of cells with the healthy myocardium (Myo). Panel F is hematoxylin-eosin staining and G is DAPI filtered. Bar represents 100  $\mu$ m.

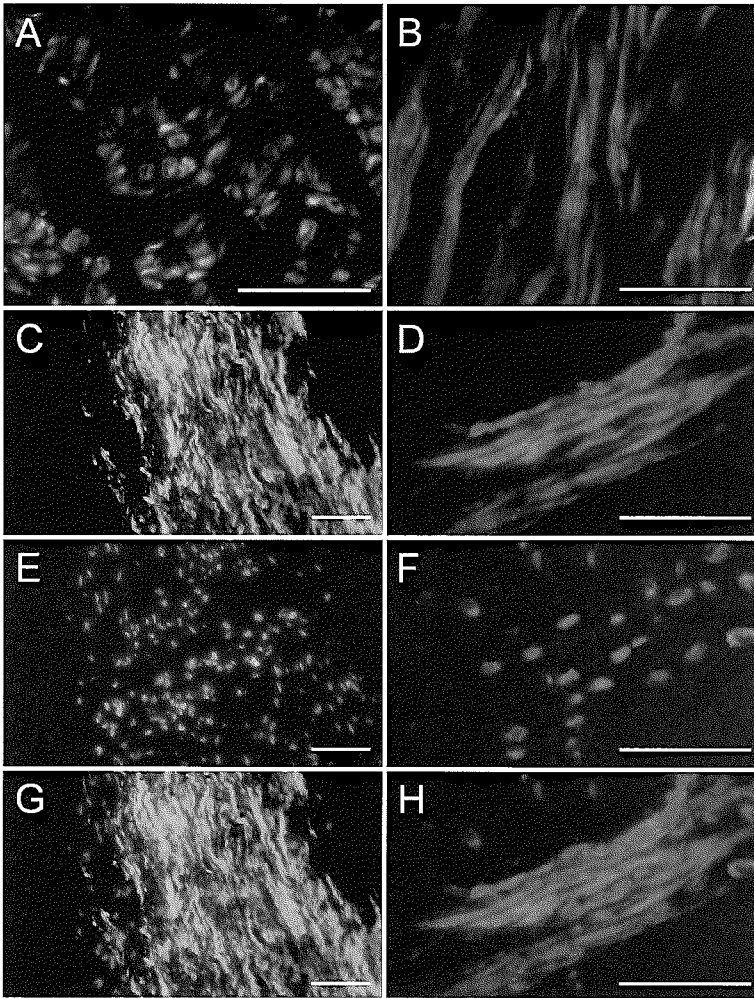


Figure 4. Fluorescence micrographs of sections of scar engrafted with myoblasts. Desmin staining shows that injected myoblasts form patches of unfused single cells (A) or patches of myotubes (B) throughout the scar area (400X). Engrafted myoblasts (identified by their DAPI nuclear staining) further show positive immunostaining for the slow (C and E; G is a merged image; 200X) and fast isoform of myosin heavy chain (D and F; H is a merged image; 400X). Bar represents 100  $\mu$ m.

mature myotube formation (Figure 3D and 3E). Bone marrow cells, however, were more dispersed throughout the infarct, with some groups of cells in the periphery of the infarct and in close contact with healthy myocardium. All bone marrow-derived progenitors appeared as smaller elongated cells with central nuclei, showing no evidence of myotube formation.

Injected myoblasts showed positive staining for desmin,  $\alpha$ -sarcomeric actin, and the slow and fast isoform of MHC (Figure 4), though the slow isoform of MHC was more abundant than the fast isoform. Bone marrow-derived progenitors also showed patches of positive staining for desmin and  $\alpha$ -sarcomeric actin throughout the infarct. In some hearts there was also positive staining for the slow isoform of MHC.

None of the animals examined showed positive staining for connexin-43 or cardiac troponin I in the grafted areas. Further, control animals did not show any desmin expression in the scar area, indicating that there was no cardiomyocyte survival 6 weeks after the

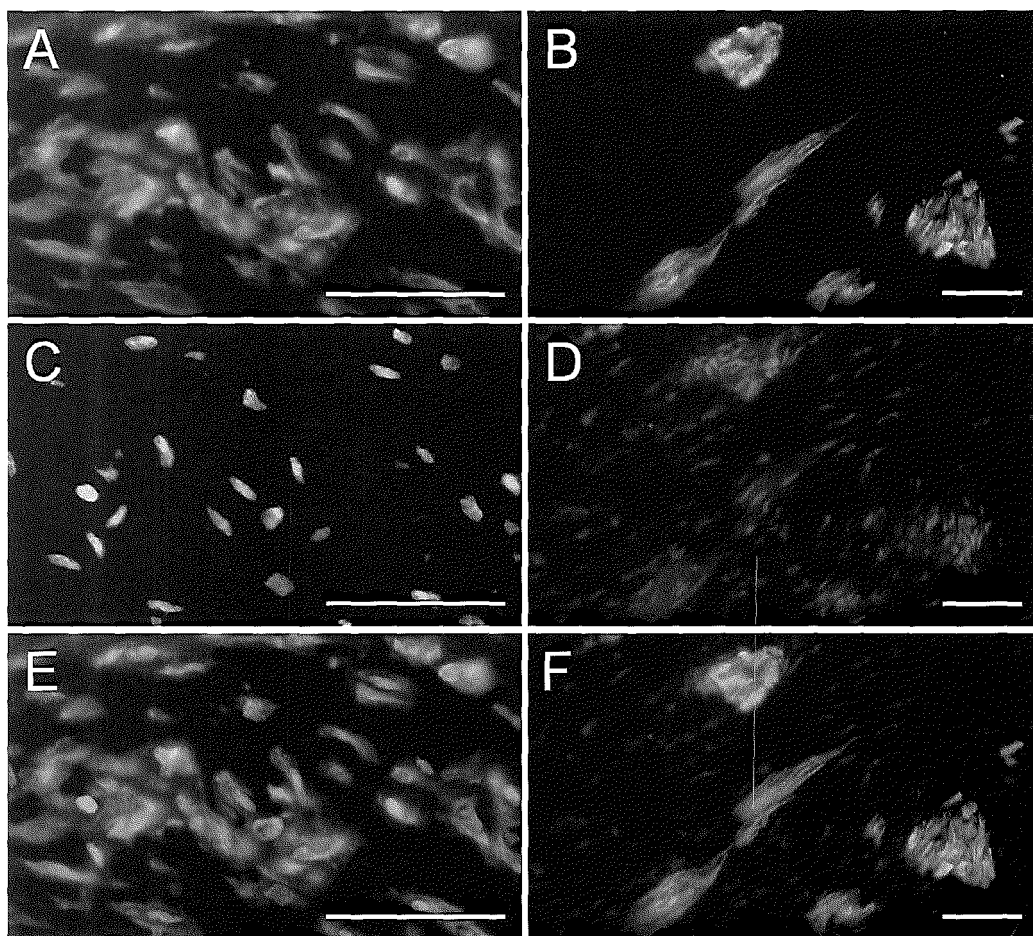


Figure 5. Sections of scar engrafted with bone marrow-derived cells showing patches of positive staining for sarcomeric actin (A and C) throughout the scar area (400X). Panel E presents a merged image showing the colocalization of the DAPI nuclear staining. Panels B and D shows desmin staining, where F is the merged image (200X). Bar represents 100  $\mu\text{m}$ .

cryoinjury, which could confound the results.

## Discussion

The data from this study demonstrate that bone marrow-derived cells and skeletal myoblasts improve regional systolic heart function to a similar degree. This is supported by the histological data that showed engraftment of cells throughout the infarct in all cell treated animals and *in vivo* differentiation of both cell types into cells that express contractile proteins.

## Study limitations

It is not clear to what extent the data of this study relate to the clinical setting in human

intracardiac cell transplantation. The main difference between this study and the clinical setting is the cryoinfarction model. This model was chosen because of the biologic variability that is associated with an ischemia/reperfusion model, which makes functional assessment very difficult.

A second question that is not answered by this study is to what extent both cell types affect cardiac remodeling and global contractile function. It has been shown that both bone marrow-derived cells and myoblasts can prevent left ventricular dilation and hypertrophy.<sup>10,13</sup> For assessing remodeling and global contractility, echocardiography or MRI should be employed.

Finally, our study was designed to find a difference in stroke work derivative of 3 mm\*mmHg over time between the cell treated groups, if in fact this difference did exist. Therefore, smaller differences between groups may have gone undetectable with the number of animals in the current study.

### Cell types for cardiac repair

Transplantation of various types of cells has been shown to augment systolic and diastolic function<sup>14</sup> in different animal models and species. The question of how different cells compare regarding their effects on function has thus far not extensively been addressed. Our lab has previously examined skeletal myoblasts in comparison with dermal fibroblasts, showing that while both cell types improved compliance, only myoblasts improved systolic function.<sup>15</sup> A study comparing myoblasts and fetal cardiomyocytes in a rat model showed that both cell types improve heart function to the same extent.<sup>16</sup> A recent study compared cardiomyocytes and bone marrow-derived cells.<sup>17</sup> Although these studies indicate that implanting contractile cells improves function, not every cell type is suitable for clinical use. Fetal or neonatal cardiomyocytes are difficult to obtain, not autologous and bring ethical dilemmas. Our study examines the only two cell types that have gained widespread clinical use.

In our study, we have shown that both autologous skeletal myoblasts and a population of autologous bone marrow-derived progenitor cells improve regional systolic function to a similar degree.

### Injected cell populations

We used desmin staining to assess the number of myogenic cells in our cultures before injection. Desmin is a cytoskeletal protein found in all contractile cells, including skeletal muscle cells, cardiomyocytes and smooth muscle cells. Desmin staining indicated a high percentage of myoblasts in our skeletal muscle cultures and a virtual absence of myogenic cells in the bone marrow population.

Although desmin staining indicates that our cultures of muscle-derived cells contain a large percentage of myoblasts - cells presumably committed to a skeletal muscle phenotype - multiple studies have found stem like cells with multi-lineage potential in muscle-derived cell cultures.<sup>18,19</sup> These cells are called muscle-derived stem cells or MDSCs. The potential

of these cells when transplanted into the heart is not clear yet. It is possible that these cells are present in our cultures as well, which makes it possible that part of the myogenic differentiation seen is from these stem-like cells. More extensive characterization of our myoblast cultures is needed to address this issue.

Our bone marrow cells were characterized by flow cytometry, which showed a high percentage (more than 80%) CD45 negative cells. This indicates that the cultured cells were primarily of mesenchymal origin. It has been shown before that progenitor cells with multi-lineage capacity co-purify with the mesenchymal stem cell fraction.<sup>20</sup> After injection and engraftment, these cells clearly underwent milieu-dependent differentiation towards a myogenic phenotype. However, the ability of bone marrow-derived cells to repopulate infarcts may not be limited to cells of a myogenic lineage, some investigators have shown that bone marrow mesenchymal stem cells take part in neovascularization and vessel regeneration.<sup>21</sup>

Previously, bone marrow-derived stromal or mesenchymal cells have also been shown to be able to differentiate into cardiomyocytes both *in vivo* and *in vitro* when specific inducers were used, such as 5-azacytidine<sup>9</sup> or when specific subpopulations were selected.<sup>22</sup> Although in this study the engrafted cells started expressing contractile proteins, no differentiation towards a cardiomyocyte phenotype was observed.

## Global indices of cardiac function

In this study we found an improvement in regional contractile function after cell treatment. However, no improvement in global function was observed as indicated by dP/dt, which did not change significantly after cell treatment. One possible explanation for this would be that the infarct area is too small to directly translate regional improvement into global functional improvement. It has been shown before that global parameters such as EF only improve in animals when baseline values are markedly decreased.<sup>8</sup> Further, both dP/dt and ejection fraction can be sensitive to baseline drift and preload and afterload differences; and, therefore, they are not the most representative parameters of global heart function.

## Histological findings

### *DAPI nuclear marker*

We used DAPI as a nuclear marker to identify the engrafted cells and performed colocalization with immunohistochemistry. The possibility that the dye had leaked to neighboring cells or had been released upon cell death was excluded, since no uptake of dye was seen 7 days after lysed DAPI-labeled cells were injected (Figure 3C)

### *Electromechanical integration*

In both cell treated groups, no expression of the gap junction marker connexin 43 was found in the engrafted areas, which indicates that the engrafted cells lack electromechanical integration with the host myocardium. This was further confirmed by our observation that

most cells are surrounded by scar tissue. But, this does not preclude contractility, since other mechanisms can be involved. Myotubes may be activated by stretch receptors that respond to the contractility of the surrounding myocardium. This proposed potential mechanism is not novel and has been discussed in the literature previously. Some recent data showing that the myotubes maintain electrical activity that is more similar to skeletal muscle than to the myocardium seems consistent with stretch receptor activation.<sup>23</sup> The same mechanism may play a role in electromechanical activation of the bone marrow cells although further study is needed to confirm this hypothesis.

### **Future studies**

More studies are needed to examine how different cell types compare when used to repopulate a chronic myocardial injury, as we have examined a relatively acute infarct that may still be undergoing some remodeling. Further, when faced with the task of trying to fully repopulate an infarct, one must consider using multiple cell types together to regenerate a myocardium with vasculature and electrical conduction, as well as functioning muscle. Some laboratories have already started pre-clinical testing of combination cell therapy.<sup>24</sup>

Bone marrow cells represent a very exciting addition to the pool of potential cell types for use in cell transplantation. While we gain more knowledge of their differentiation *in vivo* and the varying phenotypes they may be able to generate, it is important to remember the record of pre-clinical data supporting the use of skeletal myoblasts. Thus, direct comparison of other cell populations with skeletal myoblasts remains important in future studies.

## References

1. Taylor DA, Atkins BZ, Hungspreugs P, Jones TR, Reedy MC, Hutcheson KA, Glower DD, Kraus WE. Regenerating functional myocardium: improved performance after skeletal muscle myoblast transplantation. *Nat Med* 1998;4:929-33.
2. Pouzet B, Vilquin JT, Hagege AA, Scorsin M, Messas E, Fiszman M, Schwartz K, Menasche P. Intramyocardial transplantation of autologous myoblasts: can tissue processing be optimized? *Circulation* 2000;102:III210-5.
3. Strauer BE, Brehm M, Zeus T, Kosterling M, Hernandez A, Sorg RV, Kogler G, Wernet P. Repair of infarcted myocardium by autologous intracoronary mononuclear bone marrow cell transplantation in humans. *Circulation* 2002;106:1913-8.
4. Orlic D, Kajstura J, Chimenti S, Jakoniuk I, Anderson SM, Li B, Pickel J, McKay R, Nadal-Ginard B, Bodine DM, Leri A, Anversa P. Bone marrow cells regenerate infarcted myocardium. *Nature* 2001;410:701-5.
5. Toma C, Pittenger MF, Cahill KS, Byrne BJ, Kessler PD. Human mesenchymal stem cells differentiate to a cardiomyocyte phenotype in the adult murine heart. *Circulation* 2002;105:93-8.
6. Marelli D, Desrosiers C, El-Alfy M, Kao RL, Chiu RCJ. Cell transplantation for myocardial repair: an experimental approach. *Cell Transplant* 1992;1:383-90
7. Murry CE, Wiseman RW, Schwartz SM, Hauschka SD. Skeletal myoblast transplantation for repair of myocardial necrosis. *J Clin Invest* 1996;98:2512-23.
8. Pouzet B, Vilquin JT, Hagege AA, Scorsin M, Messas E, Fiszman M, Schwartz K, Menasche P. Factors affecting functional outcome after autologous skeletal myoblast transplantation. *Ann Thorac Surg* 2001;71:844-50.
9. Makino S, Fukuda K, Miyoshi S, Konishi F, Kodama H, Pan J, Sano M, Takahashi T, Hori S, Abe H, Hata J, Umezawa A, Ogawa S. Cardiomyocytes can be generated from marrow stromal cells in vitro. *J Clin Invest* 1999;103:697-705.
10. Tomita S, Mickle DA, Weisel RD, Jia ZQ, Tumiati LC, Allidina Y, Liu P, Li RK. Improved heart function with myogenesis and angiogenesis after autologous porcine bone marrow stromal cell transplantation. *J Thorac Cardiovasc Surg* 2002;123:1132-40.
11. Atkins BZ, Lewis CW, Kraus WE, Hutcheson KA, Glower DD, Taylor DA. Intracardiac transplantation of skeletal myoblasts yields two populations of striated cells in situ. *Ann Thorac Surg* 1999;67:124-9
12. Atkins BZ, Hueman MT, Meuchel JM, Cottman MJ, Hutcheson KA, Taylor DA. Myogenic cell transplantation improves in vivo regional performance in infarcted rabbit myocardium. *J Heart Lung Transplant* 1999;18:1173-80.
13. Jain M, DerSimonian H, Brenner DA. Cell therapy attenuates deleterious ventricular remodeling and improves cardiac performance after myocardial infarction. *Circulation* 2001;103:1920-7.
14. Atkins BZ, Hueman MT, Meuchel J, Hutcheson KA, Glower DD, Taylor DA. Cellular

- cardiomyoplasty improves diastolic properties of injured heart. *J Surg Res* 1999;85:234-42.
15. Hutcheson KA, Atkins BZ, Hueman MT, Hopkins MB, Glower DD, Taylor DA. Comparison of benefits on myocardial performance of cellular cardiomyoplasty with skeletal myoblasts and fibroblasts. *Cell Transplant* 2000;9:359-68.
  16. Scorsin M, Hagege A, Vilquin JT, Fiszman M, Marotte F, Samuel JL, Rappaport L, Schwartz K, Menasche P. Comparison of the effects of fetal cardiomyocyte and skeletal myoblast transplantation on postinfarction left ventricular function. *J Thorac Cardiovasc Surg* 2000;119:1169-75.
  17. Yau TM, Tomita S, Weisel RD, Jia ZQ, Tumiati LC, Mickle DA, Li RK. Beneficial effect of autologous cell transplantation on infarcted heart function: comparison between bone marrow stromal cells and heart cells. *Ann Thorac Surg* 2003;75:169-76.
  18. Jiang Y, Vaessen B, Lenvik T, Blackstad M, Reyes M, Verfaillie CM. Multipotent progenitor cells can be isolated from postnatal murine bone marrow, muscle, and brain. *Exp Hematol* 2002;30:896-904.
  19. Howell JC, Yoder MC, Srour EF. Hematopoietic potential of murine skeletal muscle-derived CD45(-)Sca-1(+)c-kit(-) cells. *Exp Hematol* 2002;30:915-24.
  20. Hirschi KK, Goodell MA. Hematopoietic, vascular and cardiac fates of bone marrow-derived stem cells. *Gene Ther* 2002;9:648-52.
  21. Reyes M, Dudek A, Jahagirdar B, Koodie L, Marker PH, Verfaillie CM. Origin of endothelial progenitors in human postnatal bone marrow. *J Clin Invest* 2002;109:337-46.
  22. Toma C, Pittenger MF, Cahill KS, Byrne BJ, Kessler PD. Human mesenchymal stem cells differentiate to a cardiomyocyte phenotype in the adult murine heart. *Circulation* 2002;105:93-8.
  23. Leobon B, Garcin I, Vilquin JT, Menasche P, Audinat E. Do engrafted skeletal myoblasts contract in infarcted myocardium? *Circulation* 2002;106:II549.
  24. Min JY, Sullivan MF, Yang Y, Zhang JP, Converso KL, Morgan JP, Xiao YF. Significant improvement of heart function by cotransplantation of human mesenchymal stem cells and fetal cardiomyocytes in postinfarcted pigs. *Ann Thorac Surg* 2002;74:1568-75.



## Part 6

Tracking cells after intramyocardial transplantation  
using magnetic resonance imaging



# Chapter 7

## Improved efficacy of stem cell labeling for magnetic resonance imaging studies by the use of cationic liposomes

van den Bos EJ, Wagner A, Mahrholdt H, Thompson RB, Morimoto Y, Sutton BS, Judd RM, Taylor DA. Cell Transplant 2003;12:743-56.



## Abstract

Labeling stem cells with FDA approved superparamagnetic iron oxide particles makes it possible to track cells *in vivo* with magnetic resonance imaging (MRI) but high intracellular levels of iron can cause free radical formation and cytotoxicity. We hypothesized that the use of cationic liposomes would increase labeling efficiency without toxic effects.

Rabbit skeletal myoblasts were labeled with iron oxide by: (1) uptake of iron oxide incorporated into cationic transfection liposomes (Group I); or (2) customary endocytosis (Group II). In both groups, cell proliferation and differentiation were measured and toxicity was assayed using trypan blue and ratio fluorescence microscopy with BODIPY® 581/591 C<sub>11</sub>. The effects of the intracellular iron oxide on magnetic resonance image intensities were assessed *in vitro* and *in vivo*.

Both methods resulted in uptake of iron intracellularly, yielding contrast inducing properties on MRI images. In Group II, however, incubation with iron oxide at high concentrations required for endocytosis, caused generation of free radicals, a decrease in proliferation and cell death. Cytotoxic effects in the remaining cells were still visible 24 hours after incubation. Conversely in Group I, sufficient intracellular uptake for detection *in vivo* by MRI could be achieved at 100 fold lower concentrations of iron oxide, which resulted in a high percentage of labeled cells, high retention of the label, and no cytotoxic effects even after stressing the cells with a hypoxia-reoxygenation insult.

The use of cationic liposomes for iron oxide stem cell labeling increases labeling efficiency approximately 100 fold without toxic effects. This technique results in high contrast inducing properties on MRI images both *in vitro* and *in vivo* and could thus be a valuable tool for tracking stem cells non-invasively.

## Introduction

Transplantation of stem or progenitor cells is a revolutionary new technique proposed for the treatment of various injured tissues or organs. Because cells can be isolated from different tissues, expanded *in vitro* and replace or repair defective endogenous cell populations,<sup>1-4</sup> they offer new promise for tissue repair and disease correction. Yet, following the status of stem cells *in vivo* is critical if therapy is to be optimized or evaluated. Since it allows for 3D, high resolution whole body imaging and tracking of cells *in vivo*, magnetic resonance imaging (MRI) is an ideal technique to determine the fate of cells after transplantation and migration of cells after injection, without the need for tissue biopsies and histological assessment. However, following cells by MRI requires that they contain magnetic probes.

## Cell labeling techniques

Recently, techniques have been described for labeling cells with iron oxide probes to make them highly magnetic and make it possible to visualize them on MR images. Iron oxide particles are highly suitable for this purpose because they cause a strong local disruption of the homogeneity of the magnetic field and a loss in MR signal, which makes labeled cells appear black. Most current labeling techniques use one of two approaches: (1) extracellular labeling by attaching iron particles to the cell surface,<sup>5</sup> or (2) internalizing magnetic markers inside the cell.<sup>6-9</sup> For intracellular uptake of iron particles several different techniques are used: fluid phase endocytosis,<sup>7,8</sup> conjugated antibodies<sup>9</sup> and magnetodendrimers.<sup>6</sup> These methods all have their disadvantages. After extracellular labeling, the label can either be easily lost or it can interfere with cell to cell interactions. The intracellular methods are either relatively ineffective (fluid phase endocytosis), require specialized laboratory techniques (magnetodendrimers) or are cell-type specific (conjugated antibodies). Recently, a new method was reported - based upon the use of cationic liposome transfection reagents - that lacks these disadvantages.<sup>10</sup>

## Iron toxicity

Although efficient labeling with iron oxide has been demonstrated in a variety of cell types, the use of any labeling agent, especially metals, is limited by its potential toxicity. Even though iron is an essential component of many enzymes and proteins, it can be toxic in high concentrations.<sup>11,12</sup> In some cells, such as liver macrophages, relatively small increases in intracellular iron can have deleterious effects on cellular signaling and function.<sup>13,14</sup> Iron accumulation in tissues also catalyzes the Fenton reaction and potentiates oxygen toxicity by the generation of a wide range of free radical species, including hydroxyl radicals, which are the most active free radicals known that have the ability to react with a wide range of intracellular constituents.<sup>15,16</sup> Thus, prior to its use *in vivo*, iron loading of cells should be shown to be non-toxic and to have no effect on cell proliferation and differentiation.

## Feridex, a FDA approved agent

During the last several years, clinical trials have begun to evaluate the use of stem cell transplantation for tissue and organ repair. Yet, no good non-invasive method exists for following cells *in vivo*. Clinically approved cell labeling with iron could mean a breakthrough in stem cell transplantation, because it allows potential monitoring of the biodistribution of cells over time and therefore provides a way to assess the success of stem cell therapy. In evaluating the potential for following stem cells *in vivo*, we labeled progenitor cells with Feridex. This is a FDA approved superparamagnetic contrast agent that consists of iron oxide crystals of 4.8 to 5.6 nm, coated with a dextran monolayer to make them biocompatible, so they can readily be biodegraded.<sup>17,18</sup> The safety of intravenously administered Feridex during clinical MRI imaging has been confirmed in animal models.<sup>18</sup> However, for effective MRI visualization of cells *in vivo*, the concentration of iron intracellularly has to be much higher (~10 pg per cell).<sup>6</sup> This concentration exceeds physiological concentrations ~100 fold and thus may be toxic. Furthermore, at this high concentration, leakage of iron or death of the labeled cells could cause release of iron oxide crystals into the tissue, which could, in turn, result in a potentially toxic uptake in surrounding healthy cells. In the present study we investigated a novel mechanism to potentially overcome this toxicity.

We assessed the uptake of Feridex in rabbit skeletal myoblasts, a population of progenitor cells, which have been used for cardiac repair after myocardial infarction.<sup>3,19</sup> We investigated whether the use of liposome-based cationic transfection reagents, which are normally used for DNA incorporation into cells, could enhance cellular uptake of Feridex in a non-toxic way. We postulated that the negative charges of the Feridex crystals could form complexes with the hydrophilic ends of the liposomes and could then be easily taken up intracellularly. We compared this liposomal method with customary endocytosis with respect to uptake efficiency, cytotoxicity and effects on myoblast proliferation and differentiation.

## Methods

### Isolation of rabbit skeletal myoblasts

All animal experiments were conducted in accordance with “Principles of Animal Care”, formulated by the National Society for Medical Research and “Guide for the Care and Use of Laboratory Animals”, published by the National Institutes of Health and were approved by the Duke University Institution Animal Care and Use Committee.

Muscle cells were isolated from an excisional muscle biopsy from 3 female New Zealand White rabbits as previously described.<sup>3</sup> Briefly, a biopsy of ~0.5 mg was taken from the soleus muscle under general anaesthesia. Fascia and aponeurotic tissue were removed. The biopsy was minced with scissors to 1 mm<sup>3</sup> pieces and incubated for 3 days in Dulbecco’s Modified Eagle’s Medium (DMEM) containing 10% fetal bovine serum (FBS) and 0.5% gentamicin (10 mg/ml; Gibco, Gaithersburg, MD). After 3 days the tissue was triturated through a 10 ml pipette for 3 minutes. Once cells began migrating out of the tissue, FBS was replaced with 20% horse serum (HS). Cells were passaged 1:4 when reaching ~70%

confluence. Cells were used at passage 4.

### **Desmin immunofluorescence**

To determine the percentage of myoblasts (desmin positive cells), rabbit muscle-derived cells were passaged and replated on glass coverslips, grown overnight and stained for desmin as follows: cells were fixed in 5% paraformaldehyde for 10 minutes, washed in PBS and permeabilized in PBS with 0.2% NP40 and 0.2% Tween for 10 minutes. Blocking was done in PBS with 5% HS and 5% FBS for 1 hour at 37°C. Cells were then incubated for 90 minutes in primary monoclonal anti-desmin antibody (Sigma, St. Louis, MO), diluted 1:200 in blocking buffer at 37°C, followed by a secondary PE conjugated anti-mouse antibody (Molecular Probes, Leiden, the Netherlands) for 1 hour. Extensive washing in blocking buffer was performed between the steps. Staining was analyzed on a Nikon Eclipse TE 200 inverted fluorescence microscope. Photographs were taken and the number of desmin positive cells per high power field was counted and expressed as a percentage of the total cell number.

### **Feridex labeling**

Feridex was purchased from Berlex laboratories. The Feridex-liposome complexes (Group I) were made as follows: 30  $\mu$ l of Lipofectamine 2000 (Gibco, Gaithersburg, MD) was diluted in 0.5 ml of Opti-MEM reduced serum medium (Gibco, Gaithersburg, MD). Separately, Feridex was diluted in different concentrations in a range of 2.5, 5, 10, 20, 40 and 100  $\mu$ g total iron, in 0.5 ml of Opti-MEM. After 5 minutes the suspensions were combined and gently mixed by pipetting. After 20 minutes the complexes containing each concentration of Feridex were added dropwise to the dishes. For uptake via endocytosis (Group II) cells were incubated in Feridex (at 0.1, 0.5, 1, 2.5, 5, 7.5, 10 and 20 mg iron per 150 mm dish) diluted in Opti-MEM. The Feridex incubation was done in a total of 10 ml of Opti-MEM for 24 hours. After this period cells were washed 6 times with PBS to eliminate any Feridex attached to the dish, detached with trypsin-EDTA (0.25%; Gibco, Gaithersburg, MD) and replated for 4 hours before the experiments were performed.

### **Transmission electron microscopy**

The Feridex, liposome transfection reagent and the formed Feridex-liposome complexes were analyzed on a Philips EM 301 transmission electron microscope. The complexes were formed as described above. The suspensions were loaded on a glow discharged copper grid and negatively stained in 2% aqueous uranyl acetate. Photographs were taken. Particle size was measured on different fields and at least 25 particles were counted.

### **Magnetic cell sorting**

After incubation with Feridex or Feridex-liposome complexes, cell suspensions were run through a magnetic cell sorter (Miltenyi Biotec GmbH, Bergisch Gladbach, Germany). Cell numbers were counted on a hemacytometer before and after sorting. The number of bound

cells was determined by subtracting the number of cells after sorting from the number prior to sorting and expressed as a percentage of the total number of cells. Labeled cells ( $2 \times 10^3$  from each group) were then plated and passaged twice during 8 days. The total number of labeled cells was then counted in the same way.

### **Prussian Blue stain**

To visualize intracellular iron content, a Prussian Blue staining was performed using a kit (Newcomer Supply, Middleton, WI). Directly after labeling, cells were fixed in 10% paraformaldehyde for 10 minutes, washed in PBS and stained with a freshly prepared solution of 5% potassium ferrocyanide and 10% hydrochloric acid for 20 minutes. Cells were washed and photographs were taken of representative fields.

### **Phenanthroline assay for iron content**

Four hours after Feridex labeling, cells were harvested and counted prior to a phenanthroline assay to determine iron content as follows. Equivalent numbers of cells were pelleted by centrifugation and dried for 12 hours at 70°C. Cells were digested in 25  $\mu$ l of a 3:1 mixture of ultrapure perchloric acid (EM Science, Cincinnati, OH) and ultrapure nitric acid (JT Baker, Phillipsburg, NJ), at 60°C for 3 hours. The samples were then incubated for 10 minutes at room temperature with a mixture of 50  $\mu$ l 0.1% 1,10-phenanthroline monohydrate (Sigma, St. Louis, MO) in methanol and 10  $\mu$ l and 80  $\mu$ l respectively of 10% solutions of hydroxylammonium chloride and sodium acetate (both from Sigma, St. Louis, MO) in distilled water. Absorbance was measured at 492 nm on a spectrophotometer.

### **Proliferation and differentiation assays**

To measure proliferation,  $3 \times 10^3$  labeled cells were plated in each well of a 6 well plate and counted in triplicate on a hemacytometer for 4 consecutive days. To assay differentiation,  $2 \times 10^5$  labeled cells were plated in each well of a 6 well plate, grown to 100% confluence for 2 days and then shifted to differentiation medium, consisting of DMEM with 2% HS and 0.5% gentamicin (10 mg/ml) for 7 days. On day 7, cells were labeled with 4',6-diamidino-2-phenylindole (DAPI; Sigma, St. Louis, MO) at a concentration of 10  $\mu$ g/ml in PBS for 10 minutes to label each nucleus. The total number of nuclei and the total number of myotubes were counted under fluorescence. Fusion index was expressed as the total number of nuclei inside myotubes (cells with 3 or more nuclei) divided by the total number of nuclei and used as a measure for differentiation.

### **Cytotoxicity assays**

Directly after labeling cell death was determined by a trypan blue viability assay. Formation of free radicals and subsequent lipid oxidation is a measure of iron toxicity. To determine the effects of incorporated iron on radical formation, 4,4-difluoro-5-(4-phenyl-1,3-butadienyl)-4-bora-3a, 4a-diaza-s-indacene-3-undecanoic acid (BODIPY® 581/591 C<sub>11</sub>; Molecular Probes,

Leiden, the Netherlands) was used. Upon oxidation the fluorescence of this fluorophore shifts from red to green. The red to green ratio is thus a direct measure of lipid oxidation and free radical formation. Cells were incubated for 24 hours with Feridex (Group II) in concentrations in the range of 20, 5 and 0.1 mg total iron or with 100 µg Feridex-liposome complexes (Group I), replated for 24 hours in normal growth medium and incubated for 60 minutes with BODIPY® 581/591 C<sub>11</sub> at a final concentration of 1 µM in PBS with 0.2% methanol. After a second 24 hours, cells were washed in PBS, incubated in normal growth medium and analyzed by fluorescence microscopy using Image Pro analysis software. The ratio of red to green fluorescence intensity per cell was then calculated as described.<sup>20</sup> Dimethyl sulfoxide (DMSO; Sigma, St. Louis, MO) in a concentration of 10% (v/v) diluted in growth medium was used as a positive control for lipid oxidation.

To assess the influence of hypoxia on the formation of free radicals induced by the presence of intracellular iron, cells labeled with 100 µg Feridex and liposome complexes were incubated for 48 hours in a hypoxia chamber at 0.3% O<sub>2</sub> and then reoxygenated for 3 hours before being analyzed.

### MRI imaging

Four hours after Feridex labeling and replating, cells were washed, detached from the plate with trypsin, collected by centrifugation and counted. Approximately  $8 \times 10^5$  cells for each concentration of Feridex were diluted in 500 µl of growth medium in Eppendorf tubes. A standard calibration curve of Feridex was created by diluting known concentrations in growth medium (2, 1, 0.75, 0.5, 0.25, 0.1,  $5 \times 10^{-2}$ ,  $1 \times 10^{-2}$ ,  $1 \times 10^{-3}$  and  $1 \times 10^{-4}$  mg/500 µl). The tubes were briefly shaken to evenly distribute cells or iron particles and imaged in a plastic holder in a Siemens Sonata 1.5 Tesla MRI scanner. An image plane through the fluid level was chosen. Each sample was imaged with a three-dimensional TrueFISP MRI technique with TR=10.2 ms, TE=5.1 ms, bandwidth=130 kHz, flip angle=70° and pixel size=0.8x0.8x1.0 mm<sup>3</sup>. The mean signal intensity in each Eppendorf was then calculated, using standard Siemens software, and expressed as a measure of total iron per Eppendorf. Total iron in the the Eppendorfs with cells was calculated by multiplying the intracellular iron concentrations per cell with the total cell number per Eppendorf.

For *in vivo* imaging of labeled cells, myoblasts were incubated with 100 µg Feridex per 150 mm plate and liposome transfection reagent for 24 hours and  $\sim 4 \times 10^7$  labeled myoblasts were injected autologously into 4 cryo-injured rabbit hearts, 2 weeks after infarction. A second control injection with  $\sim 4 \times 10^7$  cells was performed with unlabeled cells more apical and parallel to the first injection. The location of the injections relative to the borders of the infarct scar and to the apex was measured. Three days after cell injection, the rabbit was sedated with ketamine (50 mg/kg) and acepromazine (1 mg/kg). Cine MRI images and contrast enhanced images were acquired after injection of gadolinium (0.3 mmol/kg). For cine images a Flash sequence was used with TR=35 ms, TE=4.8 ms, bandwidth=195 kHz and flip angle=30°. Contrast enhanced images were acquired using a Flash technique with

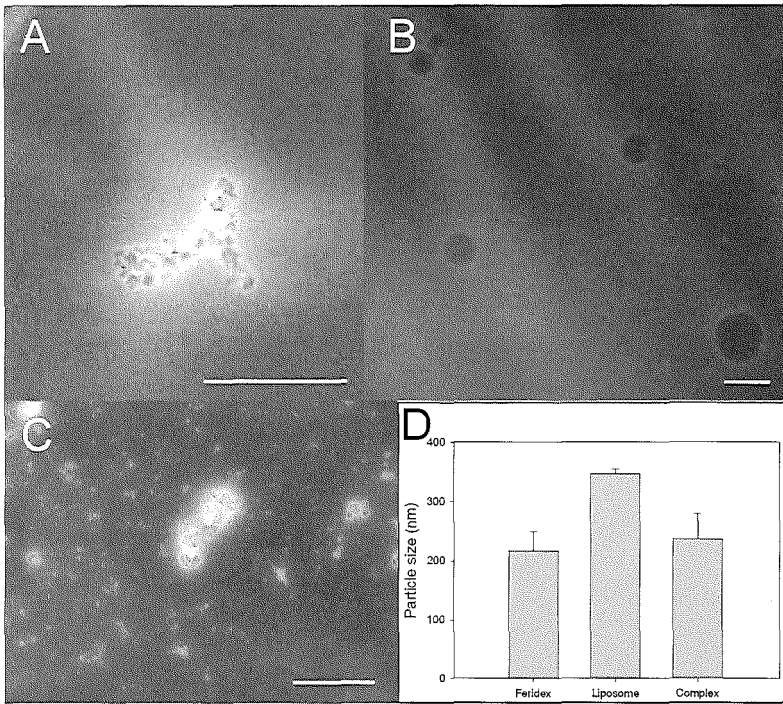


Figure 1. Transmission electron micrographs showing Feridex particles (Panel A), liposomes (Panel B) and the Feridex-liposome complexes (Panel C) formed after 20 minutes incubation. Panel D shows the mean particle size  $\pm$  SEM in each group. At least 25 particles were counted in multiple fields. Bar indicates 200 nm.

TR=1350 ms, TE=4.8 m and bandwidth=130 kHz. Pixel size was  $0.3 \times 0.3 \times 2 \text{ mm}^3$ . Inversion time for the image shown was 270 ms.

After scanning the animals were euthanized with an overdose of pentobarbital and the hearts were taken out, frozen in liquid nitrogen-cooled isopentane and sliced on a cryostat in  $6 \mu\text{m}$  sections. After air drying overnight, a Prussian Blue staining was carried out in the same way as described for the labeled cells.

### Statistical analysis

Comparisons between multiple groups were performed by one-way ANOVA followed by the Student-Newman-Keul post hoc test. A value of  $P < 0.05$  was considered statistically significant.

## Results

### Isolation of skeletal myoblasts

Rabbit skeletal myoblasts were stained with desmin to confirm their muscle phenotype. Desmin is a specific cytoskeletal protein present in cardiomyocytes and skeletal muscle cells. The isolation procedure resulted in more than 90% desmin positive cells on immunofluorescence ( $94\% \pm 2.3\%$ , mean  $\pm$  SEM,  $n=3$ ), confirming the highly myogenic cultures obtained.

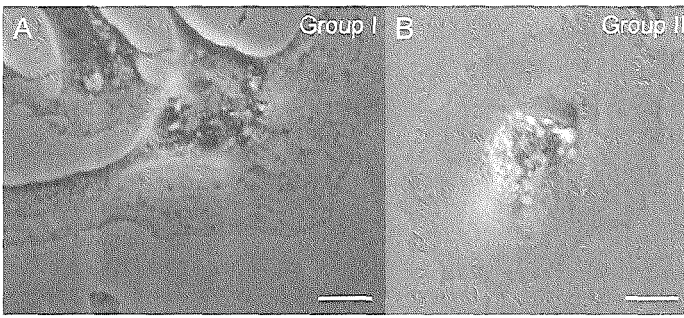
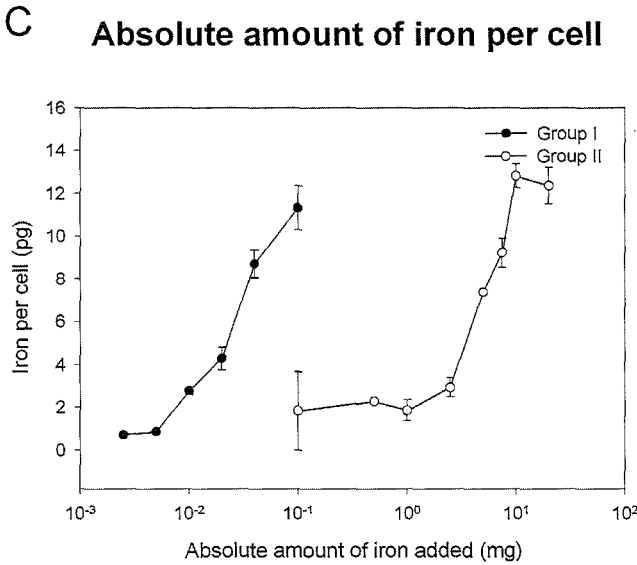


Figure 2. Light micrographs of rabbit skeletal myoblasts after incubation with the Feridex-liposome complexes (100 µg iron, Group I) (A) or Feridex (20 mg iron, Group II) (B): Prussian Blue stain. Intracellular iron oxide is visible as perinuclear iron deposits. No extracellular or intranuclear iron is visible. Bar indicates 10 µm. As indicated in Panel C, a phenanthroline-based assay showed that equal amounts of Feridex can be internalized using both methods, but 100 fold higher concentrations of Feridex are needed in Group II to obtain the same uptake. Data are shown as mean ± SEM from 2 separate experiments.



### Formation of Feridex-liposome complexes

We used electron transmission microscopy to study the formation and size of Feridex particles, transfection reagent liposomes and the Feridex-liposome complexes. As shown in Figure 1, the mean particle size of the Feridex, the liposome particles and the Feridex-liposome complexes was 217 nm, 346 nm and 236 nm, respectively.

### Cellular uptake of Feridex

The cellular uptake of Feridex was evaluated by Prussian Blue staining and a phenanthroline assay. As shown in Figure 2A and B, both Feridex delivery methods resulted in intracellular uptake. With both techniques, no extracellular iron was visible on light microscopy. Most iron complexes were located around the nucleus, but no intranuclear staining was observed. Phenanthroline assay results, depicted in Figure 2C, showed that equal concentrations of intracellular Feridex were achieved via liposome-based endocytosis (Group I) at 100 fold lower concentrations of exogenous iron. For example, in group I after exposure to liposomes

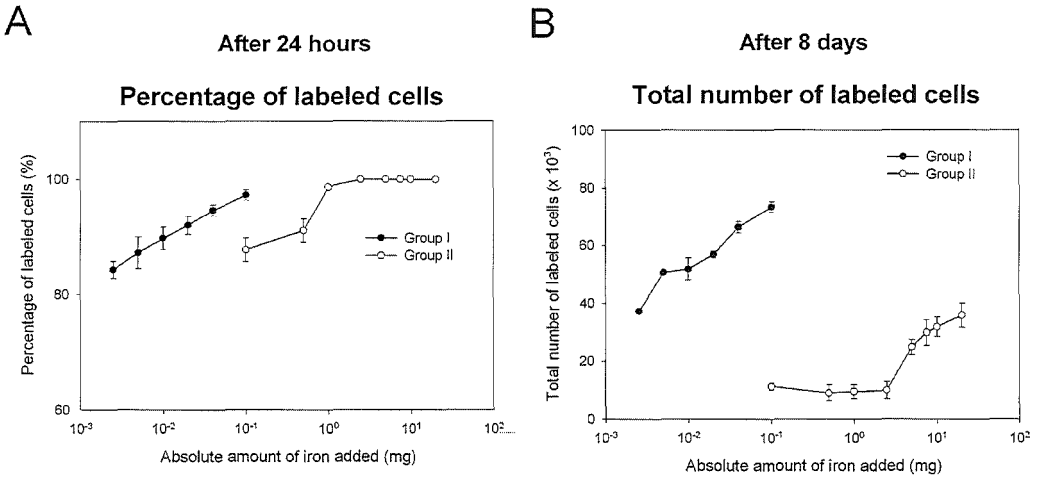


Figure 3. Percentage of iron-labeled cells as determined by magnetic cell sorting after 24 hours (Panel A) and the absolute number of labeled cells after 8 days in culture and 2 passages which arose from  $2 \times 10^3$  labeled cells (Panel B). Incubation with 100  $\mu\text{g}$  iron in Group I resulted in almost 100% labeling, whereas in Group II, 1 mg of iron was needed to obtain similar results. After 8 days, a significant higher number of labeled cells is found in Group I than in Group II. The labeled population forms 51% of the total cell number in Group I indicating the high retention of the label, even after several passages and cell doublings. Data are expressed as mean  $\pm$  SEM from 3 separate experiments performed in duplicate.

and 100  $\mu\text{g}$  iron per dish, an uptake of 11.3 pg iron per cell was measured, whereas the maximum uptake of Feridex by endocytosis (Group II) was 12.8 pg per cell but only after exposure to 10 mg iron per dish, a 100 fold difference.

Magnetic sorting was performed 24 hours and 8 days after labeling to assess the percentage of labeled cells (Figure 3). Although both methods resulted in high percentages of labeled cells, up to 98% in Group I (with liposomes) and 100% in Group II (without liposomes), the absolute number of labeled cells was significantly lower in Group II after 8 days and 2 passages ( $P < 0.05$  for all concentrations, Group II vs. Group I).

### Proliferation and differentiation assay

Proliferation assays were performed during 4 consecutive days after exposure of myoblasts to iron and compared with control cells. A significant difference was observed between the myoblasts labeled with liposomes (Group I) and those without (Group II) (Figure 4). Cells in group I showed no difference in growth rate as compared with unlabeled cells (controls). However, Group II showed a marked decrease in proliferation rate beginning at day 2 and continuing for the duration of the experiment as depicted in Figure 4 ( $P < 0.05$  for all concentrations, after 4 days, Group II vs. control and vs. Group I).

Differentiation of myoblasts was assessed by determining the ability to fuse and form multinucleated myotubes. No difference was observed between Groups I or II

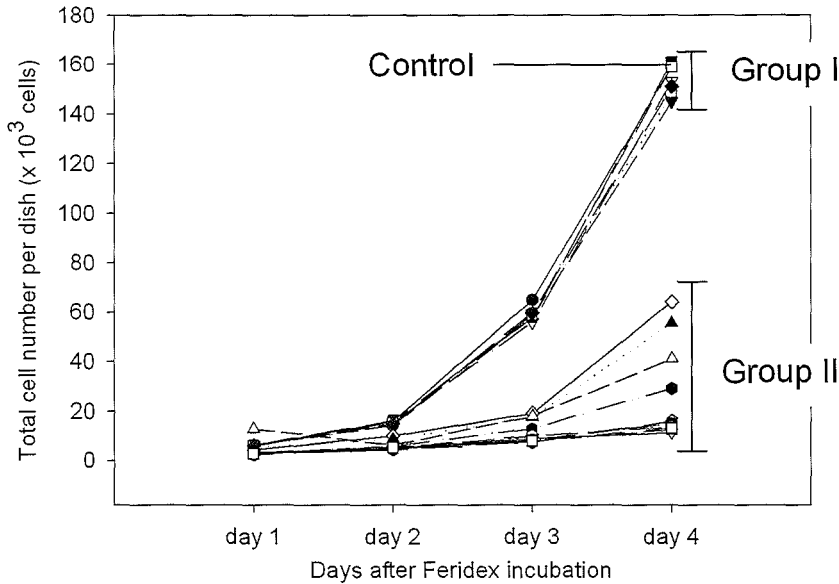


Figure 4. Growth curve of rabbit myoblasts after incubation with Feridex, with (Group I) or without liposomes (Group II). Cells were plated in 6 well plates at  $3 \times 10^3$  cells per well after labeling with different concentrations of Feridex and counted for 4 consecutive days. Growth is significantly decreased in Group II, whereas in Group I, no significant difference is observed compared to control cells. Data are expressed as the mean of 3 separate experiments.  $P < 0.05$  for all Group II curves compared to control or Group I after 4 days.

or the control group (fusion indices were for example  $34.3 \pm 2.6\%$ ,  $33.2 \pm 1.7\%$  and  $35.4 \pm 3.2\%$ , for the control group, Group II and Group I respectively, after labeling with the highest iron concentrations, mean  $\pm$  SEM,  $n=3$ ).

### Cytotoxicity assays

The presence of intracellular iron can induce Fenton type reactions, which generate multiple forms of free radicals and cause cell death. Therefore, cell viability directly after the incubation period was assessed by a trypan blue viability assay (Figure 5). A high percentage of cell death of up to 20.4% was observed in Group II (without liposomes) even at low intracellular iron concentrations, whereas in Group I (with liposomes) a 10 fold lower degree of cell death was observed of up to 2.4%, that did not differ from control cells.

To assess the effect of the presence of intracellular iron after the incubation period, cells were replated for 24 hours and grown in normal growth medium. To determine the effects of free radical formation we used a BODIPY dye that binds specifically to lipids sensitive to oxidation. Under normal conditions it fluoresces red. However, on oxidation there is a shift from red to green. As shown in Figure 6, liposome-based labeling with Feridex (Group I) does not cause free radical formation (Figure 6I), whereas in Group II, the cells

## Cell death

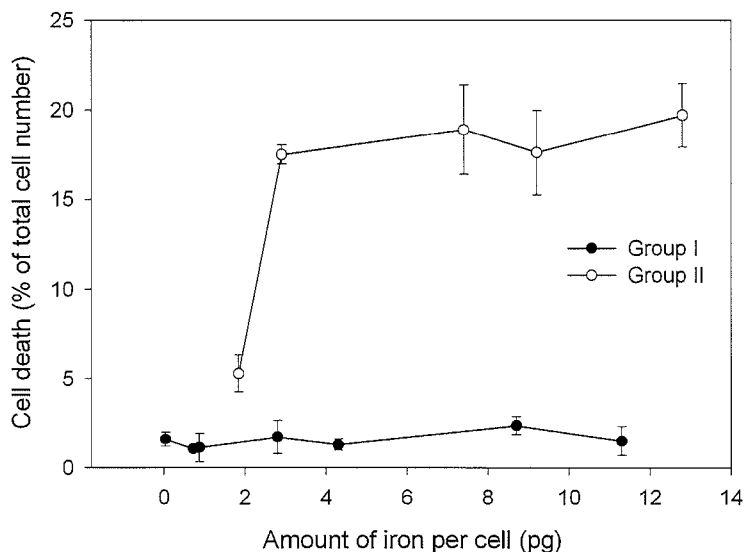


Figure 5. Cell death expressed as a function of total iron content per cell in Group I and II directly after incubation with Feridex. Cell death is as high as 20.4% in Group II after 24 h incubation with Feridex. However, in Group I cell death is comparable with control cells. Data are expressed as mean  $\pm$  SEM from 3 separate experiments ( $P < 0.05$  for all concentrations in Group II vs. control and group I).

treated with Feridex without liposomes, free radical formation was present, which was in the same range as when 10% DMSO was added to the medium (Figure 6B, C, D and E). This occurred even at lower concentrations of intracellular iron. To determine whether stressful conditions such as hypoxia, affected the lipid oxidation state in the cells in Group I, they were incubated under hypoxic conditions for 48 hours and reoxygenated. No increase in lipid oxidation above control cells was observed (13.3% in group I vs. 12.6% in control cells, Figure 6G and H).

## MRI imaging

To confirm the superparamagnetic properties of intracellular Feridex, labeled cells were imaged in Eppendorf tubes in a clinical MRI scanner (Figure 7). The contrast inducing effects were assessed by measuring the mean signal intensity in each tube. In both experimental groups, such an effect could be observed, however a 100 fold higher concentration of Feridex was needed for the same effect in Group II (without liposomes).

To demonstrate the feasibility of *in vivo* imaging of these cells, 4 rabbits received intracardiac injections in the infarct region of labeled autologous myoblasts, containing  $\sim 4 \times 10^7$  myoblasts. This concentration is consistent with the concentration used in animal studies for regeneration of the myocardium. In all animals the location of the cells could be visualized in the infarct, in a region that matched exactly with the surgical injection location. On contrast enhanced images it was possible to visualize both the hyperenhanced infarct region and the labeled cells, void of signal. The injected unlabeled cells were not visible (Figure 8).

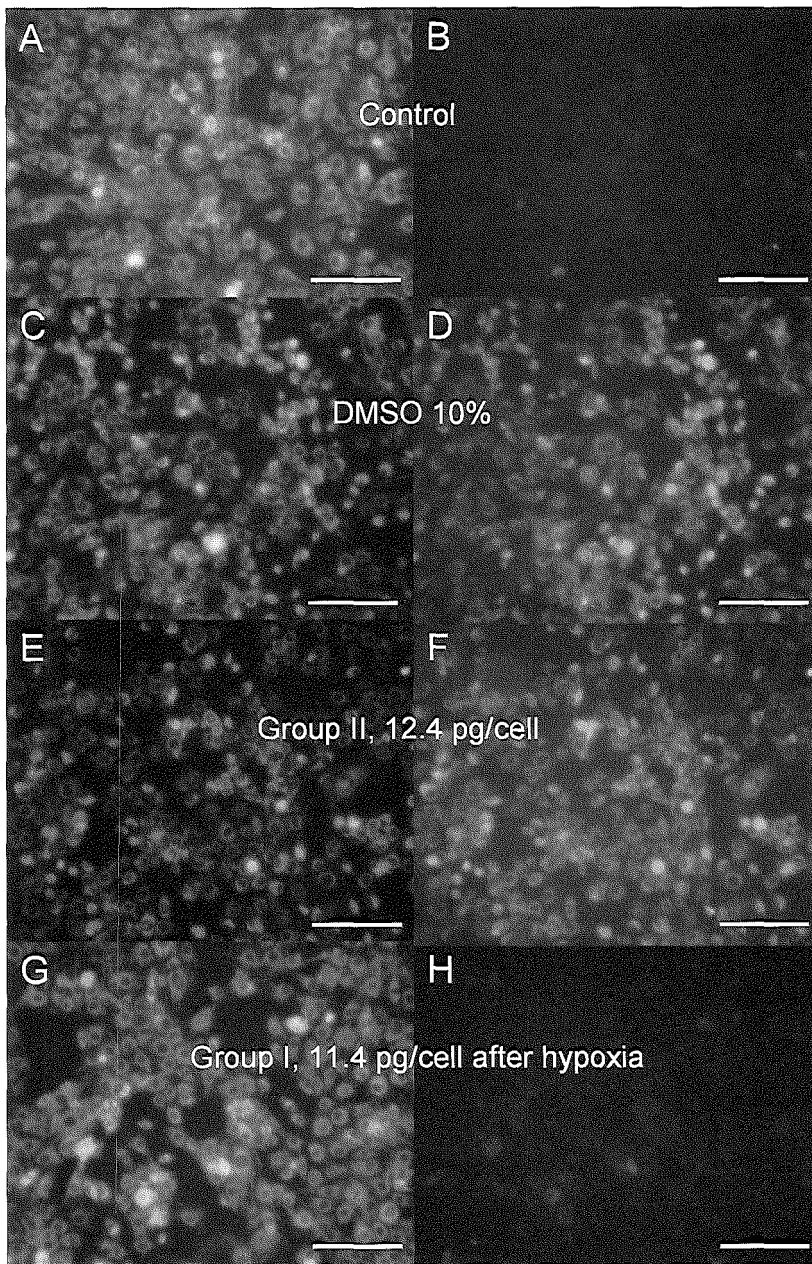


Figure 6. Red and green fluorescence after staining with BODIPY® 581/591 C<sub>11</sub>. (A and B) Control myoblasts during normal growth show no red to green shift. (C and D) Myoblasts treated with 10% DMSO in growth medium for 30 minutes; a shift in red to green ratio is observed, indicating lipid oxidation, comparable with the situation 24 hours after incubation with 20 mg Feridex without liposomes (Group II, 12.4 pg iron per cell; E and F). (G and H) Myoblasts after incubation with 100 µg Feridex with liposomes (Group I, 11.3 pg iron per cell) and 48 hours hypoxia and 3 hours reoxygenation, which causes a small increase in lipid oxidation, as calculated by the red to green ratio, which is comparable with control cells in hypoxia. Bar indicates 250 µm.

## Lipid oxidation

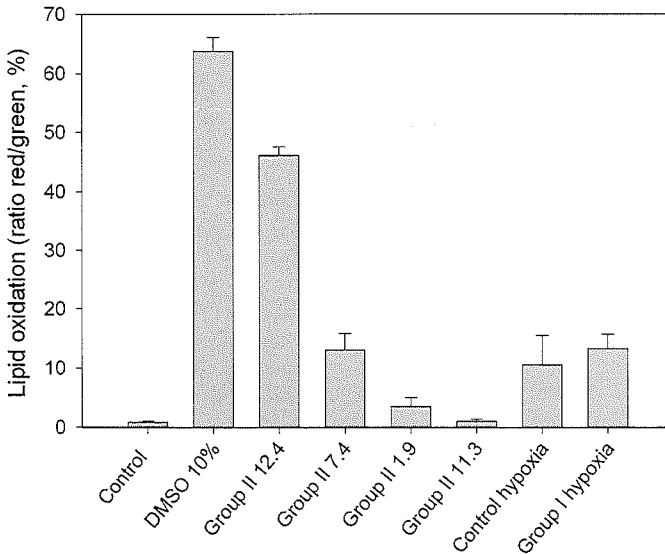


Figure 6I. Red and green fluorescence after staining with BODIPY® 581/591 C<sub>11</sub>. Chart shows the ratios red to green oxidation, indicative of lipid oxidation. Along the x-axis the amount of intracellular iron is shown. Data are expressed as mean  $\pm$  SEM from 3 separate experiments.

## Discussion

We found that cationic liposomes improved the efficiency of iron oxide stem cell labeling approximately 100-fold (Figure 2), without reducing cellular differentiation or proliferation (Figures 3 and 4) and resulted in a strong effect on the magnetic resonance signal (Figures 7 and 8). All of which point to the potential for this method to be used safely to evaluate transplantation of progenitor cells *in vivo*.

Cell labeling with superparamagnetic particles such as iron oxide crystals has been previously described.<sup>5-7</sup> However, the methods that are currently in use to label cells, all have disadvantages. The liposome-based method described here is easy to use, can be performed using standard laboratory techniques and is highly effective at labeling cells without cytotoxicity.

## Intracellular uptake of Feridex

Feridex is a MRI contrast agent with a wide field of clinical applications. It belongs to the class of standard size superparamagnetic iron oxide contrast agents (SPIO).<sup>17,18</sup> It has mainly been used for imaging of the reticuloendothelial system and detection of liver lesions<sup>21</sup> but is not currently used for intracellular labeling. Normally after intravenous injection, 90% of Feridex localizes in the spleen and in the liver. Focal liver lesions such as metastases maintain their signal intensity, while the liver parenchyma is rendered void of signal because of Feridex uptake by reticuloendothelial cells via phagocytosis. The blood half-life is approximately 6 minutes.<sup>18</sup> Because of the dextran coat, Feridex is easily taken up by phagocytosing cells.

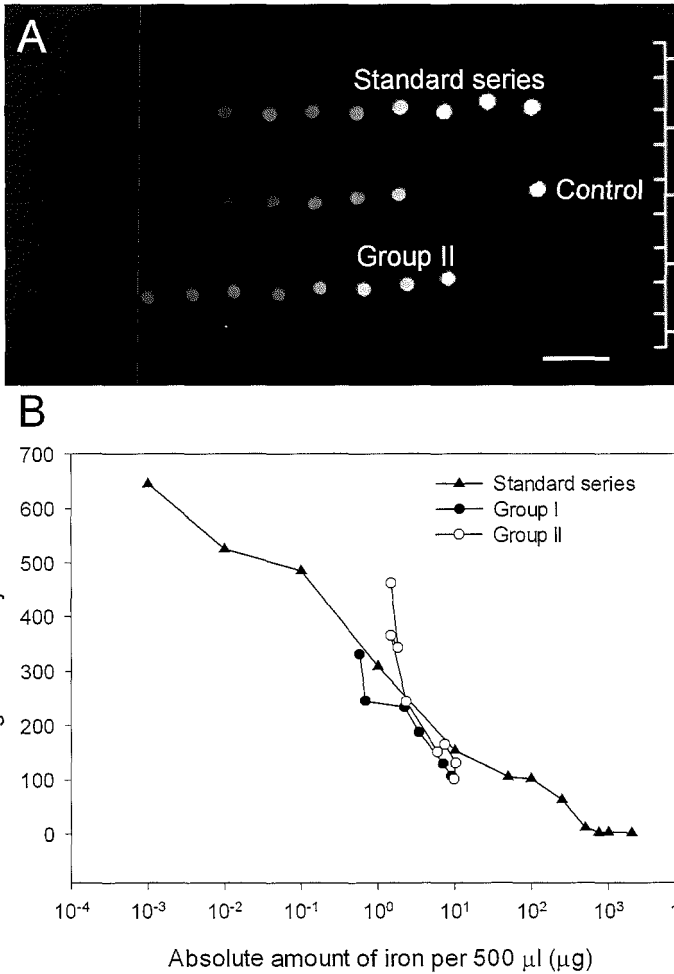


Figure 7. MRI contrast inducing properties. (A) Approximately  $8 \times 10^5$  labeled cells were resuspended in 500 µl growth medium in Eppendorf tubes and imaged in a holder. Signal intensities decreased with higher concentrations of iron. Bar indicates 2 cm. (B) Signal intensities plotted against the absolute amount of iron in each Eppendorf. The amount of iron in Group I and II was calculated by multiplying the cell number per Eppendorf by the amount of intracellular iron per cell as depicted in Figure 2C.

However, as this study shows, non-phagocytosing cells can also take it up via endocytosis. The exact mechanism of the endocytic uptake of Feridex is not clear. The organization of the endocytic pathways in muscle cells remain obscure, although it has been shown that whole muscle fibers are capable of endocytosis of a wide range of fluid phase markers such as dextran.<sup>22</sup> Further, transferrin mediated endocytosis may play an important role in the uptake of Feridex.<sup>23</sup>

The amount of Feridex that is needed for clinical MR imaging of whole organs is small compared with physiological iron stores. Moreover, Feridex can be easily biodegraded, enter the plasma iron pool and be incorporated into red cell production or other natural uses of iron. However, for imaging of cells with a small spatial volume, a high concentration of intracellular iron oxide is required.<sup>6</sup> Even though uptake via customary endocytosis can result in high levels of intracellular iron (Group II), it requires a 100 fold higher extracellular iron concentration than does the use of liposome transfection reagents (Group I). Further,

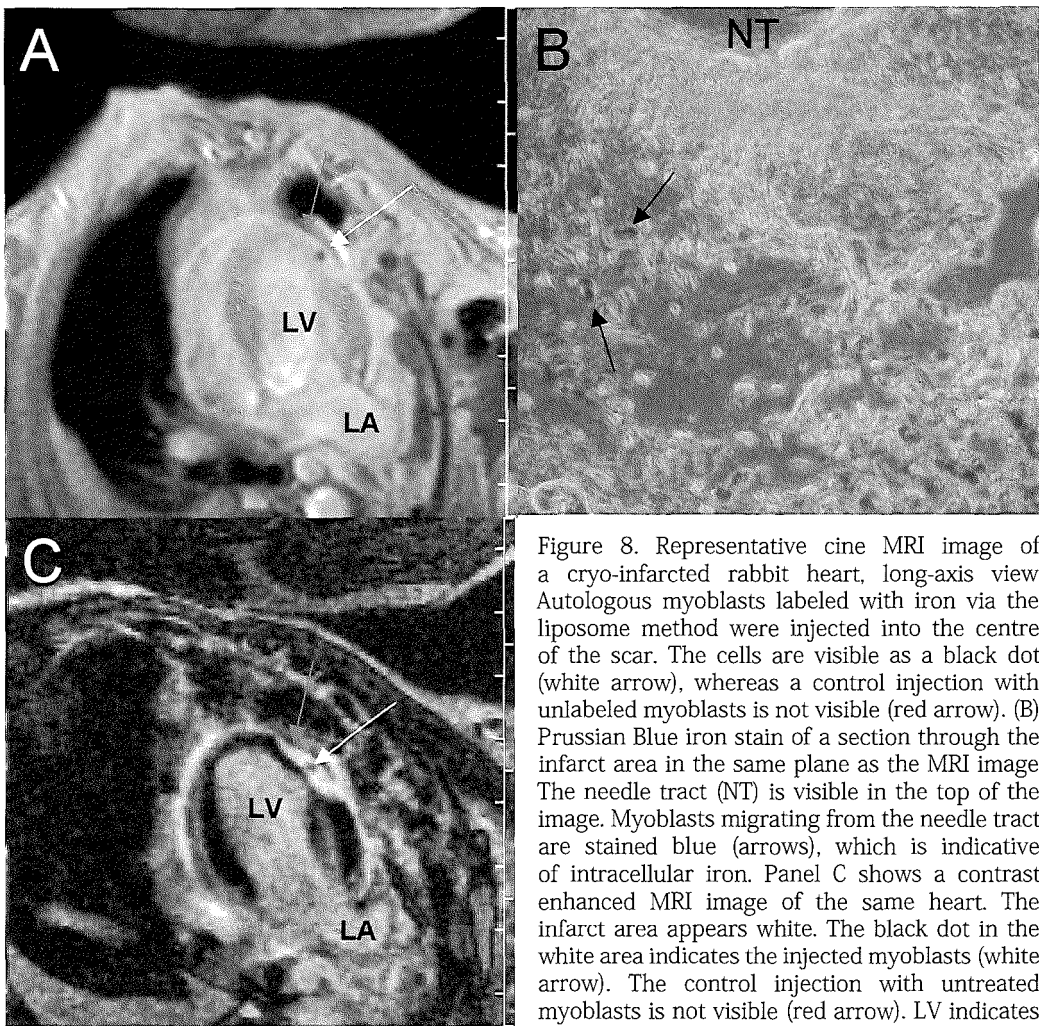


Figure 8. Representative cine MRI image of a cryo-infarcted rabbit heart, long-axis view. Autologous myoblasts labeled with iron via the liposome method were injected into the centre of the scar. The cells are visible as a black dot (white arrow), whereas a control injection with unlabeled myoblasts is not visible (red arrow). (B) Prussian Blue iron stain of a section through the infarct area in the same plane as the MRI image. The needle tract (NT) is visible in the top of the image. Myoblasts migrating from the needle tract are stained blue (arrows), which is indicative of intracellular iron. Panel C shows a contrast enhanced MRI image of the same heart. The infarct area appears white. The black dot in the white area indicates the injected myoblasts (white arrow). The control injection with untreated myoblasts is not visible (red arrow). LV indicates left ventricle, LA indicates left atrium.

we show here that the Feridex-liposome complexes are easily retained inside the cells during proliferation, which implies that these complexes are not easily biodegraded and could thus be used to track cells for longer periods. Although, in Group II, more cells retained their label (93%) after 8 days, versus 51% of the cells in Group I (data not shown), these numbers probably reflect the decreased proliferation rate in Group II. During proliferation part of the iron label will be lost in the mitotic process.

### Toxicity of intracellular iron

Until now, few data exist on the possible cytotoxic effects of intracellular iron label and its influence on biological functions such as proliferation and differentiation that can significantly impact cell homing and engraftment *in vivo*. The results of this study show

that under certain conditions a high intracellular uptake of iron can be established without generating free radicals and without altering proliferation or differentiation. This implies that the intracellular presence of the liposomes prevents the toxic interaction between iron and vital cell constituents.

Normally, when iron enters a cell it is stored as ferritin. In conditions where there is an overload of iron, the ferritin is degraded in lysosomes to hemosiderin. The effects of high intracellular iron levels have been well documented. Cytotoxicity is mainly caused by generation of free radicals such as hydroxyl radicals via a Fenton type reaction:<sup>16</sup>



Free radicals are able to react with DNA as well as with membrane lipids, initiating a free radical chain, known as lipid peroxidation. The extent of toxicity of the intracellular iron complexes is further determined by its localization in the cytosol or lysosomes and its biological form (i.e. in the form of hemosiderin or ferritin) as well as by the ability of the cell to prevent generation and propagation of free radical species.<sup>12</sup> Because of their high levels of anti-oxidative molecules, cells as macrophages or hepatocytes are capable of handling high levels of intracellular iron.<sup>13</sup> Other mammalian cell types normally used for cell transplantation, such as myoblasts are more susceptible to oxidative stress.

One could argue that the extracellular presence of high concentrations of iron oxide during the incubation period in Group II is responsible for the damage in itself. Although this could explain the high level of cell death observed directly after the incubation period, it cannot account for the high degree of cellular lipid oxidation found 48 hours after removal of the extracellular iron in this group or for the marked decrease in proliferation 4 days after removal of extracellular iron, effects that were not seen in Group I, with the liposomes, although the intracellular iron concentrations in both groups were comparable.

The reason for the protective effect of the liposomes against oxidative damage remains unclear. It is possible that in the liposome complex the ferrous (Fe(II)) iron is more stable and less easily oxidised to ferric iron (Fe(III)). To test this hypothesis, we used a hypoxia-reoxygenation model to determine whether conditions that induce generation of free radicals could increase iron-based toxicity. During hypoxia and reoxygenation, mitochondria produce superoxide, which in turn is converted to hydrogen peroxide and acts as a substrate for Fenton type reactions.<sup>24</sup> Although this model caused increased lipid oxidation in the Feridex-liposome treated cells, the observed effect was small and was not different from control, unlabeled cells. Since stem cell therapy is often applied to regenerate tissue with impaired perfusion, it is important that the labeled cells can survive these stress conditions.

### MRI imaging of Feridex-labeled cells

During *in vitro* imaging the contrast inducing properties of intracellular Feridex in both Groups closely matched the standard curve, implying that the loss in signal is merely an effect

of the total amount of iron in each Eppendorf tube and is not influenced by the intracellular presence. During *in vivo* imaging of the cell-injected rabbit hearts, it was shown that the contrast inducing properties can be especially useful here to visualize cells in the contrast enhanced area. Of course, the observed effects depend on various factors including the composition of the incorporated iron, concentration of particles within a given imaging voxel and data acquisition parameters. Accordingly, the amount of intracellular Feridex needed for different applications may vary with the image sequence used. Further, it remains unclear whether the effects on the magnetic resonance signal are sufficient to enable visualization of circulating cells.

Although we do not describe the long-term outcome of transplantation of iron oxide-labeled cells, the *in vitro* results are encouraging and imply that this method could be employed for longer term tracking of cells. Since label retention is high even after multiple doublings *in vitro*, it is feasible to assume that the cells can be visualized after several weeks *in vivo*.

Since Feridex is an FDA approved drug and MRI is a widely available technique, this cell labeling method could be used in a clinical setting for monitoring stem cell therapy over time in a wide variety of diseases.

## Conclusions

This study shows that mammalian cells can be easily labeled with Feridex for *in vitro* and *in vivo* tracking with MRI. Utilizing liposomes is 100 fold more effective than endocytosis of Feridex and prevents negative effects on cell viability and proliferation. The feasibility of tracking cells *in vivo* is shown in a rabbit model of intracardiac autologous cell transplantation after myocardial infarction. The ability to visualize cells *in vivo* could mean a breakthrough in evaluating the effects of stem cell therapy both in animal models as well as in a clinical setting, by eliminating the need for tissue biopsies and histological assessment. Since this method involves a FDA approved drug, translation to the patient bedside is within imminent reach. In future studies we propose to evaluate long term MRI tracking of stem and progenitor cells in different models of disease.

## References

1. Kuehnle I, Goodell MA. The therapeutic potential of stem cells. *Brit Med J* 2002;325:372-6.
2. McKay R. Stem cells – hype and hope. *Nature* 2000;406:361-4.
3. Taylor DA, Sylvestry SC, Bishop SP, Annex BH, Lilly RE, Glower DD, Kraus WE. Delivery of primary autologous skeletal myoblasts into rabbit heart by coronary infusion: a potential approach to myocardial repair. *Proc Assoc Am Physicians* 1997;109:245-53.
4. Tsonis PA. Regenerative biology: the emerging field of tissue repair and restoration. *Differentiation* 2002;70:397-409.
5. Handgrettinger R, Lang P, Schumm M, Taylor G, Neu S, Koscielnak E, Niethammer D, Klingebiel T. Isolation and transplantation of autologous peripheral CD34+ progenitor cells highly purified by magnetic-activated cell sorting. *Bone Marrow Transplant* 1998;21:987-93.
6. Bulte JWM, Douglas T, Witwer B, Zhang SC, Strable E, Lewis BK, Zywicke H, Miller B, van Gelderen P, Moskowitz BM, Duncan ID, Frank JA. Magnetodendrimers allow endosomal magnetic labeling and in vivo tracking of stem cells. *Nat Biotechnol* 2001;19:1141-7.
7. Lewin M, Carlesso N, Tung CH, Tang XW, Cory D, Scadden DT, Weissleder R. Tat peptide-derivatized magnetic nanoparticles allow in vivo tracking and recovery of progenitor cells. *Nat Biotechnol* 2000;18:410-4.
8. Schoepf U, Marecos E, Melder R, Jain R, Weissleder R. Intracellular magnetic labeling of lymphocytes for in vivo trafficking studies. *BioTechniques* 1998;24:642-51.
9. Yeh TC, Zhang W, Ildstad ST, Ho C. Intracellular labeling of T-cells with superparamagnetic contrast agents. *Magn Reson Imaging* 1997;30:617-25.
10. Frank JA, Zywicke H, Jordan EK, Mitchell J, Lewis BK, Miller B, Bryant LH Jr, Bulte JW. Magnetic intracellular labeling of mammalian cells by combining (FDA-approved) superparamagnetic iron oxide MR contrast agents and commonly used transfection agents. *Acad Radiol* 2002;9:S484-7.
11. Chrichton RR. Inorganic biochemistry of iron metabolism from molecular mechanisms to clinical consequences. 2<sup>nd</sup> Edition. Wiley, Chichester, NY, 2001.
12. Chrichton RR, Wilmet S, Legssyer R, Ward RJ. Molecular and cellular mechanisms of iron homeostasis and toxicity in mammalian cells. *J Inorg Biochem* 2002;91:9-18.
13. Legssyer R, Ward RJ, Chrichton RR, Boelaert JR. Effect of chronic chloroquine administration on iron loading in the liver and reticuloendothelial system and on oxidative responses by the alveolar macrophages. *Biochem Pharmacol* 1999;57:907-11.
14. Ward RJ, Wilmet S, Legssyer R, Chrichton RR. The influence of iron homeostasis on macrophage function. *Biochem Soc Trans* 2002;30:762-5.

15. Qian SY, Buettner GR. Iron and dioxygen chemistry is an important route to initiation of biological free radical oxidations: an electron paramagnetic resonance spin trapping study. *Free Radic Biol Med* 1999;26:1447-56.
16. Wardman P, Candeias LP. Fenton chemistry: an introduction. *Radiat Res* 1996;145:523-31.
17. Wang YXJ, Hussain SM, Krestin GP. Superparamagnetic iron oxide contrast agents: physiochemical characteristics and applications in MR imaging. *Eur Radiol* 2001;11:2319-31.
18. Weissleder R, Stark DD, Engelstad BL, Bacon BR, Compton CC, White DL, Jacobs P, Lewis J. Superparamagnetic iron oxide: pharmacokinetics and toxicity. *Am J Roentgenol* 1989;152:167-73.
19. Taylor DA, Atkins BZ, Hungspreugs P, Jones TR, Reedy MC, Hutcheson KA, Glower DD, Kraus WE. Regenerating functional myocardium: Improved performance after skeletal myoblast transplantation. *Nat Med* 1998;4:929-33.
20. Pap EHW, Drummen GPC, Winter VJ, Kooij TWA, Rijken P, Wirtz KWA, Op den Kamp JAF, Hage WJ, Post JA. Ratio-fluorescence microscopy of lipid oxidation in living cells using C11-Bodipy<sup>581/591</sup>. *FEBS Letters* 1999;453:278-82.
21. Reimer P, Tombach B. Hepatic MRI with SPIO: detection and characterization of focal liver lesions. *Eur Radiol* 1998;8:1198-1204.
22. Lucas KL, Baynes JW, Thorpe SR. Intracellular processing of residualizing labels in different cell types in vitro. *J Cell Physiol* 1990;142:581-5.
23. Sorokin LM, Morgan EH, Yeoh GC. Transferrin endocytosis and iron uptake in developing myogenic cells in culture: effects of microtubular and metabolic inhibitors, sulphhydryl reagents and lysosomotropic agents. *J Cell Physiol* 1988;137:483-9.
24. Li C, Jackson RM. Reactive species mechanisms of cellular hypoxia-reoxygenation injury. *Am J Physiol Cell Physiol* 2002;282:C227-41.



# Chapter 8

## High resolution magnetic resonance imaging of iron-labeled myoblasts using a standard 1.5T clinical scanner



## Abstract

**Objectives-** Myoblast transplantation is a promising method for restoring cardiac function in infarcted areas. For optimization of transplantation protocols, tracking the location and fate of the injected cells is necessary. An attractive imaging modality for this is magnetic resonance imaging (MRI): It is non-invasive and iron-labeled myoblasts provide a signal attenuation in T2\* weighted protocols. The aim of this study was to develop an efficient iron-labeling protocol for myoblasts and to visualize single labeled cells using a clinical 1.5T scanner.

**Materials and methods-** Pig primary myoblasts were labeled with a superparamagnetic iron oxide (SPIO) agent using a liposome transfection reagent. Labeling efficiency, toxicity, cell viability, and proliferative capacity were measured during 10 days. MR of myoblast cultures used a T2\* weighted three-dimensional protocol with a maximum in-plane resolution of  $19.5 \times 26.0 \mu\text{m}^2$  and 50  $\mu\text{m}$  slices.

**Results-** Use of liposomes improved SPIO labeling efficiency. Labeling did not induce toxicity or affect cell viability or proliferation. The cell distribution as observed with light and fluorescence microscopy matched the signal voids observed in the MRI datasets.

**Conclusion-** Liposomes promote fast, non-toxic and efficient SPIO-labeling of myoblasts that can be tracked by MRI microscopy in clinical scanners using susceptibility-weighted protocols.

## Introduction

Over the past decade, transplantation of stem or progenitor cells has been proposed as a revolutionary new technique for the treatment of malfunctioning endogenous cell populations.<sup>1</sup> The introduction of myoblasts to replace damaged or dysfunctional myocardium to restore cardiac performance is of great interest. Intracardiac transplantation of myoblasts has been previously shown to improve function in a variety of animal models and in patients.<sup>2-4</sup> However, non-invasive monitoring of the distribution of myoblasts in tissue is required to enhance our understanding of how cell therapy improves cardiac function.

MR imaging offers both near-cellular (15-50  $\mu\text{m}$ ) resolutions and whole-body imaging capabilities. To distinguish the introduced myoblasts from the surrounding myocardium, myoblasts must be labeled with an intracellular probe with high contrast inducing properties that makes it possible to depict and monitor them by MR imaging. Recent advances in tracer technology now facilitate labeling of myoblasts intracellularly with FDA approved iron-based MRI contrast agents.<sup>5</sup> One of these contrast agents, Endorem (Guerbet SA, Paris, France), a superparamagnetic iron oxide (SPIO) agent has iron oxide crystals ( $\text{Fe}_2\text{O}_3$  and  $\text{Fe}_3\text{O}_4$ ) with a low molecular weight dextran coating (mean particle diameter of 150 nm, iron oxide core of 4 nm). Efficient labeling has been achieved using transfection reagents to increase the uptake of SPIOs without affecting cell function and division.<sup>5,6</sup>

The aim of the present study was to validate a method of SPIO labeling of myoblasts using Lipofectamine 2000 (Gibco, Breda, the Netherlands) and to perform *in vitro* experiments to assess whether single cell visualization is possible with a standard clinical MRI scanner.

## Methods

### Isolation and culture of pig skeletal myoblasts

All animal experiments were performed in accordance with the National Institutes of Health Guide for the Care and Use of Laboratory Animals (NIH Pub. No. 86-23, Revised 1996) and the approval of the local animal ethics committee.

Skeletal myoblasts were isolated from an excisional muscle biopsy from pigs as previously described.<sup>6</sup> A biopsy from the semitendinosus muscle was excised under pentobarbital anesthesia.<sup>7</sup> The tendon and the aponeurotic tissue were carefully removed from the muscle. Approximately 5 g of tissue was minced with scissors to 1 mm<sup>3</sup> pieces and incubated for 3 days in Dulbecco's Modified Eagle's Medium (DMEM) containing 10% fetal bovine serum (FBS) and 0.5% gentamicin (10 mg/ml; all from Gibco, Breda, the Netherlands). After 3 days the tissue was triturated through a 10 ml pipette for 3 minutes. Once cells began growing out of the tissue blocks, the medium was replaced with medium containing 20% horse serum (HS). Cells were passaged twice and grown to 90% confluence before starting the experiments.

## Cell labeling

To facilitate SPIO uptake by myoblasts, SPIOs were ligated with liposomes. The SPIO-liposome complexes were made as described before:<sup>6</sup> 30  $\mu$ l of Lipofectamine 2000 (Gibco, Breda, the Netherlands) was diluted in 0.5 ml of Opti-MEM reduced serum medium in a tube. SPIOs (Endorem) were diluted to yield a suspension of 100  $\mu$ g total iron in 0.5 ml of Opti-MEM in another tube. After 5 minutes, the two suspensions were mixed by pipetting and incubated at room temperature for 20 minutes. The resulting suspension was added drop wise to standard culture dishes containing  $1 \times 10^6$  myoblasts in 10 ml of Opti-MEM and incubated at 37°C and 5% CO<sub>2</sub> for 23 hours. The cells were labeled with DAPI (4',6-diamidino-2-phenylindole dihydrochloride), a fluorescent probe that forms complexes with DNA, and fixed in 10% buffered formalin for 1 hour. Cells were then washed 3 times with phosphate buffered saline (PBS) and prepared for MRI scanning.

## Labeling efficiency

### *Prussian blue staining*

Cells that had been labeled with SPIO with and without the addition of Lipofectamine 2000 were washed and fixed with 10% paraformaldehyde 24 hours after addition of SPIO. After 10 minutes of fixation, the samples were washed again and stained for 20 minutes with a freshly-prepared solution containing 0.12 M K<sub>4</sub>Fe(CN)<sub>6</sub> and 1 M HCl. Finally, the samples were washed, mounted, and examined by light microscopy (Olympus Optical Company Ltd, Tokyo, Japan). The number of blue labeled cells was counted and expressed as a percentage of total cells. At least 500 cells were counted in each sample in multiple fields.

### *Magnetic Activated Cell Sorting (MACS) analysis*

After labeling cells were trypsinized and resuspended in degassed PBS with 0.5% BSA. The cells were then run through a MINI MACS cell separator column (Miltenyi Biotec GmbH, Bergisch Gladbach, Germany). The number of cells was counted before and after separation. The number of magnetic, iron-labeled cells attaching to the column was then calculated and expressed as a percentage of the total number of unseparated cells.

### *Electron microscopy*

Myoblasts ( $3 \times 10^6$ ) labeled with SPIO and DAPI were fixed with 1.25% glutaraldehyde in 0.1 M phosphate buffer at 4°C for 10 hours. The cells were post-fixed in 1% osmium tetroxide; dehydrated in a graded alcohol series, and embedded in Epoxyresin. Ultra thin sections were obtained and stained with uranyl acetate and lead citrate and examined with a FEI Morgagni transmission electron microscope (Philips, Eindhoven, the Netherlands).

## Toxicity, viability and proliferation assays

JC-1 was used to quantify toxicity and viability. JC-1 is a fluorescent molecular probe (5,5',6,6'-tetrachloro-1,1',3,3'-tetraethylbenzimidazolylcarbocyanine iodide) that preferentially

accumulates in the polarized membranes of healthy mitochondria. In the mitochondrial membrane, the probe molecules aggregate, fluorescing red. Early in apoptosis, the mitochondrial membrane depolarizes. In these cells, the JC-1 diffuses out of the mitochondrial membrane and converts to its monomeric form, fluorescing green. The red-green shift is a good measure of toxicity and cell viability.

SPIO-labeled cells were cultured in DMEM containing 10% FBS. Unlabeled cells were used as control. After 0, 1, 3, 5, or after 10 days and one passage, the samples were labeled after trypsinization with 10 µg/ml JC-1 (Gibco-Invitrogen, Breda, the Netherlands) in PBS for 15 minutes at 37°C. The cells were then washed with PBS and immediately inspected by fluorescence microscopy. Cells only fluorescing green (dead cells) were counted and expressed as a percentage of total number of counted cells. For comparison each sample was also analyzed by Trypan Blue staining using a standard protocol. Cell viability was calculated as 100% minus percentage dead cells. The day 0 sample (immediately after labeling) was also analyzed by Fluorescence Activated Cell Sorting (FACS) scanning (FacsCan; Becton Dickinson, Franklin Lakes, NJ) to calculate mitochondrial polarization as a measure of iron toxicity. JC-1 was excited at 488 nm and the monomeric signal (green) was analyzed at 525 nm (FL1). Simultaneously, the aggregate signal (red) was analyzed at 590 nm (FL2). Mitochondrial depolarization was expressed as the percentage cells in quadrant 4 as a percentage of total number of cells.

For proliferation data  $5 \times 10^3$  cells from each sample were plated on standard culture dishes and counted in triplicate at days 1, 3, 5 and 10 after labeling using a hemacytometer.

### **Sample preparation for fluorescence microscopy and MRI**

Labeled myoblasts were collected by trypsinization, washed and fixed. They were diluted to the desired concentration in 0.5% Gd-DTPA/3% gelatin in PBS to provide better signal-to-noise (SNR) and contrast-to-noise (CNR) ratios for the MRI scanning protocol. Ten µl of each cell suspension was added to a 1 cm diameter plastic tissue culture insert. The total number of labeled cells per insert was 100, 225, 550, 820 or 1100. The samples were then inspected with normal light and fluorescence microscopy (Olympus Optical Company Ltd, Tokyo, Japan). After microscopy, an additional 0.4 ml of the gelatin/Gd-DTPA preparation was added to cover the cells prior to the MRI examination. Samples of unlabeled cells were prepared in the same fashion and used as controls.

### **Cellular MRI**

High-resolution MR imaging was performed using a GE 1.5T Signa CVi MRI (General Electric Medical Systems, Milwaukee, WI). The conventional imaging gradient set of 40 mT/m and 235 msec rise time (SR170) and a body transmitter coil was used. The imaging protocol used a 3D SPGR sequence with TR=108.00 ms, TE=15.36 ms, flip angle=60°, FOV=1x1 cm<sup>2</sup>, matrix=512x384, NEX=8.0 and scan time=3 hours. Slice thickness was varied between

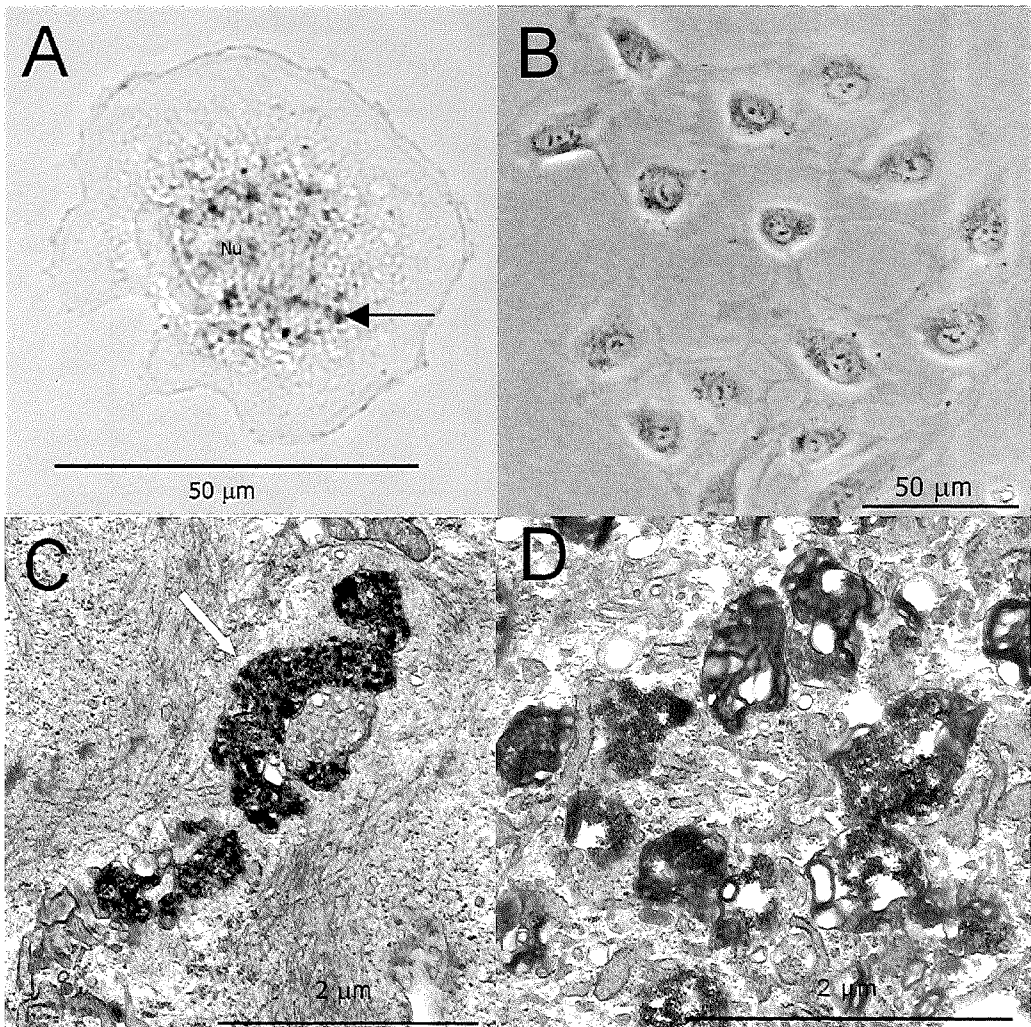


Figure 1. Optical microscope view of pig myoblasts stained with Prussian blue to demonstrate the uptake of SPIO particles (Panel A and B). SPIO particles are visible as dark iron deposits (arrow) around the nucleus (Nu) in Panel A. No intranuclear or extracellular uptake of SPIOs could be detected. Panel C and D show electron microscopy images (14000X and 20000X, respectively) with a conglomeration of SPIOs within membrane-bound vacuoles (arrow). The particle size of a single SPIO is 150 nm with an iron oxide core of 4 nm. The size of the organelle here, on the order of 2 μm, therefore demonstrates a high particle density.

200 μm and 50 μm, maintaining the same number of 32 scanned sections. Zero filling was used to reconstruct double the number of sections and a square matrix. Scanned in-plane resolution was 19.5x26.0 μm<sup>2</sup> (interpolated resolution of 19.5x19.5 μm<sup>2</sup> by zero-filling). A fractional echo was selected to provide a reasonable short TE at the target resolution using a low readout bandwidth of 7.81 KHz. A single loop solenoid coil containing the sample fully (inner diameter 1.5 cm) was used for signal reception. Scanning was performed in the

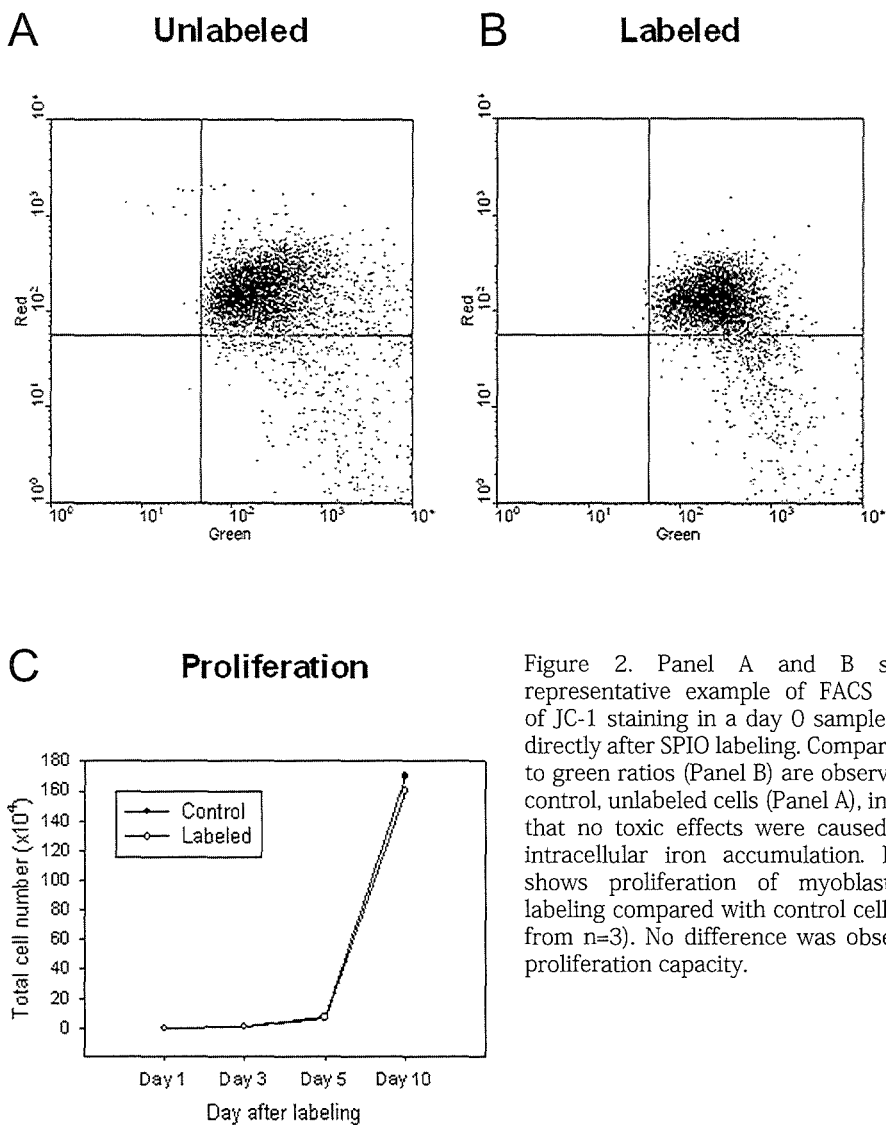


Figure 2. Panel A and B show a representative example of FACS analysis of JC-1 staining in a day 0 sample of cells directly after SPIO labeling. Comparable red to green ratios (Panel B) are observed as in control, unlabeled cells (Panel A), indicating that no toxic effects were caused by the intracellular iron accumulation. Panel C shows proliferation of myoblasts after labeling compared with control cells (mean from n=3). No difference was observed in proliferation capacity.

coronal plane with the frequency encoding gradient along the B<sub>0</sub> field. One sample was scanned per session. The T<sub>1</sub> relaxation time of the gelatin/Gd-DTPA doped preparation was measured using an inversion recovery echo planar imaging (EPI) sequence.

## Results

### Labeling efficiency

Prussian blue staining confirmed iron uptake. Figure 1 illustrates a Prussian blue-stained preparation. Most iron complexes surround the cell nucleus. No intranuclear or extracellular staining could be detected. Myoblasts combined with SPIO in medium

without the addition of Lipofectamine failed to show consistent labeling in all cells. MACS separation showed  $70 \pm 8\%$  ( $n=3$ ) labeling efficiency after labeling without Lipofectamine versus 100% labeling in the Lipofectamine labeled samples ( $n=3$ ). This was confirmed by Prussian Blue staining: 100% blue labeled cells were counted in the Lipofectamine labeled samples versus  $60 \pm 5\%$  without Lipofectamine ( $n=3$  in both groups).

### Electron microscopy

Electron microscopy showed intracellular SPIO particles, with encasement of the particles within membrane-bound vacuoles (Figure 1C and D).

### Toxicity, viability and proliferation

The percentage of viable cells as determined by Trypan Blue staining was more than 96.5% at any time point measured (1, 3, 5, 10 days;  $n=3$ ) and did not differ between the cultures with control myoblasts and those with SPIO-labeled myoblasts. FACS scanning showed comparable membrane depolarization of  $11.8 \pm 3.1\%$  in unlabeled samples and  $13.9 \pm 0.9\%$  in labeled samples ( $n=3$ ;  $P=0.56$ ; Figure 2A and B). This indicates that in viable cells no toxic effect by the presence of intracellular iron on mitochondrial function could be observed. SPIO-labeled myoblasts grew as efficiently as myoblasts that were not labeled. The doubling time of the myoblasts was around 21 hours as calculated from the growth curve. After 10 days total cell numbers were  $160 \pm 2.0 \times 10^4$  in the labeled group versus  $170 \pm 3.0 \times 10^4$  in the control group (Figure 2C).

### MRI scanning and microscopy

The T1 relaxation time of the Gd-DTPA doped gelatin was  $60 \pm 5$  ms using a simple exponential fit to an inversion recovery curve. Doping the gel with Gd-DTPA provided better SNR and CNR for cell delineation using the 3D T1-weighted protocol (owing to the shorter T1 relaxation time around the cells) as compared to a pilot protocol using lower flip angles with the undoped gel (T1 relaxation time of gel similar to that of water). The addition of Gd-DTPA provided sufficient SNR to enable high resolution scans to be collected with resolution approaching single cell dimensions and a reasonably short imaging time at 1.5 Tesla for such resolution (3 hours). An example is illustrated in Figure 3 demonstrating one slice from the corresponding 3D data set collected from the sample dish with 225 labeled myoblasts. We believe that a voxel resolution of  $19.5 \times 19.5 \times 100.0 \mu\text{m}^3$  proved sufficient to separately see single cells in this sample preparation. Cell visualization was more difficult with the larger number of cells given that the signal void from a labeled cell could extend over several slices. Border enhancements were appreciated around the signal void, similar to those apparent with large magnetic susceptibility interfaces such as with ferromagnetic materials and air bubbles (Figure 3). In pilot experiments, the choice of a full echo acquisition (symmetric k-space sample about the echo) extended TE, resulting in T2\* attenuation in the gel (TE~25 ms) and defining a larger signal void, however at the expense of a longer TR combination

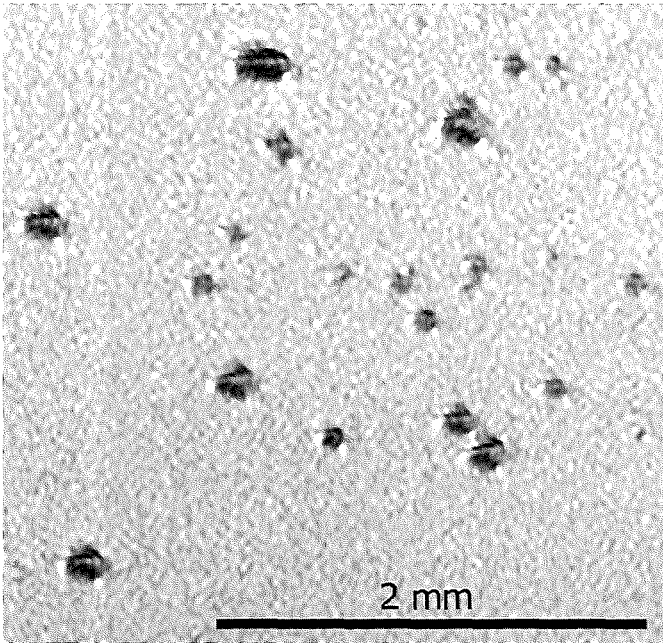


Figure 3. Slice obtained from the 3D SPGR acquisition of the SPIO-labeled cell suspension with 225 cells ( $0.0225 \times 10^3/\mu\text{l}$  concentration). Cells appear as black signal voids. Signal enhancement around the cells can also be observed from the magnetic susceptibility gradients induced. Imaging parameters: TR=108.00 ms, TE=15.36 ms (partial echo), flip angle=60°, FOV=1.0x1.0 cm<sup>2</sup>, matrix=512x384, NEX=8.0 and scan time=3 hours. Scanned resolution=19.5x19.5x100.0  $\mu\text{m}^3$ . Reconstructed resolution=19.5x19.5x100.0  $\mu\text{m}^3$ .

and scan time (data not shown).

Comparison of the sample with 100 labeled cells with fluorescence and normal light microscopy showed exact correlations, as shown in Figure 4. Even after a 8 minutes low resolution localizer scan a pattern of signal voids could be detected matching cell groups of 2 cells as photographed by light microscopy (Figure 4A and B). Higher resolution scans showed single cells matching cell distribution patterns as detected by both normal light and fluorescence microscopy (Figure 4C to E).

Figure 5 shows four slices of the 3D acquisition with the highest resolution achieved of  $19.5 \times 26.0 \times 50.0 \mu\text{m}^3$  in the sample with 820 cells. Unlabeled cells could not be detected in any of the control samples used. Figure 6 illustrates the extent of the signal void along the slice direction using a 0.5 mm thick perpendicular minimum intensity projection (mIP) reformation on the suspension of 550 cells with a scanned resolution of  $19.5 \times 26.0 \times 100.0 \mu\text{m}^3$  voxels. The 10  $\mu\text{l}$  cell suspension placed in each of the inserts investigated was estimated from the 3D reformats using mIP. The volumes obtained were similar to the 10  $\mu\text{l}$  volume delivered per insert ( $11.0 \pm 2.1 \mu\text{l}$ ). The extent of the cell preparation was approximately 1.2 mm.

## Discussion

In our present study, we were able to visualize SPIO-labeled myoblasts using a high resolution protocol on a clinical 1.5T MRI scanner with a standard gradient imaging set. Endorem, the agent used for delivering the SPIO, was effective for delineating the cells as demonstrated in the figures presented. Endorem, developed under license from Advanced Magnetics Inc,

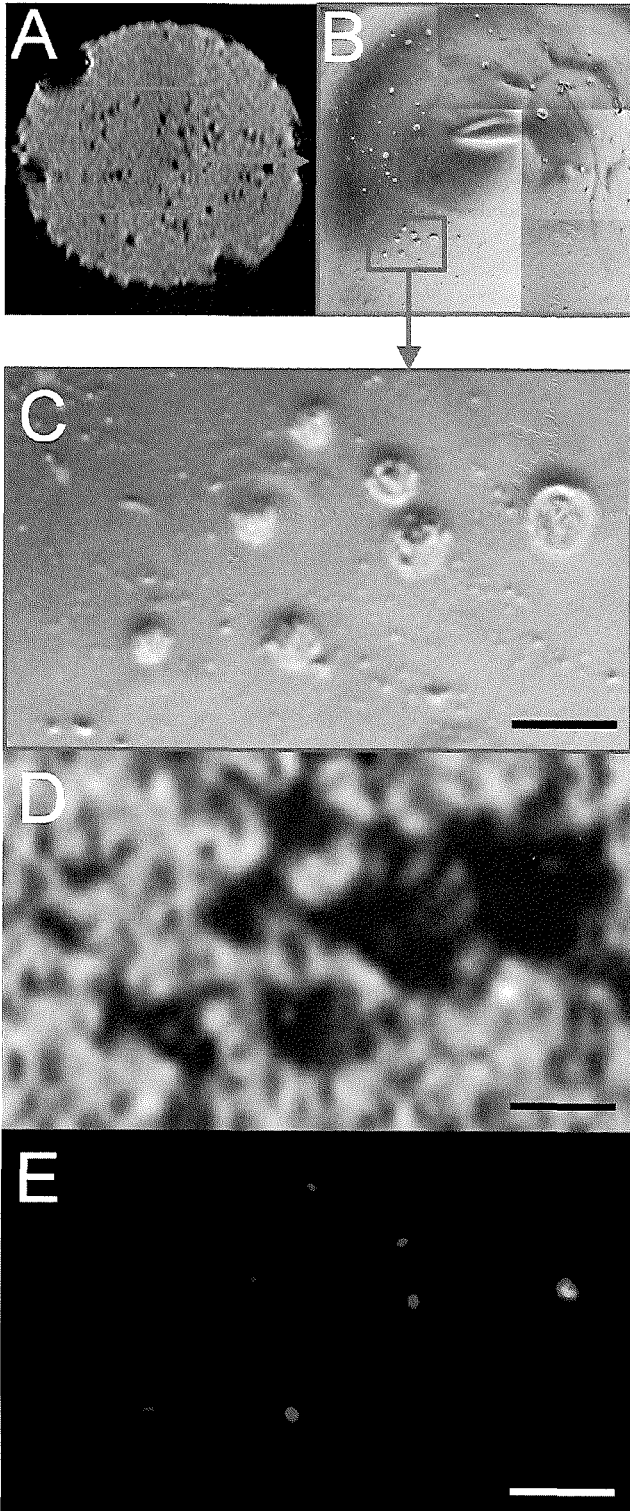


Figure 4. Comparison between MR images and microscopy. Panel A shows a slice from a scout image obtained in 8 minutes scan time. Signal voids correspond to clusters of cells as shown in the corresponding normal light microscopy field (Panel B). Panel C shows a group of 7 cells at higher magnification. The corresponding slice from the high resolution scan is shown in Panel D. The signal voids correspond exactly with the location of single cells. Fluorescence microscopy in Panel E shows DAPI nuclear staining of the same field. Imaging parameters: Panel A: TR=60.9 ms, TE=6.3 ms, flip angle=60°, thickness=100 μm, FOV=1.0x1.0 cm<sup>2</sup>, matrix=256x128, NEX=1.0, scan time=8 minutes. Panel D: TR=101 ms, TE=13.8 ms, flip angle=60°, thickness=100 μm, FOV=1.0x1.0 cm<sup>2</sup>, matrix 448x320, NEX=8, scan time=3 hours. Scanned resolution=19.5x26.0x100.0 μm<sup>3</sup>. Reconstructed resolution=19.5x19.5x50.0 μm<sup>3</sup>. Bar represents 100 μm.

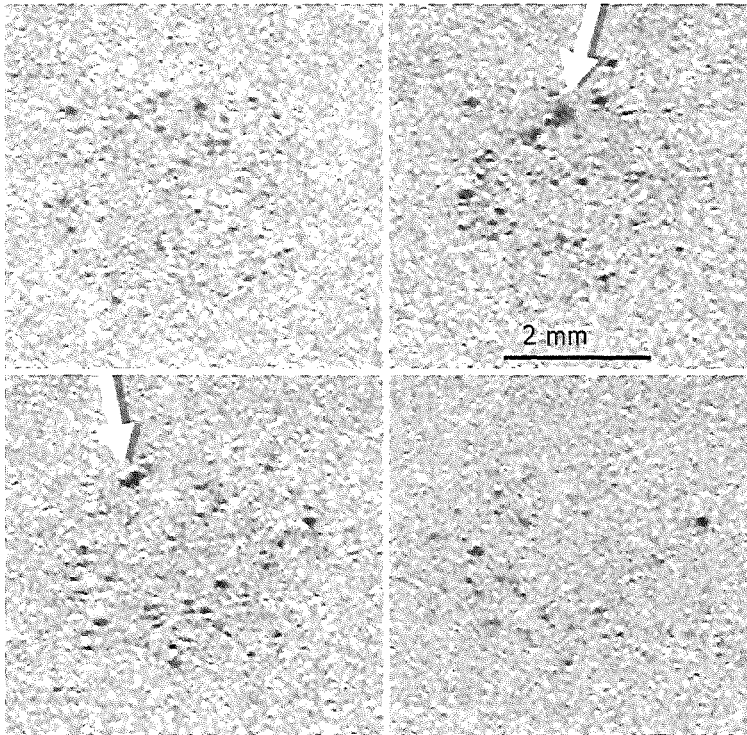


Figure 5. Four slices from the 3D SPGR acquisition on the cell suspension with 820 cells ( $0.082 \times 10^3$  cells/ $\mu\text{l}$ ). The gap between the slices shown is 100  $\mu\text{m}$ . Cell conglomerations can be appreciated from the larger artefacts present (arrows). Imaging parameters: TR= 108.00 ms, TE= 5.36 ms (partial echo), flip angle=60°, thickness=0.05 mm, FOV=1.0×1.0 cm<sup>2</sup>, matrix=512×384, NEX=8.0, scan time=3 hours. Scanned resolution =19.5×26.0×50.0  $\mu\text{m}^3$ .

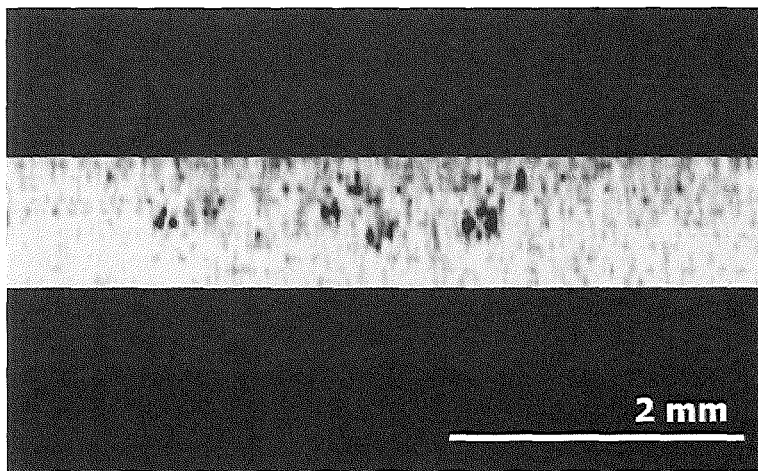


Figure 6. Minimum intensity projection (mIP) of the SPIO-labeled cell suspension with 550 cells ( $0.055 \times 10^3$  cells/ $\mu\text{l}$ ). The thickness of the projection was 0.5 mm. Signal voids larger than 100  $\mu\text{m}$ s can be appreciated. Larger voids can originate from cell conglomerates and from overprojections during the mIP process. Imaging parameters: TR=108.00 ms, TE=15.36 ms (partial echo), flip angle=60°, thickness=100  $\mu\text{m}$  interpolated to 50  $\mu\text{m}$  slices, FOV=1.0×1.0 cm<sup>2</sup>, matrix=512×384, NEX=8.0, scan time=3 hours. Scanned resolution=19.5×26.0×100.0  $\mu\text{m}^3$ . Reconstructed resolution=19.5×19.5×50.0  $\mu\text{m}^3$ .

USA, has also been used in other investigations under names such as Feridex® (Berlex Laboratories Inc, NJ). The biocompatibility of Endorem is ensured by a low molecular weight dextran coating around the iron core that stabilizes the particulate. The use of this agent and others has been previously reported in other cell lines and has proven to be non-toxic both *in vitro* and *in vivo*.<sup>5,6</sup>

SPIO uptake improves dramatically with the use of “liposomes”. The liposomes employed are sold as cationic lipid-based transfection reagents designed specifically to provide extremely high transfection efficiencies using mammalian cells. Our results show that Lipofectamine improved the labeling efficiency up to 100% in porcine myoblast preparations as compared to  $70 \pm 8\%$  without Lipofectamine, which is comparable to values reported in the literature.<sup>5,6</sup>

The combination of gelatin and Gd-DTPA provided an effective means to increase our SNR and CNR with shorter scan times for the detection of cells at the target resolution. Enhancement of cell detection *in vivo* could be envisioned in a similar fashion, although we do not expect the same CNR enhancement levels as observed for *in vitro* imaging. For SPIO-labeled myoblasts injected into the myocardium, detection can be attempted after the myocardium or damaged region has been adequately enhanced with contrast agents, e.g. Manganese-DPDP or Gd-DTPA. We also do not anticipate toxicity of Gd-DTPA at 1:200 dilutions. This concentration is well within typical values used in day-to-day clinical practice.

Depending on magnetic field strength and echo times employed, SPIO or iron particles can produce signal voids that may extend over several times the mean diameter of the SPIO iron core, even as much as 50 times the particle diameter. The core of the iron oxide crystals of Endorem ( $\text{Fe}_2\text{O}_3$  and  $\text{Fe}_3\text{O}_4$ ) has a mean diameter of only 4 nm.<sup>8</sup> Provided that the accumulation of SPIOs in vacuoles can induce vacuole sizes as large as 2  $\mu\text{m}$  (Figure 2), artefacts/signal voids in the image may extend beyond 100  $\mu\text{m}$ , which approaches the slice thickness typically used in the imaging experiments. In our experiments cell signal voids could be measured of about up to 4 times the cell size. The small deviation in the volume size recorded using mIP as compared to the volume of the labeled cells could therefore be accounted for by the size of the signal void extending beyond the cell diameter towards other slices.

We would like to stress that the detection of low numbers of labeled cells within a target tissue by MRI requires high spatial resolution. Slices thicker than 200  $\mu\text{m}$  and an in-plane resolution of  $80 \times 80 \mu\text{m}^2$  (as used in our pilot 3D scans) demonstrated substantial partial volume effects in the samples: Artefacts from cells could be detected but individual cells could not be clearly delineated. The ability to reconstruct thicker slices using multiplanar reformats from the highest resolution data sets collected ( $19.5 \times 26.0 \times 50.0 \mu\text{m}^3$ ; Figure 5) provided the same fading effect. Minimum intensity projections (mIP), as exemplified in Figure 6, present an easy alternative to demonstrate SPIO-labeled cells within a particular volume. Using mIP, the rays traced along the viewing angle only report the signal from

the least intense tissues which, in our case, are the labeled myoblasts. Depending on the thickness of the projection used, the artefacts created by the cells may be much larger than those originally created and could ease detection. We may expect a similar behavior when imaging *in vivo* at high resolution.

A necessary condition for MR detection of individual labeled cells in samples of uniformly distributed labeled cells is that the spatial resolution is high enough that the number of image voxels per unit volume is greater than the number of labeled cells per unit volume.<sup>9</sup> Resolutions that could be achieved using a standard clinical scanner matched the expected parameters for good detection sensitivity ( $19.5 \times 26.0 \times 50.0 \mu\text{m}^3$ ). Comparison of MR with microscopy of the same sample provided a matching pattern between signal voids in MRI and fluorescence and normal light microscopy. In comparison with Foster et al.,<sup>10</sup> who used a small, high gradient insert coil; our resolution of  $19.5 \times 26.0 \times 50.0 \mu\text{m}^3$  in our best resolved data was much higher than the resolution of  $100.0 \times 100.0 \times 100.0 \mu\text{m}^3$  in that study but was achieved at the expense of imaging time and longer TR/TE. Furthermore, in their study, Foster et al. used a Steady State Free Precession (SSFP, trueFISP) sequence. The ultrahigh gradient amplitudes possible in their gradient coil set to achieve bright signal for the gel in which cells were imaged. In contrast, we doped the gel containing the cells with Gd-DTPA in order to achieve high signal levels with our standard imaging gradient set. Unfortunately, SSFP for tracking cells *in vivo* is difficult because the MR pulse sequence requires very short TRs to achieve signal uniformity within the FOV and consequently, resolution will be limited to what will be possible by the clinical imaging gradient set.

In contrast to SPIO labeling of cells, more recently labeling techniques have been described using other MR contrast agents, such as in the study by Crich et al.<sup>11</sup> who used Gd-chelates for tracking cells both *in vitro* and *in vivo*. We used SPIO labeling for 2 reasons. First, the study by Crich et al. shows that the minimum number of cells that can be visualized *in vitro* using Gd-chelates is in the order of  $10^3$ . Since our aim was to study the possibility of single cell tracking, Gd-chelates were not a likely candidate. Secondly, our specific interest in myoblast tracking relates to infarct repair by myoblast transplantation. In studies of intracardiac cell transplantation, contrast enhanced imaging using Gadolinium is used to delineate the infarct area. For cell tracking this would be an ideal background to image cells labeled with T2-agents producing black signal voids. A disadvantage of using SPIO versus Gd-chelates could be the toxicity caused by high intracellular concentrations of iron. However, both in this study as well as in our previous work<sup>6</sup> no toxic effects could be observed *in vitro*. Nonetheless, in future studies the effect of high iron concentrations after injection *in vivo* should be studied, especially after death of the transplanted cells and release of the intracellular iron stores in the target organ, in order to exclude toxic effects or overestimation of the number of transplanted cells residing at a certain location.

A number of other cell types, including neural cells, lymphocytes and tumor cells, have been labeled with SPIOs and imaged by MR by others.<sup>12-15</sup> In this study, our aim was to demonstrate the possibility of high spatial resolution MRI for single cell detection *in vitro*

with SPIOs using an efficient myoblast labeling procedure. Without any doubt, the detection *in vivo* will be several fold more challenging as compared to our *in vitro* experiments because of cardiac and respiratory movement and an imaging region with large susceptibility changes such as tissue-air interfaces. However, the present study is a step towards *in vivo* tracking of cellular cardiomyoplasty after ischemic injury.

## References

1. McKay R. Stem cells - hype and hope. *Nature* 2000;406:361-4.
2. Smits PC, van Geuns RJ, Poldermans D, Bountiukos M, Onderwater EE, Lee CH, Maat AP, Serruys PW. Catheter-based intramyocardial injection of autologous skeletal myoblasts as a primary treatment of ischemic heart failure: clinical experience with six-month follow-up. *J Am Coll Cardiol* 2003;42:2063-9.
3. Hassink RJ, Brutel de la Riviere A, Mummery CL, Doevendans PA. Transplantation of cells for cardiac repair. *J Am Coll Cardiol* 2003;41:711-7.
4. van den Bos EJ, Thompson RB, Wagner A, Mahrholdt H, Morimoto Y, Thomson LEJ, Wang LH, Duncker DJ, Judd RM, Taylor DA. Functional assessment of myoblast transplantation for cardiac repair with magnetic resonance imaging. *Eur J Heart Failure* 2005;7:435-43.
5. Frank JA, Zywicke H, Jordan EK, Mitchell J, Lewis BK, Miller B, Bryant LH Jr, Bulte JW. Magnetic intracellular labeling of mammalian cells by combining (FDA-approved) superparamagnetic iron oxide MR contrast agents and commonly used transfection agents. *Acad Radiol* 2002;9:S484-7.
6. van den Bos EJ, Wagner A, Mahrholdt H, Thompson RB, Morimoto Y, Sutton BS, Judd RM, Taylor DA. Improved efficacy of stem cell labeling for magnetic resonance imaging studies by the use of cationic liposomes. *Cell Transplant* 2003;12:743-56.
7. Lameris TW, de Zeeuw S, Duncker DJ, Tietge W, Alberts G, Boomsma F, Verdouw PD, van den Meiracker AH. Epinephrine in the heart: uptake and release, but no facilitation of norepinephrine release. *Circulation* 2002;106:860-5.
8. Wang YX, Hussain SM, Krestin GP. Superparamagnetic iron oxide contrast agents: physicochemical characteristics and applications in MR imaging. *Eur Radiol* 2001;11:2319-31.
9. Dodd SJ, Williams M, Suhan JP, Williams DS, Koretsky AP, Ho C. Detection of single mammalian cells by high-resolution magnetic resonance imaging. *Biophys J* 1999;76:103-9.
10. Foster-Gareau P, Heyn C, Alejski A, Rutt BK. Imaging single mammalian cells with a 1.5 T clinical MRI scanner. *Magn Reson Med* 2003;49:968-71.
11. Crich SG, Biancone L, Cantaluppi V, Duo D, Esposito G, Russo S, Camussi G, Aime S. Improved route for the visualization of stem cells labeled with a Gd-/Eu-chelate as dual (MRI and fluorescence) agent. *Magn Reson Med* 2004;51:938-44.
12. Fleige G, Seeberger F, Laux D, Kresse M, Taupitz M. In vitro characterization of two different ultrasmall iron oxide particles for magnetic resonance cell tracking. *Invest Radiol* 2002;37:482-8.
13. Bulte JW, Zhang S, van Gelderen P, Herynek V, Jordan EK, Duncan ID, Frank JA. Neurotransplantation of magnetically labeled oligodendrocyte progenitors: magnetic resonance tracking of cell migration and myelination. *Proc Natl Acad Sci*

USA 2004;96:15256-61.

14. Yeh T, Zhang W, Ilstad S, Ho C. Intracellular labeling of T-cells with Superparamagnetic contrast agents. *Magn Reson Med* 1993;30:617-25.
15. Moore A, Grimm J, Han B, Santamaria P. Tracking the recruitment of diabetogenic CD8+ T-cells to the pancreas in real time. *Diabetes* 2004;53:1459-66.



## Chapter 9

*In vitro* imaging of single living human umbilical vein endothelial cells with a clinical 3.0T MRI scanner

Zhang Z, van den Bos EJ, Wielopolski PA, de Jong-Popijus M, Bernsen MR, Duncker DJ, Krestin GP. *MAGMA* 2005;18:175-85.



## Abstract

**Objective-** To image single, living, iron oxide-labeled human umbilical vein endothelial cells (HUVECs) over time *in vitro* using magnetic resonance (MR) microscopy.

**Material and methods-** Iron oxide-labeled, single, living HUVECs were imaged *in vitro* using a clinical 3.0T MR system. Labeling efficiency, toxicity, cell viability, proliferation and differentiation were assessed using flow cytometry, magnetic cell sorting and a phenanthroline assay. MR images were compared with normal light and fluorescence microscopy.

**Results-** Efficient uptake of iron oxide into HUVECs was shown, although with higher label uptake dose-dependent cytotoxic effects were observed affecting cell viability. For MR imaging, a T2\* weighted three-dimensional protocol was used with in-plane resolution of 39x48  $\mu\text{m}^2$  and 100  $\mu\text{m}$  slices with a scan time of 13 minutes. MRI could detect living cells in standard culture dishes at single cell resolution, although label loss was observed that corresponded with the intracellular iron measurements.

**Conclusion-** MR microscopy using iron oxide labels is a promising tool for studying HUVEC migration and cell biology *in vitro* and *in vivo*, but possible toxic effects of label uptake and loss of label over time should be taken into account.

## Introduction

Present approaches to angiogenic therapy contemplate the transplantation of endothelial cells (ECs) and endothelial precursor cells (EPCs) as an alternative to gene or protein therapy.<sup>1,2</sup> The introduction of therapeutic cells in patients, however, requires non-invasive monitoring of transplanted cells to follow their biodistribution and biological function.<sup>3-6</sup> The importance of angiogenesis and the possible role of cell therapy in cardiovascular disease raises the question whether magnetic resonance microscopy (MRM) can aid in the design of non-invasive clinical methods to monitor responses to endothelial cell therapy.

In order for transplanted cells to be detected with MRI, the cells must be labeled with intracellular probes. One of the probes that has been described for efficient cell labeling is superparamagnetic iron oxide (SPIO).<sup>7</sup> Cells of interest are isolated and labeled *in vitro* before their transplantation *in vivo*. It is then possible to detect their migration, homing, bio-distribution and recruitment by MRI as a result of the signal void caused by intra-voxel dephasing due to the presence of intracellular iron.

*In vitro* studies have shown the possibility of imaging single cells at high resolution<sup>8-14</sup> and *in vivo* studies have shown the feasibility of detecting large groups of transplanted cells over time.<sup>15-20</sup> However, to understand the *in vivo* behaviour of transplanted cells, it is necessary to study living cells *in vitro* over longer time periods.

In view of the considerations above, the aims of the present study were to: (1) assess the efficacy by which human umbilical vein endothelial cells (HUVECs) can be labeled using a previously described labeling technique that combines a transfection reagent and a clinically used and FDA-approved contrast agent<sup>21-25</sup> and (2) to image single, living HUVECs over time in a clinical 3.0 Tesla (T) MRI system and correlate the obtained MR images with light and fluorescence microscopy at corresponding time points.

## Methods

### Cell culture and SPIO labeling

Early passage, primary culture, HUVECs ( $\sim 3 \times 10^6$ ) were grown in endothelial growth medium (EGM-2 bulletkit CC 3156 with CC4176; Cambrex, Verviers, Belgium) in standard tissue culture dishes with a diameter of 150 mm. Passage and labeling of HUVECs was performed at 70% confluence.

Labeling of HUVECs with SPIO was performed using Endorem (Guerbet SA, Paris, France) and Lipofectamine 2000 (Invitrogen, Breda, The Netherlands). Endorem is a FDA-approved SPIO agent consisting of iron oxide crystals ( $\text{Fe}_2\text{O}_3$  and  $\text{Fe}_3\text{O}_4$ ) with a dextran coating (mean particle diameter of 150 nm, iron oxide core of 4 nm). Lipofectamine 2000 is a liposome-based transfection agent that facilitates SPIO uptake as described before.<sup>21,22</sup> The labeling procedure was as follows: 30  $\mu\text{l}$  of Lipofectamine 2000 (1 mg/ml) was diluted in 0.5 ml of Opti-MEM (Invitrogen, Breda, The Netherlands). SPIO particles were diluted to the desired iron dosage in 0.5 ml Opti-MEM. After 5 minutes, the diluted Lipofectamine 2000

was added to the SPIO suspension and mixed by pipetting. The resulting suspension (1 ml) was incubated at room temperature for 15 minutes. For labeling of HUVECs, culture medium was replaced by 14 ml Opti-MEM and the SPIO-lipofectamine suspension (1 ml) was added drop-wise to the medium such that an equal distribution of SPIO-lipofectamine complexes was obtained in the culture dish. Subsequently, the cells were incubated at 37°C/5% CO<sub>2</sub> for 24 hours. The final doses used for labeling were 100 µg, 200 µg, 400 µg and 800 µg per 150 mm dish in a total volume of 15 ml. For controls, cells cultured without the addition of iron oxide were used. Before further use of labeled cells, the monolayer cultures were rinsed three times with phosphate buffered saline (PBS).

### Labeling efficiency

Intracellular uptake of iron by HUVECs was verified by Prussian blue staining and electron microscopy as described before.<sup>11</sup> In short: For Prussian blue staining labeled HUVECs were stained for 20 minutes with a freshly-prepared solution containing 0.12 M K<sub>4</sub>Fe(CN)<sub>6</sub> and 1 M HCl. Then the samples were examined by light microscopy (Axiovert S100; Zeiss, Oberkochen, Germany). For electron microscopy labeled HUVECs (~3x10<sup>6</sup>) were fixed with 1.25% glutaraldehyde in 0.1 M phosphate buffer at 40°C for 10 hours. The cells were post-fixed in 1% osmium tetroxide. Ultra thin sections were stained with uranyl acetate and lead citrate and examined with a FEI Morgagni transmission electron microscope (Philips, Eindhoven, The Netherlands).

A magnetic activated cell sorter (MINI MACS; Miltenyi Biotec, Bergisch Gladbach, Germany) was used to quantify the number of labeled cells 1 day and 5 days after labeling. Labeled cells were harvested with trypsin and resuspended in degassed PBS with 0.5% BSA. The cells were counted using an automated cell counter and then run through the MACS cell separator column. The number of cells was counted again after separation. The number of magnetic, iron-labeled cells attaching to the column was calculated and expressed as a percentage of total number of cells.

A phenanthroline assay<sup>16</sup> was used for quantitative assessment of intracellular iron content. Cell pellets of equivalent numbers (~5x10<sup>6</sup> cells) of unlabeled and labeled cells were dried for 72 hours at 60°C. Cell pellets were digested in 25 µl of a 3:1 mixture of ultrapure perchloric acid (EM Science, Gibbstown, NJ) and ultrapure nitric acid (JT Baker, Deventer, The Netherlands), at 60°C for 6 hours. To the digested samples a 130 µl mixture consisting of 0.1% (w/v) 1,10-phenanthroline monohydrate (Sigma, St. Louis, MO) in methanol, 10% (w/v) hydroxylammonium (Sigma, St. Louis, MO) in distilled water and 10% (w/v) sodium acetate in distilled water (Sigma, St. Louis, MO) in a ratio of 5:1:3 respectively, and incubated for 10 minutes at room temperature. The amount of complex formed is a measure for the amount of ferrous iron present and can be determined by absorbance at 490 nm on a spectrophotometer. Calibration of the absorbance level as a measure for intra-cellular iron

content was done with known amounts of iron.

### **Toxicity of intra-cellular SPIO**

Toxicity of intra-cellular iron for HUVECs was studied by determining proliferative capacity, cell death, mitochondrial membrane potential and differentiation capacity of labeled and unlabeled cells.

**Proliferative capacity:** The proliferative capacity of labeled cells in comparison to unlabeled cells was determined by plating  $5 \times 10^3$  cells in standard culture dishes, followed by counting of the number of cells on days 1 and 5 using a hemacytometer. Cells were passaged when reaching 80% confluency.

**Cell death assay:** Cell death was determined by a propidium iodide (PI; Sigma, St. Louis, MO) inclusion assay. Propidium iodide is a non-permeant fluorescent dye that penetrates the membranes of dead cells. Cells were labeled with PI at a concentration of 10  $\mu\text{g/ml}$  in PBS. The percentage of dead cells was then determined by Fluorescence Activated Cell Sorting (FACS) (Facsan; Becton Dickinson, Franklin Lakes, NJ) analysis.

**Mitochondrial membrane potential detection:** Loss of mitochondrial membrane potential can be determined using the fluorescent probe JC-1 (5,5',6,6'-tetrachloro-1,1',3,3'-tetraethyl benzimidazolyl carbocyanine iodide; Molecular Probes, Leiden, The Netherlands). JC-1 can exist as monomer (green fluorescent) in the cytoplasm of cells and as aggregates (red fluorescent) in mitochondria. In healthy cells JC-1 accumulates as aggregates in mitochondria. When loss of mitochondrial membrane potential occurs, the JC-1 aggregate formation in mitochondria is reduced.<sup>26</sup> After trypsinization the cells were labeled with 10  $\mu\text{g/ml}$  JC-1 in PBS for 15 minutes at 37°C. JC-1 was excited at 488 nm and the monomeric signal (green) was analyzed by FACS at 525 nm (FL1). Simultaneously, the aggregate signal (red) was analyzed at 590 nm (FL2). Mitochondrial depolarization was expressed as the percentage of cells in quadrant 4 as percentage of total number of cells. Mitochondrial depolarization of control, unlabeled cells was used for normalization, and set at 100%.

**Differentiation capacity:** Differentiation capacity of labeled and unlabeled cells was studied using a Matrigel capillary network formation assay as described before.<sup>27</sup> In short,  $1 \times 10^5$  cells were seeded in 24-well plates precoated with 250  $\mu\text{L}$  of Matrigel (Becton Dickinson, Franklin Lakes, NJ) at 37°C. After 24 hours of incubation, capillary-like structure formation was examined under a microscope (Axiovert S100; Zeiss, Oberkochen, Germany), and formation was quantitated by counting the number of intersection points at 50X magnification.

### **Sample preparation and handling for MRI**

Twelve samples containing between 5 to 25 labeled cells were seeded into three 4-well culture dishes with EGM and cultured for 4-6 hours before the first MRI scan. The culture dish contained 4 wells each with an internal diameter of 1.3 cm. One of the 4 samples per culture dish was selected for scanning following inspection by light microscopy (Olympus

Optical Company Ltd, Tokyo, Japan). Two samples were also labeled at day 2 after scanning with the fluorescent probe 5-(and-6)-carboxyfluorescein diacetate (CFSE; 5  $\mu\text{M}$  for 15 minutes) and inspected by fluorescence microscopy (Axiovert S100; Zeiss, Oberkochen, Germany). Directly before each MRI, the medium was replaced with fresh EGM containing Gd-DTPA at a v/v ratio of 1:200 to provide better signal-to-noise (SNR) and contrast-to-noise (CNR) ratios to decrease imaging time. Each sample was placed over a single loop solenoid coil with an inner diameter of 1.0 cm (Flick Engineering, The Netherlands). The distance between the loop and the cell monolayer was 1.3 mm, which was the thickness of the well bottom. After MRI, the imaged cells were photographed with light microscopy, and placed again in the incubator. This procedure was performed repeatedly for 5 consecutive days. A grid was imprinted on the bottom of each well using a scalpel. The grid localized a region-of-interest suitable for comparison between light microscopy and MRI. The grid was filled with ultrasound gel to make it visible during MRI scanning.

### MR microscopy

Cellular imaging was performed on a clinical 3.0T MRI scanner (General Electric Medical Systems, Milwaukee, WI) with the standard imaging gradient set. As described in the previous section, one sample from the 4-well culture dish was selected, prepared and positioned over the 1.0-cm diameter surface coil after appropriate mechanical fixation to reduce sample motion. After suitable image localization scans (using an in-plane resolution of  $38 \times 38 \mu\text{m}^2$  and a section thickness of 1 mm), a three-dimensional (3D) rf-spoiled gradient recalled (SPGR) sequence was selected with the imaging volume positioned parallel to the bottom of the well, including the imprinted reference grid plane. Imaging parameters were as follows: TR=37.2 ms, TE=10.54 ms, flip angle=50°, readout bandwidth=7.81 Khz, FOV=2x2 cm<sup>2</sup>, matrix=512x416, NEX=1.0, scan time=13 minutes. Scanning was performed with the frequency-encoding gradient perpendicular to the B<sub>0</sub> field. Section thickness was set to 100  $\mu\text{m}$  and 50 encoded sections spanned an imaging volume of 5 mm. These parameters yielded a voxel size of  $39 \times 48 \times 100 \mu\text{m}^3$ . Higher resolution scans were additionally performed at day 1 and at the end of the 5-day detecting period with a voxel size of  $26 \times 44 \times 100 \mu\text{m}^3$ . The scanning parameters were: TR=77.5 ms, TE=13.5 ms, flip angle=60°, readout bandwidth=7.81 Khz, FOV=1x1 cm<sup>2</sup>, matrix=384x224, NEX=2.0, scan time=29 minutes. The same volume coverage of 5 mm was selected with 50 encoded sections. The T1 relaxation time of the EGM/Gd-DTPA doped preparation was measured using an inversion recovery echo planar imaging (EPI) sequence.

SNR and CNR were measured at day 1 between signal voids and surrounding medium according to the relation ( $\text{SNR} = \text{SI}_{\text{sv}} / \text{SD}_{\text{noise}}$  and  $\text{CNR} = [|\text{SI}_{\text{medium}} - \text{SI}_{\text{sv}}|] / \text{SD}_{\text{noise}}$ ), where  $\text{SI}_{\text{medium}}$  represents signal intensity of the surrounding medium,  $\text{SI}_{\text{sv}}$  represents signal intensity of a signal void and  $\text{SD}_{\text{noise}}$  standard deviation of background noise. Measurements were performed in 3 samples of 20 randomly selected signal voids. Further, signal void areas were calculated with Clemex Vision PE analysis software (Clemex Technologies, Longueuil,

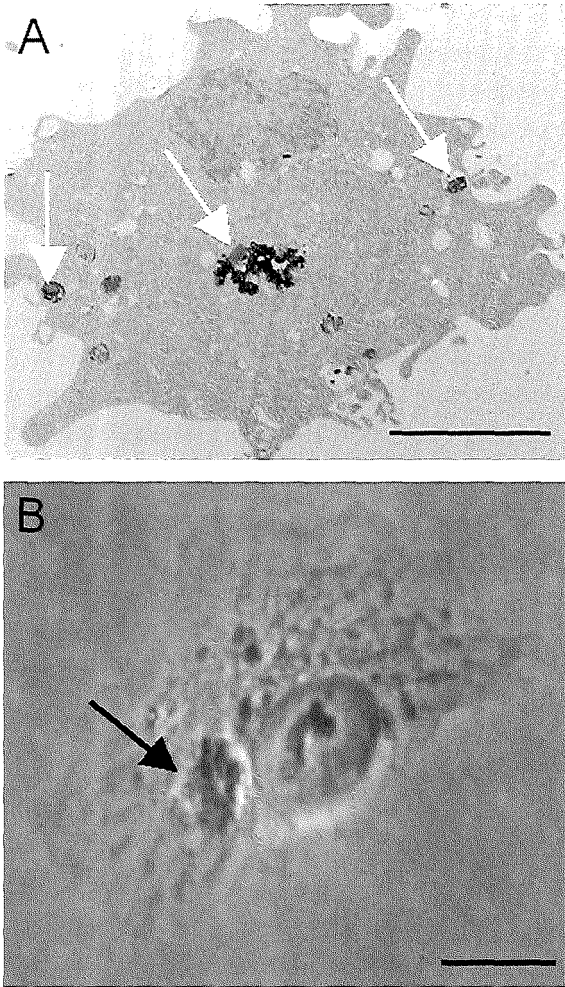


Figure 1. Panel A shows an electron microscope image of a single SPIO-labeled HUVEC, demonstrating accumulation of iron particles in membrane-bound organelles (arrows). Original magnification 5600X. Panel B shows a normal light image of a Prussian blue stain. Iron is visible as perinuclear dark spots (black arrow). Bar represents 10  $\mu$ m.

Canada) from a higher resolution scan of a sample containing ~400 cells at day 1.

## Statistics

Statistical analysis of multiple group comparisons was performed using one-way ANOVA followed by t-testing with Bonferroni's correction. All data are presented as means  $\pm$  SEM, unless otherwise stated. Statistical analysis was performed using SigmaStat software version 2.03 (SPSS Inc, Chigago, IL).

## Results

### Labeling efficiency

Uptake of SPIO was confirmed by Prussian blue staining, electron microscopy (Figure 1) and MACS sorting after the 24 hours incubation period. At all doses tested, a labeling efficiency

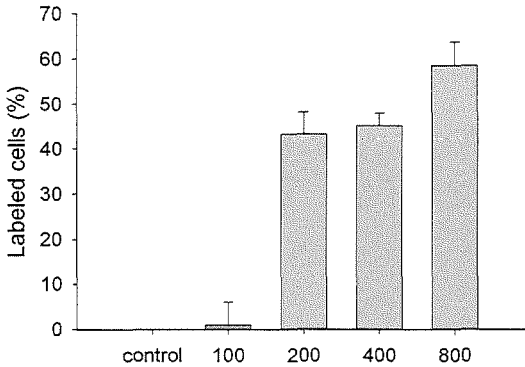
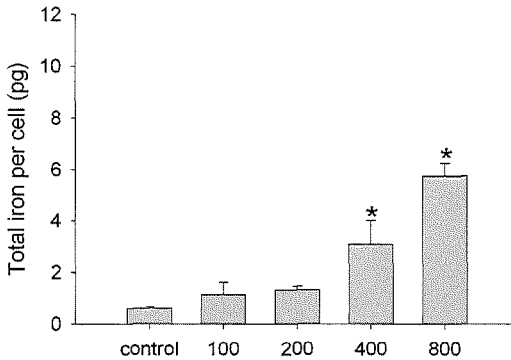
**A****Labeled cells at 5 days**

Figure 2. Panel A shows the percentage of magnetic cells containing SPIO as determined by MACS sorting after 5 days of culturing. After 24 hours 100% of cells were labeled with SPIO at all concentrations tested (not shown). At day 5 percentage labeled cells varied from 1.3% (100 µg total iron) to 60% (800 µg total iron; n=3 in each group). Panel B shows intracellular iron content of SPIO-labeled HUVECs at day 5 as determined with the phenanthroline assay. \*P<0.05 versus control, n=3 for all groups.

**B****Intracellular iron content day 5**

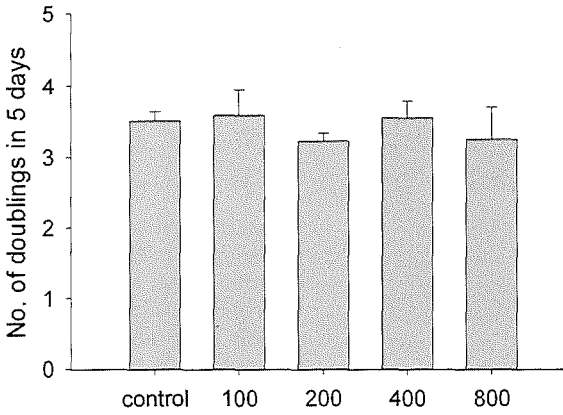
of 100% was obtained as determined by MACS sorting. Retention of the SPIO label was also determined after 5 days by magnetic cell sorting. As shown in Figure 2A significant loss of label occurred since only 1.3% to 60% of the cells could be magnetically isolated, depending on the initial concentration used. The intra-cellular iron content as assessed by the phenanthroline assay after 24 hours of labeling with 200 µg SPIO was 9.2 pg/cell and was 1.3 pg/cell after 5 days. At day 5 retention increased gradually with the initial labeling dosage (Figure 2B). Maximally, after labeling with 800 µg SPIO intracellular iron was 5.8 pg/cell after 5 days.

**Toxicity of intra-cellular SPIO**

Proliferation and differentiation was not affected after SPIO labeling (Figure 3A and Figure 4). However, as shown in Figure 3B labeling doses of 200 µg and more SPIO resulted in a decreased mitochondrial membrane potential of HUVECs. Only for a dose of 800 µg of SPIO

**A**

**Proliferation**



**B**

**Mitochondrial membrane potential**

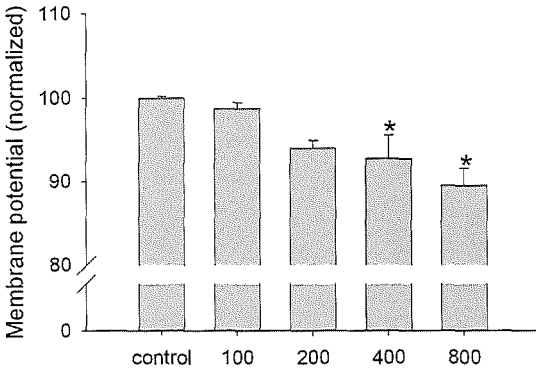
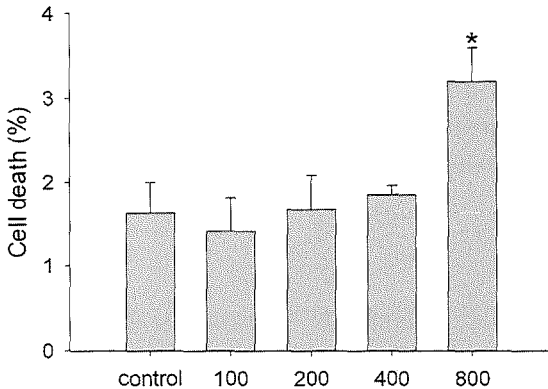


Figure 3. Panel A shows HUVEC proliferation. The number of cell doublings is shown over a 5 day period after labeling as compared with control cells. Panel B shows the normalized mitochondrial membrane potential in relation to the amount of SPIO used for labeling. Panel C shows relative cell death in relation to the amount of SPIO used. \*P<0.05 versus control, n=3 for all groups.

**C**

**Cell death**



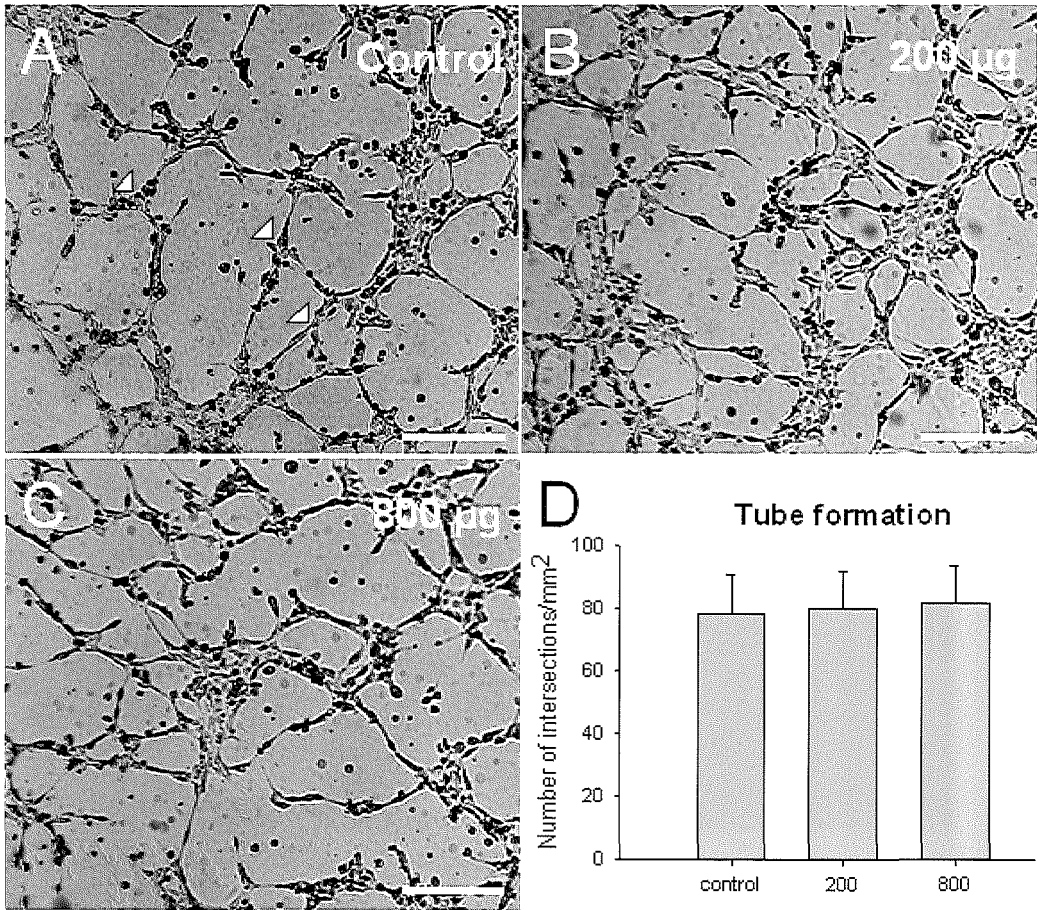


Figure 4. Panel A to C show normal light microscopy images of tube formation of control, unlabeled as well as labeled HUVECs after 24 hours culturing on Matrigel. Original magnification is 50X. Panel D shows the number of network intersections per mm<sup>2</sup>. Examples of network intersections are indicated by white arrows in Panel A. n=3 for all groups. Bar represents 200 µm.

did this result in a slight but significant increase in cell death (Figure 3C;  $P < 0.05$ ,  $n=3$ ). Based on these results we chose a dose of 200 µg for MRM of living HUVECs.

### MRM of single living HUVECs

The T1 relaxation time of the Gd-DTPA with EGM was  $60 \pm 5$  ms using a simple exponential fit to an inversion recovery curve. SNR and CNR of the signal voids in relation to the surrounding medium were  $10.7 \pm 1.3$  and  $20.5 \pm 1.2$ , respectively. A CNR of 10 (~20.5–2 standard deviations) was therefore used as a cut-off point to discriminate between signal voids induced by the presence of labeled cells and background artefacts.

Single living cells could be detected *in vitro* using MRI with each signal void corresponding to the position of a labeled cell as determined with normal light microscopy

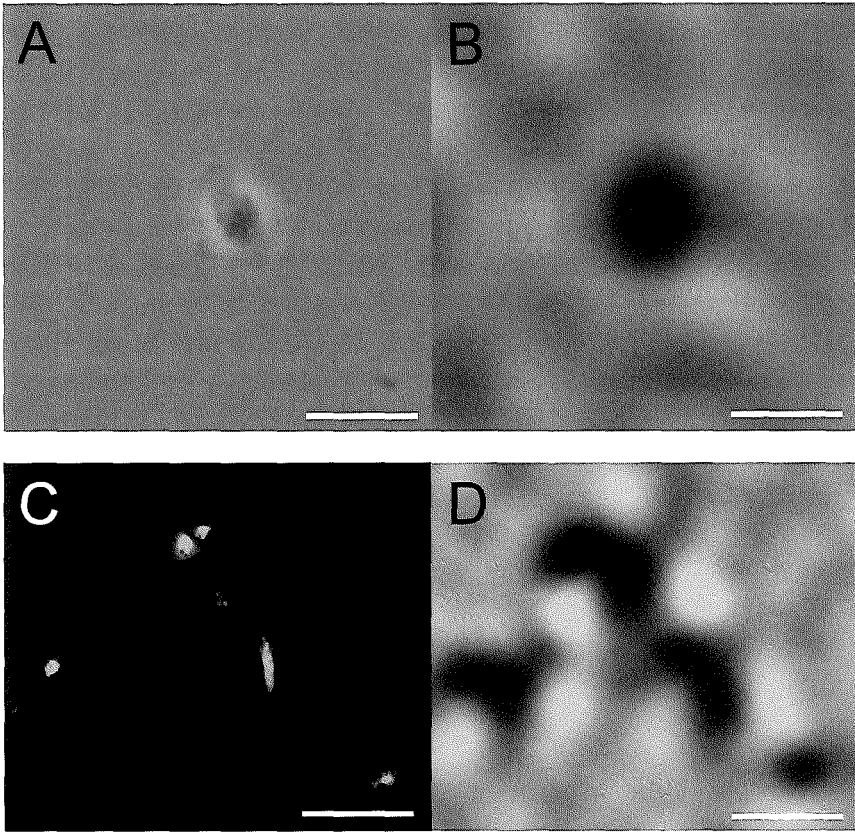


Figure 5. Panel A and C show normal light and fluorescent microscopy images of different samples at day 1 with corresponding MR images in Panel B and D, respectively. MR imaging parameters were as follows: TR=37.2 ms, TE=10.54 ms, flip angle=50°, FOV=2x2 cm<sup>2</sup>, matrix=512x416, NEX=1.0, and scan time=13 minutes. Resolution=39x48x100 μm<sup>3</sup>.

(Figure 5A and B) and fluorescence microscopy (Figure 5C and D).

Figure 6 shows one slice from the 3-dimensional data set obtained by imaging a dish containing living HUVECs labeled with 200 μg total iron at day 1 directly after labeling and at day 5. In all cases the spatial resolution is 39x48x100 μm<sup>3</sup>. The same groups of cells could be repeatedly scanned for 5 days. However, some cell groups lost their label as shown in Figure 6D. Three cell groups are imaged at day 5 that originated from 5 labeled cells as shown in Panel A and B. At the location of the cell with initially a signal void too small to be detected (white arrow), a colony was found after 5 days comprising 12 cells, that could not be detected by MRM (white ovals). In contrast, at the location of 3 cells with large signal voids (middle of grid) a group of 17 cells was present after 5 days that all could be detected by MRM (Figure 6C and D). At the location of the cell pointed at with the yellow arrow a group of 13 cells arose, of which 11 were visible on MRM. The 2 cells that are not visible anymore are indicated with yellow circles.

Analysis of signal void areas showed a wide spread distribution in size ranging from

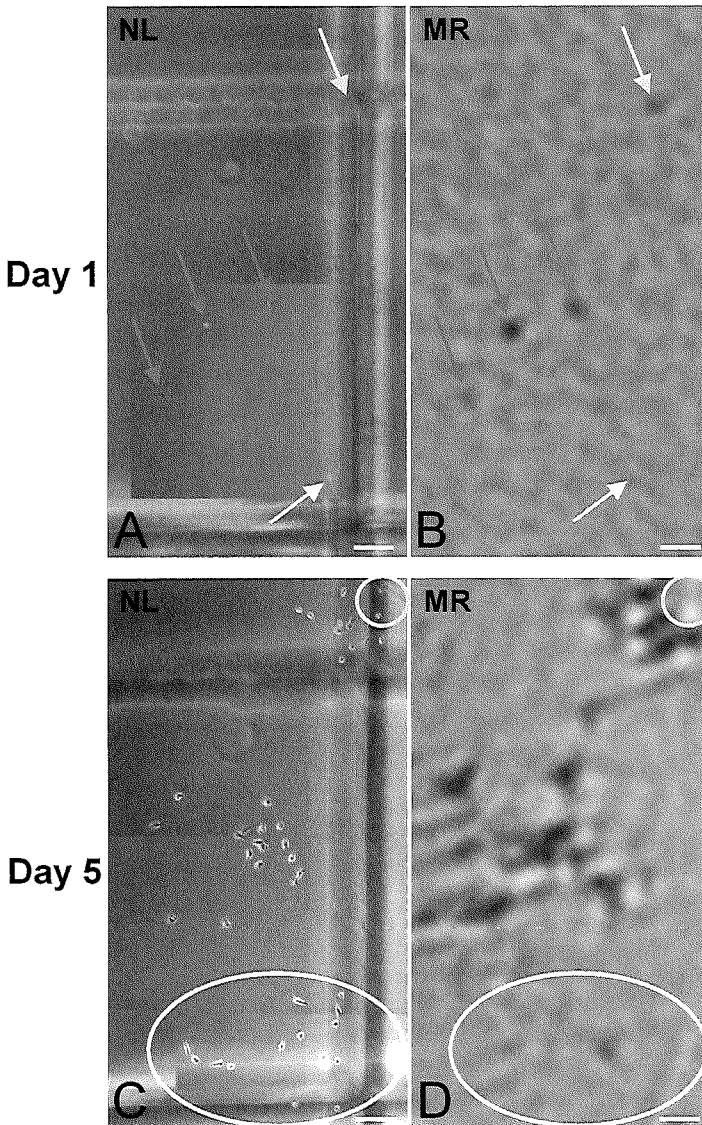
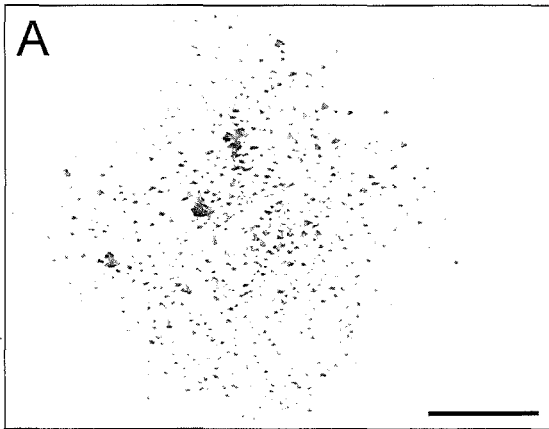


Figure 6. Signal voids in the MR image (Panel B) correspond to cells as shown in the corresponding normal light microscopy field (Panel A) at day 1 (grey arrows). The signal voids in Panel B are relatively small since the cells are not fully flattened out, shortly after plating in comparison to Panel D where the cells have fully adhered and stretched out at day 5. The white arrow at the bottom points to a cell without any signal void on MR as a result of insufficient iron uptake during labeling. The arrow in the upper right corner points to a cell that is not visible in the normal light image because it is in the shadow of the grid lines. Panel C shows the same cell sample after 5 days with the corresponding MR image (Panel D). The 2 cell groups originating from the cells with the grey arrows and the group in the upper right corner are clearly visible. Two cells from this latter group are not visible because of label loss. The cell with the white arrow in Panel A gave rise to a cell group without any signal void (white ovals). MR imaging parameters were as follows: TR=37.2 ms, TE=10.54 ms, flip angle=50°, FOV=2x2 cm<sup>2</sup>, matrix=512x416, NEX=1.0, and scan time=13 minutes. Resolution=39x48x100 μm<sup>3</sup>. The grid imprinted in the bottom of the well can be appreciated on Panels A and C as blurred lines (out of focus). White bar indicates 100 μm.



**B** Distribution signal void size

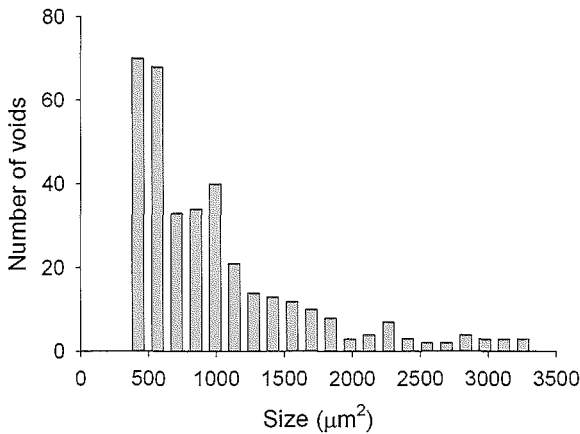


Figure 7. Panel A shows a MR image of a fixed sample containing ~400 cells at day 1. Signal void area distribution is shown in Panel B. Labeling dose was 200  $\mu\text{g}$  total iron. The scanning parameters were: TR=77.5 ms, TE=13.5 ms, flip angle=60°, readout bandwidth=7.81 Khz, FOV=1x1 cm<sup>2</sup>, matrix=384x224, NEX=2.0, scan time=29 minutes. Resolution=26x44x100  $\mu\text{m}^3$ . Bar indicates 1 cm.

400 up to 3500  $\mu\text{m}^2$  (Figure 7).

## Discussion

### Previous studies

The ability to localize or track specific cell populations *in vitro* and *in vivo* with MRI has been studied intensively during the last decade.<sup>6-20</sup> Recently, Foster et al. used the steady-state free precession (SSFP) sequence and ultrahigh gradient amplitudes for fixed cells embedded in gelatine to achieve a high SNR with resolutions down to 100x100x100  $\mu\text{m}^3$ .<sup>9</sup> Gelatine exhibits high SNR at large flip angle settings in SSFP protocols, similar to the gadolinium-doped medium in our study. This allows high CNR for the detection of labeled cells. The gradient amplitudes used in the study by Foster et al.,<sup>9</sup> however, cannot be achieved in a

clinical setting. Large cell clusters would be required to provide a signal void at resolutions that maintain a short repetition time (TR) regime. More recently the feasibility of imaging single, fixed porcine myoblasts with a 1.5T clinical scanner at even higher resolutions of  $19 \times 19 \times 50 \mu\text{m}^3$  was demonstrated,<sup>11</sup> although relatively long scanning times were needed of up to 3 hours.

The study by Foster et al.<sup>9</sup> and Zhang et al.<sup>11</sup> were based upon the use of nanometer-sized SPIOs. The use of micrometer-sized iron oxide particles or MPIOs was recently introduced,<sup>10,12</sup> which have the characteristic that a single intracellular particle is sufficient for single cell detection. Furthermore, these particles can yield higher amounts of intracellular iron<sup>14</sup> up to ~400 pg. These MPIO studies were performed using a 11.7T scanner with relatively long scanning times of 80 minutes or 14.5 hours to obtain  $100 \times 100$  or  $50 \times 50 \mu\text{m}^2$  in plane resolutions, respectively.<sup>10,12,14</sup> In contrast, the scanning time in the present study was only 13 minutes. However, a direct comparison with these previous studies is difficult, since smaller FOVs were used in the present study ( $2 \times 2$  or  $1 \times 1 \text{ cm}^2$  versus  $6 \times 6 \text{ cm}^2$  or  $2.56 \times 2.56 \text{ cm}^2$ ,<sup>10,12,14</sup> further Gd-DTPA was used in the present study to improve SNR and CNR.<sup>12,14</sup>

In the present study a labeling dose of 200  $\mu\text{g}$  total iron was used per dish resulting in 9.2 pg iron per cell. Iron uptake depends on several factors, such as cell type,<sup>22</sup> labeling dose, incubation time, cell number and cell density,<sup>23</sup> ratio iron oxide and transfection reagent,<sup>25</sup> and type of transfection reagent.<sup>25</sup> For the most widely studied cell type, mesenchymal stem cells (MSCs), intracellular iron concentrations of 12 to 16 pg/cell have been described using transfection reagents and SPIO concentrations of 25 to 50  $\mu\text{g}/\text{ml}$ .<sup>22-24,28,29</sup> For other cell types, such as  $\text{C}_2\text{C}_{12}$  myoblasts or T-lymphocytes, intracellular concentrations of 4.4<sup>19</sup> and 1.53 pg/cell<sup>23</sup> have been described, respectively, using similar labeling protocols.

The present study demonstrates for the first time, the feasibility to image single living SPIO-labeled HUVECs *in vitro* using a clinical 3.0T scanner with a scan time of 13 minutes. Further, this study demonstrated for the first time the possibility to track the fate of the same cells after several cell doublings. Therefore, this study provides additional clues on the behaviour of the iron oxide label and its redistribution over a 5 day period as detected by MRI.

## MRI protocol

A high-resolution protocol was used with a standard gradient imaging set. 3.0T and higher field scanners have demonstrated a clear advantage over 1.5T and lower fields in many applications that require  $T2^*$  weighted protocols for contrast enhancement such as functional MRI, tissue oxygenation and susceptibility weighted venography scans. This also applies to detection of iron-labeled cell populations because susceptibility artefacts increase quadratically with  $B_0$ .<sup>30</sup> Signal-to-noise improves also at higher fields as a result of the increased polarization of the nuclear spins present in the magnetic field, making it possible to increase either the speed of the imaging protocols or the spatial resolution. For

cell detection, spatial resolution can be increased by up to 40% compared with 1.5T using the same imaging time at equivalent SNR with some additional CNR gains because of the shorter T2\* relaxation times in the presence of iron at the same echo time (TE).<sup>30</sup>

The SPGR sequence proved a better choice for imaging than a SSFP scan taking into account the possibilities of the imaging gradient system available. SPGR sequences would allow for cell detecting *in vivo* without restrictions on nominal achievable resolution, e.g. using low readout bandwidths and longer TEs and TRs, as compared to the very short TRs that would be necessary for SSFP scans to realize the required signal uniformity across the ROI with the same target voxel.

All cells were visible on the T2\* weighted image as signal voids. Some voids were darker and larger than others, owing to both partial volume effects inherent to the imaging parameters and most probably to different amounts of label incorporated into each cell. Doping the cell culture medium with Gd-DTPA provided better SNR and CNR for cell delineation using the 3D T1-weighted protocol owing to the shorter T1 relaxation time. In comparison to a pilot scan protocol using lower flip angles with proton-density weighted settings of the undoped sample, the addition of Gd-DTPA provided sufficient SNR to allow for resolutions that approached single cell dimensions and a reasonably short imaging time at 3.0T for such resolution (13 minutes). This is a 10-fold scan time shortening at equivalent SNR.

Careful planning of the scanning plane using the high resolution scouts was necessary to determine the obliqueness of the imaged sample and to obtain precise alignment of the bottom of the well and cell monolayer in one single section. The orientation of the scanning plane would not be as precise if the cells would be placed in the middle of a solid physiologic matrix. Minimum intensity projections would, in this case, make it possible to collapse all the signal voids produced by the cells into the resulting projection.<sup>11</sup>

Resolutions achieved were in the order of  $26 \times 44 \times 100 \mu\text{m}^3$ . However, we may actually have achieved even higher resolutions than that defined solely by the imaging parameter prescription itself, because the actual section thickness was often much less than  $100 \mu\text{m}$ . Even though the orientation of the imaging volume was selected parallel to the bottom of the well, the actual section containing the labeled cells also contained part of the signal from the plastic bottom under the cell monolayer, thereby reducing partial volume artefacts. The effective section thickness was determined by roughly dividing the signal intensities of the Gd-doped EGM solution for the section where cells appear and that of the section right above. It ranged between  $20$  and  $70 \mu\text{m}$  (mean of  $45 \mu\text{m}$ ).

### SPIO toxicity

The biocompatibility of Endorem is assured by a low molecular weight dextran coating around the iron core that stabilizes the particulate. The use of this reagent has been previously reported in many different cell types.<sup>6,11,13,16,18-25,28,29,31</sup> Toxic effects were only reported at high labeling concentrations of around  $500 \mu\text{g/ml}$  iron *in vitro* in macrophages.<sup>31</sup> Mesenchymal

stem cells that showed comparable iron oxide uptake of around 12 pg/cell, did not show any toxic effects even after 4 weeks.<sup>31</sup> Even higher intracellular iron concentrations, up to ~400 pg/cell, could be achieved using MPIOs.<sup>12,14</sup> Although it was reported that cell death was not affected by these high concentrations, other parameters of cytotoxicity were not studied in these studies. However, it is possible that the toxicity of MPIOs is less because of their inert outer matrix in contrast with the dextran-coated SPIO particles.

In the present study we tried to improve label retention in order to follow the same cells over a time span of 5 days. To achieve high intracellular iron concentrations we used amounts of up to 800 µg/dish (150 mm in diameter, with approximately  $3 \times 10^6$  cells) of iron oxide during labeling. The major disadvantage of high intracellular iron is toxicity. Cytotoxicity is mainly caused by generation of free radicals such as hydroxyl radicals via a Fenton type reaction.<sup>32</sup> Free radicals are able to react with membrane lipids, initiating lipid peroxidation. The extent of toxicity of the intracellular iron is further determined by the ability of the cell to prevent generation and propagation of free radical species.<sup>33</sup> Because of their high levels of anti-oxidative molecules, cells as macrophages or hepatocytes are capable of handling high levels of intracellular iron.<sup>34</sup> Other mammalian cell types, such as the HUVECs used in this study maybe more susceptible to oxidative stress, especially with aging.<sup>35</sup>

In this study we observed increasing toxicity with iron doses of 200 µg or more corresponding with intracellular concentrations of about 9.2 pg/cell directly after labeling. For assessing the effects of oxidative stress, not only cell death was studied by evaluating propidium iodide inclusion, we also calculated JC-1 ratio fluorescence as a measure of mitochondrial membrane potential. Although cell death was only increased at the highest iron concentration of 800 µg total iron, mitochondrial membrane potential was already affected at concentrations above 100 µg total iron. To obtain high label retention with limited toxicity we finally chose a labeling concentration of 200 µg total iron per dish for the MR study.

Differentiation was not affected after labeling even at the highest SPIO dose of 800 µg/dish, despite the toxic effects of this dose on mitochondrial membrane potential. The importance of assessing differentiation capacity is illustrated by two previous reports describing partial inhibition of chondrogenic differentiation of mesenchymal stem cells, although adipogenic and osteogenic differentiation were not affected.<sup>28,29</sup> Intracellular iron concentrations in these studies were in the range of 12-16 pg/cell. These findings imply that intracellular iron loading can have unpredictable and varying effects on proliferation, differentiation and cell viability, thereby stressing the need to assess each of these parameters in detail.

### **Label retention**

MACS sorting showed that after labeling with 200 µg iron more than 50% of the total population was still labeled after 5 days in contrast with 1.3% using half that amount. Although MACS sorting is probably limited in the sense that cells labeled with low concentrations

pass through the column, and therefore is not a reliable method to indicate absolute iron concentrations, it can be used as an indicator of iron distribution after several mitotic events. Our hypothesis was that initially equal amounts of iron were taken up by each cell during labeling and that therefore iron should be evenly distributed between cells during mitosis. However, even after labeling with the highest concentration of 800  $\mu\text{g}$  total iron, the percentage of labeled cells was below 60% after 5 days. This implies that either (1) iron distribution is unequal during mitosis, resulting in a population with high label retention and one with low label retention or (2) that initially different amounts of iron are taken up by cells. To further evaluate initial distribution of iron in the cell population, we imaged cells directly after labeling and measured size of signal voids as a measure of intracellular iron distribution in the population. This showed a wide spread distribution in signal void sizes ranging from 400 up to 3500  $\mu\text{m}^2$ , as shown in Figure 7B. Therefore, it is likely that the number of cells with low amounts of iron label cannot be detected by MACS after several mitoses, favouring explanation 2. MR imaging confirmed this as shown in Figure 6.

Further, intracellular iron concentrations after 5 days were lower than could be expected based upon cell proliferation. After labeling with 200  $\mu\text{g}$ , the total amount of iron taken up by the cells was in the order of 10  $\mu\text{g}$  at day 1, however at day 5 the total amount of iron that could be extracted was in the order of 5  $\mu\text{g}$ . This implies that iron was released from intracellular stores. The mechanism by which cells release their iron is unclear. Loss of intracellular SPIO has only been reported in one previous study.<sup>24</sup> However, in this study it was concluded that it mainly occurs because of dilution via cell division and that only a small part could be explained by exocytosis or biodegradation. Future studies should be aimed at investigating the possible mechanisms, since the present study was not specifically designed for this purpose.

The use of MPIOs could theoretically offer some advantages in the sense of better intracellular retention and detectability, as discussed before.<sup>10,12,14</sup> Therefore, a study directly comparing label retention, detectability and toxicity of both MPIOs and SPIOs using MR microscopy of living cells is necessary.

## Summary

The present study was designed to evaluate the benefit of high spatial resolution MRI for detection of single living cells over time and to demonstrate the behaviour and toxicity of the label in HUVECs. The results obtained provide us with a qualitative estimate of the degree to which HUVEC detectability will be possible *in vivo*. Clinical MR imaging of living cell groups and, in particular, of single cells requires very high spatial resolution, SNR, CNR and shorter scanning times. Resolutions achieved in this work using a standard clinical unit were in the order of 39x49x100  $\mu\text{m}^3$ , matching the expected parameters for good detection sensitivity.

In conclusion, the concept that single living cell detection in *in vivo* and clinical experiments is feasible opens the door to new information regarding *in vivo* biology of endothelial cells. However, this study also points out several pitfalls that should be addressed

and studied in more detail *in vitro* to allow us achieving these goals. Loss of label detectability is a limiting factor in single cell tracking studies. It cautions future *in vitro* and *in vivo* studies that study cell migration over periods of 5 days or longer. Iron distribution and retention should therefore be assessed for each cell type used since differences in cell biology, doubling time and initial intracellular iron uptake could markedly differ and influence detectability over time.

## References

1. Folkman J, Shing Y. Angiogenesis. *J Biol Chem* 1992;267:10931-4.
2. Takahashi T, Kalka C, Masuda H, Chen D, Silver M, Kearney M, Wagner M, Isner JM, Asahara T. Ischemia- and cytokine- induced mobilization of bone marrow-derived endothelial progenitor cells for neovascularization. *Nat Med* 1999;5:434-8.
3. Massoud TF, Gambhir SS. Molecular imaging in living subjects: seeing fundamental biological processes in a new light. *Genes Dev* 2003;17:545-80.
4. Bulte JW, Duncan ID, Frank JA. In vivo magnetic resonance tracking of magnetically labeled cells after transplantation. *J Cereb Blood Flow Metab* 2002;22:899-907.
5. Neeman M. Preclinical MRI experience in imaging angiogenesis. *Cancer Metastasis Rev* 2000;19:39-43.
6. Anderson SA, Glod J, Arbab AS, Noel M, Ashari P, Fine HA, Frank JA. Noninvasive MR imaging of magnetically labeled stem cells to directly identify neovasculature in a glioma model. *Blood* 2005;105:420-5.
7. Bulte JW, Kraitchman DL. Iron oxide MR contrast agents for molecular and cellular imaging. *NMR Biomed* 2004;17:484-99.
8. Dodd SJ, Williams M, Suhan JP, Williams DS, Koretsky AP, Ho C. Detection of single mammalian cells by high-resolution magnetic resonance imaging. *Biophys J* 1999;76:103-9.
9. Foster-Gareau P, Heyn C, Alejski A, Rutt BK. Imaging single mammalian cells with a 1.5 T clinical MRI scanner. *Magn Reson Med* 2003;49:968-71.
10. Hinds KA, Hill JM, Shapiro EM, Laukkanen MO, Silva AC, Combs CA, Varney TR, Balaban RS, Koretsky AP, Dunbar CE. Highly efficient endosomal labeling of progenitor and stem cells with large magnetic particles allows magnetic resonance imaging of single cells. *Blood* 2003;102:867-72.
11. Zhang Z, van den Bos EJ, Wielopolski PA, de Jong-popijus MA, Duncker DJ, Krestin GP. High resolution magnetic resonance imaging of iron-labeled myoblasts using a standard 1.5T clinical scanner. *MAGMA* 2004;3:1-9.
12. Shapiro EM, Skrtic S, Sharer K, Hill JM, Dunbar CE, Koretsky AP. MRI detection of single particles for cellular imaging. *Proc Natl Acad Sci USA* 2004;101:10901-6.
13. Heyn C, Bowen CV, Rutt BK, Foster PJ. Detection threshold of single SPIO-labeled cells with FIESTA. *Magn Reson Med* 2005;53:312-20.
14. Shapiro EM, Skrtic S, Koretsky AP. Sizing it up: cellular MRI using micron-sized iron oxide particles. *Magn Reson Med* 2005;53:329-38.
15. Jacobs RE, Fraser SE. Magnetic resonance microscopy of embryonic cell lineages and movements. *Science* 1994;263:681-4.
16. van den Bos EJ, Wagner A, Mahrholdt H, Thompson RB, Morimoto Y, Sutton BS, Judd RM, Taylor DA. Improved efficacy of stem cell labeling for magnetic resonance imaging studies by the use of cationic liposomes. *Cell Transplant* 2003;12:743-56.

17. Dunning MD, Lakatos A, Loizou L, Kettunen M, French-Constant C, Brindle KM, Franklin RJ. Superparamagnetic iron oxide-labeled schwann cells and olfactory ensheathing cells can be traced in vivo by magnetic resonance imaging and retain functional properties after transplantation into the CNS. *J Neurosci* 2004;24:9799-810.
18. Bos C, Delmas Y, Desmouliere A, Solanilla A, Hauger O, Grosset C, Dubus I, Ivanovic Z, Rosenbaum J, Charbord P, Combe C, Bulte JW, Moonen CT, Ripoche J, Grenier N. In vivo MR imaging of intravascularly injected magnetically labeled mesenchymal stem cells in rat kidney and liver. *Radiology* 2004;233:781-9.
19. Cahill KS, Gaidosh G, Huard J, Silver X, Byrne BJ, Walter GA. Noninvasive monitoring and tracking of muscle stem cell transplants. *Transplantation* 2004;78:1626-33.
20. Daldrup-Link HE, Rudelius M, Piontek G, Metz S, Brauer R, Debus G, Corot C, Schlegel J, Link TM, Peschel C, Rummeny EJ, Oostendorp RA. Migration of iron oxide-labeled human hematopoietic progenitor cells in a mouse model: in vivo monitoring with 1.5-T MR imaging equipment. *Radiology* 2005;234:197-205.
21. Frank JA, Zywicke H, Jordan EK, Mitchell J, Lewis BK, Miller B, Bryant LH Jr, Bulte JW. Magnetic intracellular labeling of mammalian cells by combining (FDA-approved) superparamagnetic iron oxide MR contrast agents and commonly used transfection agents. *Acad Radiol* 2002;9:S484-7.
22. Frank JA, Miller BR, Arbab AS, Zywicke HA, Jordan EK, Lewis BK, Bryant LH Jr, Bulte JW. Clinically applicable labeling of mammalian and stem cells by combining superparamagnetic iron oxides and transfection agents. *Radiology* 2003;228:480-7.
23. Arbab AS, Bashaw LA, Miller BR, Jordan EK, Bulte JW, Frank JA. Intracytoplasmic tagging of cells with ferumoxides and transfection agent for cellular magnetic resonance imaging after cell transplantation: methods and techniques. *Transplantation* 2003;76:1123-30.
24. Arbab AS, Bashaw LA, Miller BR, Jordan EK, Lewis BK, Kalish H, Frank JA. Characterization of biophysical and metabolic properties of cells labeled with superparamagnetic iron oxide nanoparticles and transfection agent for cellular MR imaging. *Radiology* 2003;229:838-46.
25. Arbab AS, Yocum GT, Wilson LB, Parwana A, Jordan EK, Kalish H, Frank JA. Comparison of transfection agents in forming complexes with ferumoxides, cell labeling efficiency, and cellular viability. *Mol Imaging* 2004;3:24-32.
26. Reers M, Smiley ST, Mottola-Hartshorn C, Chen A, Lin M, Chen LB. Mitochondrial membrane potential monitored by JC-1 dye. *Methods Enzymol* 1995;260:406-17.
27. Bernardini G, Spinetti G, Ribatti D, Camarda G, Morbidelli L, Ziche M, Santoni A, Capogrossi MC, Napolitano M. I-309 binds to and activates endothelial cell functions and acts as an angiogenic molecule in vivo. *Blood* 2000;96:4039-45.
28. Kostura L, Kraitchman DL, Mackay AM, Pittenger MF, Bulte JW. Feridex labeling

- of mesenchymal stem cells inhibits chondrogenesis but not adipogenesis or osteogenesis. *NMR Biomed* 2004;17:513-7.
29. Bulte JW, Kraitchman DL, Mackay AM, Pittenger MF. Chondrogenic differentiation of mesenchymal stem cells is inhibited after magnetic labeling with ferumoxides. *Blood* 2004;104:3410-2.
  30. Haacke EM, Brown RW, Thompson MR, Venkatesan R. *Magnetic resonance imaging: Physical principles and sequence design*. Wiley-Liss, New York, 1999.
  31. Arbab AS, Yocum GT, Kalish H, Jordan EK, Anderson SA, Khakoo AY, Read EJ, Frank JA. Efficient magnetic cell labeling with protamine sulfate complexed to ferumoxides for cellular MRI. *Blood* 2004;104:1217-23.
  32. Wardman P, Candeias LP. Fenton chemistry: an introduction. *Radiat Res* 1996;45:523-31.
  33. Chrichton RR, Wilmet S, Legssyer R, Ward RJ. Molecular and cellular mechanisms of iron homeostasis and toxicity in mammalian cells. *J Inorg Biochem* 2002;91:9-19.
  34. Legssyer R, Ward RJ, Chrichton RR, Boelaert JR. Effect of chronic chloroquine administration on iron loading in the liver and reticuloendothelial system and on oxidative responses by the alveolar macrophages. *Biochem Pharmacol* 1999;57:907-11.
  35. Unterluggauer H, Hampel B, Zwerschke W, Jansen-Durr P. Senescence-associated cell death of human endothelial cells: the role of oxidative stress. *Exp Gerontol* 2003;38:1149-60.





# Chapter 10

Magnetic resonance imaging of hemorrhage within  
reperfused myocardial infarcts: Possible interference  
with iron oxide–labeled cell tracking?



## Abstract

**Aims-** Magnetic resonance imaging (MRI) has been proposed as a tool to track iron oxide-labeled cells within myocardial infarction (MI). However, infarct reperfusion aggravates microvascular obstruction (MO) and causes hemorrhage. We hypothesized that hemorrhagic MI causes magnetic susceptibility-induced signal voids that may interfere with iron oxide-labeled cell detection.

**Methods and results-** Pigs (n=23) underwent 2 hours occlusion of the left circumflex artery. Cine, T2\*-weighted, perfusion and delayed enhancement MRI was performed at 1 and 5 weeks, followed by *ex vivo* high-resolution scanning. At 1 week, MO was observed in 17 out of 21 animals. Signal voids were observed on T2\*-weighted scans in 5 out of 8 animals, comprising  $24 \pm 22\%$  of the infarct area. A linear correlation was found between area of MO and signal voids ( $R^2=0.87$ ;  $P=0.002$ ). At 5 weeks MO was observed in 2 out of 13 animals. Signal voids were identified in 3 out of 7 animals. *Ex vivo* scanning showed signal voids on T2\*-weighted scanning in all animals due to the presence of hemorrhage, as confirmed by histology. Signal voids interfered with the detection of iron oxide-labeled cells *ex vivo* (n=21 injections).

**Conclusion-** Hemorrhage in reperfused MI produces MRI signal voids, which may hamper tracking of iron oxide-labeled cells.

## Introduction

Transplantation of cells after myocardial infarction (MI) has emerged as a promising therapy to restore heart function.<sup>1-4</sup> To evaluate cell engraftment, non-invasive tracking of cells with magnetic resonance imaging (MRI) has been proposed as a valuable tool. Cells labeled with iron oxide, paramagnetic probes cause a T2\* signal void<sup>5</sup> and can thus be detected up to single cell resolution *in vitro*.<sup>6-8</sup> *In vivo*, clusters of labeled cells could be detected after injection into infarcted myocardium of mouse,<sup>9,10</sup> rabbit<sup>11</sup> and pig hearts.<sup>12-17</sup>

However, in clinical practice acute MI is treated by reperfusion therapy,<sup>18</sup> aggravating microvascular obstruction (MO) and causing hemorrhage.<sup>19,20</sup> Hemoglobin degradation products, such as methemoglobin and hemosiderin, have strong magnetic susceptibility effects,<sup>21</sup> that may mimic the signal voids caused by iron oxide-labeled cells.

We hypothesized that hemoglobin degradation products in reperfused MI produce signal voids that interfere with reliable iron oxide-labeled cell tracking. Therefore, we evaluated the MRI characteristics of subacute (1 week old) and chronic (5 weeks old) infarcts in a porcine model of reperfused MI and compared the MRI findings with histology of the infarct tissue.

## Methods

### Myocardial infarction

Experiments were performed in 23 Yorkshire-Landrace pigs (2-3 months old, ~25 kg). The study complied with the regulations of the Animal Care Committee of the Erasmus MC and the National Institutes of Health Publication 86 to 23, revised 1996. Animals were sedated (ketamine, 20 mg/kg IM and midazolam, 1 mg/kg IM), anesthetized (thiopental, 12 mg/kg IV), intubated and mechanically ventilated (mixture of oxygen and nitrogen, 1:2). Analgesia was maintained initially with fentanyl (12 µg/kg/minute IV). Subsequently, animals underwent left coronary catheterization, followed by balloon occlusion of the left circumflex coronary artery (LCx), proximal of the first margo obtusus branch. After 2 hours the balloon was deflated and the infarct reperfused, as confirmed by TIMI III flow on angiography. Anesthesia was maintained with isoflurane (0.6-0.8 %), starting after occlusion of the LCx.

### Magnetic resonance imaging

A 1.5 T MRI scanner with a dedicated four-element phased array receiver coil was used (Signa CV/i; GE Medical Systems, Milwaukee, WI). One week after MI, pigs were anesthetized and ventilated as described above and underwent clinically applied,<sup>22</sup> electrocardiogram (ECG)-gated cine, T2\*-weighted, first-pass perfusion (FPP) and delayed enhancement (DE) MRI. The T2\*-weighted sequence was applied in a subset of animals (n=8 and n=7 at 1 and 5 weeks, respectively), due to technical limitations of the scanner software at the start of the study. Cine images were acquired using a steady-state free precession sequence. Typical imaging parameters were: repetition time (TR)=3.8 ms, echo time (TE)=1.7 ms,

bandwidth=62.5 kHz, flip angle= 45°, in plane resolution=1.5x1.8 mm<sup>2</sup> and slice thickness=8 mm. To obtain T2\*-weighted scans, a fast gradient echo (FGRE) sequence was used. Typical imaging parameters were: TR=18 ms, TE=10 to 12 ms, flip angle=15°, bandwidth=8.0 kHz, in plane resolution=0.8x0.8 mm<sup>2</sup> and slice thickness=6 mm. FPP imaging was performed during 30-40 consecutive heart beats during administration of gadolinium-DTPA (0.1 mmol/kg IV, Magnevist; Schering, Berlin, Germany). A dedicated pulse sequence was used, consisting of a saturation preparation period followed by an interleaved gradient-echo echo-planar sequence. Typical imaging parameters were: TR=6.8 ms, TE=1.4 ms, flip angle=20°, bandwidth=125.0 kHz, in plane resolution=2.1x1.8 mm<sup>2</sup> and slice thickness=8 mm. DE MRI was performed 14±1 minutes after the administration of gadolinium-DTPA. T1-weighting was achieved using an inversion-recovery gradient echo sequence. Inversion time (TI) was adjusted to obtain the highest contrast between healthy and infarcted myocardium. Typical imaging parameters were: TR=6.8 ms, TE=1.7 ms, TI=200-350 ms, flip angle=20°, bandwidth=17.9 kHz, in plane resolution=1.2x1.5 mm<sup>2</sup> and slice thickness=8 mm. DE MR images were ECG-gated to end-diastole. Breath-holding was achieved by interrupting the ventilation.

After scanning, 8 animals were euthanized using an overdose of pentobarbital. Hearts were excised, immersed in saline and scanned *ex vivo* using gradient echo (GE) and spin echo (SE) sequences with multiple echo times and flip angles to obtain T1-, proton density-, T2- and T2\*-weighted images (T1W, PDW, T2W and T2\*W, respectively). For the GE sequence typical imaging parameters were: TR=40 ms, TE=5 to 20 ms (to obtain more T2\*-weighting with longer TE), flip angle=4 to 40° (to obtain either PDW or T1W scans, respectively), bandwidth=16.0 KHz, in plane resolution=195x195 μm<sup>2</sup> and slice thickness=0.8 mm. For the SE, T2W images, typical imaging parameters were: TR=1600 ms, TE=60 ms, bandwidth=16.0 KHz, in plane resolution=195x195 μm<sup>2</sup> and slice thickness=0.8 mm. The minimum time interval between *in vivo* scanning and sacrifice was at least 3 hours and in most cases more than 12 hours (overnight), to make sure that all Gd-DTPA had been washed out.

One animal died following the 1 week scan. Five weeks after infarction the remaining 14 animals underwent a follow-up MRI using a similar imaging protocol as at 1 week. In one animal at 1 week and again at 5 weeks no vascular access could be assured during scanning for injection of contrast, therefore in this animal no FPP and DE scans could be obtained. In one animal at 1 week, FPP scanning was not reliable for assessment of MO due to movement artefacts, therefore it was not included in the analysis. Three infarct specimens were scanned a second time after standard paraffin embedding. Finally, of 3 animals no *ex vivo* scans could be obtained due to technical limitations during scanning.

In order to compare signal voids induced by the presence of iron oxide-labeled cells and hemoglobin degradation products, *ex vivo* scanning was repeated after local injections with either 0.1, 1 or 4 x10<sup>6</sup> iron oxide-labeled human umbilical vein endothelial cells. A total of 21 injections were performed in 4 subacute and 3 chronic infarct specimens. Cells were labeled as described previously,<sup>8</sup> resulting in ~9.2 pg iron per cell, and fixed in 4%

formaldehyde.

A flow-chart (Figure 1) summarizes the protocol and the number of animals studied at each time point.

### Image analysis

MR images were analysed using Cine Display Application Version 3.0 (GE Medical systems, Milwaukee, WI). Signal voids were identified on mid-papillary, single slice T2\*W scans, and expressed as a percentage of the infarct area as defined by DE MRI. Signal void volumes were calculated by multiplying their area by slice thickness. MO was identified on mid-papillary, single slice FPP images as an area of persistent subendocardial hypoenhancement.<sup>23</sup> MI was identified on DE images as an area with delayed hyperenhancement and its size was expressed as a percentage of the left ventricular wall volume.

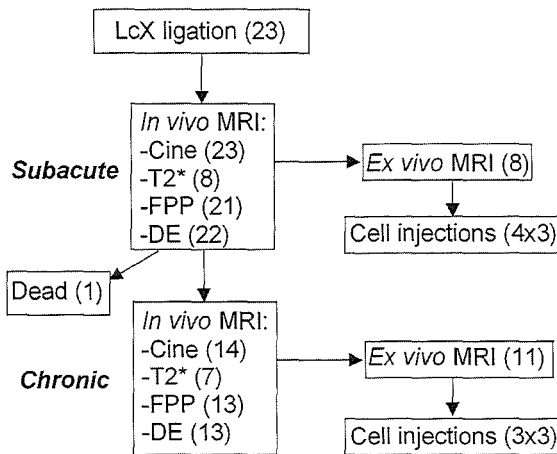


Figure 1. Flow chart of the study protocol. Numbers between brackets indicate the number of animals or specimens used at a certain time point.

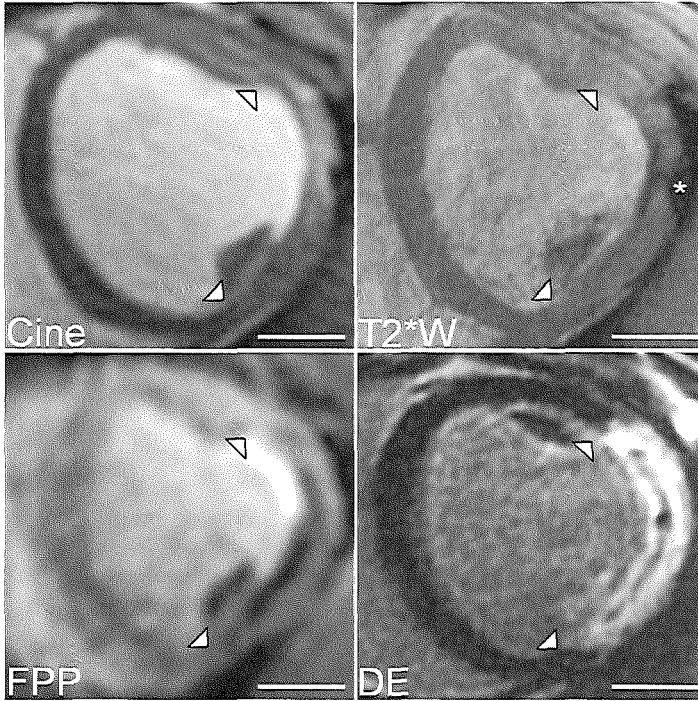
Contrast-to-noise ratio (CNR) was measured in the T2\*W *in vivo* and *ex vivo* scans at 1 and 5 weeks, according to the relation  $CNR = [SI_{myo} - SI_{void}] / SD_{noise}$ , where  $SI_{myo}$  represents signal intensity of remote or infarcted myocardium,  $SI_{void}$  signal intensity of signal voids and  $SD_{noise}$  standard deviation of background noise measured in the air outside the pig.

Total hemorrhagic areas were measured at mid-papillary levels in PD-T2\*W *ex vivo* scans using Clemex Vision PE analysis software (Clemex Technologies, Longueuil, Canada) and expressed as a percentage of the total infarct area.

### Histology

Hearts were transversally cut in ~1 cm thick slices and stained with 1% triphenyltetrazolium chloride (TTC; 37°C, 15 minutes; Sigma, St. Louis, MO) and subsequently with Prussian blue (PB), which stains hemosiderin deposits deep blue. After standard paraffin embedding, 5 µm serial sections were cut in the same plane as the MRI scans. Sections were stained with hematoxylin-eosin (HE), von Kossa's (VK) or restained with PB. VK was counterstained with von Gieson (VG). This approach allowed for identification of fat (HE), calcium (VK), collagen (VG) as well as hemosiderin (PB). Staining was analysed and compared with matching MR images at the same location and imaging plane.

1 week



5 weeks

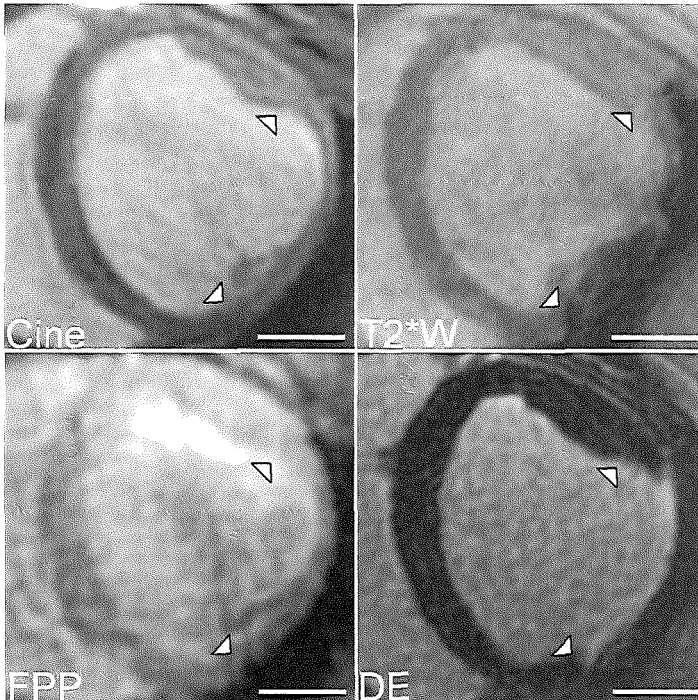


Figure 2. *In vivo* scans of one animal at 1 week (subacute) and 5 weeks (chronic) after infarction. Depicted are the end-diastolic frame of a cine, T2\*W, FPP and DE scan at the same level. The infarct area is indicated by white arrows. In the T2\*W image endo- and epicardial rims of signal voids are present at 1 week. The artefact caused by the heart-air interface is indicated by the asterisk. The rims of signal voids correspond with a zone of hypoperfusion in the FPP scan at 1 week, indicating MO. Furthermore, a zone of persistent hypoenhancement can be appreciated in the DE scan within the hyperenhanced infarct area. At 5 weeks, the area of signal voids in the T2\*W image takes up a larger part of the infarct area. Neither MO nor an area of persistent hypoenhancement is observed in the FPP or DE scans. Bar indicates 2 cm.

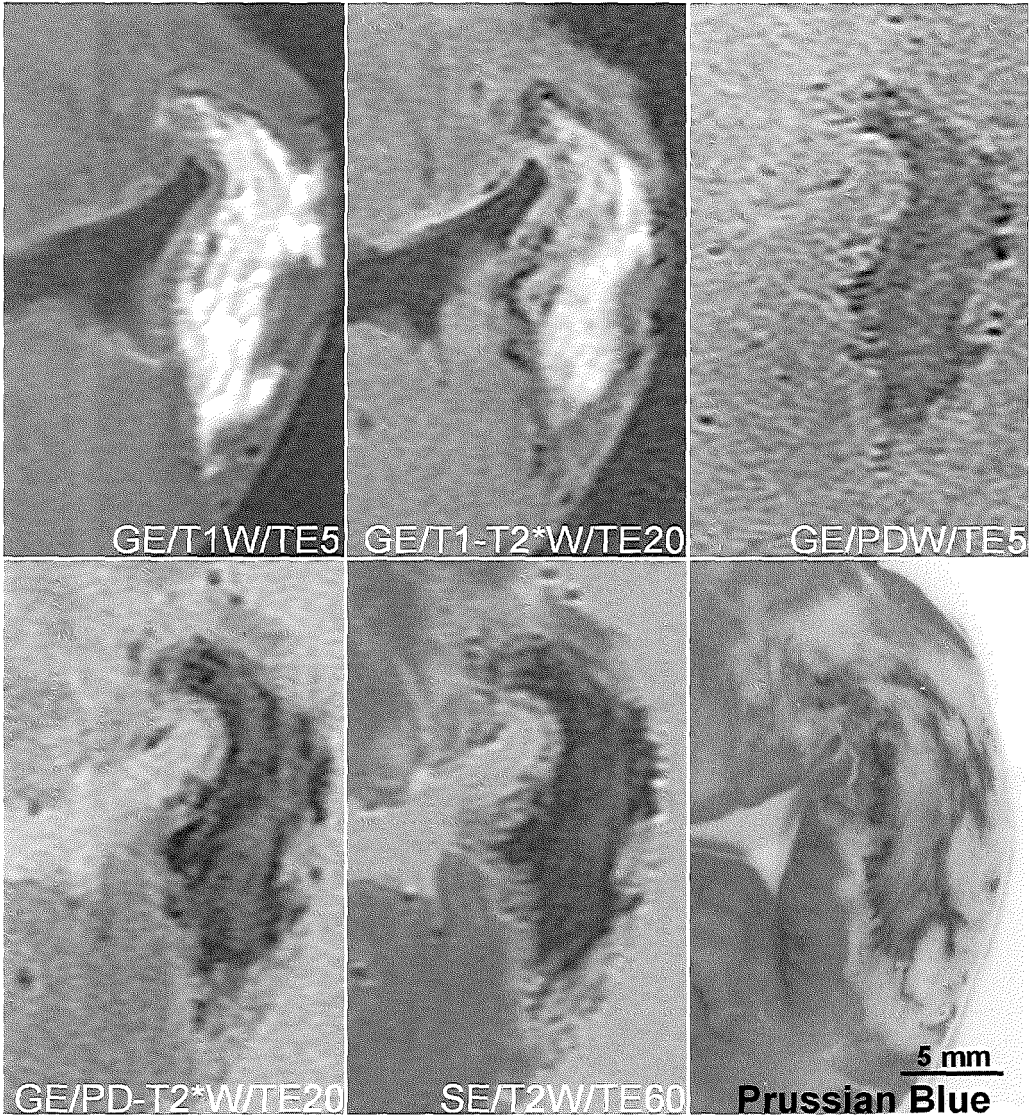


Figure 3. *Ex vivo* scans 1 week after infarction using different types of tissue contrast: T1W, PDW, T2W and T2\*W with a TE of 5, 20 or 60 ms (TE5, TE20 or TE60, respectively). Either a gradient echo (GE) or spin echo (SE) sequence was used. A ring of black signal voids is identified best in the T1W scan with a TE of 20 ms (T1-T2\*W). It corresponds with the dark hemosiderin deposits in the Prussian blue image. The ring surrounds a hyperenhanced area on T1W scans, which is hypoenhanced on SE/T2 and PD-T2\*W scans, corresponding with methemoglobin within intact erythrocytes.

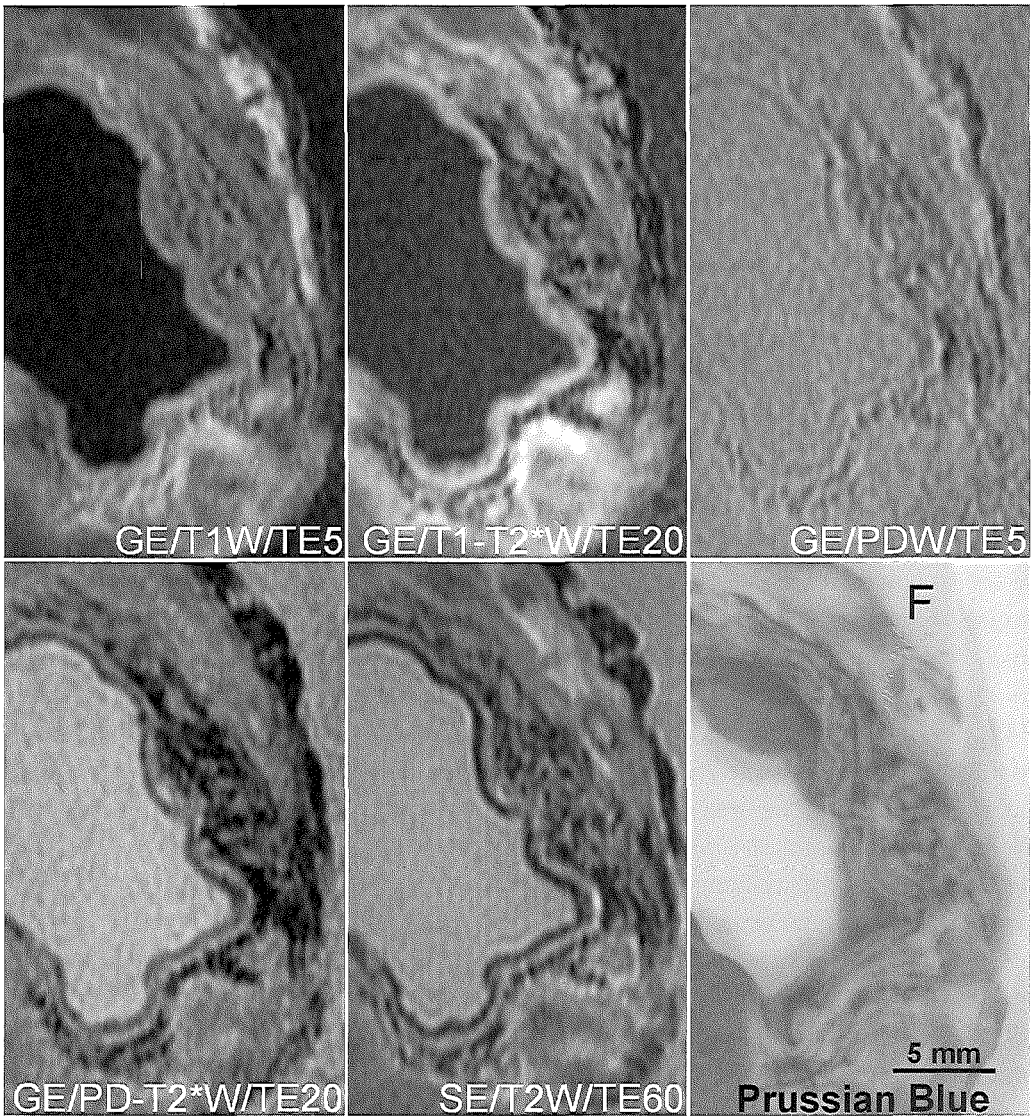


Figure 4. *Ex vivo* scans 5 weeks after infarction using various types of tissue contrast as described in Figure 3. Magnetic susceptibility-induced signal voids are observed throughout the infarct. Their size increases with T2\*-weighting (TE 20 ms). Furthermore, signal voids correspond with dark hemosiderin deposits in the Prussian blue image. Epicardial fat, indicated by F, causes a hyperintense signal on the T1W scan and a hypointense signal on T2 and T2\*W scans.

## Statistical analysis

Data are reported as mean  $\pm$  SD. Data from subacute and chronic infarcts were compared using paired or unpaired t-testing as appropriate. The correlation between area of MO and signal voids was assessed using linear regression analysis, including all animals assessed by T2\*W scanning. Proportions were compared using a z-test (SigmaStat software version 2.03; SPSS Inc., Chigago, IL). Sample size was determined with the following assumptions: Type I error of 0.05, power of 80%, an estimated proportion of animals with an *in vivo* MRI detectable hemorrhage-induced signal void of 35%, based upon the literature, with the assumption that a proportion of 5% would not be relevant. Therefore, 8 animals would yield 80% power to detect a significant proportion of animals with such a signal void. Based upon pilot studies, the proportion of *ex vivo* detected signal voids was estimated to be ~90%. A value of  $P < 0.05$  (two-tailed) was considered statistically significant.

## Results

### *In vivo* MRI

In subacute infarcts, signal voids could be identified in 5 out of 8 animals using the T2\*W sequence (Figure 2). In the remaining 3 animals, signal voids were either not observed ( $n=2$ ) or could not be reliably discerned from the air-heart interface susceptibility artefact ( $n=1$ ). The size of the signal voids was  $0.53 \pm 0.51$  cm<sup>3</sup>. The area of signal voids comprised  $24 \pm 22\%$  of the infarct area. MO was observed in 17 out of 21 animals, comprising  $35 \pm 23\%$  of the infarct area (Table 1). A linear relationship was found between the area of signal voids on T2\*W scans and the area of MO on the corresponding FPP scans at 1 week ( $R^2=0.87$ ;  $P=0.002$ ;  $n=8$ ). Infarct size was  $25 \pm 6\%$  of total left ventricular wall volume ( $n=22$ ). CNR between remote myocardium and areas of signal voids was  $27 \pm 16$  and between infarcted, non-hemorrhagic myocardium and areas of signal voids  $34 \pm 11$  ( $n=5$ ).

In chronic infarcts, an area of signal voids could be identified in 3 out of 7 animals, comprising  $15 \pm 19\%$  of the infarct area. MO was identified in 2 out of 13 animals, comprising  $13 \pm 31\%$  of the infarct area ( $P=0.0007$  and  $0.02$  versus 1 week, respectively; Table 1). Infarct size was  $15 \pm 5\%$  ( $P=0.00003$  versus 1 week;  $n=13$ ). CNR between remote myocardium and areas of signal voids was  $34 \pm 21$  and between infarcted, non-hemorrhagic myocardium and areas of signal voids was  $23 \pm 6$  ( $n=3$ ).

### *Ex vivo* MRI and histology

In subacute infarcts, the *ex vivo* high-resolution scans showed rings of magnetic susceptibility-induced signal voids on T1W and PDW scans (Figure 3). The size of the signal voids increased with a longer TE (T1-T2\*W). The rings surrounded large hyperintense areas on T1W scans, which appeared hypointense on T2W and PD-T2\*W scans. At histology, these rings of signal voids corresponded with blue deposits on Prussian blue staining and surrounded large areas

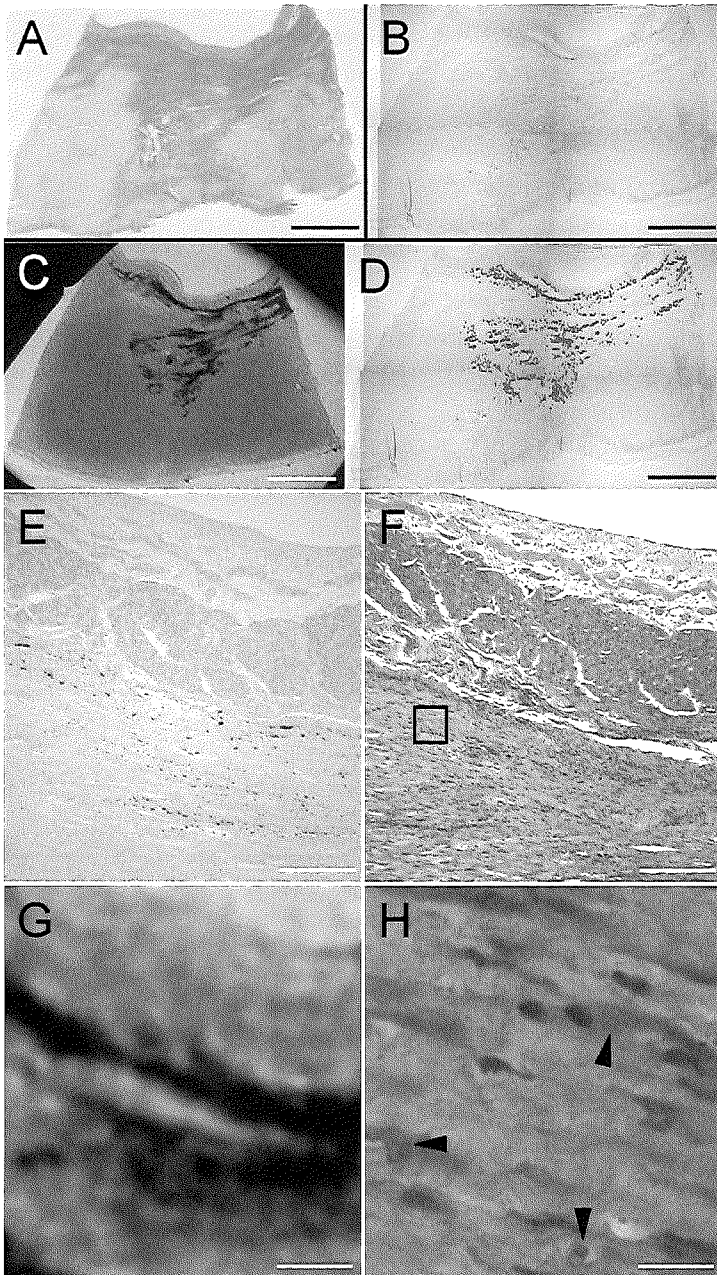


Figure 5. A tissue block from the infarct border of a 5-week old infarction was scanned at high-resolution *ex vivo*. Panel A shows the von Kossa's (calcium) and von Gieson (collagen) staining. Dark grey staining corresponds with collagenous (scar) tissue. Light grey staining corresponds with muscle fibers. Black calcium deposits were not observed in this section. In Panel B a serial section is shown after Prussian blue staining. Panel C shows the corresponding slice from the MRI T2\*W data set. Panel D show the same section as in Panel B, however stained regions are artificially enhanced. MRI signal voids correspond with hemidesiderin particles and not with calcium, fat or collagenous tissue. Panel E shows the same section as in Panel B at higher magnification. Dark hemidesiderin deposits can be appreciated. Panel F shows a serial section after HE staining. Panel G shows the corresponding region in the image of Panel A. Area of signal voids correspond with hemidesiderin deposits in Panel E. Panel H shows the boxed region in Panel F at higher magnification; hemidesiderin deposits are visible as brownish particles (black arrows). Bar indicates 4 mm in Panels A to D. Bar indicates 400  $\mu$ m in Panels E to G and 40  $\mu$ m in Panel H.

of erythrocytes.

In chronic infarcts, *ex vivo* scans showed magnetic susceptibility-induced signal voids on T1W, PDW, T2W and T1- or PD-T2\*W scans throughout the infarct area (Figure 4). Hyperintense areas were observed on T1W scans, which appeared hypointense on T2W and T1- or PD-T2\*W scans (data not shown). Furthermore, hyperintense areas were observed on T2W scans, which appeared hypointense on T1W scans (data not shown). At histology, areas of signal voids matched the pattern of blue hemosiderin deposits after Prussian blue staining (Figure 5). No correlation was found with collagen, fat or calcium deposits.

Total hemorrhagic areas at mid-papillary level as a percentage of the total infarct area as determined by T2\*W MRI were significantly larger in subacute than in chronic infarcts (P=0.00001; n=8 and 11, respectively; Table 1).

Post mortem injections with iron oxide-labeled cells could be located in remote, non-infarcted myocardium. CNR between depots of  $4 \times 10^6$  labeled cells and infarcted, non-hemorrhagic myocardium was  $18 \pm 4$  in subacute infarcts (n=4) and  $15 \pm 1$  in chronic infarcts (n=3; Table 1). This was comparable with the CNR between hemorrhage-induced signal voids and infarcted, non-hemorrhagic myocardium in subacute infarcts ( $17 \pm 9$ ; n=8) and chronic infarcts ( $14 \pm 8$ ; n=11; Table 1). As a cause, in the infarct region, none of the injection sites could be reliably located and discerned from hemorrhage-induced signal voids (Figure 6).

**Table 1. Results of MRI scanning.**

	Subacute infarcts (number of animals)	Chronic infarcts (number of animals)	P value
<i>In vivo</i> MRI			
LV wall volume (cm <sup>3</sup> )	63 ± 15 (23)	85 ± 13 (14)	0.00006
Infarct volume (% of LV volume)	25 ± 6 (22)	15 ± 5 (13)	0.00003
Animals with FPP defect	17 (21)	2 (13)	0.0007
FPP defect area (% of infarct area)	35 ± 23 (21)	13 ± 31 (13)	0.02
Animals with T2* signal void	5 (8)	3 (7)	NS
Area of T2* signal void (% of infarct area)	24 ± 22 (8)	15 ± 19 (7)	NS
CNR signal void vs. infarct area	34 ± 11 (5)	23 ± 6 (3)	NS
<i>Ex vivo</i> MRI			
Area of T2* signal void (% of infarct area)	42 ± 5 (8)	19 ± 7 (11)	0.00001
CNR signal voids vs. infarct area	17 ± 9 (8)	14 ± 8 (11)	NS
CNR cells ( $4 \times 10^6$ ) vs. infarct area	18 ± 4 (4)	15 ± 1 (3)	NS

LV=left ventricle; FPP=first-pass perfusion; CNR=contrast-to-noise ratio.

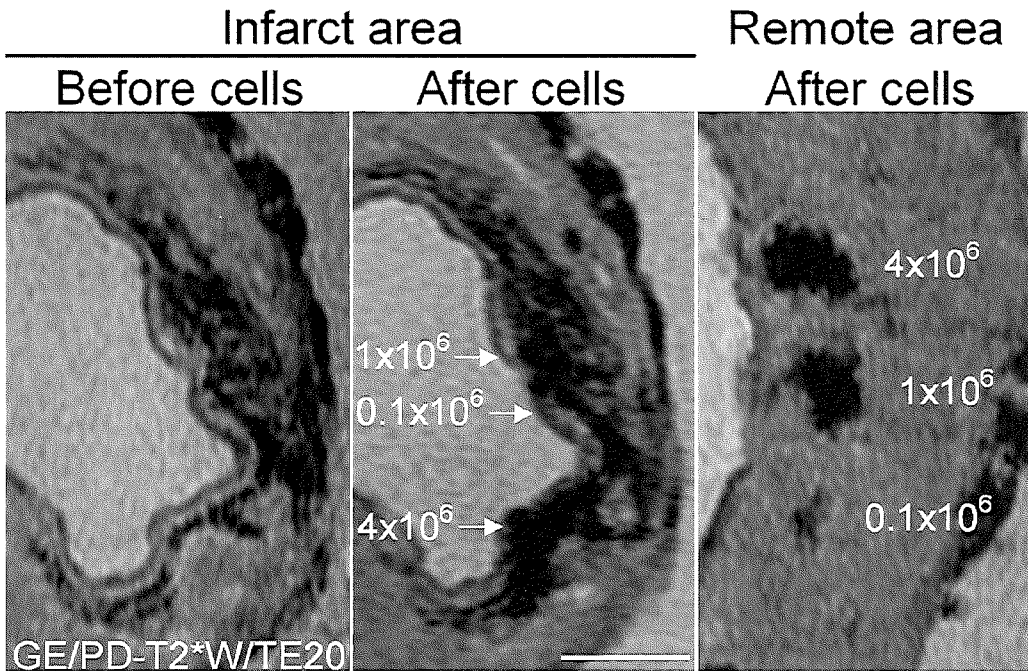


Figure 6. The left Panel shows the GE/PD-T2\*W/TE20 scan, depicted in Figure 4, before injection with iron oxide-labeled cells. The middle Panel shows the same slice after injection with 0.1, 1 or 4  $\times 10^6$  iron oxide-labeled cells. The right Panel shows a similar series of injections in remote, non-infarcted myocardium. Although the cell injections create larger areas of signal voids in the middle Panel, their precise location cannot be determined due to the signal voids induced by the presence of hemoglobin degradation products. Bar indicates 0.5 cm.

## Discussion

### Myocardial infarct reperfusion and hemorrhage

Reperfusion of MI is known to induce progressive MO, also described as the “no-reflow” phenomenon.<sup>19</sup> As shown in both animal and clinical studies, MO is followed by the development of hemorrhage, probably due to loss of microvascular integrity.<sup>20,24</sup> The extent of the hemorrhagic area has been shown to correlate with the size of MO,<sup>20</sup> which was also observed in the present study.

### Hemorrhage and MRI appearance

Few studies have been performed to evaluate the extent of the hemorrhagic area after reperfusion of MI using MRI.<sup>24,25,26</sup> One study demonstrated the presence of hemorrhage by spin echo imaging within 72 hours after reperfused MI in dogs.<sup>25</sup> Hypointense lesions corresponding with hemorrhage were found in 14 out of 16 animals. These lesions were not found in non-reperfused animals. Furthermore, in 2 clinical studies MRI was performed shortly after infarct reperfusion. The first study of 24 patients using gradient echo and

contrast enhanced imaging showed hypointense areas within the infarct region in 38% of patients by both techniques.<sup>24</sup> In the second study, 39 patients were imaged using a T2\*W GE sequence and hemorrhage could be identified as a hypointense zone within the infarct region in 33% of patients.<sup>26</sup> Because the 2 latter studies were done in patients, no histological comparison was possible. Furthermore, MRI was performed, on average, 6 days after MI, which is much shorter than the follow-up of 5 weeks used in the present study.

In contrast with intramyocardial hemorrhage, MRI appearance of intracranial hemorrhage has been given extensive attention.<sup>21</sup> Intracranial hemorrhage causes accumulation of deoxyhemoglobin within hours. Within days, deoxyhemoglobin is oxidized to methemoglobin, which causes T1 and T2 shortening due to its paramagnetic properties and magnetic susceptibility effect.<sup>27,28</sup> Therefore, the presence of methemoglobin within intact erythrocytes causes hyperintense signals on T1W scans and hypointense signals on T2W scans, a pattern observed in the present study in subacute infarcts. With further degradation, hemosiderin deposits are formed,<sup>21</sup> which remain chronically present.<sup>29</sup> Hemosiderin has a high magnetic susceptibility effect and thereby causes T2 shortening, resulting in signal voids on T1W, T2\*W and T2W images surrounding the brain hemorrhage from 2 weeks onwards, the so called “ring” pattern. In the present study, the same ring pattern was observed in subacute infarcts in the *ex vivo* scans. This difference in time course might be due to the higher in plane resolution of *ex vivo* scanning, allowing early detection of such a pattern.

### Iron oxide-labeled cell detection by MRI

Detection of iron oxide-labeled cells within MI has been described for mouse<sup>9,10</sup> and rabbit<sup>11</sup> models. Recently, several studies showed the feasibility of using iron oxide-labeled cells for clinically relevant, catheter-based delivery and cell tracking within MI in pigs. Infarcts were created by permanent coil occlusion<sup>16,17</sup> or a 60-90 minutes balloon occlusion followed by reperfusion of the infarct artery.<sup>12,13,15</sup> Cells were injected immediately after infarction<sup>12,14</sup> or into 1 day,<sup>17</sup> 1 week<sup>15</sup> or 4 week<sup>13</sup> old infarcts.

None of these studies mentioned the presence of MO or hemorrhage within the infarct center. In contrast, in the present study, MO was present in 17 out of 21 animals in subacute infarcts and signal voids were identified in all animals on the *ex vivo* scans corresponding with hemorrhage on histology. The high frequency of MO and hemorrhage could possibly be explained by the longer occlusion times used in our study (i.e. 2 hours versus 60 or 90 minutes),<sup>12,13,15</sup> approximating the time to reperfusion in the clinical setting more closely. The frequency of MO in the present study is indeed comparable to the frequency in patients reperfused early after MI.<sup>22</sup> Despite the longer occlusion times, it has been shown that hemorrhage already occurs in the pig heart after coronary occlusions more than 45 minutes.<sup>30</sup>

In a previous study, examining iron oxide-labeled cell detection in a mouse cryoinfarction model,<sup>10</sup> the presence of “spontaneous” signal voids within the infarct region was discussed. These signal voids were attributed to necrosis and fibrosis within the

infarct scar. However, a recent study showed that cryoinfarction results in large areas of hemorrhage,<sup>31</sup> which have most likely caused those signal voids. Furthermore, the problem of those spontaneous signal voids was purportedly solved by using a combination of PD- and T2\*-weighted scanning: The areas with signal voids that were exclusively due to the tissue lesions would lead to similar signal void sizes in both imaging modalities. In contrast, the size of the signal voids generated by the presence of labeled cells, was proposed to increase on T2\*-weighted scans, thereby making unequivocal detection possible. However, Figures 3 and 4 clearly illustrate that the usefulness of this method could not be demonstrated in the present study, as the size of the hemorrhage-induced signal voids increased with a longer TE.

In studies of spinal cord regeneration by transplanted iron oxide-labeled cells,<sup>32,33</sup> interference of hemorrhage with cell detection has been described as an important confounding factor. In one study, the discrimination between cells and hemorrhage was made by assessing the “blooming” effect induced by iron oxide-labeled cells, where the distortion of the magnetic field occurs over a greater area than the presence of the contrast agent.<sup>32</sup> In another study, the use of imaging sequences less susceptible to hemorrhage-induced signal voids was proposed as a solution.<sup>33</sup>

For cell detection *in vivo* a certain number of labeled cells is necessary to obtain sufficient contrast with background tissue. For MI the smallest number of cells needed for detection was reported to be  $10^5$  cells/150  $\mu\text{l}$ ,<sup>14</sup> generating signal void volumes of 0.36  $\text{cm}^3$ . This study however was performed in a model of permanent occlusion in pigs. In 3 studies of porcine, reperfused infarct models the number of cells per injection exceeded  $28 \times 10^6$ .<sup>12,13,15</sup> In the present study, the hemorrhage-associated signal voids in the *in vivo* scans had a mean total size of  $0.53 \pm 0.51 \text{ cm}^3$  in subacute infarcts, and therefore would possibly obscure detection of cell groups of  $\sim 10^5$  cells. Furthermore, CNR of signal voids identified on the T2\*W *in vivo* scans were similar to the values previously reported for groups of iron oxide-labeled cells using similar scanning sequences.<sup>14</sup> Finally, the *ex vivo* injections of iron oxide-labeled cells in the present study generated signal voids with a CNR similar to the hemorrhage-induced signal voids, thereby interfering with detection of the injected cells.

The presence of hemorrhage and visualisation with longer TE's is important in relation to the injection route as visualization of labeled cells was reported with local injections<sup>12-17</sup> while intracoronary injections have been used in most human studies.<sup>3</sup> Using iron labeling to track these cells, which will presumably spread over a larger area, requires sequences with long TE and the artefacts described in the present study are to be expected.

### Study limitations

Since it is a very subjective process to match the image locations of *in vivo* scans with the locations of *ex vivo* scans based upon anatomical landmarks only, and since the slice thickness of *in vivo* scans was 6 or 8 mm as compared with 0.8 mm of *ex vivo* scans, we

chose to describe *in vivo* and *ex vivo* findings separately. Therefore, our data do not allow for a direct comparison between *in vivo* and *ex vivo* scans.

In the present study a model of reperfused MI was used, causing large areas of hemorrhage. Therefore, it is not clear whether there is a difference in hemorrhage-induced artefacts in reperfused versus non-reperfused infarcts in porcine models *in vivo*, although in similar canine models no hemorrhage was observed when perfusion was not reinstated.<sup>25</sup>

Only intramyocardial injections were performed in the present study using fixed, iron oxide-labeled cells, which were imaged after tissue preparation. Future studies are required to investigate whether hemorrhage-induced signal voids cause similar interference with cell detection after intracoronary injection *in vivo*.

## **Conclusion**

The present study demonstrates that hemorrhage in reperfused MI produces MRI signal voids, which may interfere with reliable tracking of iron oxide-labeled cells.

## References

1. Orlic D, Kajstura J, Chimenti S, Jakoniuk I, Anderson SM, Li B, Pickel J, McKay R, Nadal-Ginard B, Bodine DM, Leri A, Anversa P. Bone marrow cells regenerate infarcted myocardium. *Nature* 2001;410:701-5.
2. van den Bos EJ, Thompson RB, Wagner A, Mahrholdt H, Morimoto Y, Thomson LE, Wang LH, Duncker DJ, Judd RM, Taylor DA. Functional assessment of myoblast transplantation for cardiac repair with magnetic resonance imaging. *Eur J Heart Fail* 2005;7:435-43.
3. Schachinger V, Assmus B, Britten MB, Honold J, Lehmann R, Teupe C, Abolmaali ND, Vogl TJ, Hofmann WK, Martin H, Dimmeler S, Zeiher AM. Transplantation of progenitor cells and regeneration enhancement in acute myocardial infarction: final one-year results of the TOPCARE-AMI Trial. *J Am Coll Cardiol* 2004;44:1690-9.
4. Smits PC, van Geuns RJ, Poldermans D, Bountiokos M, Onderwater EE, Lee CH, Maat AP, Serruys PW. Catheter-based intramyocardial injection of autologous skeletal myoblasts as a primary treatment of ischemic heart failure: clinical experience with six-month follow-up. *J Am Coll Cardiol* 2003;42:2063-9.
5. Yeh TC, Zhang W, Ildstad ST, Ho C. Intracellular labeling of T-cells with superparamagnetic contrast agents. *Magn Reson Med* 1993;30:617-25.
6. Foster-Gareau P, Heyn C, Alejski A, Rutt BK. Imaging single mammalian cells with a 1.5 T clinical MRI scanner. *Magn Reson Med* 2003;49:968-71.
7. Shapiro EM, Skrtic S, Sharer K, Hill JM, Dunbar CE, Koretsky AP. MRI detection of single particles for cellular imaging. *Proc Natl Acad Sci USA* 2004;101:10901-6.
8. Zhang Z, van den Bos EJ, Wielopolski PA, de Jong-Popijus M, M. Bernsen, Duncker DJ, Krestin GP. In vitro imaging of single living human umbilical vein endothelial cells with a clinical 3.0T MRI scanner. *MAGMA* 2005;18:175-85.
9. Himes N, Min JY, Lee R, Brown C, Shea J, Huang X, Xiao YF, Morgan JP, Burstein D, Oettgen P. In vivo MRI of embryonic stem cells in a mouse model of myocardial infarction. *Magn Reson Med* 2004;52:1214-9.
10. Kustermann E, Roell W, Breitbach M, Wecker S, Wiedermann D, Buehrle C, Welz A, Hescheler J, Fleischmann BK, Hoehn M. Stem cell implantation in ischemic mouse heart: a high-resolution magnetic resonance imaging investigation. *NMR Biomed* 2005;18:362-70.
11. van den Bos EJ, Wagner A, Mahrholdt H, Thompson RB, Morimoto Y, Sutton BS, Judd RM, Taylor DA. Improved efficacy of stem cell labeling for magnetic resonance imaging studies by the use of cationic liposomes. *Cell Transplant* 2003;12:743-56.
12. Kraitchman DL, Heldman AW, Atalar E, Amado LC, Martin BJ, Pittenger MF, Hare JM, Bulte JW. In vivo magnetic resonance imaging of mesenchymal stem cells in myocardial infarction. *Circulation* 2003;107:2290-3.
13. Garot J, Untersee T, Teiger E, Champagne S, Chazaud B, Gherardi R, Hittinger L,

- Gueret P, Rahmouni A. Magnetic resonance imaging of targeted catheter-based implantation of myogenic precursor cells into infarcted left ventricular myocardium. *J Am Coll Cardiol* 2003;41:1841-6.
14. Hill JM, Dick AJ, Raman VK, Thompson RB, Yu ZX, Hinds KA, Pessanha BS, Guttman MA, Varney TR, Martin BJ, Dunbar CE, McVeigh ER, Lederman RJ. Serial cardiac magnetic resonance imaging of injected mesenchymal stem cells. *Circulation* 2003;108:1009-14.
  15. Baklanov DV, Demuinck ED, Thompson CA, Pearlman JD. Novel double contrast MRI technique for intramyocardial detection of percutaneously transplanted autologous cells. *Magn Reson Med* 2004;52:1438-42.
  16. Karmarkar PV, Kraitchman DL, Izbudak I, Hofmann LV, Amado LC, Fritzges D, Young R, Pittenger M, Bulte JW, Atalar E. MR-trackable intramyocardial injection catheter. *Magn Reson Med* 2004;51:1163-72.
  17. Dick AJ, Guttman MA, Raman VK, Peters DC, Pessanha BS, Hill JM, Smith S, Scott G, McVeigh ER, Lederman RJ. Magnetic resonance fluoroscopy allows targeted delivery of mesenchymal stem cells to infarct borders in Swine. *Circulation* 2003;108:2899-904.
  18. Giugliano RP, Braunwald E; The TIMI Study Group. Selecting the best reperfusion strategy in ST-elevation myocardial infarction: it's all a matter of time. *Circulation* 2003;108:2828-30.
  19. Rochitte CE, Lima JA, Bluemke DA, Reeder SB, McVeigh ER, Furuta T, Becker LC, Melin JA. Magnitude and time course of microvascular obstruction and tissue injury after acute myocardial infarction. *Circulation* 1998;98:1006-14.
  20. Reffelmann T, Kloner RA. Microvascular reperfusion injury: rapid expansion of anatomic no reflow during reperfusion in the rabbit. *Am J Physiol Heart Circ Physiol* 2002;283:H1099-107.
  21. Bradley WG Jr. MR appearance of hemorrhage in the brain. *Radiology* 1993;189:15-26.
  22. Baks T, van Geuns RJ, Biagini E, Wielopolski P, Mollet NR, Cademartiri F, Boersma E, van der Giessen WJ, Krestin GP, Duncker DJ, Serruys PW, de Feyter PJ. Recovery of left ventricular function after primary angioplasty for acute myocardial infarction. *Eur Heart J* 2005;26:1070-7.
  23. Lund GK, Stork A, Saeed M, Bansmann MP, Gerken JH, Muller V, Mester J, Higgins CB, Adam G, Meinertz T. Acute myocardial infarction: evaluation with first-pass enhancement and delayed enhancement MR imaging compared with 201Tl SPECT imaging. *Radiology* 2004;232:49-57.
  24. Asanuma T, Tanabe K, Ochiai K, Yoshitomi H, Nakamura K, Murakami Y, Sano K, Shimada T, Murakami R, Morioka S, Beppu S. Relationship between progressive microvascular damage and intramyocardial hemorrhage in patients with reperfused anterior myocardial infarction: myocardial contrast echocardiographic study.

- Circulation 1997;96:448-53.
25. Lotan CS, Bouchard A, Cranney GB, Bishop SP, Pohost GM. Assessment of postreperfusion myocardial hemorrhage using proton NMR imaging at 1.5 T. *Circulation* 1992;86:1018-25.
  26. Ochiai K, Shimada T, Murakami Y, Ishibashi Y, Sano K, Kitamura J, Inoue S, Murakami R, Kawamitsu H, Sugimura K. Hemorrhagic myocardial infarction after coronary reperfusion detected in vivo by magnetic resonance imaging in humans: prevalence and clinical implications. *J Cardiovasc Magn Reson* 1999;1:247-56.
  27. Vymazal J, Brooks RA, Patronas N, Hajek M, Bulte JW, Di Chiro G. Magnetic resonance imaging of brain iron in health and disease. *J Neurol Sci* 1995;134:19-26.
  28. Anzalone N, Scotti R, Riva R. Neuroradiologic differential diagnosis of cerebral intraparenchymal hemorrhage. *Neurol Sci* 2004;25:S3-5.
  29. Hardy PA, Kucharczyk W, Henkelman RM. Cause of signal loss in MR images of old hemorrhagic lesions. *Radiology* 1990;174:549-55.
  30. Garcia-Dorado D, Theroux P, Alonso J, Elizaga J, Botas J, Fernandez-Aviles F, Soriano J, Munoz R, Solares J. Intracoronary infusion of superoxide dismutase and reperfusion injury in the pig heart. *Basic Res Cardiol* 1990;85:619-29.
  31. van den Bos EJ, Mees BM, de Waard MC, de Crom R, Duncker DJ. A novel model of cryoinjury-induced myocardial infarction in the mouse: A comparison with coronary artery ligation. *Am J Physiol Heart Circ Physiol* 2005;289:H1291-1300.
  32. Dunning MD, Lakatos A, Loizou L, Kettunen M, French-Constant C, Brindle KM, Franklin RJ. Superparamagnetic iron oxide-labeled Schwann cells and olfactory ensheathing cells can be traced in vivo by magnetic resonance imaging and retain functional properties after transplantation into the CNS. *J Neurosci* 2004;24:9799-810.
  33. Dunn EA, Weaver LC, Dekaban GA, Foster PJ. Cellular imaging of inflammation after experimental spinal cord injury. *Mol Imaging* 2005;4:53-62.



# Chapter 11

General discussion, conclusions and future directions



It has been more than 14 years since the first pre-clinical experiments were performed investigating intracardiac cell transplantation. As a result of a long list of pre-clinical studies showing successful regeneration of myocardium and functional improvement using a variety of cell types, cell-based therapy for myocardial repair has now risen to the forefront of clinical research. However, as described in **chapter 1** several aspects of cell transplantation still need further investigation and understanding at a pre-clinical level. These include: the injection technique with the highest efficiency, the dynamics and mechanisms of cell death after transplantation, the mechanisms underlying functional improvement in response to cell therapy and the homing and migration of cells to and through the infarct area after transplantation. In this thesis several of these aspects of cell transplantation using various animal models as well as new tools that could be helpful in future research have been described.

## **Animal models for cell transplantation studies**

A variety of animal models from small to large has been used for studies of intracardiac cell transplantation, each with its own advantages and disadvantages. Most studies use a myocardial infarction (MI) model. In **chapter 2** a novel MI model is presented in a small animal: the mouse. The major advantages of smaller animals such as the mouse for cell-transplantation studies include: low-cost, high throughput and the possibility of genetic modification. Furthermore, multiple diagnostic tools have been designed specifically for the mouse, such as a broad array of monoclonal antibodies for immunohistochemistry. Mouse models are likely to become increasingly important in the future mainly because of the possibility to use syngeneic donor cells from genetically modified animals. These animals could carry either lineage-restricted or ubiquitously expressed reporter genes which make it possible to unambiguously track cells and monitor cell fate after transplantation. The importance of using reporter genes has been highlighted by several reports<sup>1,2</sup> that questioned earlier studies<sup>3,4</sup> claiming transdifferentiation of hematopoietic stem cells into cardiomyocytes *in vivo*, thereby regenerating infarcts for more than 50%. These earlier studies used immunohistochemistry for cardiomyocyte-specific antigens to determine cell fate, which can be hampered by the high level of auto-fluorescence within the infarct region,<sup>5</sup> or the fluorescence of infiltrating leucocytes.<sup>6</sup> Furthermore, cell fusion can account for the observation of transdifferentiation.<sup>7-9</sup> A combination of both lineage-restricted and ubiquitously expressed reporter genes would therefore make it possible to confirm simultaneously the presence of donor cells at a certain location as well as the degree and amount of transdifferentiation.

Thus far most mouse studies used ligation of the left anterior descending artery (LAD) as infarct model.<sup>10,11</sup> Although this is a pathophysiologically relevant model, it has many disadvantages. The most important one may be the extensive infarct remodeling that occurs in the mouse causing marked infarct thinning, which makes histological evaluation of myocardial regeneration by the transplanted cells very difficult due to the very thin tissue

and the difficulty to find the injection location in the remodeled infarct area. This is even more hampered by the fact that when cells are injected early after ligation the size of the resulting infarct cannot be discerned. Cells could therefore be mistakenly injected outside the infarcted area. Even so, several studies used the mouse LAD ligation model with direct epicardial injection for cell transplantation studies.<sup>3</sup> The percentage of successful injections in those models was reported to be around 54%, however, in the cryoinfarction model described in **chapter 4**, successful injections into the infarct area were observed in 58 of 60 animals (97%).

Cryoinjury is a method to induce myocardial necrosis by freezing part of the muscle with liquid nitrogen. This method has been extensively evaluated in animals such as in the rat<sup>12,13</sup> and rabbit<sup>14-16</sup> but not in mice. In this thesis it was shown that cryoinjury results in reproducible infarcts, with less infarct remodeling, with an easily visualized infarct region directly after injury. Furthermore, a decline in global systolic and diastolic function, assessed with echocardiography and LV pressure measurements, was observed comparable with LAD ligation after 8 weeks making this model suitable for evaluation of the functional effect of various interventions. The hypothetical benefits of cryoinjury were shown to be realistic in the study described in **chapter 4**: Cells could be easily located in nearly 100% of animals at pre-defined locations within the infarct area, thereby allowing detailed study of the number of surviving cells after transplantation. In **chapter 5 and 6** it was demonstrated that regional function at the site of cryoinjury could be assessed using both sonomicrometry and (magnetic resonance imaging (MRI) in rabbits. These methods have been used to assess regional cardiac function in mouse models before.<sup>17,18</sup> Whether these methods could potentially also be applied in a mouse model of cryoinjury needs to be investigated.

Despite the advantages offered by smaller animal models, many aspects of human cardiovascular physiology cannot be accurately reproduced. This is for example illustrated by the fact that potential safety issues such as the arrhythmogeneity of transplanted myoblasts were only first noted in clinical trials.<sup>19</sup> The higher heart rate of smaller animals could prevent detection of arrhythmias. Therefore extensive validation in large animal models such as pigs, sheep or dogs is necessary before starting clinical trials. A disadvantage of using dogs is their extensive collateral circulation that causes large variations in infarct size.<sup>20</sup> Pigs have a well-characterized cardiovascular physiology<sup>21,22</sup> which makes them very suitable for such validation studies. Thus far, strikingly few large animal studies have been performed to confirm the beneficial effects of myoblasts found in smaller animal studies. Myoblasts were mainly tested in sheep<sup>23,24</sup> and dogs.<sup>25</sup> Bone marrow-derived cells (BMCs) were studied in pigs<sup>26,27</sup> and dogs.<sup>28</sup>

In conclusion, the ease of genetic modification makes the mouse an ideal experimental animal to study basic molecular and cellular mechanisms that are necessary to improve the efficiency of cell transplantation. The mouse cryoinfarction model described in this thesis is very suitable for future cell transplantation studies. However, larger, more physiologically relevant animal models such as the pig are still necessary to confirm the efficacy of a certain

cell type and technique before its clinical implementation.

## Cell delivery techniques

**Chapter 3** describes a video-assisted thoracoscopic approach (VATS) in pigs for cell delivery. In this study, successful cell delivery was possible under direct visualization of the injection site even in areas difficult to reach such as the posterior wall. Thus far, visualized cell delivery has only been possible using thoracotomy. The possibility to visualize the injection site offers several potential advantages over other methods such as catheter-based delivery: (1) The injection site can be exactly chosen, e.g. scarred areas or scarred areas interspersed with viable tissue; (2) thin areas can be injected without being afraid of perforation; (3) the size and length of the cell deposit can be directly modified; (4) the distance between cell deposits can be accurately chosen and the injection angle can be varied. Despite these advantages, thus far, clinical studies have not adopted this injection modality. Since a definitive proof of efficacy of cell transplantation has not been shown yet in randomised clinical studies, it is not justified to perform a thoracotomy merely for cell transplantation when there is no need for surgical intervention for other reasons, such as coronary bypass surgery. Furthermore, patients with co-morbidity might not be candidates for thoracotomy. Therefore the VATS approach could be meaningful for future clinical studies.

The VATS approach adds a new delivery method to the existing arsenal: Direct epicardial injection via thoracotomy and catheter-based delivery via the endocardial route, via the coronary sinus or via the intracoronary route. All these methods have their specific applications. Techniques employing needle injections purportedly enable more targeted delivery as compared with techniques releasing cells into the vessel lumen. Especially the application of catheter-based injections using newer imaging modalities, such as MRI in combination with 3D electromechanical mapping (NOGA),<sup>29</sup> or MRI in combination with fluoroscopy,<sup>30</sup> or 3D ultrasound-guided catheter injections<sup>31</sup> could enhance the efficacy to deliver endocardial cell injections at the right location. The intracoronary route is still the preferred method in clinical bone marrow trials, probably because cardiologists are more familiar with this procedure. However, it has been shown that the percentage of cells reaching the heart is very limited after intracoronary injection, in the order of 1 to 3% using bone marrow-derived mononuclear cells (MNCs), as compared with 10 to 20% after direct intramyocardial injection.<sup>32</sup> This percentage will probably also depend on the cell type used: A study using MSCs, which have a bigger size than MNCs, documented 6% retention at 14 days.<sup>33</sup> In this study injection of cells was associated with decreased coronary blood flow, suggesting that entrapment of these bigger cells in arterioles will enhance retention, but can also cause microinfarctions. Based on these studies it must be concluded that the majority of cells is lost and engraft at other locations in the body, such as the lungs, liver and spleen, with potential damaging effects. Therefore it is important to find new methods to improve cell retention, which was also demonstrated in this thesis.

In **chapter 4**, only 18% of the initial injected cell population could be detected

immediately after injection. Limited retention after direct intramyocardial injection has been noted in more studies,<sup>34</sup> however thus far this has not resulted in optimization of injection techniques. Several straightforward techniques have been proposed to optimise direct intramyocardial injection: These include injecting cells within a matrix or hydrogel,<sup>35</sup> using microneedle<sup>36</sup> arrays to improve cell distribution or surgically closing the injection site after retracting the needle. Methods to improve cell retention after intracoronary injection as well as injection via the coronary sinus could consist of adjusting the pressure during injection,<sup>32</sup> changing stop-flow conditions<sup>32</sup> and modulating the injected cell population, to enhance cell adhesion to the vascular wall and to promote cell migration through the wall. Future studies should eventually determine what is the best injection method for each cell type and for each injection location as well as for each patient.

In conclusion, VATS cell transplantation is a promising alternative for patients when thoracotomy is not possible due to comorbidity. Future studies should compare different injection techniques, both direct and catheter-based, in terms of total accumulation of cells at the target location and subsequent migration of cells using non-invasive imaging of labeled cells with techniques as MRI or nuclear imaging. Furthermore, in a setting of cell transplantation in acute MI, cell retention is extremely limited, therefore future studies should investigate new methods to improve retention.

## Survival and engraftment of cells after transplantation

In chapter 4 survival and engraftment of myoblasts was studied after transplantation into an acute cryoinfarction. The results from this study show that myoblast death is the result of acute necrosis likely as a result of oxidative stress. Thus far, few studies have investigated myoblast survival or survival of other cell types after transplantation.<sup>37-43</sup> Several important modulators of cell survival seem to play an important role: Oxidative stress, the acute inflammatory response and ischemia. It has to be taken into account that these are time-related events: Oxidative stress likely plays a major role in the hyperacute phase, when massive necrosis of cardiomyocytes occurs and probably peaks during the first 24 hours. Inflammation is a later event, in part caused by oxidative stress, and regulated by a large number of pro-inflammatory cytokines such as IL-1, IL-6, IL-10 and TNF- $\alpha$ .<sup>44,45</sup> The influence of ischemia on cell survival has only been studied indirectly: Physical or genetic measures rendering cells more ischemia-resistant or inducing angiogenesis have been shown to improve survival. Ischemia will probably be the most important factor influencing survival in chronic non-reperfused infarcts and even more after direct intramyocardial injection than after intracoronary injection.

Several other factors could probably influence cell survival: The surrounding matrix promoting initial cell attachment as well as the change in matrix environment during infarct remodeling with increasing collagen deposition; the concentration of injected cells, with an increasing metabolic demand with higher cell concentrations causing hypoxia; movement of the heart and injection site creating shear forces on the cells and finally the injection

location.

Because all these factors are time-related events, the interval between infarction and cell injection could have a major impact on cell survival and thus on functional benefit. This has also been suggested by some pre-clinical as well as clinical studies. The positive effects on remodeling and function of fetal cardiomyocytes in a rat model of MI were optimal when transplanted 2 weeks after infarction as opposed to 1 week or 4 weeks.<sup>46</sup> A recent randomised clinical trial studied three different time points of BMC injection: The effect on function was comparable with injections within the first week, between one and two weeks or more than three weeks after infarction.<sup>47</sup> Two other clinical trials did not show any benefit with injections 24 hours after infarction<sup>48</sup> or less benefit with early injections<sup>49</sup> as compared with 5 or 6 days after infarction. Of course it has to be taken into account that functional improvement of cell therapy does not rely upon cell survival and final grafted cell numbers only. Future studies should therefore focus on the potential relationship between cell survival and timing of injection to determine the optimal time point for each cell type, injection modality and infarct type (e.g. reperfused, versus non-reperfused).

To improve survival and engraftment of cells, three types of treatment can be considered for this purpose: Physiological, pharmacological and genetic. Physiological methods include for example heat-shock treatment of cells before injection,<sup>37</sup> ischemic preconditioning of the cells before transplantation or injecting cells within a protective scaffold.<sup>35</sup> Pharmacological methods consists of co-administration of drugs with the injectate as performed in **chapter 4**, pharmacological pretreatment of cells before injection or systemic administration of drugs to the animal. Genetic methods include the use of donor cells that express genes that enhance survival or proliferation,<sup>50</sup> thereby stimulating engraftment. One could think of genes encoding anti-apoptotic activity or pro-angiogenic activity, genes that reduce reperfusion injury, or stimulate proliferation. The increasing availability of transgenic mouse models as a source of donor cells offers ample opportunity to explore the most efficient pathways to improve cell survival and engraftment in the future.

In conclusion, cell death after transplantation in the acute setting of MI mainly occurs via necrosis as a result of oxidative stress. However, since many more factors are involved at different time points, future studies should investigate the role of different modulators on cell survival in relation to the time after infarction in order to construct an optimal time interval for cell transplantation to promote successful survival and subsequent engraftment.

## Functional improvement after cell transplantation

The functional assessment of both myoblast and BMC transplantation is described in **chapter 5 and 6**. The ultimate goal of cell transplantation is the improvement of global systolic and diastolic cardiac function. Several mechanism could attribute to this goal. First of all: Cells could contribute directly to regeneration of the lost myocardium by anatomical integration. Cells could either differentiate into (cardio)myogenic, contractile cells that functionally integrate with the surrounding myocardium and generate systolic force thereby contributing

to the cardiac work cycle, or cells could differentiate into vasculogenic cells, for example endothelial cells, thereby promoting vasculogenesis and improving perfusion of ischemic myocardium within the infarct area. Initially, during the first decade of cell transplantation studies this first mechanism was thought to be the most important one and research was mainly focused on demonstrating improved regional contractility. However, cells could exert a beneficial effect on function via other, non-contractile mechanisms. First of all, cells could reduce adverse remodeling of the infarct area, by preventing infarct dilation, thinning and improving compliance and subsequently attenuate remodeling of the remote myocardium. This could be the result of the release of growth factors or cytokines that influence for example the myofibroblasts, cells that organize the normal sequela of infarct healing. Furthermore, transplanted cells could thicken the infarct scar thereby directly reducing dyskinesia and wall stress, which could have a beneficial effect as well on remodeling of infarct and remote regions. Finally, transplanted cells could stimulate angiogenesis within the infarct scar and border zones via paracrine ways thereby improving recovery of hibernating myocardium, sparing ischemic myocardium within borderzones and infarct area and possibly generating new blood vessels that act as a scaffold, thereby reducing dyskinesia of the infarct area.

Several pre-clinical studies provided evidence for these so-called alternative mechanisms. First of all, injection of cells without any suitable contractile apparatus contributed to improvement in diastolic function;<sup>51,52</sup> an increase in regional angiogenesis was noted in several studies of myoblast<sup>53</sup> and BMC transplantation,<sup>54-59</sup> several studies documented infarct thickening or a reduction in infarct size after cell transplantation,<sup>60-62</sup> paracrine pathways are discovered that can explain some of the earlier reports of improved function attributed to extensive myocardial regeneration,<sup>63</sup> which is further strengthened by the fact that injection of conditioned medium of donor cells also leads to enhanced function;<sup>64,65</sup> contractile function is restored by injection of growth factors without concomitant increase in new muscle mass;<sup>66</sup> functional improvement is noted at early time points, when extensive cardiac regeneration cannot have taken place yet;<sup>67</sup> furthermore, functional benefit is still demonstrated when the original donor cell population is no longer present;<sup>68</sup> in most of the pre-clinical studies improvement in global function was accompanied by less global adverse remodeling; finally in clinical studies improvement in regional perfusion of the infarct area was described<sup>69</sup> and in the first double-blind randomised bone marrow trial, the only beneficial outcome was reduction in infarct volume.<sup>48</sup>

The studies in **chapter 5 and 6** mainly focused on the first hypothesis that cells with myogenic potential improve regional contractile function. In **chapter 6** transplantation of MSCs and myoblasts improved regional stroke work as measured by micromanometry and sonomicrometry, in **chapter 5** regional wall thickening was improved. Furthermore, histology was used to demonstrate the presence of contractile proteins within the transplanted and grafted cells. Several other pre-clinical as well as clinical studies showed improved regional function, however, thus far none of these studies has been able to directly identify the underlying mechanism and correlate it with the extent of regional functional improvement.

It is noteworthy that both studies described in this thesis, using two different methods of measuring global and regional systolic function, did not show an improvement in global function: Left ventricular dP/dt or ejection fraction did not increase. However, using MRI it was possible to demonstrate an improvement in 2D ejection fraction at the level of infarction, as well as a reduction in global left ventricular remodeling, arguing for a direct regional effect. The development of new imaging-based assays to directly monitor the excitation coupling between donor and host cells at a cellular level<sup>70</sup> could be helpful in designing new studies that provide some more insight into the mechanisms behind the benefit. These should be combined with more detailed histological analysis of the infarct area in respect to angiogenesis and fibrosis around the grafted areas, throughout the infarct area and border zones. Furthermore, the potential paracrine effects of the injected cell populations should be investigated in representative *in vitro* models in conjunction with *in vivo* studies. Finally newer imaging modalities, such as strain and strain rate imaging using echocardiography or MRI could be helpful in studying regional function.

It is important to keep in mind that cell therapy for chronic infarcts may require a different strategy than acute infarcts. After acute infarction the whole remodeling process of infarct and remote myocardium still needs to take place. Potentially, cells that exert a positive influence on scar reduction, infarct thickening and angiogenesis could have more impact when transplanted in this acute setting than when the scar area is fully remodeled after a few months. However, the fully remodeled scar may benefit more from cells that potentially have a direct effect on contractility such as cardiomyocytes, cells that transdifferentiate into myogenic cells, or cells that recruit hibernating myocardium in the border zones. Based on this assumption, BMCs may be more beneficial for repairing acute infarcts as compared with myoblasts that would be more useful for chronic infarct repair.

Studies comparing myoblasts and bone BMCs in relation to timing of injection could sort this out. In **chapter 6** a direct comparison between bone marrow-derived MSCs and myoblasts was performed with injections 3 weeks after infarction, a situation when infarct remodeling is halfway. This study could not demonstrate a difference in efficacy between both cell types at this time point. Thus far few other studies have directly compared BMCs with myoblasts. In one study bone marrow-derived CD133+ cells did not improve function to a greater extent than myoblasts when injected 10 days after infarction in rats,<sup>71</sup> despite the fact that the CD133+ cells, in contrast with myoblasts could not be detected with histology, but only by PCR. Furthermore, the extent of angiogenesis was comparable between the two cell types. This argues for a different mechanism of functional improvement between the two cell types: Myoblasts that directly improve systolic function and BMCs that enhance cardiomyocyte survival or reduce remodeling, but not via enhanced angiogenesis. In another study MSCs did not improve function in contrast with myoblasts when injected 9 days after infarction in rats,<sup>72</sup> despite more angiogenesis after MSC transplantation. These studies illustrate that direct side-to-side comparisons could not only clarify which is the best cell type for cardiac regeneration, but also shed more light on possible mechanisms behind the

regional functional improvement of each cell type. A next step would be to combine different cell types to maximize the usefulness of the specific individual effect of each cell type,<sup>73,74</sup> however, these studies should only be undertaken when the effects of each cell type on its own have been carefully characterized.

In conclusion, myoblast transplantation restores wall thickening at the infarct site, arguing for a direct effect of transplanted cells on contractility of the infarct region. Furthermore, both bone marrow-derived MSCs as well as myoblasts do improve regional systolic function after cryoinfarction to the same extent. Future studies assessing functional benefit of cell transplantation should use imaging modalities and functional parameters that better define the regional effect of the transplanted cells such as strain imaging by MRI, preferably in combination with regional perfusion imaging and non-invasive cell tracking to link cell location with regional changes.

## Tracking cells using magnetic resonance imaging

In the last part of the thesis the potential of MRI was studied as a tool to track labeled cells, *ex vivo* as well as *in vivo* in MI models. In **chapter 7** a labeling procedure was introduced using transfection reagents and superparamagnetic iron oxide (SPIO), which could be successfully used to track cells directly after injection, as well as to track living cells *in vitro* down to single cell level (**chapter 8 and 9**). Although the use of SPIO labeling for cell tracking has been described after injection into a MI, thus far no study has addressed the potential hampering effect of hemorrhage-induced signal voids after myocardial infarct reperfusion: This effect was described in **chapter 10**. It was demonstrated that a significant proportion of the infarct region is covered up with signal voids generated by hemorrhage degradation products that interfere with reliable tracking of iron oxide-labeled cells.

Imaging of cells and cell behaviour is important to elucidate specific mechanisms that contribute to the success or failure of cell transplantation in the time frame before the assessment of clinically established parameters that determine final outcome. The following roles for imaging can be discerned: (1) Determining the best delivery method by quantifying cell accumulation at a certain target location; (2) assessing cell migration by quantifying biodistribution over time; (3) elucidating therapeutic mechanisms by linking cell location to regional functional improvement or geometrical change; (4) assessing cell differentiation by the use of reporter gene imaging; (5) assessing cell metabolism by correlating cell location to regional metabolic changes.

Thus far, basically two imaging modalities have been studied for these purposes: MRI and nuclear imaging. Both of these have their specific advantages. Basically, MRI offers high spatial resolution but suffers from background signal, impairing signal-to-noise ratio and sensitivity, in contrast, nuclear imaging has less spatial resolution, but profits from the near absence of background signal.

For cell detection with MRI two different contrast agents can be used: So-called “positive” contrast agents such as iron oxide-based agents, or “negative” contrast agents such

as gadolinium-based agents. Thus far, more extensive experience has been gained using iron oxide-based agents for cell tracking in the heart, merely because these have a far lower threshold of detectability as compared with gadolinium-based agents, and are presumably better biodegradable. However, due to the limitations described in **chapter 10**, it is likely that the use of iron oxide-based agents will be limited to determining the success of injecting large deposits of cells into infarct regions, or tracking cells outside hemorrhagic areas, for example in the zones bordering the infarct. Therefore it is necessary that “negative” contrast agents are revisited as potential cell markers for tracking. Ongoing developments are promising in this regard: For example new gadolinium chelates such as gadolinium fullerene compounds, could improve T1 relaxivities and cell detectability.<sup>75</sup> Furthermore, several new techniques that enhance intracellular uptake of iron oxide compounds have been studied for cell labeling with gadolinium compounds, such as liposomes<sup>76</sup> or D-tat peptides.<sup>77</sup> Since gadolinium-chelates have much stronger T1-reducing effect in solution than intracellular, possibly due to sequestration, steric changes or intracellular motion characteristics,<sup>75</sup> additional studies are needed to identify the ideal chelate in combination with a labeling method that exerts a strong T1 effect intracellularly *in vivo*. Finally, gadolinium-chelates can be combined with fluorescent tags, facilitating detection at histology.<sup>76</sup> On the other hand, a potential drawback of using “negative” contrast agents is the presence of hemoglobin degradation products with a strong effect on T1 relaxivity such as methemoglobin as demonstrated in **chapter 10**, even though this effect declines with time.

Nuclear imaging of transplanted cells using a variety of radionuclides has been applied in pre-clinical as well as clinical studies. The potentially higher sensitivity as compared with MRI of SPIO-labeled cells has been suggested by the fact that cells could be detected in the heart after intravenous administration, with intracardiac radioactivity measured at 1% of the injected dose.<sup>79,80</sup> In humans, BMCs labeled with <sup>18</sup>F-fluorodeoxyglucose could be traced after intracoronary injection within the centre and border of the infarct using 3D positron emission tomography.<sup>81</sup> However, a drawback of radionuclides is the decay of the label. This could potentially be solved by the new technique of reporter gene imaging.<sup>82</sup> Donor cells expressing those genes can be detected after transplantation by intravenous administration of a radiolabeled reporter probe that is specific for this gene product. Since this can be repeatedly done, decay of the label is not a problem. Furthermore, this method could offer insight into differentiation of cells when the reporter gene is active in only certain differentiated cell types.

In conclusion, with MRI, detection and tracking of iron oxide-labeled, living, single cells is possible *in vitro*. Furthermore, within reperfused myocardial infarcts, hemorrhage-induced signal voids hamper MRI detection of iron oxide-labeled cells. To circumvent some of the drawbacks of iron oxide-labeled cell tracking, “negative” contrast agents for cell labeling should be studied such as new gadolinium-chelates. Finally, applying animal models and donor cells that permit the use of lineage-restricted reporter genes in combination with ubiquitously expressed reporter genes is necessary to determine unambiguously the fate

and differentiation of each new cell type after transplantation.

## Conclusions and future directions

Extensive basic and pre-clinical research during the last decade has yielded a vast amount of evidence that cell transplantation does improve cardiac function after myocardial infarction. This applies for multiple cell types and animal models. Meanwhile the first clinical trials have started. Although clinical trials are warranted since safety and efficacy have been established in animal models, the exact mechanism of functional improvement still needs to be elucidated. To address this issue in the future, more mechanistic pre-clinical studies are needed. In this thesis several aspects of cell transplantation were investigated that could play a key-role in the design of these future studies. These include: animal models for cell transplantation studies, cell injection techniques, the survival of cells after transplantation, the functional benefit of cell transplantation and tracking of cells using magnetic resonance imaging.

Several conclusions can be drawn from the studies in this thesis. These are in summary: 1) The mouse cryoinfarction model is very suitable for future cell transplantation studies, 2) VATS cell transplantation is a promising alternative for patients when thoracotomy is not possible due to comorbidity, 3) cell death after transplantation in the acute setting of MI mainly occurs via necrosis as a result of oxidative stress, 4) myoblast transplantation restores wall thickening at the infarct site, arguing for a direct effect of transplanted cells on contractility of the infarct region, 5) both bone marrow-derived MSCs as well as myoblasts do improve regional systolic function after cryoinfarction to the same extent, 6) with MRI, detection and tracking of iron oxide-labeled, living, single cells is possible *in vitro* and 7) within reperfused myocardial infarcts, hemorrhage-induced signal voids hamper MRI detection of iron oxide-labeled cells.

With reference to the first question posed in the introduction of this thesis: “What is the exact mechanism of functional improvement observed in pre-clinical as well as clinical studies?”, we propose that future cell transplantation studies should adhere to several guidelines based upon the outcomes of the studies in this thesis. First of all, transgenic mouse models and donor cells are required to gain insight into basic mechanisms of molecular and cellular pathways that determine the outcome of transplantation of different cell types. Furthermore, they should be employed in conjunction with reporter genes to unambiguously track the fate of the donor cells. The mouse cryoinfarction model is a helpful tool to design these studies.

Once the cell-lineage and the resulting phenotype of the donor cell after transplantation have been assessed in a mouse model, its physiology should be studied using imaging-based assays such as the direct monitoring of the excitation coupling between donor and host cells at a cellular level. In order to determine the paracrine effects of the donor cells, *in vitro* assays should be set up in conjunction with the *in vivo* studies. When these experiments show the potential mechanistic benefit of a certain cell type, the effect of the cells on cardiac

function as well as geometry should be assessed in mouse or larger animal models. Again, as demonstrated in this thesis, the mouse cryoinfarction model is a useful tool to perform these studies. However, these functional studies should still use histology as a principal guide and the cells should be appropriately tracked to determine their fate.

MRI is probably the most versatile tool to assess multiple parameters simultaneously as illustrated by this thesis: MRI can determine different state-of-the-art measures of regional and global function as well as geometry within one scanning session and this can be combined with tracking the location of the injected cells, as well as measuring the metabolism of the cells using nuclear MR spectroscopy. As illustrated by this thesis, for MRI tracking in clinically relevant reperfused infarct models, more versatile “negative” contrast agents should be developed.

When the optimal cell type and phenotype have been determined and the mechanisms of functional and geometrical cardiac improvement are known, the optimal grafted cell number should be studied together with optimization of cell delivery, timing of delivery, retention, cell survival and migration. As illustrated by this thesis, cell delivery, retention and survival together are likely the principal factors that influence the final graft size.

Since this outline for future studies as presented here, involves many specialized techniques and knowledge, collaboration between different departments and research groups is necessary. This is illustrated by the recent debate about the plasticity of bone marrow-derived cells, where several groups have criticized earlier reports of extensive myocardial regeneration by these cells. Parallel experiments and exchanging reagents and protocols among diverging group could clarify this dispute.

Finally, while it certainly is of interest to study cell transplantation in patients after myocardial infarction or with severe heart failure, it should be emphasized that more research is needed to optimize this procedure. Too early testing in patients carries the risk that negative clinical results will “kill the concept” before the basic principles have been properly elucidated. Indeed, collaborative clinical and basic research is required to exploit the unique perspective of therapy to regenerate damaged cardiac tissue.

## References

1. Balsam LB, Wagers AJ, Christensen JL, Kofidis T, Weissman IL, Robbins RC. Haematopoietic stem cells adopt mature haematopoietic fates in ischaemic myocardium. *Nature* 2004;428:668-73.
2. Murry CE, Soonpaa MH, Reinecke H, Nakajima H, Nakajima HO, Rubart M, Pasumarthi KB, Virag JI, Bartelmez SH, Poppa V, Bradford G, Dowell JD, Williams DA, Field LJ. Haematopoietic stem cells do not transdifferentiate into cardiac myocytes in myocardial infarcts. *Nature* 2004;428:664-8.
3. Kajstura J, Rota M, Whang B, Cascapera S, Hosoda T, Bearzi C, Nurzynska D, Kasahara H, Zias E, Bonafé M, Nadal-Ginard B, Torella D, Nascimbene A, Quaini F, Urbanek K, Leri A, Anversa P. Bone marrow cells differentiate in cardiac cell lineages after infarction independently of cell fusion. *Circ Res* 2005;96:127-37.
4. Orlic D, Kajstura J, Chimenti S, Limana F, Jakoniuk I, Quaini F, Nadal-Ginard B, Bodine DM, Leri A, Anversa P. Mobilized bone marrow cells repair the infarcted heart, improving function and survival. *Proc Natl Acad Sci USA* 2001;98:10344-9.
5. Dowell JD, Rubart M, Pasumarthi KB, Soonpaa MH, Field LJ. Myocyte and myogenic stem cell transplantation in the heart. *Cardiovasc Res* 2003;58:336-50.
6. Laflamme MA, Murry CE. Regenerating the heart. *Nat Biotechnol* 2005;23:845-56.
7. Nygren JM, Jovinge S, Breitbach M, Säwén P, Röhl W, Hescheler J, Taneera J, Fleischmann BK, Jacobsen SEW. Bone marrow-derived hematopoietic cells generate cardiomyocytes at a low frequency through cell fusion, but not transdifferentiation. *Nat Med* 2004;10:494-501.
8. Reinecke H, Minami E, Poppa V, Murry CE. Evidence for fusion between cardiac and skeletal muscle cells. *Circ Res* 2004;94:56-60.
9. Zhang S, Wang D, Estrov Z, Raj S, Willerson JT, Yeh ETH. Both cell fusion and transdifferentiation account for the transformation of human peripheral blood CD34-positive cells into cardiomyocytes in vivo. *Circulation* 2004;110:3803-7.
10. Michael LH, Entman ML, Hartley CJ, Youker KA, Zhu J, Hall SR, Hawkins HK, Berens K, Ballantyne CM. Myocardial ischemia and reperfusion: a murine model. *Am J Physiol* 1995;269:H2147-54.
11. Patten RD, Aronovitz MJ, Deras-Mejia L, Pandian NG, Hanak GG, Smith JJ, Mendelsohn ME, Konstam MA. Ventricular remodeling in a mouse model of myocardial infarction. *Am J Physiol* 1998;274:H1812-20.
12. Ciulla MM, Paliotti R, Ferrero S, Braidotti P, Esposito A, Gianelli U, Busca G, Cioffi U, Bulfamante G, Magrini F. Left ventricular remodeling after experimental myocardial cryoinjury in rats. *J Surg Res* 2004;116:91-7.
13. Murry CE, Wiseman RW, Schwartz SM, Hauschka SD. Skeletal myoblast transplantation for repair of myocardial necrosis. *J Clin Invest* 1996;98:2512-23.
14. Taylor DA, Atkins BZ, Hungspreugs P, Jones TR, Reedy MC, Hutcheson KA, Glower

- DD, Kraus WE. Regenerating functional myocardium: improved performance after skeletal muscle myoblast transplantation. *Nat Med* 1998;4:929-33.
15. Thompson RB, Emani SM, Davis BH, van den Bos EJ, Morimoto Y, Craig D, Glower D, Taylor DA. Comparison of intracardiac cell transplantation: autologous skeletal myoblasts versus bone marrow cells. *Circulation* 2003;108:II264-71.
  16. van den Bos EJ, Thompson RB, Wagner A, Mahrholdt H, Morimoto Y, Thomson LE, Wang LH, Duncker DJ, Judd RM, Taylor DA. Functional assessment of myoblast transplantation for cardiac repair with magnetic resonance imaging. *Eur J Heart Fail* 2005;7:435-43.
  17. Sebag IA, Handschumacher MD, Ichinose F, Morgan JG, Hataishi R, Rodrigues AC, Guerrero JL, Steudel W, Raheer MJ, Halpern EF, Derumeaux G, Bloch KD, Picard MH, Scherrer-Crosbie M. Quantitative assessment of regional myocardial function in mice by tissue Doppler imaging: comparison with hemodynamics and sonomicrometry. *Circulation* 2005;111:2611-6.
  18. Bove CM, Gilson WD, Scott CD, Epstein FH, Yang Z, Dimaria JM, Berr SS, French BA, Bishop SP, Kramer CM. The angiotensin II type 2 receptor and improved adjacent region function post-MI. *J Cardiovasc Magn Reson* 2005;7:459-64.
  19. Menasche P, Hagege AA, Vilquin JT, Desnos M, Abergel E, Pouzet B, Bel A, Sarateanu S, Scorsin M, Schwartz K, Bruneval P, Benbunan M, Marolleau JP, Duboc D. Autologous skeletal myoblast transplantation for severe postinfarction left ventricular dysfunction. *J Am Coll Cardiol* 2003;41:1078-83.
  20. Schaper W, Wüsten B. The collateral circulation of the heart. North-Holland Publishing Company, Amsterdam, 1971.
  21. Swindle MM. Swine as replacements for dogs in the surgical teaching and research laboratory. *Lab Anim Sci* 1984;34:383-5.
  22. Mc Kirnak MD, White FC, Guth BD, Bloor CM. Cardiovascular and metabolic responses to acute and chronic exercise in swine. In: *Swine in Biomedical research*, Ed: Tumbleson, ME, Plenum Press, New York and London, 1986, pp: 1379-4.
  23. Brasselet C, Morichetti MC, Messas E, Carrion C, Bissery A, Bruneval P, Vilquin JT, Lafont A, Hagege AA, Menasche P, Desnos M. Skeletal myoblast transplantation through a catheter-based coronary sinus approach: an effective means of improving function of infarcted myocardium. *Eur Heart J* 2005;26:1551-6.
  24. Ghostine S, Carrion C, Souza LC, Richard P, Bruneval P, Vilquin JT, Pouzet B, Schwartz K, Menasche P, Hagege AA. Long-term efficacy of myoblast transplantation on regional structure and function after myocardial infarction. *Circulation* 2002;106: I131-6.
  25. He KL, Yi GH, Sherman W, Zhou H, Zhang GP, Gu A, Kao R, Haimes HB, Harvey J, Roos E, White D, Taylor DA, Wang J, Burkhoff D. Autologous skeletal myoblast transplantation improved hemodynamics and left ventricular function in chronic heart failure dogs. *J Heart Lung Transplant* 2005;24:1940-9.

26. Amado LC, Saliaris AP, Schuleri KH, St John M, Xie JS, Cattaneo S, Durand DJ, Fitton T, Kuang JQ, Stewart G, Lehrke S, Baumgartner WW, Martin BJ, Heldman AW, Hare JM. Cardiac repair with intramyocardial injection of allogeneic mesenchymal stem cells after myocardial infarction. *Proc Natl Acad Sci USA* 2005;102:11474-9.
27. Kamihata H, Matsubara H, Nishiue T, Fujiyama S, Tsutsumi Y, Ozono R, Masaki H, Mori Y, Iba O, Tateishi E, Kosaki A, Shintani S, Murohara T, Imaizumi T, Iwasaka T. Implantation of bone marrow mononuclear cells into ischemic myocardium enhances collateral perfusion and regional function via side supply of angioblasts, angiogenic ligands, and cytokines. *Circulation* 2001;104:1046-52.
28. Silva GV, Litovsky S, Assad JA, Sousa AL, Martin BJ, Vela D, Coulter SC, Lin J, Ober J, Vaughn WK, Branco RV, Oliveira EM, He R, Geng YJ, Willerson JT, Perin EC. Mesenchymal stem cells differentiate into an endothelial phenotype, enhance vascular density, and improve heart function in a canine chronic ischemia model. *Circulation* 2005;111:150-6.
29. Reddy VY, Malchano ZJ, Holmvang G, Schmidt EJ, d'Avila A, Houghtaling C, Chan RC, Ruskin JN. Integration of cardiac magnetic resonance imaging with three-dimensional electroanatomic mapping to guide left ventricular catheter manipulation: feasibility in a porcine model of healed myocardial infarction. *J Am Coll Cardiol* 2004;44:2202-13.
30. Dick AJ, Guttman MA, Raman VK, Peters DC, Pessanha BS, Hill JM, Smith S, Scott G, McVeigh ER, Lederman RJ. Magnetic resonance fluoroscopy allows targeted delivery of mesenchymal stem cells to infarct borders in Swine. *Circulation* 2003;108:2899-904.
31. Baklanov DV, de Muinck ED, Simons M, Moodie KL, Arbuckle BE, Thompson CA, Palac RT. Live 3D echo guidance of catheter-based endomyocardial injection. *Catheter Cardiovasc Interv* 2005;65:340-5.
32. Hou D, Youssef EA, Brinton TJ, Zhang P, Rogers P, Price ET, Yeung AC, Johnstone BH, Yock PG, March KL. Radiolabeled cell distribution after intramyocardial, intracoronary, and interstitial retrograde coronary venous delivery: implications for current clinical trials. *Circulation* 2005;112:1150-6.
33. Freyman T, Polin G, Osman H, Crary J, Lu M, Cheng L, Palasis M, Wilensky RL. A quantitative, randomized study evaluating three methods of mesenchymal stem cell delivery following myocardial infarction. *Eur Heart J* 2006;27:1114-22.
34. Muller-Ehmsen J, Whittaker P, Kloner RA, Dow JS, Sakoda T, Long TI, Laird PW, Kedes L. Survival and development of neonatal rat cardiomyocytes transplanted into adult myocardium. *J Mol Cell Cardiol* 2002;34:107-16.
35. Christman KL, Vardanian AJ, Fang Q, Sievers RE, Fok HH, Lee RJ. Injectable fibrin scaffold improves cell transplant survival, reduces infarct expansion, and induces neovasculature formation in ischemic myocardium. *J Am Coll Cardiol* 2004;44:654-60.

36. Laflamme MA, Murry CE. Regenerating the heart. *Nat Biotechnol* 2005;23:845-56.
37. Suzuki K, Smolenski RT, Jayakumar J, Murtuza B, Brand NJ, Yacoub MH. Heat shock treatment enhances graft cell survival in skeletal myoblast transplantation to the heart. *Circulation* 2000;102:III216-21.
38. Suzuki K, Murtuza B, Beauchamp JR, Smolenski RT, Varela-Carver A, Fukushima S, Coppen SR, Partridge TA, Yacoub MH. Dynamics and mediators of acute graft attrition after myoblast transplantation to the heart. *FASEB J* 2004;18:1153-5.
39. Suzuki K, Murtuza B, Beauchamp JR, Brand NJ, Barton PJ, Varela-Carver A, Fukushima S, Coppen SR, Partridge TA, Yacoub MH. Role of interleukin-1beta in acute inflammation and graft death after cell transplantation to the heart. *Circulation* 2004;110:II219-24.
40. Maurel A, Azarnoush K, Sabbah L, Vignier N, Le Lorc'h M, Mandet C, Bissery A, Garcin I, Carrion C, Fiszman M, Bruneval P, Hagege A, Carpentier A, Vilquin JT, Menasche P. Can cold or heat shock improve skeletal myoblast engraftment in infarcted myocardium? *Transplantation* 2005;80:660-5.
41. Azarnoush K, Maurel A, Sebbah L, Carrion C, Bissery A, Mandet C, Pouly J, Bruneval P, Hagege AA, Menasche P. Enhancement of the functional benefits of skeletal myoblast transplantation by means of coadministration of hypoxia-inducible factor 1alpha. *J Thorac Cardiovasc Surg* 2005;130:173-9.
42. Zhang M, Methot D, Poppa V, Fujio Y, Walsh K, Murry CE. Cardiomyocyte grafting for cardiac repair: graft cell death and anti-death strategies. *J Mol Cell Cardiol* 2001;33:907-21.
43. Mangi AA, Noiseux N, Kong D, He H, Rezvani M, Ingwall JS, Dzau VJ. Mesenchymal stem cells modified with Akt prevent remodeling and restore performance of infarcted hearts. *Nat Med* 2003;9:1195-201.
44. Frangogiannis NG, Smith CW, Entman ML. The inflammatory response in myocardial infarction. *Cardiovasc Res* 2002;53:31-47.
45. Nian M, Lee P, Khaper N, Liu P. Inflammatory cytokines and postmyocardial infarction remodeling. *Circ Res* 2004;94:1543-53.
46. Li RK, Mickle DA, Weisel RD, Rao V, Jia ZQ. Optimal time for cardiomyocyte transplantation to maximize myocardial function after left ventricular injury. *Ann Thorac Surg* 2001;72:1957-63.
47. Bartunek J, Vanderheyden M, Vandekerckhove B, Mansour S, De Bruyne B, De Bondt P, Van Haute I, Lootens N, Heyndrickx G, Wijns W. Intracoronary injection of CD133-positive enriched bone marrow progenitor cells promotes cardiac recovery after recent myocardial infarction: feasibility and safety. *Circulation* 2005;112:I178-83.
48. Janssens S, Dubois C, Bogaert J, Theunissen K, Deroose C, Desmet W, Kalantzi M, Herbots L, Sinnaeve P, Dens J, Maertens J, Rademakers F, Dymarkowski S, Gheysens O, Van Cleemput J, Bormans G, Nuyts J, Belmans A, Mortelmans L, Boogaerts M, Van de Werf F. Autologous bone marrow-derived stem-cell transfer in patients with ST-

- segment elevation myocardial infarction: double-blind, randomised controlled trial. *Lancet* 2006;367:113-21.
49. Cleland JG, Freemantle N, Coletta AP, Clark AL. Clinical trials update from the American Heart Association: REPAIR-AMI, ASTAMI, JELIS, MEGA, REVIVE-II, SURVIVE, and PROACTIVE. *Eur J Heart Fail* 2006;8:105-10.
  50. Yau TM, Kim C, Li G, Zhang Y, Weisel RD, Li RK. Maximizing ventricular function with multimodal cell-based gene therapy. *Circulation* 2005;112:1123-8.
  51. Hutcheson KA, Atkins BZ, Hueman MT, Hopkins MB, Glower DD, Taylor DA. Comparison of benefits on myocardial performance of cellular cardiomyoplasty with skeletal myoblasts and fibroblasts. *Cell Transplant* 2000;9:359-68.
  52. Li RK, Jia ZQ, Weisel RD, Merante F, Mickle DA. Smooth muscle cell transplantation into myocardial scar tissue improves heart function. *J Mol Cell Cardiol* 1999;31:513-22.
  53. Van Meter CH Jr, Claycomb WC, Delcarpio JB, Smith DM, deGruiter H, Smart F, Ochsner JL. Myoblast transplantation in the porcine model: a potential technique for myocardial repair. *J Thorac Cardiovasc Surg* 1995;110:1442-8.
  54. Tomita S, Mickle DA, Weisel RD, Jia ZQ, Tumiati LC, Allidina Y, Liu P, Li RK. Improved heart function with myogenesis and angiogenesis after autologous porcine bone marrow stromal cell transplantation. *J Thorac Cardiovasc Surg* 2002;123:1132-40.
  55. Kamihata H, Matsubara H, Nishiue T, Fujiyama S, Amano K, Iba O, Imada T, Iwasaka T. Improvement of collateral perfusion and regional function by implantation of peripheral blood mononuclear cells into ischemic hibernating myocardium. *Arterioscler Thromb Vasc Biol* 2002;22:1804-10.
  56. Yokoyama S, Fukuda N, Li Y, Hagikura K, Takayama T, Kunimoto S, Honye J, Saito S, Wada M, Satomi A, Kato M, Mugishima H, Kusumi Y, Mitsumata M, Murohara T. A strategy of retrograde injection of bone marrow mononuclear cells into the myocardium for the treatment of ischemic heart disease. *J Mol Cell Cardiol* 2006;40:24-34.
  57. Nishida M, Li TS, Hirata K, Yano M, Matsuzaki M, Hamano K. Improvement of cardiac function by bone marrow cell implantation in a rat hypoperfusion heart model. *Ann Thorac Surg* 2003;75:768-73.
  58. Kocher AA, Schuster MD, Szabolcs MJ, Takuma S, Burkhoff D, Wang J, Homma S, Edwards NM, Itescu S. Neovascularization of ischemic myocardium by human bone-marrow-derived angioblasts prevents cardiomyocyte apoptosis, reduces remodeling and improves cardiac function. *Nat Med* 2001;7:430-6.
  59. Dohmann HF, Perin EC, Takiya CM, Silva GV, Silva SA, Sousa AL, Mesquita CT, Rossi MI, Pascarelli BM, Assis IM, Dutra HS, Assad JA, Castello-Branco RV, Drummond C, Dohmann HJ, Willerson JT, Borojevic R. Transendocardial autologous bone marrow mononuclear cell injection in ischemic heart failure: postmortem anatomicopathologic and immunohistochemical findings. *Circulation* 2005;112:521-6.

60. Tambara K, Sakakibara Y, Sakaguchi G, Lu F, Premaratne GU, Lin X, Nishimura K, Komeda M. Transplanted skeletal myoblasts can fully replace the infarcted myocardium when they survive in the host in large numbers. *Circulation* 2003;108:II259-63.
61. Shake JG, Gruber PJ, Baumgartner WA, Senechal G, Meyers J, Redmond JM, Pittenger MF, Martin BJ. Mesenchymal stem cell implantation in a swine myocardial infarct model: engraftment and functional effects. *Ann Thorac Surg* 2002;73:1919-25
62. Hiasa K, Egashira K, Kitamoto S, Ishibashi M, Inoue S, Ni W, Zhao Q, Nagata S, Katoh M, Sata M, Takeshita A. Bone marrow mononuclear cell therapy limits myocardial infarct size through vascular endothelial growth factor. *Basic Res Cardiol* 2004;99:165-72.
63. Uemura R, Xu M, Ahmad N, Ashraf M. Bone marrow stem cells prevent left ventricular remodeling of ischemic heart through paracrine signaling. *Circ Res* 2006;98:1414-21.
64. Takahashi M, Li TS, Suzuki R, Kobayashi T, Ito H, Ikeda Y, Matsuzaki M, Hamano K. Cytokines produced by bone marrow cells can contribute to functional improvement of the infarcted heart by protecting cardiomyocytes from ischemic injury. *Am J Physiol Heart Circ Physiol* April 2006; published online.
65. Gneocchi M, He H, Liang OD, Melo LG, Morello F, Mu H, Noiseux N, Zhang L, Pratt RE, Ingwall JS, Dzau VJ. Paracrine action accounts for marked protection of ischemic heart by Akt-modified mesenchymal stem cells. *Nat Med* 2005;11:367-8.
66. Sesti C, Hale SL, Lutzko C, Kloner RA. Granulocyte colony-stimulating factor and stem cell factor improve contractile reserve of the infarcted left ventricle independent of restoring muscle mass. *J Am Coll Cardiol* 2005;46:1662-9.
67. Gneocchi M, He H, Noiseux N, Liang OD, Zhang L, Morello F, Mu H, Melo LG, Pratt RE, Ingwall JS, Dzau VJ. Evidence supporting paracrine hypothesis for Akt-modified mesenchymal stem cell-mediated cardiac protection and functional improvement. *FASEB J* 2006;20:661-9.
68. Limbourg FP, Ringes-Lichtenberg S, Schaefer A, Jacoby C, Mehraein Y, Jager MD, Limbourg A, Fuchs M, Klein G, Ballmaier M, Schlitt HJ, Schrader J, Hilfiker-Kleiner D, Drexler H. Haematopoietic stem cells improve cardiac function after infarction without permanent cardiac engraftment. *Eur J Heart Fail* 2005;7:722-9.
69. Schachinger V, Assmus B, Honold J, Lehmann R, Hofmann WK, Martin H, Dimmeler S, Zeiher AM. Normalization of coronary blood flow in the infarct-related artery after intracoronary progenitor cell therapy: intracoronary Doppler substudy of the TOPCARE-AMI trial. *Clin Res Cardiol* 2006;95:13-22.
70. Rubart M, Soonpaa MH, Nakajima H, Field LJ. Spontaneous and evoked intracellular calcium transients in donor-derived myocytes following intracardiac myoblast transplantation. *J Clin Invest* 2004;114:775-83.
71. Agbulut O, Vandervelde S, Al Attar N, Larghero J, Ghostine S, Leobon B, Robidel E,

- Borsani P, Le Lorc'h M, Bissery A, Chomienne C, Bruneval P, Marolleau JP, Vilquin JT, Hagege A, Samuel JL, Menasche P. Comparison of human skeletal myoblasts and bone marrow-derived CD133+ progenitors for the repair of infarcted myocardium. *J Am Coll Cardiol* 2004;44:458-63.
72. Guarita-Souza LC, Carvalho KA, Rebelatto C, Senegaglia A, Hansen P, Furuta M, Miyague N, Francisco JC, Olandoski M, Faria-Neto JR, Oliveira SA, Brofman PR. Cell transplantation: Differential effects of myoblasts and mesenchymal stem cells. *Int J Cardiol* November 2005; published online.
73. Memon IA, Sawa Y, Miyagawa S, Taketani S, Matsuda H. Combined autologous cellular cardiomyoplasty with skeletal myoblasts and bone marrow cells in canine hearts for ischemic cardiomyopathy. *J Thorac Cardiovasc Surg* 2005;130:646-53.
74. Ott HC, Bonaros N, Marksteiner R, Wolf D, Margreiter E, Schachner T, Laufer G, Hering S. Combined transplantation of skeletal myoblasts and bone marrow stem cells for myocardial repair in rats. *Eur J Cardiothorac Surg* 2004;25:627-34.
75. Anderson SA, Lee KK, Frank JA. Gadolinium-fullerenol as a paramagnetic contrast agent for cellular imaging. *Invest Radiol* 2006;41:332-8.
76. Daldrup-Link HE, Rudelius M, Oostendorp RA, Settles M, Piontek G, Metz S, Rosenbrock H, Keller U, Heinzmann U, Rummeny EJ, Schlegel J, Link TM. Targeting of hematopoietic progenitor cells with MR contrast agents. *Radiology* 2003;228:760-7.
77. Prantner AM, Sharma V, Garbow JR, Piwnica-Worms D. Synthesis and characterization of a Gd-DOTA-D-permeation peptide for magnetic resonance relaxation enhancement of intracellular targets. *Mol Imaging* 2003;2:33-41.
78. Vuu K, Xie J, McDonald MA, Bernardo M, Hunter F, Zhang Y, Li K, Bednarski M, Guccione S. Gadolinium-rhodamine nanoparticles for cell labeling and tracking via magnetic resonance and optical imaging. *Bioconjug Chem* 2005;16:995-9.
79. Aicher A, Brenner W, Zuhayra M, Badorff C, Massoudi S, Assmus B, Eckey T, Henze E, Zeiher AM, Dimmeler S. Assessment of the tissue distribution of transplanted human endothelial progenitor cells by radioactive labeling. *Circulation* 2003;107:2134-9.
80. Brenner W, Aicher A, Eckey T, Massoudi S, Zuhayra M, Koehl U, Heeschen C, Kampen WU, Zeiher AM, Dimmeler S, Henze E. <sup>111</sup>In-labeled CD34+ hematopoietic progenitor cells in a rat myocardial infarction model. *J Nucl Med* 2004;45:512-8.
81. Hofmann M, Wollert KC, Meyer GP, Menke A, Arseniev L, Hertenstein B, Ganser A, Knapp WH, Drexler H. Monitoring of bone marrow cell homing into the infarcted human myocardium. *Circulation* 2005;111:2198-202.
82. Serganova I, Blasberg R. Reporter gene imaging: potential impact on therapy. *Nucl Med Biol* 2005;32:763-80.





# Chapter 12

## Summary - Samenvatting



## Summary

Heart failure after myocardial infarction (MI) is caused by the loss in cardiomyocytes and subsequent remodeling of the infarcted and remote myocardium. Transplanting cells into the infarct region that are able to differentiate and replace dead or dysfunctional cardiomyocytes and vasculature or can improve regional or global function through a reduction in adverse remodeling or by paracrine mechanisms could be a new, definitive therapy for cardiac ischemic injury. **Chapter 1** gives a general introduction to this topic and gives an overview of the present status of pre-clinical and clinical research. The next part focuses on animal models for cell transplantation studies. In **chapter 2** a novel model of MI is described in the mouse that can be useful for future cell transplantation studies. In this model part of the anterior wall is injured by freezing with a liquid nitrogen-cooled cryoprobe. The effect on systolic and diastolic heart function is assessed by echocardiography and left ventricular pressure measurements. Furthermore detailed histological analysis of the infarct area is performed. Functionally, cryoinjury results in a decrease in left ventricular pump function as well as diastolic function, which is accompanied by adverse left ventricular remodeling without overt heart failure. Histologically, cryoinjury results in well-defined, reproducible infarcts, with macrovascular reperfusion and large areas of microscopic no-reflow. Cell injection techniques are discussed in the next part of the thesis. In **chapter 3** a video-assisted thoracoscopic approach to myoblast transplantation is described that allows for direct visualization of the injection procedure in a pig model, without the morbidity associated with thoracotomy. The thesis then focuses on survival of cells after intracardiac transplantation. In **chapter 4** a study is presented describing the dynamics of myoblast death after transplantation using the mouse infarct model described in **chapter 2**. Cell necrosis and apoptosis are quantified using Alizarin Red and Tunel staining. Total cell number is quantified using DAPI staining. Furthermore, the effects of the anti-oxidant Tempol as well as the broad-spectrum caspase inhibitor ZVAD-FMK on necrosis and apoptosis are assessed. This study shows that necrosis is the predominant form of myoblast death, mainly occurring during the first 3 hours after transplantation, while apoptosis only plays a minor role. Necrosis can be reduced by co-administration of Tempol, implying an important role for oxidative stress in the acute phase of necrosis. Furthermore, this study shows that limited retention of the injected cells plays an important role. Functional assessment of cell transplantation is demonstrated in **chapters 5 and 6**. In these chapters two studies are described that investigate the functional benefits of myoblasts as well as myoblasts in comparison with mesenchymal stem cells (MSCs) in a model of cryoinjured rabbit heart. In **chapter 5**, primary myoblasts are injected 3 weeks after cryoinjury. Heart function and left ventricular and infarct geometry is assessed by magnetic resonance imaging (MRI) before cell injection and 4 weeks after injection. This study shows that myoblast transplantation restores regional wall thickening at the infarct site thereby improving 2D ejection fraction and reducing adverse global remodeling. In **chapter 6**, primary myoblasts as well as MSCs are injected 2 weeks after cryoinjury. Regional function at the infarct site is assessed by micromanometry and sonomicrometry before cell

injection and 4 weeks after injection. This study shows an improvement in regional stroke work after cell transplantation that is comparable in both cell groups. The next part of this thesis focuses on cell tracking using MRI. In **chapter 7** a new method for myoblast labeling using superparamagnetic iron oxide (SPIO) is investigated with cationic liposomes, normally used as transfection reagent and this method is compared with labeling without the use of this reagent. The effect of the labeling method with regard to proliferation, differentiation and toxicity is assessed. Furthermore, labeling efficiency is evaluated *in vitro* and *in vivo*. This study shows highly efficient label uptake by the use of cationic liposomes, without toxic effects or an effect on proliferation or differentiation and high contrast-inducing properties *in vitro* and *in vivo*. **Chapter 8 and 9** study the efficiency of the labeling method for single cell detection of fixed (**chapter 8**) and living (**chapter 9**) cells. These studies demonstrate the feasibility of using SPIO labeling to detect single fixed myoblasts in culture dishes as well as living human umbilical vein endothelial cells (HUVECs) although in this last study toxic effects affecting cell viability are observed as well as label loss over time. In **chapter 10** the potential hampering influence of hemorrhage degradation products within reperfused MI on SPIO-labeled cell tracking is studied. Reperfused infarcts are created in pigs and scanned *in vivo* and *ex vivo* 1 week and 5 weeks after infarction. Large areas of hemorrhage-induced signal voids are demonstrated *in vivo*, with a linear correlation between signal void size and areas of microvascular obstruction. *Ex vivo* the location of signal voids corresponds with hemosiderin deposits and obscures the detection of HUVECs injections, which are labeled using the protocol in **chapter 9**.

In **chapter 11** the results of the studies in this thesis are evaluated and the following conclusions are drawn: 1) The mouse cryoinfarction model is very suitable for future cell transplantation studies, 2) VATS cell transplantation is a promising alternative for patients when thoracotomy is not possible due to comorbidity, 3) cell death after transplantation in the acute setting of MI mainly occurs via necrosis as a result of oxidative stress, 4) myoblast transplantation restores wall thickening at the infarct site, arguing for a direct effect of transplanted cells on contractility of the infarct region, 5) both bone marrow-derived MSCs as well as myoblasts do improve regional systolic function after cryoinfarction to the same extent, 6) with MRI, detection and tracking of iron oxide-labeled, living, single cells is possible *in vitro* and 7) within reperfused myocardial infarcts, hemorrhage-induced signal voids hamper MRI detection of iron oxide-labeled cells. Furthermore, an outline for future studies is proposed.

## Samenvatting

Hartfalen na een myocard infarct (MI) wordt veroorzaakt door het verlies aan cardiomyocyten en daaropvolgende remodelering van het infarct gebied en het niet-geïnfarceerde myocardium. Het transplanteren van cellen in het infarct gebied die in staat zijn om te differentiëren en dode of dysfunctionele cardiomyocyten of bloedvaten te vervangen of die de regionale en globale hartfunctie verbeteren door een vermindering van remodelering of door paracriene mechanismen kan een nieuwe therapie zijn voor de gevolgen van ischemische hartziekten. **Hoofdstuk 1** geeft een algemene inleiding op dit onderwerp en geeft ook een overzicht van de huidige status van pre-klinisch en klinisch onderzoek. Het volgende deel van dit proefschrift gaat over nieuwe diermodellen voor cel transplantatie onderzoek. In **hoofdstuk 2** wordt een nieuw MI model in de muis beschreven dat geschikt is voor toekomstig onderzoek op het gebied van cel transplantatie. In dit model wordt een deel van de voorwand van het hart bevroren door gebruik te maken van een door stikstof gekoelde probe, het zogenaamde “vriesinfarct.” Het effect op de systolische en diastolische hartfunctie wordt onderzocht met behulp van echocardiografie en linker ventrikel druk meting, verder wordt het infarct gebied tot in detail histologisch geanalyseerd. Functioneel leidt dit infarct tot een afname van de linker ventrikel pompfunctie en een negatief effect op de diastolische functie, wat gepaard gaat met linker ventrikel remodelering, echter zonder gedecompenseerd hartfalen. Histologisch leidt het “vriesinfarct” tot scherp omschreven, reproduceerbare infarct gebieden met reperfusie op macrovasculair niveau en grote gebieden met microscopische “no-reflow”. Cel injectie technieken worden vervolgens besproken in het daarna volgende deel van het proefschrift. In **hoofdstuk 3** wordt een “video-assisted thoracoscopic” (VATS) benadering van myoblast transplantatie onderzocht die het mogelijk maakt om de injectie procedure direct te visualiseren in een varkens model, zonder de morbiditeit die gepaard gaat met thoracotomie. De overleving van cellen na transplantatie is het onderwerp van het vierde deel van dit proefschrift. In **hoofdstuk 4** wordt een studie beschreven van het verloop van myoblast sterfte na transplantatie in het muizen infarct model zoals beschreven in **hoofdstuk 2**. Cel necrose en apoptose worden respectievelijk gekwantificeerd met Alizarin rood kleuring en Tunel kleuring. Het totale aantal cellen wordt gekwantificeerd door gebruik te maken van DAPI kleuring. Verder wordt het effect van de anti-oxidant Tempol en de apoptose remmer ZVAD-FMK op necrose en apoptose onderzocht. Deze studie toont aan dat necrose de belangrijkste vorm van myoblast sterfte is, die voornamelijk optreedt tijdens de eerste 3 uur na transplantatie, terwijl apoptose slechts een ondergeschikte rol speelt. Necrose kan beperkt worden door gelijktijdige toediening van Tempol, wat een belangrijke rol voor oxidatieve stress impliceert in de acute fase van cel necrose. Verder toont deze studie aan dat de retentie van cellen na injectie zeer beperkt is. Het functionele effect van cel transplantatie wordt onderzocht in de **hoofdstukken 5 en 6**. Daar worden 2 studies beschreven die het functionele effect van zowel myoblasten als mesenchymale stam cellen (MSCs) beschrijven in een vriesinfarct model in het konijn. In **hoofdstuk 5** werden primaire myoblasten geïnjecteerd 3 weken na het vriesinfarct. Hartfunctie en linker ventrikel- en

infarct geometrie worden bepaald met “magnetic resonance imaging” (MRI) voorafgaand aan de myoblasten injectie en 4 weken na injectie. Deze studie toont aan dat transplantatie van myoblasten de regionale wand verdikking verbetert op de plaats van het infarct en daardoor voor een toename van de 2D ejectie fractie zorgt en de globale remodelering vermindert. In **hoofdstuk 6** worden zowel primaire myoblasten als MSCs geïnjecteerd 2 weken na het vriesinfarct. De regionale functie op de plaats van het infarct gebied wordt bepaald met micromanometrie en sonomicrometrie voorafgaande aan de cel injectie en 4 weken na injectie. Deze studie toont een verbetering aan in regionale “stroke work”, die vergelijkbaar is voor beide cel typen. In het laatste gedeelte van het proefschrift wordt het detecteren en volgen van cellen met behulp van MRI bestudeerd. In **hoofdstuk 7** wordt een nieuwe methode om myoblasten te labelen met “superparamagnetic iron oxide” (SPIO) onderzocht door gebruik te maken van catione liposomen, die normaal gebruikt worden om cellen te transfecteren. Deze labeling methode wordt vergeleken met een methode zonder gebruik te maken van deze liposomen. Het effect van deze labeling methode op cel proliferatie, differentiatie en cel toxiciteit wordt onderzocht. Verder wordt de labeling efficiëntie geëvalueerd zowel *in vitro* als *in vivo*. Deze studie toont een zeer efficiënte opname van het label aan door gebruik te maken van deze liposomen, zonder toxische bijwerkingen of een nadelig effect op cel proliferatie of differentiatie en daarnaast een sterk effect op het MRI signaal *in vitro* en *in vivo*. In **hoofdstukken 8 en 9** wordt de efficiëntie bestudeerd van deze labeling methode om een solitaire gefixeerde of levende cel te detecteren. Deze studies demonstreren de mogelijkheid om SPIO labeling te gebruiken voor het detecteren van zowel één gefixeerde cel in celkweek als enkele levende cellen gedurende enkele dagen, hoewel in de laatste studie een toxisch effect van de labeling methode wordt geconstateerd die cel sterfte veroorzaakt. Verder wordt verlies van het label gezien na een aantal dagen. In **hoofdstuk 10** wordt de potentieel nadelige invloed bestudeerd die afbraakproducten van hemorragie in gereperfundeerde myocard infarcten kunnen hebben op het detecteren van SPIO gelabelde cellen. Gereperfundeerde infarcten worden gecreëerd in varkens en de harten worden vervolgens gescand met MRI 1 week en 5 weken na het infarct. Grote hemorrhagische gebieden worden gezien die signaal verlies veroorzaken, met een sterke relatie tussen de grootte van de gebieden en het gebied met microvasculaire obstructie. Op *ex vivo* scans corresponderen de gebieden met signaal verlies met de aanwezigheid van hemosiderine deposities die het onmogelijk maken met SPIO gelabelde “human umbilical vein endothelial cells” (HUVECs) (**hoofdstuk 9**) te detecteren.

In **hoofdstuk 11** worden de resultaten van deze studie geëvalueerd en de volgende conclusies getrokken: 1) Het cryoinfarct model in de muis is zeer bruikbaar voor toekomstige cel transplantatie studies, 2) VATS cel transplantatie is een veelbelovend alternatief voor patiënten met veel comorbiditeit, 3) cel sterfte na transplantatie in een acuut myocard infarct is het gevolg van necrose als een gevolg van oxidatieve stress, 4) myoblast transplantatie herstelt wand verdikking op de plaats van het infarct, wat suggereert dat de cellen een direct effect hebben op de contractiliteit op de plaats van het infarct, 5) zowel uit beenmerg

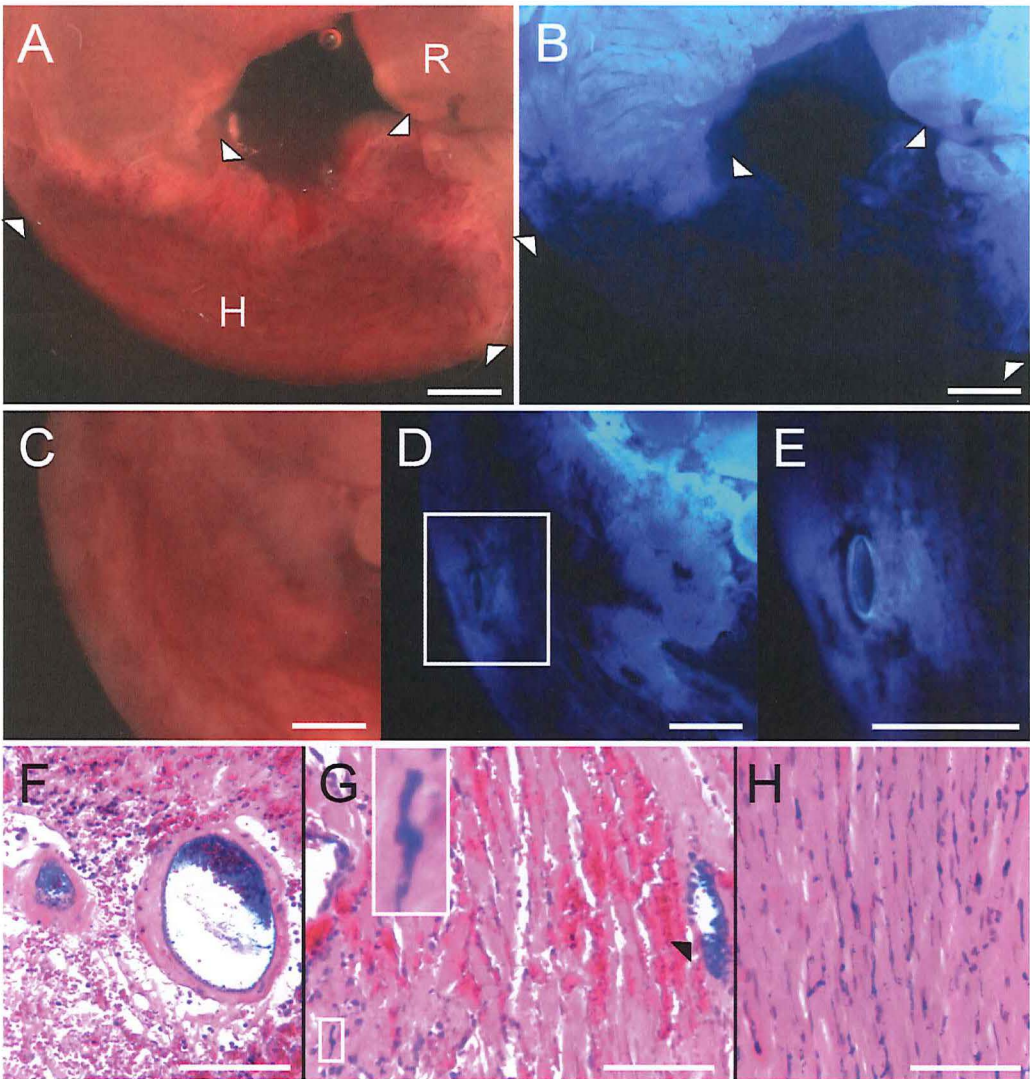
verkregen MSCs als myoblasten hebben een vergelijkbaar gunstig effect op de regionale systolische functie, 6) met MRI is de detectie en het vervolgen van met SPIO gelabelde, levende, solitaire cellen mogelijk en 7) in gereperfundeerde myocard infarcten wordt de detectie van SPIO gelabelde cellen bemoeilijkt door de aanwezigheid van hemorrhagie geïnduceerde hemosiderine deposities. Verder wordt een voorstel gedaan voor toekomstige studies.



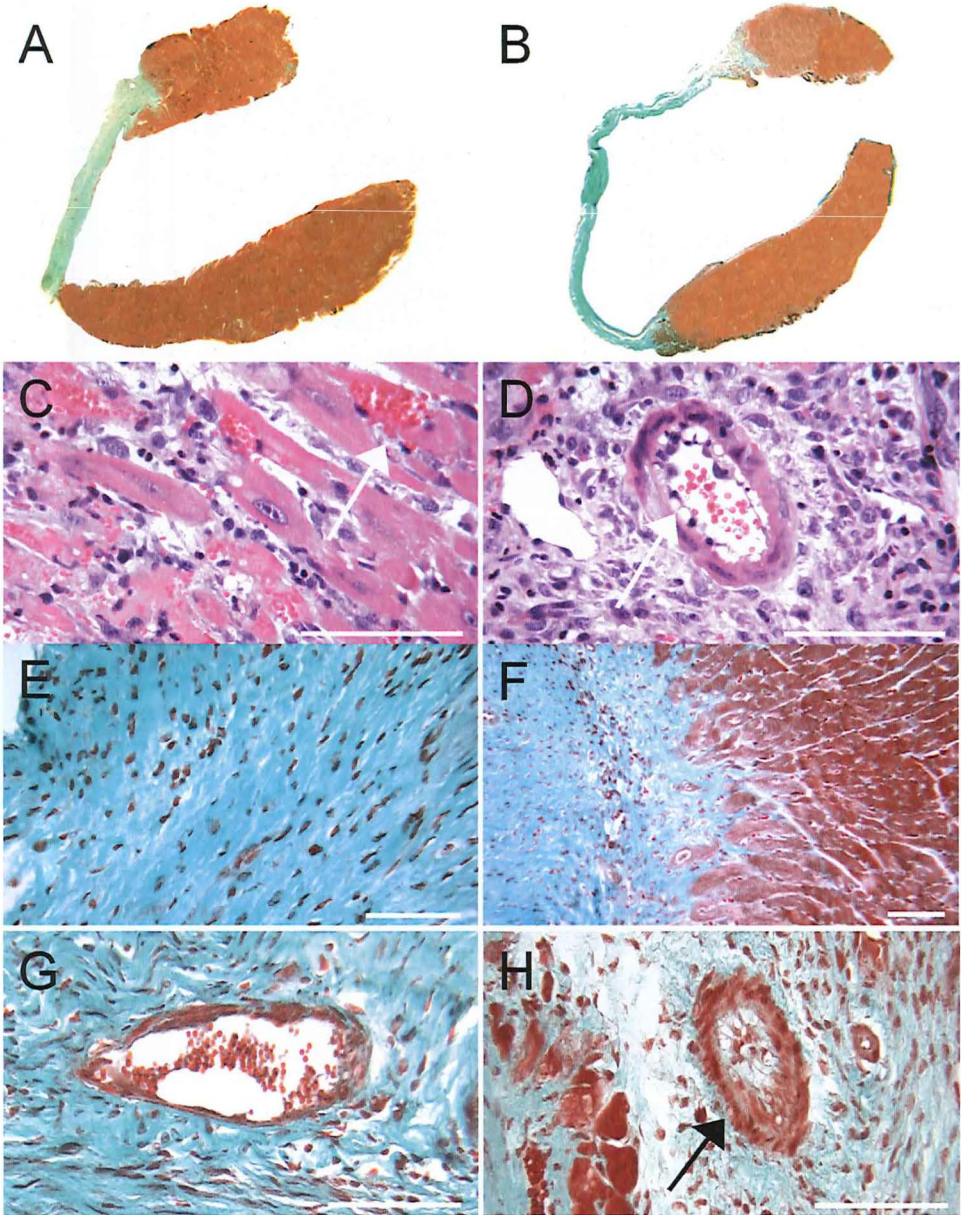
# Chapter 13

## Colour section

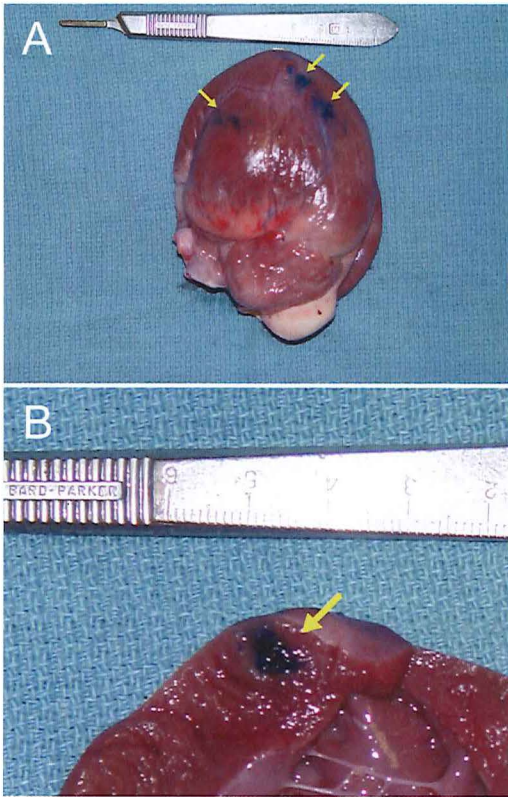




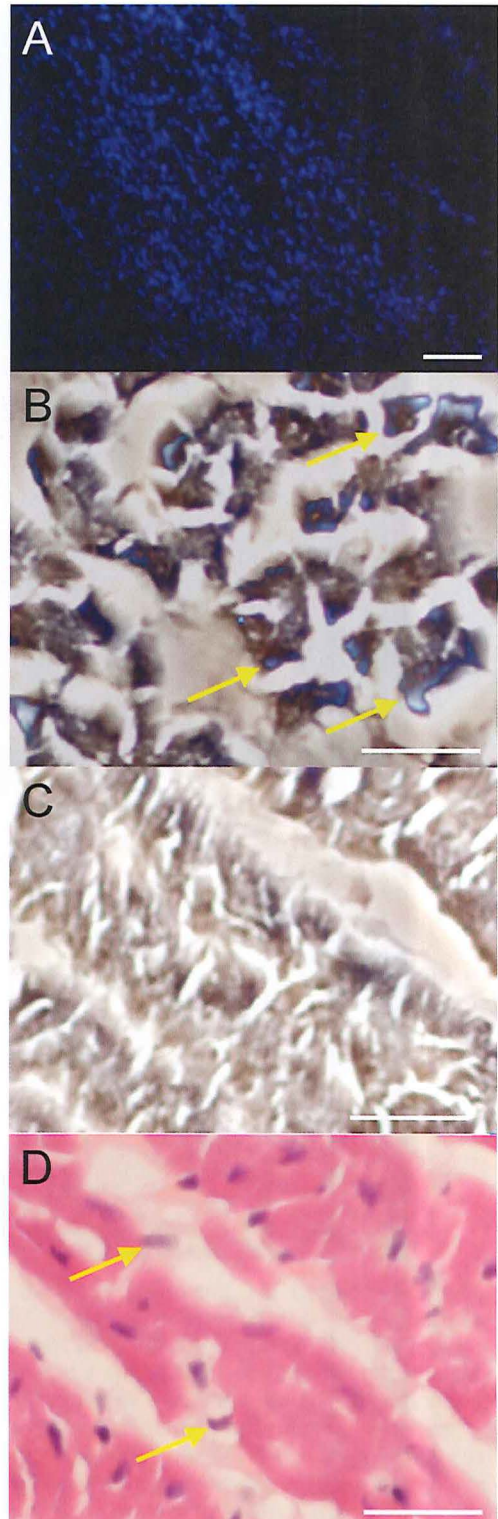
Chapter 2 - Figure 3. Panel A shows a 3 mm cryoinfarction after 2 days (delineated by white arrows). A large area of hemorrhage occupies the infarct center (indicated by H). R indicates remote healthy myocardium. The corresponding view under ultraviolet light is shown in Panel B: The infarct area is not stained indicating no-reflow caused by microvascular damage. Panel C shows a 3 mm cryoinfarction of a different heart. Less hemorrhage is visible. The corresponding view under ultraviolet light is shown in Panel D. The boxed region containing the LAD is shown at higher magnification in Panel E: Both the LAD and a small region around it are reperfused. Unisperse Blue was found in the LAD and larger vessels in all animals (arrow; Panel F and G, HE stain). Capillary reperfusion was selectively found along the endocardial borders (boxed region; Panel G, HE stain). Panel H shows reperfused capillaries in the remote non-infarcted myocardium. Bar represents 5 mm in Panels A to E and 100  $\mu\text{m}$  in Panels F to H.



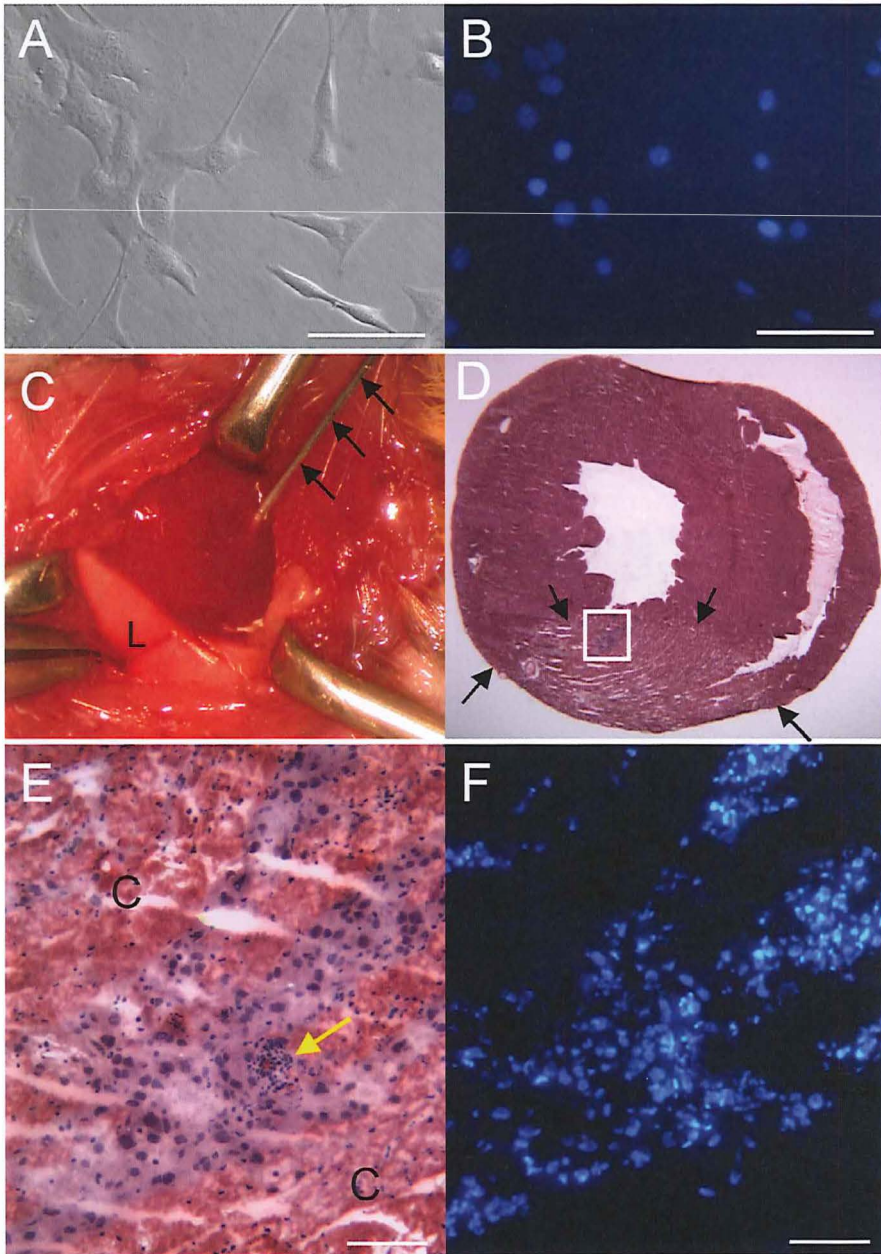
Chapter 2 - Figure 4. Panel A shows a 3 mm cryoinfarction at 8 weeks (MT stain). The infarct area is green. The infarct is smaller and thicker when compared with the 8-week old ligation infarct in Panel B. Panel C and D show a HE stain of a 4-day old cryoinfarct. Areas of hemorrhage (arrow) and a dense inflammatory infiltrate were observed (Panel C). Further, vascular lacunae were visible with endothelial discontinuities (arrow; Panel D). Four weeks after cryoinfarction a transmurular, paucicellular scar had formed, with short transition zones to healthy myocardium (Panel E and F, MT stain). At 8 weeks, the LAD was patent in all cryoinfarcted animals (Panel G, MT stain); in contrast, obliteration of the LAD and larger vessels was invariably observed in the ligation infarcts (arrow; Panel H, MT stain). Bar represents 100  $\mu$ m.



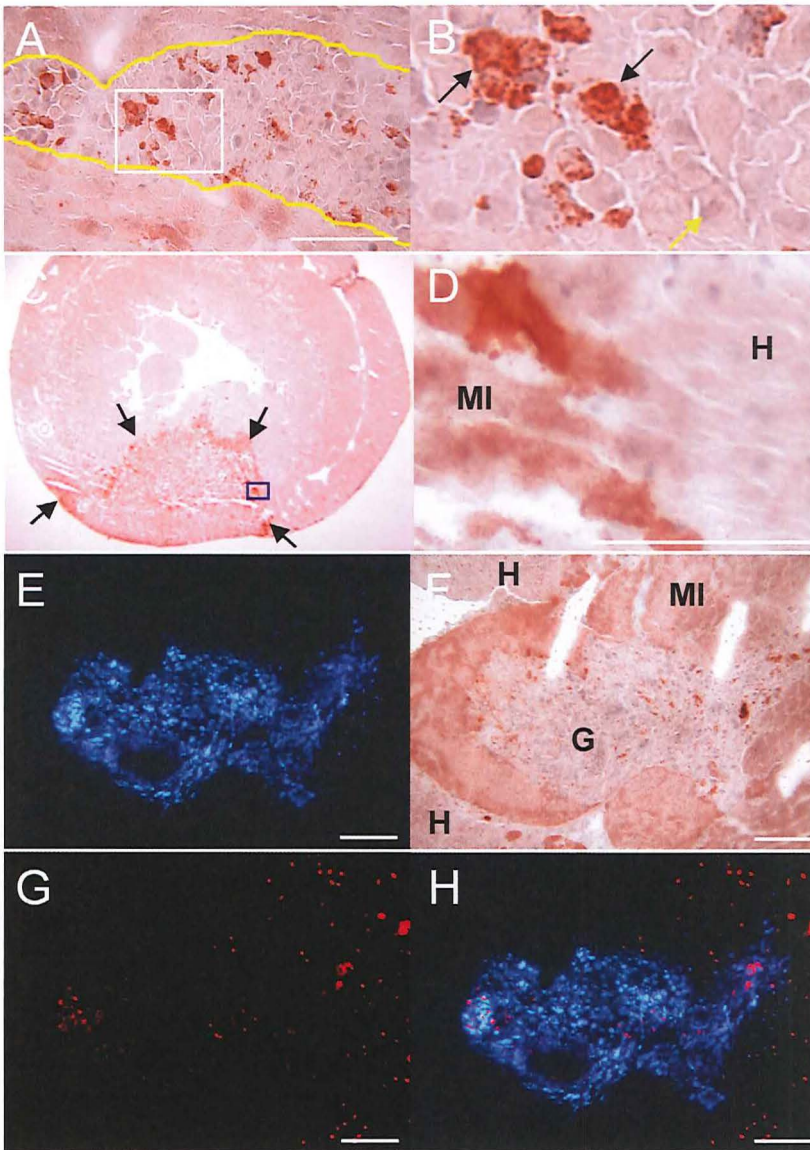
Chapter 3 - Figure 2. A representative explanted heart 4 hours post injection of  $2.5 \times 10^6$  myoblasts in each of four sites (posterior not visible) (Panel A), showing transmurial injection of pthalo blue dye (Panel B). Arrows indicate injected areas.



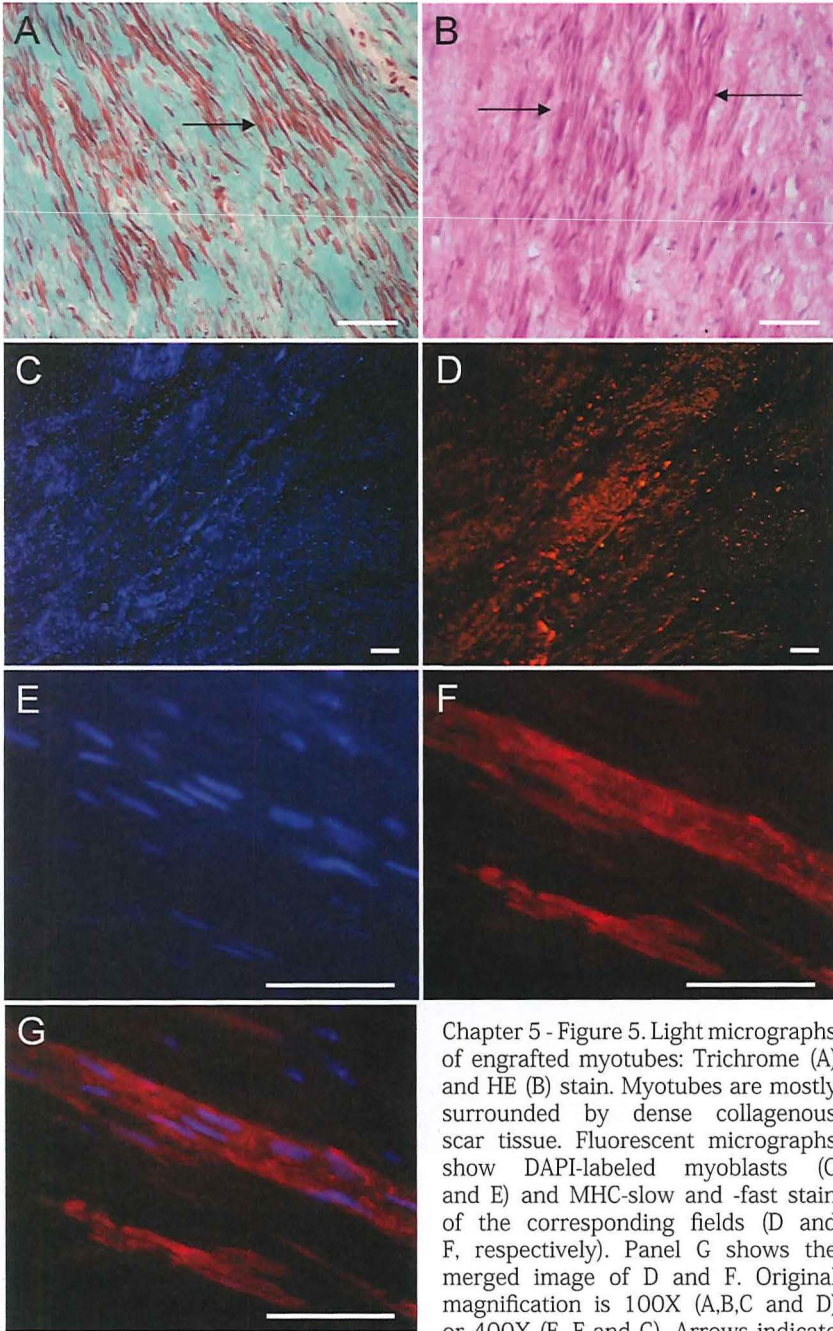
Chapter 3 - Figure 3. DAPI-labeled (Panel A) myoblasts directly injected into myocardium. Iron oxide-labeled (Panel B) skeletal myoblasts appear blue after Prussian Blue staining. Panel C is a negative control of a non-injected area. Panel D is an HE stain of the same area as in Panel B. Arrows indicate injected cells. Original magnification 200X. Bar indicates 100  $\mu$ m.



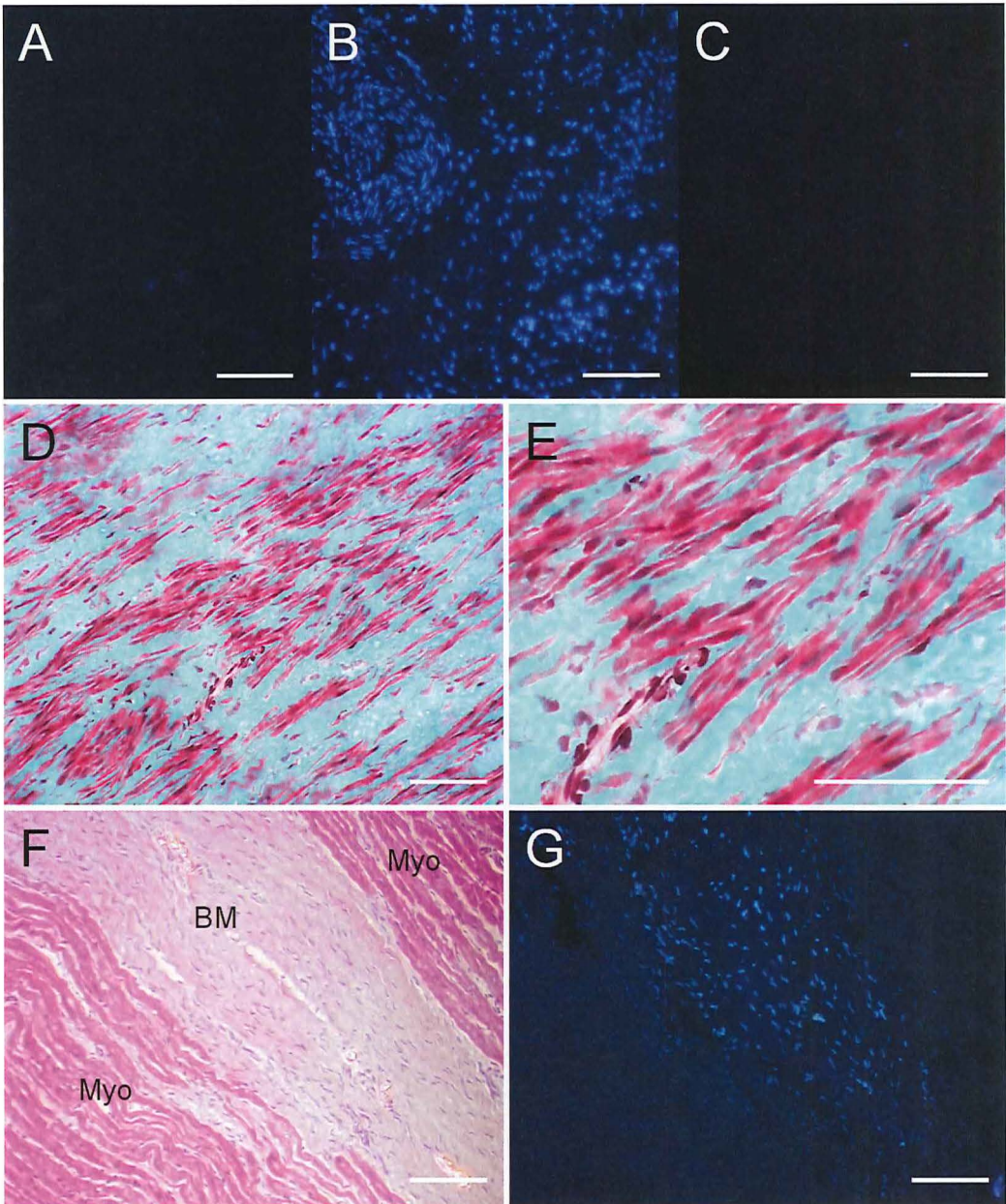
Chapter 4 - Figure 1.  $C_2C_{12}$  myoblasts (Panel A) were labeled overnight with DAPI (Panel B, same field) before injection. Cells were injected with a 30G needle (black arrows) into the centre and border of a cryoinfarction 5 minutes after injury (Panel C). The infarct area is visible as a dark, purple circle. L indicates the left lung. Panel D shows a hematoxylin-eosin stain of a transverse section through the cryoinfarction 6 hours after myoblast injection. The infarct area is indicated by black arrows. The boxed region contains the grafted area and is shown at higher magnification in Panel E. Grafted cells have larger nuclei than the surrounding necrotic cardiomyocytes (indicated by C). A small group of inflammatory cells is indicated by the yellow arrow. Panel F shows the fluorescence image of the same field: Grafted cells are identified by the blue nuclear DAPI stain. Bar indicates 100  $\mu$ m.



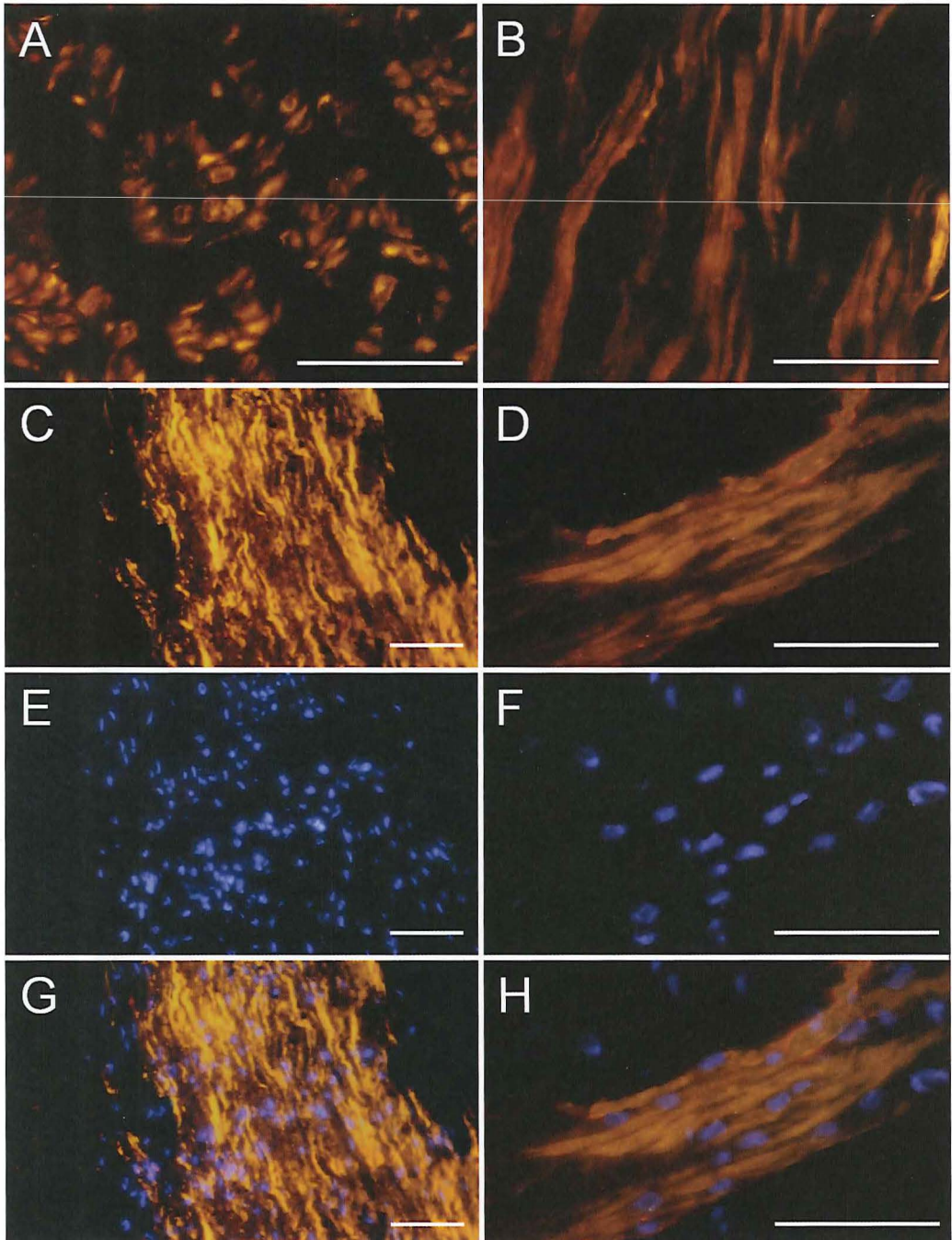
Chapter 4 - Figure 2. Panel A shows an Alizarin Red (AR) staining of an area with grafted myoblasts 3 hours after injection. The graft is delineated by the yellow line. The boxed region is shown in Panel B at higher magnification. Necrotic myoblasts stain deep red as a result of intracellular calcium uptake (black arrows). Necrotic myoblasts are surrounded by healthy, unstained myoblasts. Nuclei stain faintly grey (yellow arrow). Panel C shows an AR stain of a transverse section through a cryoinfarction, 3 hours after injection: The cone-shaped infarct area takes up the red stain and can therefore be discerned from the healthy remote myocardium. The boxed region is shown in Panel D at higher magnification. Necrotic cardiomyocytes in the infarct border (indicated by MI) also stain deep red, contrasting with the pink, healthy surrounding myocardium (indicated by H). Panel E shows a myoblast graft, 6 hours after injection. The corresponding region after AR staining is shown in Panel F. The graft is indicated by G, the cryoinfarcted area by MI and the healthy, surrounding myocardium by H. Panel G shows the same section as in Panel E after TUNEL staining. Apoptotic nuclei are red. An overlay of Panels E and G is shown in Panel H. Bar indicates 100  $\mu\text{m}$ .



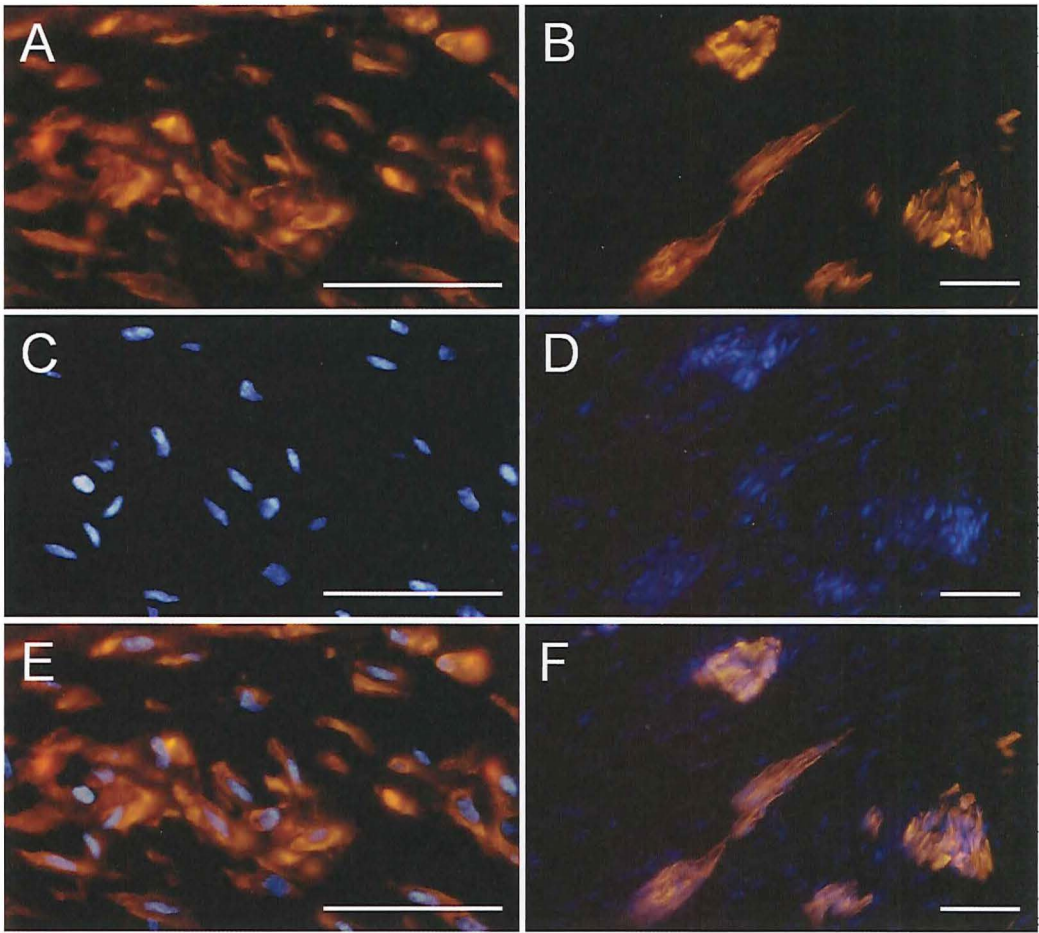
Chapter 5 - Figure 5. Light micrographs of engrafted myotubes: Trichrome (A) and HE (B) stain. Myotubes are mostly surrounded by dense collagenous scar tissue. Fluorescent micrographs show DAPI-labeled myoblasts (C and E) and MHC-slow and -fast stain of the corresponding fields (D and F, respectively). Panel G shows the merged image of D and F. Original magnification is 100X (A,B,C and D) or 400X (E, F and G). Arrows indicate engrafted myotubes. Bar indicates 100  $\mu$ m.



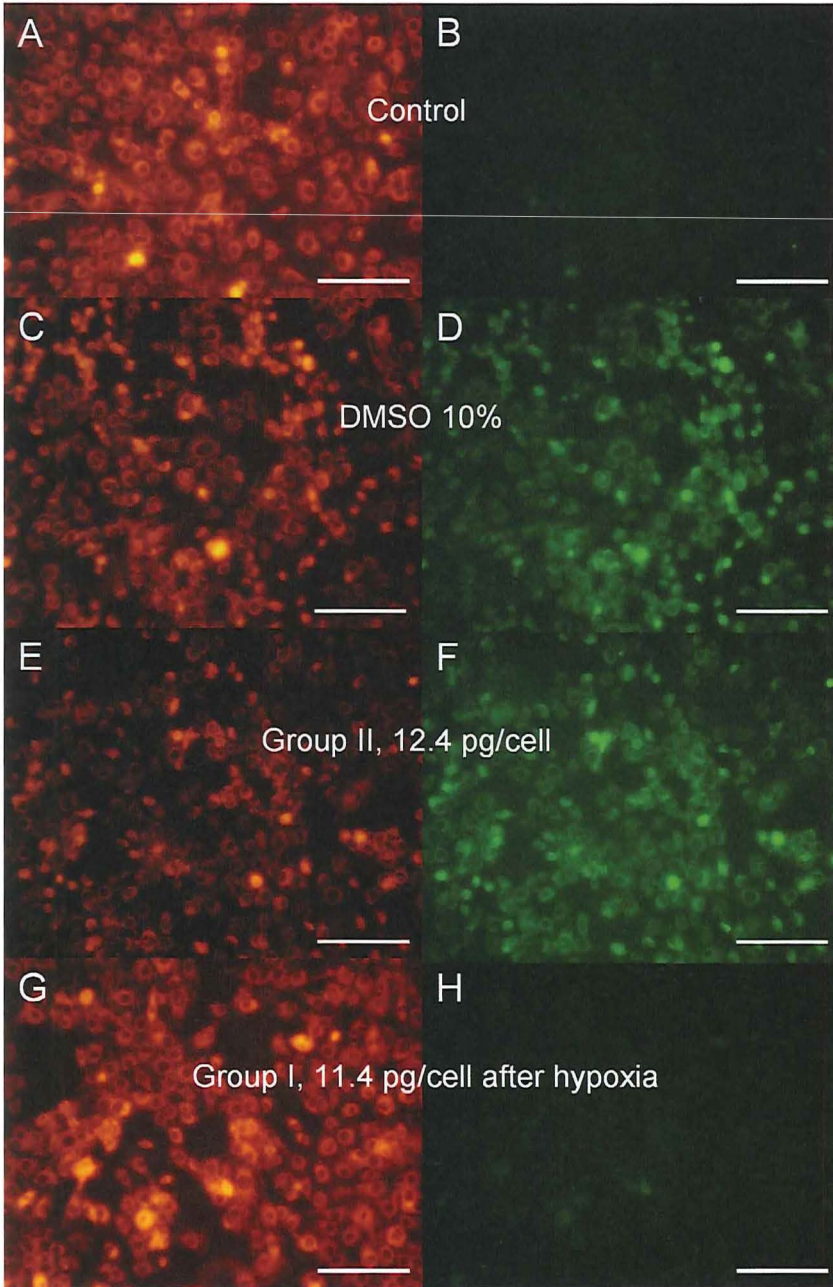
Chapter 6 - Figure 3. Fluorescence micrograph of a control heart (Panel A), a bone marrow engrafted heart (Panel B) and a heart injected with lysed, labeled cells (Panel C; 200X, original magnification). The DAPI nuclear blue stain is easily identified in Panel B. Panel D (200X) and E (400X) show a Trichrome staining of myoblast engrafted hearts. There is myotube formation with peripheral nuclei surrounded by dense collagen rich fibrous tissue in the center of the scar. Normal light and corresponding fluorescence micrographs (F and G) of engrafted bone marrow cells (BM) show close contact of cells with the healthy myocardium (Myo). Panel F is hematoxylin-eosin staining and G is DAPI filtered. Bar represents 100 μm.



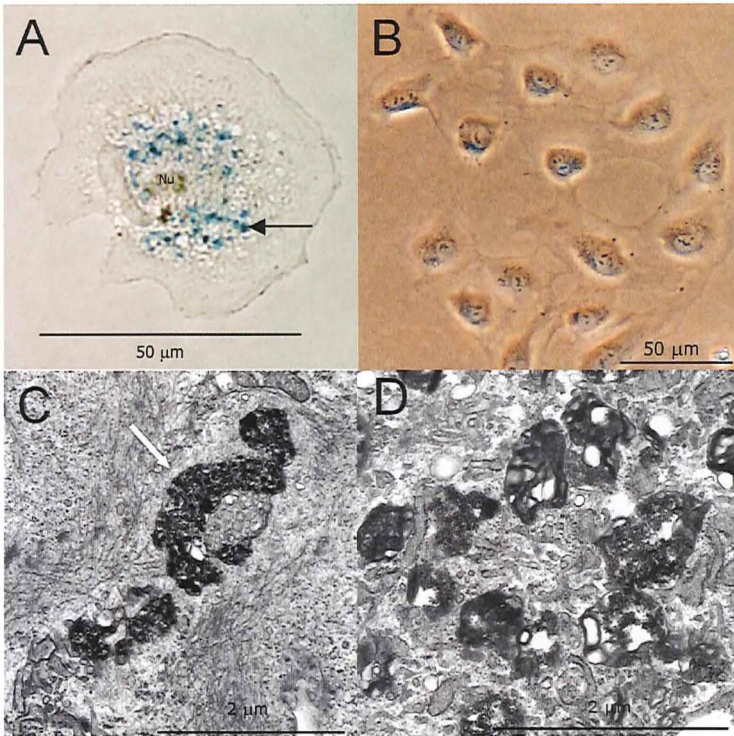
Chapter 6 - Figure 4. Fluorescence micrographs of sections of scar engrafted with myoblasts. Desmin staining shows that injected myoblasts form patches of unfused single cells (A) or patches of myotubes (B) throughout the scar area (400X). Engrafted myoblasts (identified by their DAPI blue nuclear staining) further show positive immunostaining for the slow (C and E; G is a merged image; 200X) and fast isoform of myosin heavy chain (D and F; H is a merged image; 400X). Bar represents 100  $\mu$ m.



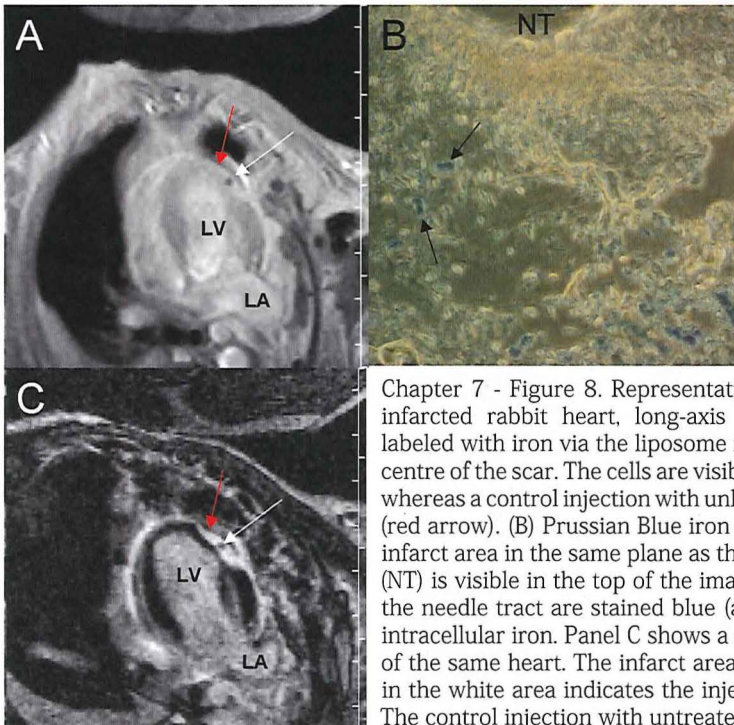
Chapter 6 - Figure 5. Sections of scar engrafted with bone marrow-derived cells showing patches of positive staining for sarcomeric actin (A and C) throughout the scar area (400X). Panel E presents a merged image showing the colocalization of the DAPI blue nuclear staining. Panels B and D shows desmin staining, where F is the merged image (200X). Bar represents 100  $\mu\text{m}$ .



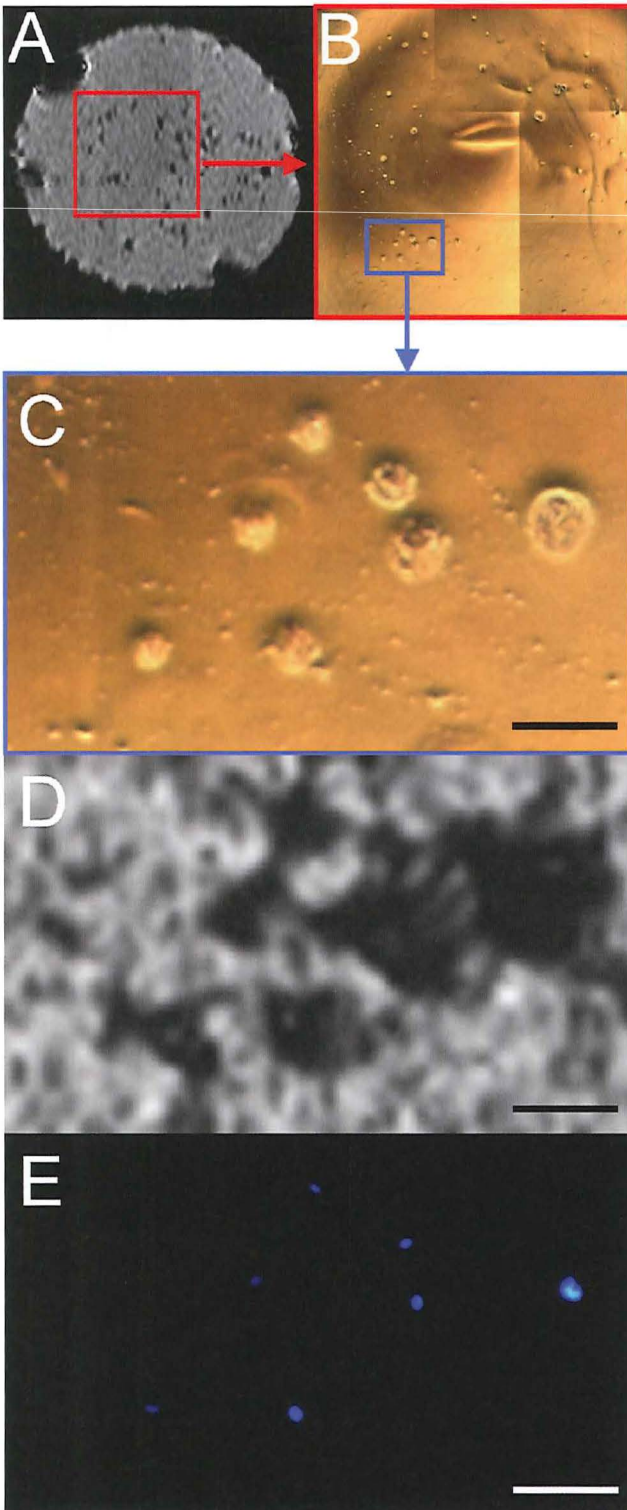
Chapter 7 - Figure 6. Red and green fluorescence after staining with BODIPY® 581/591 C<sub>11</sub>. (A and B) Control myoblasts during normal growth show no red to green shift. (C and D) Myoblasts treated with 10% DMSO in growth medium for 30 minutes; a shift in red to green ratio is observed, indicating lipid oxidation, comparable with the situation 24 hours after incubation with 20 mg Feridex without liposomes (Group II, 12.4 pg iron per cell; E and F). (G and H) Myoblasts after incubation with 100 µg Feridex with liposomes (Group I, 11.3 pg iron per cell) and 48 hours hypoxia and 3 hours reoxygenation, which causes a small increase in lipid oxidation, as calculated by the red to green ratio, which is comparable with control cells in hypoxia. Bar indicates 250 µm.



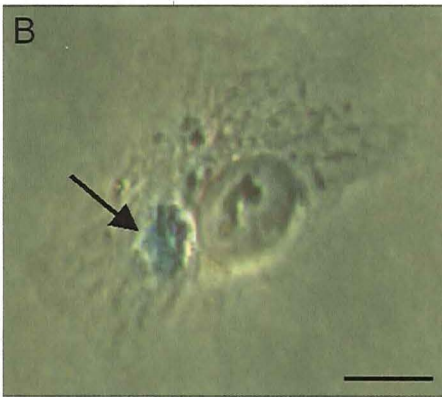
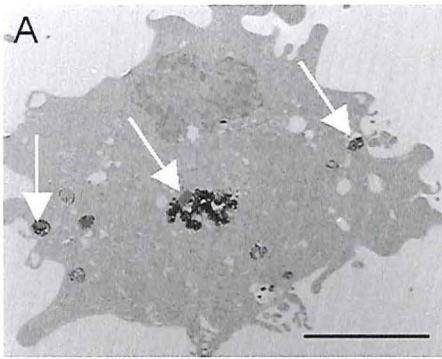
Chapter 8 - Figure 1. Optical microscope view of pig myoblasts stained with Prussian blue to demonstrate the uptake of SPIO particles (Panel A and B). SPIO particles are visible as blue iron deposits (arrow) around the nucleus (Nu) in Panel A. No intranuclear or extracellular uptake of SPIOs could be detected. Panel C and D show electron microscopy images (14000X and 20000X, respectively) with a conglomeration of SPIOs within membrane-bound vacuoles (arrow). The particle size of a single SPIO is 150 nm with an iron oxide core of 4 nm. The size of the organelle here, on the order of 2 μm, therefore demonstrates a high particle density.



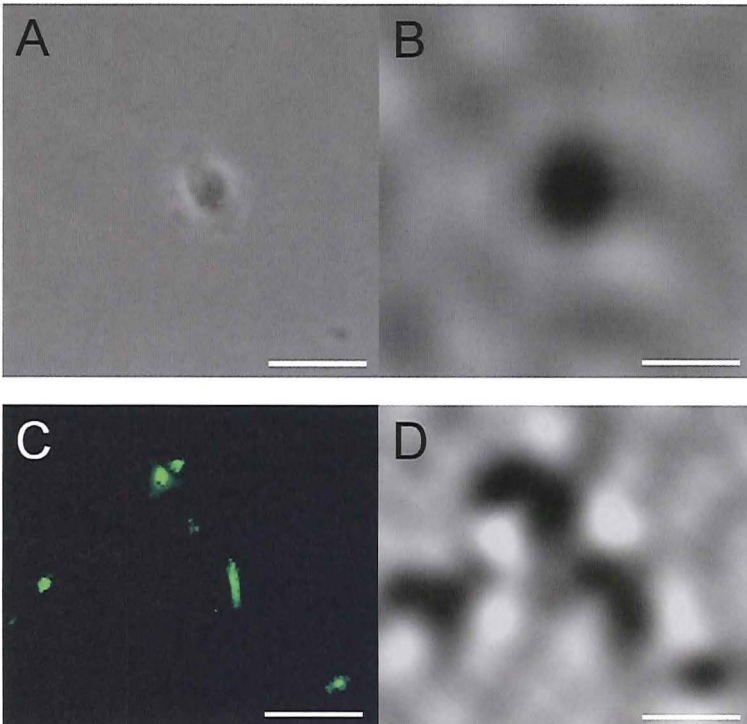
Chapter 7 - Figure 8. Representative cine MRI image of a cryo-infarcted rabbit heart, long-axis view. Autologous myoblasts labeled with iron via the liposome method were injected into the centre of the scar. The cells are visible as a black dot (white arrow), whereas a control injection with unlabeled myoblasts is not visible (red arrow). (B) Prussian Blue iron stain of a section through the infarct area in the same plane as the MRI image. The needle tract (NT) is visible in the top of the image. Myoblasts migrating from the needle tract are stained blue (arrows), which is indicative of intracellular iron. Panel C shows a contrast enhanced MRI image of the same heart. The infarct area appears white. The black dot in the white area indicates the injected myoblasts (white arrow). The control injection with untreated myoblasts is not visible (red arrow). LV indicates left ventricle, LA indicates left atrium.



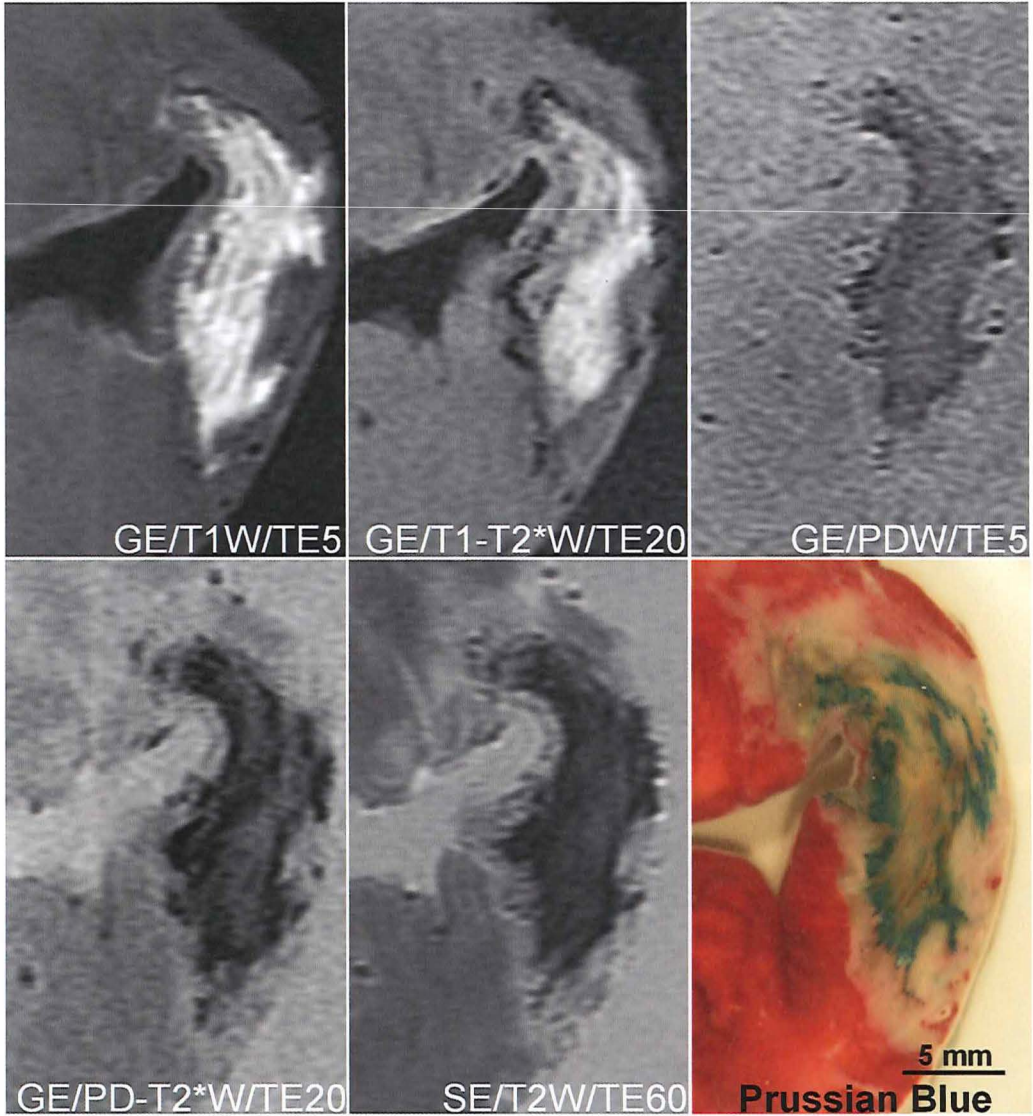
Chapter 8 - Figure 3. Slice obtained from the 3D SPGR acquisition of the SPIO-labeled cell suspension with 225 cells ( $0.0225 \times 10^3/\mu\text{l}$  concentration). Cells appear as black signal voids. Signal enhancement around the cells can also be observed from the magnetic susceptibility gradients induced. Imaging parameters: TR=108.00 ms, TE=15.36 ms (partial echo), flip angle=60°, FOV=1.0x1.0 cm<sup>2</sup>, matrix=512x384, NEX=8.0 and scan time=3 hours. Scanned resolution=19.5x19.5x100.0  $\mu\text{m}^3$ . Reconstructed resolution=19.5x19.5x100.0  $\mu\text{m}^3$ .



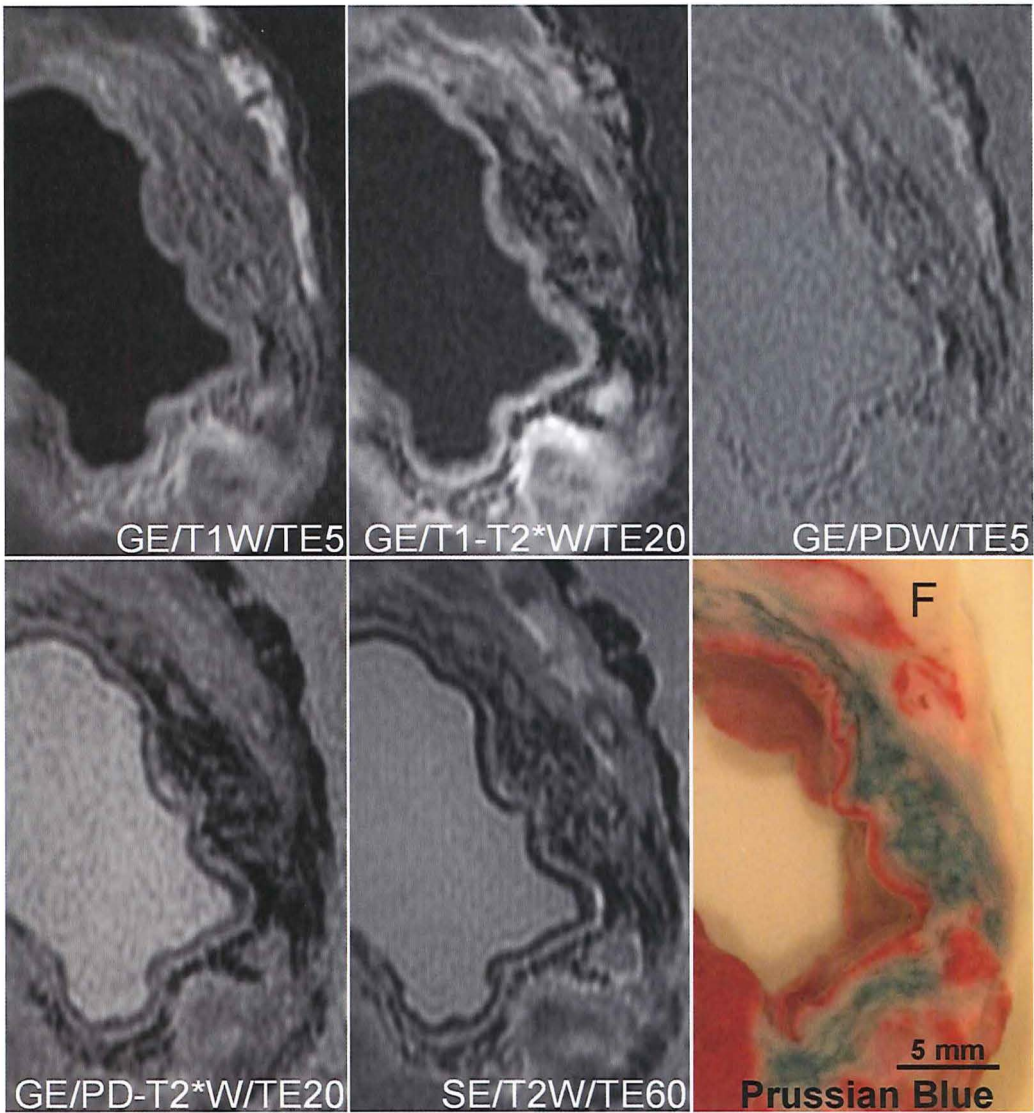
Chapter9 - Figure 1. Panel A shows an electron microscope image of a single SPIO-labeled HUVEC, demonstrating accumulation of iron particles in membrane-bound organelles (arrows). Original magnification 5600X. Panel B shows a normal light image of a Prussian blue stain. Iron is visible as perinuclear blue spots (black arrow). Bar represents 10  $\mu\text{m}$ .



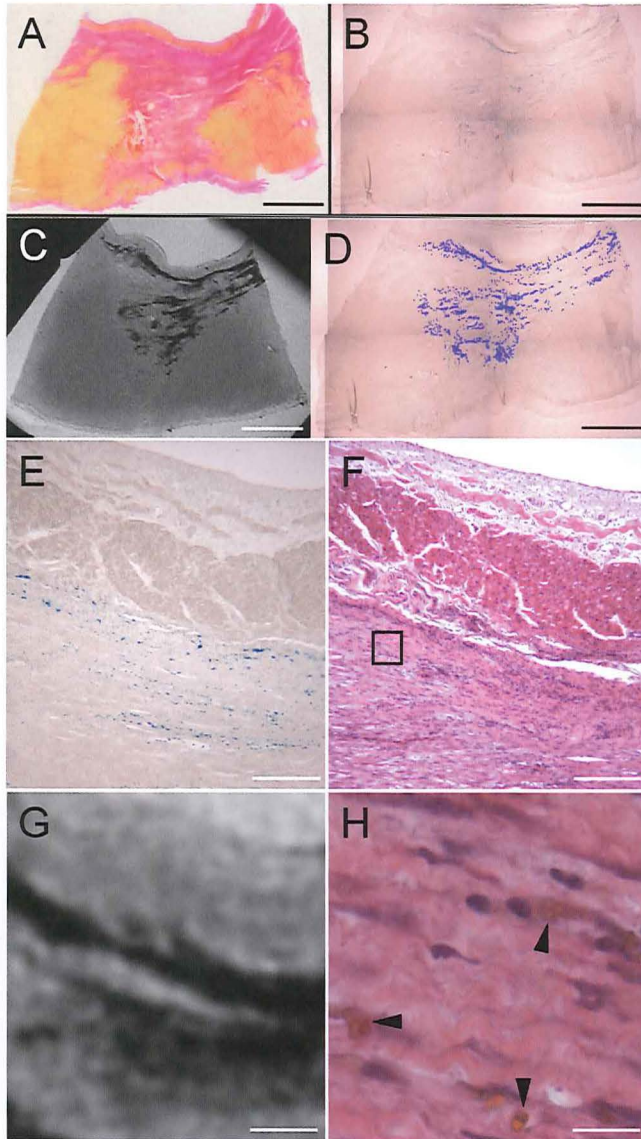
Chapter 9 - Figure 5. Panel A and C show normal light and fluorescent microscopy images of different samples at day 1 with corresponding MR images in Panel B and D, respectively. MR imaging parameters were as follows: TR=37.2 ms, TE=10.54 ms, flip angle=50°, FOV=2x2 cm<sup>2</sup>, matrix=512x416, NEX=1.0, and scan time=13 minutes. Resolution=39x48x100  $\mu\text{m}^3$ .



Chapter 10 - Figure 3. *Ex vivo* scans 1 week after infarction using different types of tissue contrast: T1W, PDW, T2W and T2\*W with a TE of 5, 20 or 60 ms (TE5, TE20 or TE60, respectively). Either a gradient echo (GE) or spin echo (SE) sequence was used. A ring of black signal voids is identified best in the T1W scan with a TE of 20 ms (T1-T2\*W). It corresponds with the blue hemosiderin deposits in the Prussian blue image. The ring surrounds a hyperenhanced area on T1W scans, which is hypoenhanced on SE/T2 and PD-T2\*W scans, corresponding with methemoglobin within intact erythrocytes.



Chapter 10 - Figure 4. *Ex vivo* scans 5 weeks after infarction using various types of tissue contrast as described in Figure 3. Magnetic susceptibility-induced signal voids are observed throughout the infarct. Their size increases with T2\*-weighting (TE 20 ms). Furthermore, signal voids correspond with blue hem siderin deposits in the Prussian blue image. Epicardial fat, indicated by F, causes a hyperintense signal on the T1W scan and a hypointense signal on T2 and T2\*W scans.



Chapter 10 - Figure 5. A tissue block from the infarct border of a 5-week old infarction was scanned at high-resolution *ex vivo*. Panel A shows the von Kossa's (calcium) and von Gieson (collagen) staining. Red staining corresponds with collagenous (scar) tissue. Yellow staining corresponds with muscle fibers. Black calcium deposits were not observed in this section. In Panel B a serial section is shown after Prussian blue staining. Panel C shows the corresponding slice from the MRI T2\*W data set. Panel D show the same section as in Panel B, however blue regions are artificially enhanced. MRI signal voids correspond with blue hemosiderin particles and not with calcium, fat or collagenous tissue. Panel E shows the same section as in Panel B at higher magnification. Blue hemosiderin deposits can be appreciated. Panel F shows a serial section after HE staining. Panel G shows the corresponding region in the image of Panel A. Area of signal voids correspond with blue hemosiderin deposits in Panel E. Panel H shows the boxed region in Panel F at higher magnification; hemosiderin deposits are visible as brownish particles (black arrows). Bar indicates 4 mm in Panels A to D. Bar indicates 400  $\mu$ m in Panels E to G and 40  $\mu$ m in Panel H.





## Acknowledgments

Allereerst wil ik mijn promotor professor Duncker bedanken. Beste Dirk, toen ik mij in 1999 bij jou meldde met de vraag of ik onderzoek kon doen in het buitenland op het gebied van de cardiologie werd ik meteen aangestoken door jouw enorme enthousiasme voor je werk maar ook voor niet-werk gerelateerde zaken. Sindsdien heb je me steeds ontzettend goed op weg geholpen. Je stimuleert mensen echt het beste uit zichzelf te halen en dat met de humor die noodzakelijk is wanneer er hard gewerkt moet worden. Ik hoop dat we nog lang samen door kunnen werken.

Beste professor Simoons, dank voor de gelegenheid die U mij geboden heeft om in 2002 als AGIKO te beginnen in het Thoraxcentrum. Zonder Uw vertrouwen toen was ik nu niet zo ver gekomen.

Beste professor Verdouw, beste Piet, dankzij Uw enthousiasme was in 1999 binnen enkele dagen een stage plek geregeld bij professor Opie waar ik voor het eerst kennis maakte met basaal onderzoek binnen de cardiologie. Die eerste experimenten in Kaapstad hebben ook mijn enthousiasme gewekt en hebben ertoe bijgedragen dat ik op het ingeslagen pad verder ben gegaan.

Graag wil ik de overige leden van de promotiecommissie hartelijk danken voor de beoordeling van dit manuscript: professor van der Giessen, professor Doevendans en professor Janssens.

De medewerkers en het secretariaat van de afdeling Experimentele Cardiologie van het Thoraxcentrum Rotterdam dank ik voor alle hulp die ik gekregen heb bij het vergaren van de data, de kritische noten en praktische ondersteuning. Rob van Bremen, bedankt voor alle hulp bij het draaiende houden van alle computers die ik versleten heb en uiteindelijk geëindigd zijn in de koelkast en voor het benodigde bakje espresso op zijn tijd. Mijn kamergenoten: Inge, Maaïke en Amber, het was erg gezellig om met zoveel vrouwen op een kamer te mogen zitten, bedankt daarvoor. Amber, succes met de afronding van jouw proefschrift. Liz, Marcel en Hans bedankt voor alle hulp bij mijn eerste schreden op celkweekgebied.

Mijn mede-AGIKO Olivier Man in 't Veld heel veel succes met jouw promotie. Ik vind het erg leuk dat we vanaf onze eerste kennismaking in de Eureka week nog steeds dezelfde richting op gaan. Het is af en toe wel zwaar om de klinische werkzaamheden te combineren met onderzoek en het kritisch doorlezen van andermans manuscripten, maar ik heb je hulp ontzettend gewaardeerd. Houd vol, je bent er bijna.

Alle medewerkers van het laboratorium van professor Taylor, Duke University, Durham, North-Carolina wil ik hartelijk danken voor de goede start die zij mij gegeven hebben in 2002. Dear Doris, thanks for giving me the opportunity to spend some time in your lab and getting acquainted with the American way of doing research. It helped me a lot getting started. Dear Bryce and Anjul, Rick, Priya, Jamie, Yoshi, Mimi, Sharon, Ruth and Pablo, thanks for making me feel at home in a strange city and teaching me my first cell culture techniques, thoracotomies, eating Mexican and the correct pronunciation of the

word “muffin”. I enjoyed being in your company although we had some tough times: I will never forget those 72 hours without power when it was freezing outside and spending the night in a lab chair.

Medewerkers van de afdeling radiologie, Timo Baks, Piotr Wielopolski, Robert-Jan van Geuns en Monique Bernsen, bedankt voor het meedenken en meehelpen met de MRI proeven. Piotr, je bent de enige echte “scientist” die ik ken, als jij iets uitlegt voel ik me nog altijd klein en erg nietig.

Merci en grazie Barend Mees, voor al je hulp en gezelligheid bij het oogsten van alle beenmergen en het maken van de cryoinfarcten. Succes met jouw wetenschappelijke en klinische carrière.

Bart Rövekamp, samen zijn we begonnen aan een groot avontuur in 1999 dat waarschijnlijk de echte basis was voor dit proefschrift: het Cape Heart Centre in Kaapstad. Jouw geestdrift om elke dag nieuwe, soms onmogelijke plannen te maken in combinatie met mijn meer nuchtere kijk op de dingen heeft ons heel ver gebracht: Niet alleen achter het Langendorff perfusie apparaat maar ook heel Afrika door. Dat was een schitterende tijd waar ik met veel plezier aan terug denk.

Een speciaal dankwoord ben ik verschuldigd aan mijn paranimfen: Monique de Waard en Kasper Wulms. Lieve Monique, jij was onmisbaar bij het uitvoeren van de muizenproeven. Jou aan het werk te zien boven de stereomicroscoop was in het begin erg ongrijpbaar, je had thoraxchirurg moeten worden heb ik vaak gezegd. Met heel veel plezier denk ik terug aan de tijd op het lab, door de gezelligheid gingen de vaak lange dagen met erg veel muizen snel voorbij. Heel veel succes met jouw eigen proefschrift, het is een kwestie van volhouden! Beste Kasper, het is niet meer dan logisch dat jij mijn tweede paranimf bent. Ook al ligt jouw kennis en kunde op een heel ander, meer kwalitatief vlak, je bent en blijft een echte wetenschapper, al maakt de praktijk het soms niet makkelijk om echte wetenschap ook te bedrijven. Al vanaf onze eerste kennismaking op de Rivierstraat in 1995 ben je altijd erg geïnteresseerd geweest in het wel en wee van mijn onderzoeksprikelen. Met veel plezier denk ik terug aan de lange avonden (en nachten!) aan de keukentafel waar alle facetten van het leven besproken werden, vaak na een zeldzaam goed diner. Je bent het aan jezelf verplicht in ieder geval nog eens een boek te schrijven, daar wacht ik op.

Fred, Paulien en Jiska, jullie zijn vanaf het begin altijd erg belangstellend geweest voor mij en mijn onderzoek. Alle gepubliceerde artikelen gingen altijd de rivier over. Dat heb ik altijd erg gewaardeerd. Een betere schoonfamilie kan ik mij niet wensen.

Uiteraard wil ik mijn familie bedanken voor de steun de afgelopen jaren. Lieve papa en mama, jullie hebben mij altijd gestimuleerd om mijn talenten zo goed mogelijk te gebruiken. Dat heeft ertoe bijgedragen dat ik uiteindelijk zo ver gekomen ben en de interesse voor de cardiologie binnen de familie blijft. Dank jullie wel voor de kansen die jullie mij geboden hebben en de steun en liefde. Lieve Martijn en Jan-Bart, 2006 wordt een jaar waarin heel erg veel gebeurd is: het waren grote veranderingen voor ons alledrie! Ik ben blij dat we allemaal ons geluk gevonden hebben.

Lieve Riet, promoveren kost erg veel tijd hebben we samen gemerkt. Het wordt dan nog eens extra lastig als je ook gaat trouwen in de week dat het boekje af moet zijn. Toch is het gelukt! Je liet me altijd vrij en stimuleerde me waar nodig om dit project succesvol af te kunnen ronden. Ik ben erg blij met jou. Dank je wel voor de fantastische tijd die we samen hebben. We gaan nu een nog veel grotere uitdaging tegemoet!

Ewout-Jan van den Bos



## List of publications

### Full papers

1. van den Bos EJ, Mees BME, de Waard MC, de Crom R, Duncker DJ. A novel model of cryoinjury-induced myocardial infarction in the mouse: a comparison with coronary artery ligation. *Am J Physiol Heart Circ Physiol* 2005;289:H1291-300.
2. Zhang Z, van den Bos EJ, Wielopolski PA, de Jong-Popijus M, Bernsen MR, Duncker DJ, Krestin GP. In vitro imaging of single living human umbilical vein endothelial cells with a clinical 3.0-T MRI scanner. *MAGMA* 2005;18:175-85.
3. van den Bos EJ, Thompson RB, Wagner A, Mahrholdt H, Morimoto Y, Thomson LE, Wang LH, Duncker DJ, Judd RM, Taylor DA. Functional assessment of myoblast transplantation for cardiac repair with magnetic resonance imaging. *Eur J Heart Fail* 2005;7:435-43.
4. Thompson RB, van den Bos EJ, Davis BH, Morimoto Y, Craig D, Sutton BS, Glower DD, Taylor DA. Intracardiac transplantation of a mixed population of bone marrow cells improves both regional systolic contractility and diastolic relaxation. *J Heart Lung Transplant* 2005;24:205-14.
5. Zhang Z, van den Bos EJ, Wielopolski PA, de Jong-Popijus M, Duncker DJ, Krestin GP. High-resolution magnetic resonance imaging of iron-labeled myoblasts using a standard 1.5-T clinical scanner. *MAGMA* 2004;17:201-9.
6. van den Bos EJ, Davis BH, Taylor DA. Transplantation of skeletal myoblasts for cardiac repair. *J Heart Lung Transplant* 2004;23:1217-27.
7. Thompson RB, Parsa CJ, van den Bos EJ, Davis BH, Toloza EM, Klem I, Glower DD, Taylor DA. Video-assisted thoracoscopic transplantation of myoblasts into the heart. *Ann Thorac Surg* 2004;78:303-7.
8. Thompson RB, van den Bos EJ, Esposito DJ, Owen CH, Glower DD. The effects of acute afterload change on systolic ventricular function in conscious dogs with normal vs. failing hearts. *Eur J Heart Fail* 2003;5:741-9.
9. Thompson RB, Emani SM, Davis BH, van den Bos EJ, Morimoto Y, Craig D, Glower D, Taylor DA. Comparison of intracardiac cell transplantation: autologous skeletal myoblasts versus bone marrow cells. *Circulation* 2003;108:II264-71.
10. van den Bos EJ, Taylor DA. Cardiac transplantation of skeletal myoblasts for heart failure. *Minerva Cardioangiol* 2003;51:227-43.
11. van den Bos EJ, Wagner A, Mahrholdt H, Thompson RB, Morimoto Y, Sutton BS, Judd RM, Taylor DA. Improved efficacy of stem cell labeling for magnetic resonance imaging studies by the use of cationic liposomes. *Cell Transplant* 2003;12:743-56.
12. Minners J, van den Bos EJ, Yellon DM, Schwalb H, Opie LH, Sack MN. Dinitrophenol, cyclosporin A, and trimetazidine modulate preconditioning in the isolated rat heart: support for a mitochondrial role in cardioprotection. *Cardiovasc Res* 2000;47:68-73.

13. van den Bos EJ, Baks T, Moelker AD, Kerver W, van Geuns RJ, van der Giessen WJ, Duncker DJ, Wielopolski PA. Magnetic resonance imaging of hemorrhage within reperfused myocardial infarcts: Possible interference with iron oxide-labeled cell tracking? *Eur Heart J* 2006;27:1620-6.
14. van den Bos EJ, de Waard MC, Davis BH, Bergen J, Taylor DA, Duncker DJ. Mechanisms and dynamics of myoblast death after transplantation into a myocardial infarction. Submitted.
15. Manintveld OC, te Lintel Hekkert M, van den Bos EJ, Suurenbroek GM, Dekkers DH, Verdouw PD, Lamers JM, Duncker DJ. Cardiac effects of postconditioning depend critically on the duration of index ischemia. Submitted.

### Book chapters

- Doris A. Taylor, Ewout J. van den Bos. Novel approaches to cardiac regeneration – The (pre-clinical) reality of myoblast transplantation.

### Abstracts published in peer reviewed journals

1. Morimoto Y, Bergen JM, Davis BH, van den Bos EJ, Taylor DA. Nonviral FasL protects allogeneic myoblasts against cell death in cardiomyogenesis. *JACC* 2004;43:A177.
2. Morimoto Y, Davis BH, van den Bos EJ, McMichael MD, Taylor D. Transplanted bone marrow derived mesenchymal stem cells fuse with cardiomyocytes. *Circulation* 2003;108:548.
3. van den Bos EJ, Thompson RB, Wagner A, Mahrholdt H, Morimoto Y, Duncker DJ, Judd RJM, Taylor DA. Functional assessment of myoblast transplantation with magnetic resonance imaging. *Eur Heart J* 2003;24:S715.
4. van den Bos EJ, Minners J, Opie LH, Sack MN. Trimetazidine abolishes ischemic and drug-induced preconditioning: Does mitochondrial protection antagonize preconditioning-like cardioprotection? *Circulation* 2000;102:S1319.
5. Minners J, Meiring JJ, van den Bos EJ, Opie LH, Sack, MN. Inner mitochondrial membrane modulation in preconditioned myotubes: A putative role for mitochondrial homeostasis in enhanced tolerance to ischemia. *Circulation* 2000;102:S1402.
6. van den Bos EJ, Minners J, Opie LH, Sack, MN. Trimetazidine (TMZ) abolishes drug-induced and attenuates ischaemic preconditioning - further support for a mitochondrial role in preconditioning. *Eur Heart J* 2000;21: P3636.
7. van den Bos EJ, Minners J, Opie LH, Sack, MN. Cyclosporin A-mediated preconditioning-like cardioprotection is abolished by trimetazidine - proposed role of mitochondrial homeostasis in preconditioning. *Eur Heart J* 2000;21:P3633.





## Curriculum Vitae

De auteur van dit proefschrift werd op 2 april 1977 geboren in Rotterdam. Na het eindexamen met succes te hebben afgelegd in 1995 aan het Stedelijk Gymnasium te Breda studeerde hij geneeskunde aan de Erasmus Universiteit te Rotterdam. Tijdens zijn studie verrichte hij onder andere onderzoek naar sikkelcelziekte in het St. Elisabeth Hospitaal te Willemstad, Curaçao (dr. A.J. Duits). Het afstudeer onderzoek dat onderdeel uitmaakt van het doctoraal examen werd verricht in het Cape Heart Centre, University of Cape Town te Kaapstad, Zuid-Afrika (prof. dr. L.H. Opie). Hij kreeg hiervoor subsidie in het kader van het dr. E. Dekker programma van de Nederlandse Hartstichting. De scriptie die hier het resultaat van was won de Gerrit Jan Mulder prijs 1999 voor beste afstudeer scriptie aan de Faculteit der Geneeskunde, Erasmus Universiteit Rotterdam. De co-schappen werden voor een deel doorlopen in het St. Elisabeth Hospitaal te Willemstad, Curaçao. Het artsexamen werd met lof behaald in januari 2002. Hierna startte hij als arts-onderzoeker op de afdeling Experimentele Cardiologie van het Erasmus MC onder leiding van prof. dr. D.J. Duncker met het promotieonderzoek waarvan dit proefschrift het eindresultaat is. Hij was hiermee de eerste assistent-geneeskundige in opleiding tot klinisch onderzoeker (AGIKO) van het Thoraxcentrum Rotterdam. Tijdens de onderzoeksperiode werd een periode van 7 maanden doorgebracht in het laboratorium van prof. dr. D.A. Taylor, Duke University, Durham, USA. In 2003 won de auteur de International Society of Heart and Lung Transplantation Research Award voor het onderzoeksvoorstel getiteld "Tracking of progenitor cells in the coronary circulation with magnetic resonance imaging." Met de klinische opleiding tot cardioloog werd in juli 2003 aangevangen (opleider prof. dr. M.L. Simoons). In juli 2005 werd begonnen met de vooropleiding Interne Geneeskunde in het Albert Schweitzer Ziekenhuis te Dordrecht (opleider dr. A.C.M van Vliet). Hij is getrouwd met Rieteke Peteroff.



The studies in this thesis were supported by:

International Society for Heart and Lung Transplantation Research Fellowship  
Award 2003

Zon-MW Agiko stipend 920-03-191

Additional financial support for the publication of this thesis was  
generously provided by:

Erasmus University Rotterdam

Netherlands Heart Foundation

Zon-MW

And by the following companies:

Bioheart

St. Jude Medical

Astellas Pharma

AstraZeneca

Boehringer-Ingelheim

Boston Scientific

Bristol-Myers Squibb

Cardialysis

Cordis

Guidant

